REPORT DOCUMENTATION PAGE

Form Approved
OMB NO. 0704-0188

1. AGENCY USE ONLY (Leave Blank)	2. REPORT DATE	3. REPORT TYPE AND DATES COVERED
	07 March 2003	Final Technical Report 01 April 1999 – 31 December 2002

4. TITLE AND SUBTITLE
Nonlinear Distortion and Disintegration of Conical Liquid Sheets at High Pressure

5. FUNDING NUMBERS
DAAD 19-99-1-0204

6. AUTHOR(S)
William A. Sirignano and Carsten Mehring

7. PERFORMING ORGANIZATION NAME(S) AND ADDRESS(ES)
Department of Mechanical & Aerospace Engineering
University of California, Irvine
Irvine, CA 92697-3975

8. PERFORMING ORGANIZATION REPORT NUMBER

9. SPONSORING / MONITORING AGENCY NAME(S) AND ADDRESS(ES)

U. S. Army Research Office
P.O. Box 12211
Research Triangle Park, NC 27709-2211

11. SUPPLEMENTARY NOTES
The views, opinions and/or findings contained in this report are those of the author(s) and should not be construed as an official Department of the Army position, policy or decision, unless so designated by other documentation.

12 a. DISTRIBUTION / AVAILABILITY STATEMENT

Approved for public release; distribution unlimited.

12 b. DISTRIBUTION CODE

13. ABSTRACT (Maximum 200 words)

The research has identified, characterized, and quantified various important domains of behavior in the nonlinear distortion and disintegration of injected liquid fuel streams. Various liquid-stream configurations resulting from fuel injectors have been analyzed: conical, annular and planar streams with and without swirl; twin-fluid and single-fluid atomizers. Linear and nonlinear theories of distortion and disintegration have been developed and have predicted initial stream break-up characteristics. Distinct regimes of ligament break-up and cellular break-up have been determined. Modulations of both liquid streams and gas streams have been studied as means of active control. The characteristics of two-dimensional capillary wave phenomena have been determined. The effects of impacting gas jets have been compared with the Kelvin-Helmholtz effect of parallel jets. Pulsed gas jets have been shown to be more effective than gas jets as a break-up mechanism. The importance of the rate of forced stretching of the liquid stream compared to the rate of disturbance propagation in the stream (i.e., capillary wave velocity or characteristic viscous velocity) has been quantified; various regimes for the forced stretching have been identified and characterized.

14. SUBJECT TERMS	15. NUMBER OF PAGES
Atomization, Sprays, Capillary Instability, Liquid Injection	216
	16. PRICE CODE

17. SECURITY CLASSIFICATION OR REPORT	18. SECURITY CLASSIFICATION ON THIS PAGE	19. SECURITY CLASSIFICATION OF ABSTRACT	20. LIMITATION OF ABSTRACT
UNCLASSIFIED	UNCLASSIFIED	UNCLASSIFIED	UL

FINAL TECHNICAL REPORT
NONLINEAR DISTORTION AND DISINTEGRATION OF CONICAL LIQUID SHEETS AT HIGH PRESSURE

ARO Grant/Contract No. DAAD19-99-1-0204

Principal Investigator: William A. Sirignano
Reporting Period: 1 April 1999 - 31 December 2002
Institution: University of California, Irvine

Prepared by William A. Sirignano and Carsten Mehring

Summary

The research has identified, characterized, and quantified various important domains of behavior in the nonlinear distortion and disintegration of injected liquid fuel streams. Various liquid-stream configurations resulting from fuel injectors have been analyzed: conical, annular, and planar streams with and without swirl; twin-fluid and single-fluid atomizers. Linear and nonlinear theories of distortion and disintegration have been developed and have predicted initial stream break-up characteristics. Distinct regimes of ligament break-up and cellular break-up have been determined. Modulations of both liquid streams and gas streams have been studied as means of active control. The characteristics of two-dimensional capillary wave phenomena have been determined. The effects of impacting gas jets have been compared with the Kelvin-Helmholtz effect of parallel jets. Pulsed gas jets have been shown to be more effective than gas jets as a break-up mechanism. The importance of the rate of forced stretching of the liquid stream compared to the rate of disturbance propagation in the stream (i.e., capillary wave velocity or characteristic viscous velocity) has been quantified; various regimes for the forced stretching have been identified and characterized.

I. Introduction

The research program focused on an extension of previous studies on planar and axisymmetric swirling and non-swirling annular liquid sheets. Effects of a surrounding gas-phase on the distortion and disintegration of the injected liquid stream has beeen analyzed for a practical two-dimensional twin-fluid atomizer configuration. Directly (through a liquid-phase) or indirectly (via a gas-jet) modulated sinuous (anti-symmetric) and dilational (symmetric) film distortion have been analyzed and evaluated with respect to the atomization efficiency.

Active control of liquid stream distintegration has been analyzed for three-dimensionally modulated swirling conical liquid films. The latter configuration is of practical relevance in state-of-the-art injector systems of combustion engines. In this context, a linear analysis of three-dimensionally distorting swirling annular liquid films has been performed in order to provide guidance for the studies of nonlinearly distorting swirling annular and conical sheets with three-dimensional disturbances. Comparison between linear and nonlinear results for

the annular case quantifies the influence of nonlinear effects on film distortion and film breakup.

In an effort to understand better the dynamics of the larger ligaments first detached from a continuous discharging liquid stream, an analysis of the dynamic stretching of a two-dimensional liquid film has been conducted. This analysis included the consideration of liquid viscosity and long range intermolecular forces in addition to surface tension and liquid inertia.

In the following three sections, we will summarize major findings from the described analyses of: planar liquid films discharging from twin-fluid atomizers; the capillary stability of modulated swirling liquid films; and the dynamic stretching of a planar liquid bridge. The details of the analyses, results and literature reviews are provided in References 1 through 5; since they are not yet in print, copies of References 1,4 and 5 are attached as addenda to this report. References 6 though 13 are conference papers and a book article, the former preceeding the primary journal articles (1-5).

II. Planar Liquid Film Discharging From Twin-Fluid Atomizer

The flowfield in the vicinity of a twin-fluid atomizer has been analyzed numerically. See Reference 1. Considered is a thin two-dimensional inviscid incompressible liquid film discharging from the atomizer centerline surrounded on both sides by gas jets that impact symmetrically (in phase) or antisymmetrically (out of phase) onto the discharging film. The value of the ambient pressure is manifested through the density ratio. Initial film distortion is enforced actively by: 1) modulation of the impacting gas jets (indirect or gas-phase modulation) with gas momentum components parallel and normal to the liquid stream, 2) modulation in the liquid-phase at the atomizer exit (direct or liquid-phase modulation) or 3) direct liquid film modulation with superposition of continuous gas streams. The investigation focused on gas-phase modulated films. Effects of different flow parameters on film breakup characteristics were studied by varying one of the flow parameters from a given base-case configuration.

For direct (i.e., gas-phase) modulated films, energy input at the gas-inlet ports was found to be inadequate in identifying effective film rupture conditions, the latter being characterized by short break-up length and times at minimum energy input into the system. For the parameter domain surrounding the considered base case, film rupture was obtained more effectively by sinuous forcing and subsequent nonlinear sinuous-dilational mode coupling rather than by dilational forcing at the same average energy flux into the system. Also, it was observed that intermediate gas-jet pulsing (without underlying continuous gas flow) can yield the same or larger amplitude disturbances than obtained through wave growth from continuous jets at the same overall energy input into the system.

Direct modulation of liquid-phase flow-parameters, i.e. axial or transverse film velocity, at the nozzle exit is more effective than gas-jet modulation, the latter transferring only a portion of the modulation energy onto the film. Computational results also indicate that for direct liquid-phase forcing, dilational modulation (i.e. modulation yielding dilational film distortion) is more effective in causing film rupture than sinuous modulations, while,

as noted earlier, the opposite is true for gas-jet modulated liquid films. Also, for liquid-phase modulated films, admission of ambient gas streams significantly reduces sinuous mode wavenumbers whereas influence on wavelengths remains small for dilationally distorting films.

For gas-phase modulated films, variations of Weber number, gas-jet-to-liquid-film momentum ratio, gas-to-liquid density ratio and pulse period were considered and their effect on film distortion was analyzed. An increase in Weber number from its base-case value (i.e. from 10 to 25) resulted in stretched band-like films and a delay in film rupture due to reduced sinuous-dilational mode coupling. On the other hand, reduction in Weber number (i.e. from 10 to 5) resulted in smaller disturbance amplitudes and larger break-up time and length despite stronger nonlinear mode coupling manifested by the contraction of the film into fluid cylinders connected by thinner fluid films. Transverse deflection of the film centerline for a five-fold increase in density ratio was similar to the one observed for the increased Weber number case; however, fluid blob formation was still observed.

A five-fold increase in vertical or parallel gas-jet-to-liquid-film-momentum ratio resulted in "immediate" film rupture caused by the dynamics of the impacting gas jets rather than by continuous growth of film disturbances downstream with energy transfer from the adjacent gas-streams.

Variation in pulse period affects film distortion in two ways: It changes the amplitude of the initial film disturbances generated by the pulsed gas-jets, since increasing the pulse period provides more time for transverse film movement (due to one-sided gas-jet impact) before being counter-acted by an opposed gas jet. On the other hand, it alters the wavelengths of the disturbances generated on the film and therefore the gas-to-liquid energy transfer downstream from Kelvin-Helmholtz-type wave growth.

At constant gas-to-liquid jet momentum ratio, higher ambient pressure conditions, i.e. higher gas-to-liquid density ratios, will affect film distortion and disintegration only through changes in the film dynamics or interface dynamics. If the ambient pressure or gas-to-liquid density ratio is increased while keeping the gas- and liquid-phase velocities constant, film distortion is determined by the interface dynamics directly but also indirectly through the changed gas-phase momentum influx which will affect the force balance at the interfaces. With increasing density ratio, larger sections of the discharging liquid film are being deflected by the impacting gas jets and film rupture time is greatly reduced. Rupture or rather film tearing occurs before the development of a wave structure on the discharging film. A similar behavior is observed if gas and liquid injection velocities are kept constant rather than the momentum ratio. The density-ratio effects described above are identical in the limit where the gas-jet-momentum influx is reduced to zero. In that case, i.e. for a liquid film moving through a quiescent gas, linear (and also nonlinear) theory shows that (temporal) growth rates of unstable sinuous (and dilational) waves present on the liquid film increase with increasing density ratio at fixed liquid Weber number.

Details of the described analysis and of the results are provided in the first addendum (Reference 1) to this report.

III. Capillary Stability of Modulated Swirling Liquid Films

Linear and nonlinear analyses of modulated three-dimensionally distorting thin inviscid free liquid films discharging into a gas of negligible density have been presented. See References 2, 3 and 4. The nonlinear numerical analysis uses a lubrication model reducing the three-dimensional problem to a system of two-dimensional unsteady equations. Linear theory for swirling annular films predicts that for We > 2 only one unstable wave is generated on the film due to its modulation at the nozzle exit. Depending on Weber number and film radius, linear growth rates for this unstable dilational mode wave might be larger for non-axisymmetric modes than for the corresponding axisymmetric case. However, for the considered parameter range, maximum growth rates for a given Weber number and annular radius are still observed for the axisymmetric case. Modulation of multiple dilational mode waves at the nozzle exit allows for uniform breakdown of swirling and non-swirling annular films indicated by the generation of uniformly sized liquid volumes which are uniformly spaced and connected by thinner liquid layers. Film topology and break-up of three-dimensionally modulated conical films were discussed. Comparison with the corresponding swirling annular film shows that for sinuous film modulation, film divergence causes the separation of initially formed larger fluid blobs into a pair of smaller fluid volumes connected by an even thinner liquid layer.

On clockwise swirling conical films, spiraling dilational and sinuous waves moving in the clock-wise direction increase in slope as the film thins out in the downstream direction. The slope of counter-clockwise propagating waves decreases with downstream distance. The described changes in slope can be attributed to a decrease in swirl velocity with increase in annular film radius downstream that results from the conservation-of-angular-momentum principle. Based on the location of the initial film rupture points and the thickness distribution at the time of film rupture, characteristic break-up pattern have been identified for the cases with pure standing or travelling dilational or sinuous mode waves modulated at the nozzle. For mixed standing/travelling and sinuous/dilational wave modulation, the break-up pattern are modified or mixed versions of the patterns identified for the pure cases. For the investigated cases with travelling dilational or sinuous mode circumferential waves, superposition with the imposed axial wave results in an oblique wave spiraling clock-wise downstream on the annular or conical film. Here, initial film breakup occurs simultaneously at various points with constant downstream distance. The perforations are expected to expand along the line of minimum film thickness which results in the formation of liquid filaments spiraling downstream in the counter-clockwise direction ("filament break-up"). On swirling annular films with superimposed dilational standing-wave modulations in the circumferential direction, film rupture first occurs after the formation of larger fluid blobs and upstream just behind these larger fluid masses. Again, initial film rupture will take place simultaneously at various locations at the same downstream position. Subsequent expansion of the film perforations can be expected to generate a more or less circular pattern within each cell formed by neighboring fluid blobs. This type of film rupture can be characterized as "cellular break-up". The same break-up pattern can also be observed for non-swirling (pressure-stabilized) annular films and for swirling conical films with similar forcing con-

ditions. However, due to film divergence the "cells" will stretch in the conical case and film thickness within the cells will be reduced. Therefore, expansion of the film perforation is expected to occur significantly faster than in the corresponding annular case. However, initial rupture of the film in the conical case is delayed. Analogous to the dilational case discussed earlier, initial film perforation for swirling annular films with modulated standing sinuous circumferential waves takes place just behind the larger fluid blobs. However, in this case the perforations are expected to propagate in the circumferential direction at a (more or less) constant downstream distance, ultimately resulting in the detachment of fluid rings with pronounced thickness fluctuations in the circumferential direction ("ring break-up"). The similar standing wave sinuous mode modulation imposed onto the conical film geometry yields a "filament break-up" pattern. The filaments are spiraling clock-wise in the downstream direction. In contrast to the single wave modulation, breakup of these filaments will be greatly influenced by the existing non-uniform mass distribution along the filaments.

Details of the three-dimensional analysis and the preceeding axisymmetric analysis of swirling annular and conical films are provided in References 2, 3 and 4. Reference 4 is not yet in print so a copy is provided as second addendum to this report.

IV. Dynamic Stretching of A Planar Liquid Bridge

A thin incompressible viscous planar free liquid film in a void and under zero gravity was analyzed by means of the previously developed reduced-dimension (lubrication) approach extended to include liquid viscosity and long-range intermolecular forces. Linear analysis focused on films with harmonic modulations in the axial film velocity enforced at the ends of the planar bridge. Effect of changes in the problem parameters on the overall distortion characteristics of the film were discussed. Nonlinear film distortion and break-up was investigated for the case of temporally increasing velocity at the end of the film resulting in continuous film stretching eventually leading to film rupture. Implementation of the employed numerical model was validated for the linear limit by comparison with the analytical linear solutions and for harmonically modulated film-end velocities.

The importance of the film stretching rate in comparison to either the capillary wave velocity or the characteristic viscous velocity has been demonstrated. If the stretching rate is large, the distortion signals are slow in reaching large distances from the forced end; so distortion is confined to a smaller portion of the sheet. For small stretching rates, the distortion is significant over a larger portion of the film.

For films with an initial length-to-thickness ratio of $O(10)$ and with a time-scale for film-end acceleration (from zero to maximum pull velocity) comparable to the propagation time of capillary waves from film end through film center, various distinct film topologies were observed, depending on Weber number and Reynolds number. Here, film topology is typically characterized by three distinct regions, i.e. a film wedge forming at the pulling end(s), the film center region and a transition region. The size and shape of these regions greatly depends on the particular case under investigation.

For cases with length-to-thickness ratio of $O(100)$ information on the acceleration of the film ends does not reach the film center region. Here, evolution of film topology is similar

for all the considered Weber number and Reynolds number combinations; with a more or less undisturbed film center region smoothly transitioning into a narrow liquid wedge at the pulling end. For cases with low film-end acceleration, film rupture is significantly delayed resulting (in all the considered cases) in a significantly stretched film prior to rupture with or without significant amounts of fluid remaining in the film center region.

Nonlinear film distortion has also been investigated for the continuously compressed planar film bridge, illustrating the relevance of the film bridge analysis for the contracting and stretching of a free planar film such as those found in the atomization process of liquid fuels in typical gas turbine combustors. Film distortion characteristics observed for continuously compressed planar films conform with observations made by other authors for the similar case of contracting free liquid films.

Details of the described stretching-film analysis are provided in Reference 5; since it is not yet in print, a copy is attached as the third addendum to this report.

References

[1] C. Mehring and W. A. Sirignano, "Disintegration of Planar Liquid Film Impacted by Two-Dimensional Gas Jets," Physics of Fluids, in press.

[2] W. A. Sirignano and C. Mehring, "Review of Theory of Distortion and Disintegration of Liquid Streams," Progr. Eng. and Comb. Science, Vol. 26, pp. 609-655.

[3] C. Mehring and W. A. Sirignano, "Nonlinear Capillary Waves on Swirling, Axisymmetric Free Liquid Films," Int. J. Multiphase Flow, Vol. 27, pp. 1707-1734.

[4] C. Mehring and W. A. Sirignano, "Capillary Stability of Modulated Swirling Liquid Films," Atomization and Sprays, submitted for publication.

[5] C. Mehring and W. A. Sirignano, "Dynamic Stretching of A Planar Liquid Bridge," Physics of Fluids, submitted for publication.

[6] W. A. Sirignano and C. Mehring, "Disintegration and Distortion of Liquid Streams," Chapter in AIAA Progress Series, in press.

[7] C. Mehring and W. A. Sirignano, "Dynamic Stretching of a Thin Planar Liquid Bridge," Proc. 15th Ann. Conf. Liquid Atom. Spray Sys., 2002.

[8] C. Mehring and W. A. Sirignano, "Three-dimensional Capillary Stability of Modulated Swirling Liquid Films," Proc. 14th Ann. Conf. Liquid Atom. Spray Sys.. 2001.

[9] C. Mehring and W. A. Sirignano, "Free Planar Liquid Films Impacted by Gas Jets," Proc. 14th Ann. Conf. Liquid Atom. Spray Sys., 2001.

[10] W. A. Sirignano and C. Mehring, "Comments on Energy Conservation in Liquid-Stream Disintegration," 8th Int. Conf. on Liquid Atom. and Spray Sys., 2000.

[11] C. Mehring and W. A. Sirignano, "Planar-Liquid-Stream Distortion from Kelvin-Helmholtz and Capillary Effects," 8th Int. Conf. on Liquid Atom. and Spray Sys., 2000.

[12] C. Mehring and W. A. Sirignano, "Nonlinear Capillary Waves on Swirling Axisymmetric Liquid Films," AIAA 2000-0432.

[13] W. A. Sirignano and C. Mehring, "Review of Theory of Distortion and Disintegration of Liquid Streams," AIAA 99-3641.

PF # 2326

Disintegration of Planar Liquid Film Impacted by Two-Dimensional Gas Jets

C. Mehring[a)] and W. A. Sirignano[a)]

Department of Mechanical and Aerospace Engineering, University of California, Irvine

(July 23, 2002)

Abstract

The distortion and break-up of a thin planar liquid film impacted by two gas jets while discharging from a twin-fluid atomizer is studied numerically. The gas momentum vector has components normal and parallel to the liquid stream. Viscosity and compressibility are neglected in both the liquid phase and the gas phase. The reduced-dimension (lubrication) approximation is employed to describe the nonlinear distortion and breakup of the thin film. The gas-phase dynamics are modelled by using a boundary-element-method formulation. For the considered parameter range and for a given energy expenditure, direct modulation of liquid-phase velocities at the nozzle exit is found to be more effective in causing film rupture than indirect modulation via adjacent impacting gas jets. In the former case, dilational film modulation results in shorter breakup lengths than sinuous modulation. On the other hand, for gas-jet modulated films, sinuous mode forcing is more effective than dilational forcing for the same energy input. Co-flowing gas streams significantly alter wavelengths and amplitudes of film disturbances generated by direct film modulation. Large ratios of gas-jet momentum to liquid-film momentum result in "immediate" film rupture in response to the dynamics

of the impacting gas jets, whereas for lower ratios films disintegration occurs further downstream after continuous growth of the initial disturbances. Film distortion is characterized by the formation of fluid blobs or long band-like films depending on Weber number values and density ratio.

I. INTRODUCTION

In the past, free liquid films have not been analyzed only for their intriguing scientific substance but also due to their relevance for a wide variety of technological applications, including the formation of liquid sprays from fluid films which discharge from so-called atomizer nozzles.[1] The manner in which these films disintegrate into droplets depends upon the type and geometry of the atomizer as well as on the operating conditions. One common type of atomizer is described as the twin-fluid atomizer, where the interfaces of the discharging liquid film are subjected to neighboring gas streams. Here, the main cause of film instability is interaction of the film with the surrounding gas flow either through gas-jet impact or continuous growth (amplification) of film disturbances via energy input from the neighboring gas streams.

Subsequently, we review previous work on discharging free liquid films in an ambient gas phase; some references are also provided considering theoretical or numerical analyses of periodically disturbed infinite films (also with the effect of an ambient gas considered). In subsection A, we review analyses dealing with films under steady discharge and ambient conditions (or boundary conditions). Subsection B addresses previous work on discharging liquid films with modulations enforced onto the liquid phase. In subsection C, we describe the flow configuration considered within the present work.

A. Steady-State Discharging Films

Until the recent past, steady-state operational conditions were imposed onto the prescribed atomization systems. Accordingly, the majority of previous experimental and analytical work focused on the aerodynamic stability of these films under steady free-stream and boundary (e.g., inflow and outflow) conditions.

Arai & Hashimoto[2,3] and Hashimoto & Suzuki[4] presented experimental results on the three-dimensional breakdown of a planar liquid sheet in a high-speed co-current uniform

gas stream under steady-state conditions; more extensive analyses of a similar configuration were later conducted by Mansour & Chigier,[5,6] by Stapper *et al.*[7,8] and discussed by Fernandes *et al.*[9]. In Ref. 9, the authors illustrate that effectiveness of atomization depends not only on gas-to-liquid momentum ratio but also on film thickness, which is attributed to the observation that, for effective film disintegration, the characteristic length scale of perturbations should be of the order of the film thickness. The authors also observe that, for high liquid momentum, the effect of viscous shear on film breakup is confined to a thin region near the gas-liquid interface. In this case, atomization can be improved by superposition of artificial film modulations which can cause disturbances of the inner core. Even though external liquid and gas-phase modulation via piezoelectric transducers or loudspeakers is described in Ref. 9, no results have been presented under such forcing conditions.

Within their work, Arai & Hashimoto[3] also presented a perturbation analysis of the corresponding inviscid three-dimensional boundary-value problem. A linear analysis based on the Orr-Sommerfeld equation was also attempted by Hashimoto & Suzuki.[4] Ibrahim & Akpan[10] presented a three-dimensional linear analysis of a periodically disturbed planar viscous liquid sheet moving in an inviscid gas medium and with axial and transverse sheet disturbances.

Kawano *et al.*[11] investigated annular liquid films discharging from a two-fluid atomizer under various steady-state conditions. The authors also provided a linear temporal analysis for inviscid incompressible annular films subject to unequal gas velocities on both sides of the annular film. A similar, experimental analysis was reported later by Berthoumieu *et al.*[12,13]

Few nonlinear analyses of planar sheets with surrounding gas streams have been reported. Rangel and Sirignano[14] and later Lozano *et al.*[17,18] employed discrete-vortex methods to describe the nonlinear distortion and rupture of two- or three-dimensionally distorting liquid films in a co-flowing gas stream.

The nonlinear calculations conducted in Ref. 14 revealed that: 1) oscillating (stable), sinuous modes exist at gas-to-liquid density ratios of order 1, and 2) sinuous distortion may

result in ligaments interspaced by half of a wavelength, whereas dilational distortion may result in ligaments interspaced by one wavelength. These break-up features were already described by Dombrowski & Hooper[15] and identified later by Jazayeri & Li[16].

In Ref. 17, aerodynamic growth of antisymmetric (sinusoidal) streamwise sheet disturbances with superimposed symmetric (dilational) or antisymmetric disturbances in the transverse direction was studied, in order to better understand the presence of transverse and longitudinal filaments observed in liquid sheet air-assisted atomization experiments. For both initially sinusoidal or dilational transverse sheet disturbances, flattening of the sheet in the transverse direction is reported. The formation of streamwise tubular sections with point edges is predicted when both air/liquid interfaces touch each other at points interspaced by one wavelength in a plane perpendicular to the main flow (i.e. streamwise) direction. As illustrated, and due to the fact that gas and liquid velocities are assumed to be initially oriented in the streamwise direction, the transverse perturbation grows at a slower rate than the streamwise one whose initial growth is exponential (by linear theory). Accordingly, the transverse perturbation growth rate might be insufficient to generate streamwise filaments. In this context, oblique waves have been studied[18] and were found to contribute to the evolution of a finite amplitude transverse wave starting from infinitesimal perturbations. Surface tension effects and edge effects were addressed very briefly in Ref. 18.

B. Modulated Discharging Films

More recently, atomization systems are being developed that aim at an active control of the film disintegration or overall spray formation process in order to optimize certain parameters within in the overall system (e.g., NO_x reduction in spray combustion of fossil fuels[19]). Several experimental and theoretical analyses have addressed this interest.

The spatial stability of thin liquid sheets subject to forced vibrations applied to the nozzle was first investigated by Hagerty & Shea[21] and later by Crapper, Dombrowski & Pyott.[20] The latter authors used the dispersion relation derived by Squire,[22] in order to analyze the spatial

(aerodynamic) growth of sinuous disturbances. Comparison of the theoretical results with experimental observations revealed considerable discrepancies: 1) unstable waves were found at frequencies where linear inviscid theory (based on spontaneous growth of infinitesimally small perturbations) predicts stable waves, and 2) the wave growth saturates (i.e., the wave amplitude eventually no longer grows) as the waves propagate away from the orifice, even for wavelengths which are unstable by the employed linear theory. The latter phenomenon was attributed to the formation of vortices cast off from the wave crests and moving into the troughs.

After Crapper *et al.*,[20] Asare, Takahashi & Hoffman[23] also investigated the stability of liquid sheets, harmonically forced at the nozzle (sinuous disturbances only). Their experimental results (for thin and thick sheets and variable air pressures) agreed well with linear theory[21,22] if the disturbance amplitudes were small and if the observations were made near the nozzle exit. As a result of nonlinear effects, deviations between experimental observations and linear theory were more pronounced at larger downstream positions and for higher forcing amplitudes. Similar to the observations made by Crapper *et al.*,[20] the wave envelope amplitude appeared to saturate at large falling distances, i.e. where the sheet jets begin to break up. Asare *et al.*[23] also provided a simplified trajectory theory based on the force balance for a fluid particle in the crest of a propagating wave. The initial wave envelope amplitudes predicted by this simplified theory agreed well with experimental results and the employed linear theory.

The questions on the discrepancies between linear theory and experimental results raised in Refs. 20 and 23 were subsequently addressed in Refs. 24 and 25. Crapper, Dombrowski & Jepson[24] presented a linear analysis for both sinuous and dilational waves on thin viscous liquid sheets in a viscous gas flow (with focus on sinusoidal waves with wavelengths much longer than the sheet-thickness). They found that liquid viscosity has no effect on the initial wave growth. Furthermore, gas viscosity was found to extend the region of instability over a greater range of frequencies than that given by the inviscid theory; which, as stated in

Ref. 24, might explain the discrepancy with respect to this issue found in Ref. 20. Crapper *et al.*[24] also observed that by their linear viscous theory (i.e. viscous gas and liquid phases), a maximum growth rate does not always exist, which (as stated) indicates that, for these situations, the experimentally observed waves cannot be the fastest growing as hitherto suggested (for example by Squire[22]) but must be imposed on the sheet by some other means, e.g. by a natural frequency of the apparatus. The importance of nozzle vibrations in practical applications was subsequently demonstrated by Crapper & Dombrowski.[25] Capillary waves on planar liquid sheets emanating from a nozzle or atomizer were also observed and investigated experimentally by Hashimoto & Suzuki[4] and held responsible by Clark & Dombrowski[26] for the prescribed discrepancy between their theoretical (infinite-sheet) analysis and experimental results for fan sheets.

More recently, an experimental study on modulated discharging films was also presented by Chung *et al.*[27] The authors provided an extensive study on disintegrating conical liquid films subject to piezoelectric transducer modulations inside the nozzle. The effect of transducer modulation on liquid film disintegration was studied for different fluid viscosities, driving frequencies and input perturbation powers. An optimum driving frequency was identified at which liquid sheet breakup length is shortest. Increased liquid viscosity was found to render liquid modulation less effective delaying liquid film disintegration. Higher input modulation power enhanced liquid disintegration. The authors suggest that break-up length is a function of $cosh^{-1}$ of input power.

The linear analysis of a sinuous and/or dilationally distorting viscous liquid film in a co-flowing ambient inviscid gas has been presented recently by Mitra *et al.*[28] For large Weber numbers (and by using Gaster's relation[29]), the authors extend their analysis to liquid films discharging from a nozzle or atomizer. Film breakup lengths and interface profiles are reported for various combinations of Reynolds number, Weber number, gas-to-liquid density ratio, gas-to-liquid velocity ratios and phase angle between sinuous and dilational mode disturbances; always assuming the presence of sinuous and dilational mode waves with maximum growth rates. Computational results are compared with experimental

observations made by Jazayeri and Li,[30] indicating the inadequateness of their linear theory for large amplitude disturbances, i.e. when nonlinear effect become important. In fact, film breakup as predicted by the described linear analysis solely depends on the dilational mode and is independent of any sinuous mode disturbances. However, large amplitude sinuous mode disturbances have been shown in Ref. 37, as well as by Jazayeri and Li[16] to cause significant dilational film distortion due to nonlinear sinuous-dilational mode coupling. Consequently, any predictions for film break-up length based on linear theory has to be considered with great caution.

Similar to the described linear analysis for viscous films, Jazayeri and Li[31] also extended their nonlinear analysis of Ref. 16 on inviscid liquid films. As in Ref. 30, the authors used Gaster's relation[29] to transform the results of their temporal analysis into a spatial analysis describing the nonlinear distortion of a discharging liquid film into a quiescent ambient gas. Based on this transformation, the authors determine nonlinear film break-up lengths under various operating conditions. Analogous to Ref. 30, the results from the perturbation expansion of Ref. 31 for the spatially developing film always assume the presence of only the dominant wavenumber at the nozzle. The results obtained for the spatially developing film by using the perturbation analysis of Ref. 31 are only valid for large Weber numbers and liquid films that discharge into an overall unrestricted quiescent ambient gas. Practical twin-fluid atomizers do not conform to this assumption. In context with the large Weber number assumption, it is worthwhile to notice that dilational capillary waves on thin films are dispersive in nature with increase in wave velocity for decreasing disturbance wavelength.[37] Consequently, for finite Weber number values, propagation velocities of shorter wavelength disturbances will always deviate from the film discharge velocity. Also, results for spatially developing films obtained from a temporal analysis via transformation using Gaster's relation[29] do not consider the physical constraints imposed at the nozzle exit in a practical situation.

The nonlinear analysis presented here differs from the analysis presented in Ref. 31. The employed nonlinear model is based on the assumption of thin films and is exact in the limit

of an infinite value for the ratio of disturbance wavelength to undisturbed film thickness.[37] Considered is the initial-and-boundary value problem of a semi-infinite sinuous and/or dilationally distorting inviscid liquid film discharging from a practical twin-fluid atomizer (with adjacent gas-stream) into a planar channel. Liquid film modulation is enforced by imposing forcing conditions onto the discharging gas streams which impact the liquid film from both sides at a specified angle. Direct modulation of the discharging film via modulation of the liquid-phase velocity at the nozzle exit is also considered. A more detailed description of the employed model is given below.

It should be noted here, that the active control and break-up of cylindrical liquid jets via liquid phase modulation has a longer history than the analysis of modulated liquid films. The first detailed experimental and (linear) analytical studies of modulated discharging liquid jets were conducted by Pimbley,[32] Pimbley and Lee[33] and Bogy[34] motivated by its application in ink-jet printing. More recently, Hilbing and Heister[35] analyzed modulated discharging nonlinear liquid jets in context with the likelihood of droplet recombination downstream from the initial jet pinch-off point. Modulation of microjets has currently received attention in context with micro-dispensing systems for pharmaceutical products and in context with the formation of precision powders having very uniform particle size. For a more complete review of previous theoretical work on free liquid films and jets, the reader is referred to Ref. 43.

C. New Configuration under Investigation

The present study is a continuation of previous work by the authors.[36] In particular, the present analysis considers the general sinuous and/or dilational nonlinear evolution of a thin semi-infinite planar liquid film downstream from a twin-fluid atomizer and under the influence of capillary and aerodynamic effects. The numerical model employs the reduced-dimension approach of Ref. 37 to describe the thin planar sheet and a Boundary-Element Method (BEM) formulation[38] for the inviscid incompressible gas streams impacting onto the

film from both sides of the injector centerline.

The unsteady Bernoulli equation in combination with the boundary-element method is used to determine the instantaneous gas pressure at the liquid-gas interfaces which is needed within the lubrication equations governing the liquid phase. The use of a discrete boundary-element method for the gas phase allows the consideration of practical applications where liquid streams are injected into a gaseous flowfield with its own physical constraints or boundary conditions. The latter is of particular importance with regard to the complicated flowfields within and/or around fuel injection elements or atomizers used for spray combustion purposes, e.g. prefilming airblast atomizers.

The particular injector configuration considered in this work is shown in Fig.1.

A thin liquid film is injected from a two-dimensional slit-nozzle located in the symmetry plane of a two-dimensional twin-fluid atomizer. The liquid film is impacted on both sides by gas-jets discharging from two inlet ports angled with respect to the film discharge plane at an angle α. Both liquid film and gas streams are injected into a two-dimensional channel. The width of the gas-jet inlet ports is s, the channel width is H and the width of the liquid-phase nozzle is h. For the analysis, the coordinate system is fixed to the nozzle exit with the $y-$axis located within the film discharge plane and the $x-$axis coinciding with the symmetry plane of the atomizer. For the spatially developing semi-infinite liquid film, capillary waves generated by the impacting gas jet do not reach the outflow boundary of the computational domain during the computation.

The specification of liquid-phase boundary conditions at the nozzle exit follows previous work by the authors on discharging semi-infinite films without gas-phase effects.[37] In Ref. 37, liquid film modulation was imposed only locally at the nozzle ($x = 0$). The number of boundary conditions specified at the nozzle was chosen according to linear theory and by employing the Sommerfeld radiation condition. The latter condition excluded any wavenumber solution with negative group velocity that resulted from the specific forcing frequency. Within the present investigation, the presence of a non-zero density incompressible ambient gas and/or impacting gas jets downstream from the nozzle exit plane allows generally for

capillary waves with negative group velocities effectively resulting in upstream energy transport on the film. However, within this work liquid-film injection velocities are assumed high enough so that upstream energy transport and upstream wave propagation across the nozzle exit plane can be neglected, eliminating the need to specify additional reflective boundary condition at this boundary. Nevertheless, it should be recalled that the incompressibility assumption within the gas-phase implies that the speed of sound is much larger than the the wave speed of any capillary waves observed on the liquid. So signals may propagate upstream (and downstream) through the gas.

Certain boundary conditions have been imposed within the gas phase. Gas-phase velocity components normal to solid-walls have been set to zero (i.e. along the walls of the discharge channel and the atomizer). This implies that, in the boundary-element analysis, the gradient of the velocity potential normal to these boundaries is zero. Parallel outflow conditions have been specified within the gas-phase. In particular, the value of the velocity potential has been prescribed as $\phi = 0$ at the nozzle exit on both sides of the liquid film.

Gas-jet injection at the two gas-jet inlet ports has been specified, in general, according to

$$u_{g;1,2}(t) = \sum_{n=0}^{\infty} u_{g;0} \sin^2 \left[\pi(\frac{t}{T_p} - (2n + n_{\theta;1,2}))\right] \quad \text{for} \quad (2n + n_{\theta;1,2}) < \frac{t}{T_p} < (2n + 1 + n_{\theta;1,2})$$
$$\text{and} \quad u_{g;1,2}(t) = 0 \quad , \quad \text{otherwise.} \tag{1}$$

Here T_p denotes the pulse period and subscripts 1 and 2 refer to the lower and upper gas jets, respectively. The prescribed forcing function indicates that a gas-jet pulse of period T_p at either inlet ports is followed by an equal-time period where there is no pulse for that particular port. Parameters $n_{\theta;1,2}$ describe any time delay or phase-shift in the pulsing of the gas jets at the lower (1) and upper (2) injection ports. In this analysis $n_{\theta;1} = 0$ always, whereas $n_{\theta;2}$ ranged from 0 to 1. Note that gas jet pulsation with $n_{\theta,1} = n_{\theta,2} = 0$ will always result in dilational film deformation whereas $n_{\theta,1} = 0$ and $n_{\theta,2} = 1$ will generate initially (predominantly) sinuous film distortions.

II. GOVERNING EQUATIONS

With the prescribed boundary conditions, the solution to Laplace's equation within the gas-phase is determined if the instantaneous location of the liquid-gas interface and the velocity component normal to this interface is known. More precisely, using the discrete boundary-element method, the solution for the gas-phase velocity potential $\phi_{g;1,2}$ at a given point within or on the boundaries of the gas-phase domains in Fig. 1 is determined by defining contributions of sources from all nodes along the boundary of each domain. Note that for dilational, i.e. symmetric, film disturbances a boundary-element solution has to be obtained only for gas-phase region on one side of the liquid film. The flowfield on the opposite side of the film is then merely a mirror image of the calculated one. However, for more general film disturbances, boundary-element solutions have to be computed simultaneously for both gas-phase regions, i.e. above and below the thin film.

The BEM approach adopted here to solve the gas-phase flow field follows the method proposed by Brebbia.[38]

The integral representation of Laplace's equation for the gas-phase velocity potential $\phi_{g;1,2}$ may be written as

$$\alpha\phi_g(\vec{r}_i) + \int_\Gamma \left[\phi_g \frac{\partial G}{\partial n} - qG\right] \mathrm{d}\Gamma = 0$$

where $\phi_{g;1,2}(\vec{r}_i)$ is the potential at a point $\vec{r}_i$ in the gas-phase region below (1) or above (2) the liquid film, $\Gamma_{1,2}$ denotes the boundary of the particular domain, $q_{1,2} = \partial\phi_{g;1,2}/\partial n$ is the gradient of $\phi_{g;1,2}$ on $\Gamma_{1,2}$ normal to the particular boundary, α is a constant (for a given node), and G is the free-space Green's function corresponding to the governing equation. Since the above equation involves an integration only around the boundary Γ_1 and/or Γ_2, we need not discretize the entire gas-phase domain. It is presumed that either $\phi_{g;1,2}$ or $q_{1,2}$ is specified at each 'node' on each boundary while the other quantity is returned as part of the solution. Details regarding the BEM solution procedure can be found in the appendix of Ref. 39, together with validation simulations of the employed method for two steady-state problems.

Coupling between the gas and liquid phase is described through kinematic and dynamic boundary conditions at the phase interface. Kinematic conditions are represented by the instantaneous interface locations and the normal velocity of the interfaces; this affects the solution for the velocity potential in the gas phase above and below the thin film. On the other hand, the flowfield in the gas phase impacts the liquid film distortion through the dynamic condition at the interfaces, requiring that the pressure inside the liquid balances with the pressure on the gas side of the interface combined with the capillary pressure.

The equations governing the nonlinear film distortion are Eqs. (2.10) through (2.16) of Ref. 37, which can be combined to yield

$$\frac{\partial \tilde{y}}{\partial t} + \frac{\partial}{\partial x}(\overline{u}\tilde{y}) = 0 \tag{2}$$

$$\begin{aligned}\frac{\partial \overline{u}}{\partial t} + \overline{u}\frac{\partial \overline{u}}{\partial x} = &-\frac{1}{2\rho}\frac{\partial (p_{g,+} + p_{g,-})}{\partial x} \\ &+\frac{\sigma}{2\rho}\left\{\frac{\partial}{\partial x}\left[\frac{f_+ + f_-}{2}\frac{\partial^2 \tilde{y}}{\partial x^2} + \underbrace{(f_+ - f_-)\frac{\partial^2 \overline{y}}{\partial x^2}}\right]\right. \\ &\left.\underbrace{-\frac{2}{\tilde{y}}\frac{\partial \overline{y}}{\partial x}\left[(f_+ + f_-)\frac{\partial^2 \overline{y}}{\partial x^2} + \frac{f_+ - f_-}{2}\frac{\partial^2 \tilde{y}}{\partial x^2}\right]}\right\}\end{aligned} \tag{3}$$

$$\begin{aligned}\frac{\partial \overline{v}}{\partial t} + \overline{u}\frac{\partial \overline{v}}{\partial x} = &-\frac{1}{\rho}\frac{p_{g,+} - p_{g,-}}{\tilde{y}} \\ &+\frac{\sigma}{\rho}\frac{1}{\tilde{y}}\left\{(f_+ + f_-)\frac{\partial^2 \overline{y}}{\partial x^2} + \underbrace{\frac{f_+ - f_-}{2}\frac{\partial^2 \tilde{y}}{\partial x^2}}\right\}\end{aligned} \tag{4}$$

$$\overline{v} = \frac{\partial \overline{y}}{\partial t} + \overline{u}\frac{\partial \overline{y}}{\partial x} \tag{5}$$

where f_+ and f_- are given by

$$f_\pm = \left[1 + \left(\frac{\partial \overline{y}}{\partial x}\right)^2 \pm \frac{\partial \overline{y}}{\partial x}\frac{\partial \tilde{y}}{\partial x} + \frac{1}{4}\left(\frac{\partial \tilde{y}}{\partial x}\right)^2\right]^{-3/2} , \tag{6}$$

with additionals term appearing on the right-hand-side of Eqs. (3, 4) due to the nonzero gas pressures $p_{g,+}$ and $p_{g,-}$ along the upper (+) and lower (−) interfaces. In the above equations

$\tilde{y}$ is the sheet thickness, $\overline{y}$ is the sheet-centerline location in the transverse direction, and $\overline{u}$ and $\overline{v}$ denote the axial and transverse film velocity averaged over the film thickness. The underbraced terms in the original Eqs. (3, 4) identify nonlinear coupling terms between sinuous and dilational film disturbances (or capillary waves) for the general nonlinear case resulting from capillary forces. Note that in the nonlinear case $f_{\pm}$ depends on both $\tilde{y}$ and $\overline{y}$ (see Eq. 6). Mode coupling is also influenced by the surrounding gas flow represented in Eqs. (3) and (4) by the gas pressures $p_{g,+}$ and $p_{g,-}$ along the gas-liquid interfaces. Eqs. (2) through (5) are valid for thin inviscid incompressible liquid films. Here "thin" implies that the film thickness h is small compared to the wavelength of any disturbance appearing on the film interfaces. A concise derivation of Eqs. (2 – 5) has been presented in Ref. 39 and in Ref. 37, as well as in Ref. 40 for the more general case of thin annular films. For dilationally distorting films, we have $\overline{y} = 0$, $\overline{v} = 0$ and $p_{g,+} = p_{g,-}$ so that Eqs. (4) and (5) are identical to zero with $f_{\pm} = [1 + (\partial\tilde{y}/\partial x)^2/4]^{-3/2}$ in Eq. (3). Eqs. (2, 3) and Eqs. (4, 5) are decoupled by linear analysis, governing linear dilational mode disturbances (i.e. $\overline{u}$ and $\tilde{y}$) and linear sinuous mode disturbances (i.e. $\overline{v}$ and $\overline{y}$), respectively.

The unsteady Bernoulli equation provides a relationship between the pressure in the gas phase $p_{g;1,2}$ and the velocity potentials $\phi_{g;1,2}$ governed by $\nabla^2\phi_{g;1,2} = 0$:

$$\frac{\partial\phi_{g;1,2}}{\partial t} + \frac{1}{2}\left(\nabla\phi_{g;1,2}\right)^2 = -\left(p_{g;1,2} - p^0_{g;1,2}\right) \tag{7}$$

where $p^0_{g;1,2} = \text{fctn}(t)$ is the stagnation pressure in the gas below (subscript 1) and above (subscript 2) the liquid film. The gas densities on both sides , $\rho_{g,1}$ and $\rho_{g,2}$, were assumed to be equal; the static pressure at the outflow boundary has been prescribed at a constant value (referenced at 0 Pa). Consequently $p^0_{g;1,2} = \frac{1}{2}(\nabla\phi^{out}_{g;1,2})^2$ in Eq. (7) since $\phi^{out}_{g;1,2} = 0$. Evaluation of Eq. (7) at the liquid-gas interfaces governs the gas pressure $p_{g,\pm}$. The adjustment of $p^0_{g;1,2}(t)$ is employed in order to prevent transverse film deflection at the outflow boundary, particularly for non-symmetric, i.e. mixed or sinuous mode film pulsing due to the non-zero pressure difference across the undisturbed film. Note that properly prescribed variations in the outflow static pressure or total pressure in both gas regions could be used to model

the effects of combustion instabilities (i.e. acoustic resonant oscillations) on the breakup of the injected liquid fuel film. Such an analysis has already been presented by Hilbing et al.[41] for finite length liquid jets using a boundary-element method to describe both liquid and gas phases. A similar analysis for the case of semi-infinite thin planar films would require modifications of the specified outflow conditions and possibly inflow conditions for the discharging liquid film.

The kinematic interface condition governing the motion of the phase interface is implicit in Eq. (2) which governs mass continuity for the liquid phase.

From Eq. (7) we observe that, in order to evaluate the local gas pressure, $\partial\phi_{g;1,2}/\partial t$ has to be known along the interface. Here, the local values of this time-derivative are obtained explicitly using previous values of $\phi_{g;1,2}$ at the interface and at the same downstream location. This corresponds to the analysis presented by Spangler, Hilbing and Heister,[42] who analyzed the two-dimensional planar sheet problem by using a BEM for the solution of Laplace's equation in both gas and liquid phases. Those authors tracked the motion of the nodes at the liquid-gas interface only in the direction vertically to the liquid stream or jet.

Eqs. (2) through (7) have to be integrated in time which also includes the simultaneous solution of Laplace's equation for $\phi_{g;1}$ and $\phi_{g;2}$ at each time step. The procedure begins with the solution of Laplace's equation for $\phi_{g;1,2}$ by using the current interface locations and the velocity normal to the interfaces, i.e. $\partial\phi_{g;1,2}/\partial n$. The solution gives the values of the velocity potentials $\phi_{g;1}$ and $\phi_{g;2}$ along the two interfaces. This information permits the updating of the gas pressures $p_{g,\pm}$ using Eq. (7). The newly determined gas pressure can now be used within Eqs. (3) and (4) which in combination with Eqs. (2, 5) is solved to update the interface locations (including the locations for the BEM surface nodes) and the velocity components normal to the interfaces. By repeating this procedure at each time step, the film shape can be determined at all times prior to droplet pinch-off. The prescribed solution procedure, illustrated schematically in Fig. 2 for the dilational case, closely follows the procedure employed by Spangler, Hilbing and Heister[42] who analyzed the nonlinear evolution of an axisymmetric liquid jet by using a boundary-element method (BEM) for the

solution of Laplace's equation in both gas and liquid phases and by employing the unsteady Bernoulli equation in both phases along the interface.

Note that the solution procedures employed for the gas-phase (discrete BEM) and the liquid phase (reduced-dimension analysis) solve for nondimensional quantities. Both solution methods use the thickness of the film as characteristic length for the nondimensionalization. The characteristic velocity for the reduced-dimension analysis of the liquid film is the capillary velocity $u_s = \sqrt{\sigma/(2\rho_l h)}$ which eliminates the Weber number from the nondimensional forms of Eqs. (3, 4). u_s is the velocity at which small amplitude sinuous capillary waves travel along a planar liquid film.[37] For the BEM solution of the gas-phase velocity potential, and the unsteady Bernoulli equation in the gas phase, the maximum gas-jet injection velocity is used as the characteristic velocity.

With the prescribed non-dimensionalization, the following (nondimensional) flow parameters are to be considered: (1) The ratio of maximum gas jet momentum to liquid film momentum $\mathrm{M} = \rho_g u_{g,0}^2 s/(\rho_l u_l^2 h)$, (2) the nondimensional square of the film injection velocity or liquid-phase Weber number $\mathrm{We}_l = \rho_l u_l^2 h/\sigma$, (3) the gas-to-liquid density ratio ρ_g/ρ_l, and three geometric parameters, i.e. the gas jet injection angle α, as well as s/h and H/h denoting the ratios of gas-jet inlet port width or discharge channel width to the thickness of the undisturbed liquid film, respectively. Within the present analysis the parameters M and α have been replaced by $\mathrm{M}_{||} = \mathrm{M}\cos\alpha$ and $\mathrm{M}_{\perp} = \mathrm{M}\sin\alpha$ representing the maximum values of the gas jet components parallel and perpendicular to the undisturbed liquid film. The former is relevant for the initial generation of film disturbances, while the latter can cause amplification of an existing disturbance through Kelvin-Helmholtz wave growth.

From Eqs. (3, 4) we see that, within the considered inviscid model, the gas-phase influences the liquid-phase dynamics solely through the static pressure at the interfaces $p_{g,\pm}$. Its nondimensional value $p^*_{g,\pm} = p_{g,\pm}/(\rho_l\, u_s^2)$ within the nondimensional form of Eqs. (3, 4) can be expressed in terms of the nondimensional pressure $p^{\#}_{g,\pm} = p_{g,\pm}/(0.5\rho_g u^2_{g;0})$ obtained from the solution of the unsteady Bernoulli equation along the interface,

$$p^*_{g,\pm} = \frac{1}{2}\frac{\rho_g}{\rho_l}\frac{u^2_{g;0}}{u^2_s}p^{\#}_{g,\pm} \tag{8}$$

The nondimensional parameter of interest in this expression is the product formed by the gas-to-liquid density ratio ρ_g/ρ_l and the ratio between the maximum gas jet velocity $u_{g,0}$ and the capillary velocity u_s on the liquid film. For practical applications this product is of the order one. In particular, for a water sheet with a thickness of 0.2mm at 20° C (i.e. $\sigma = 0.0727$ N/m and $\rho_l = 998$ kg/m^3), and a co-flowing gas stream with $\rho_g = 1.2$ kg/m^3 moving at 15 m/s, the prescribed nondimensional value is $\rho_g u^2_{g;0}/(\rho_l u^2_s) = 1.5$. $\rho_g u^2_{g,0}/(\rho_l u^2_s) = 2\mathrm{M}\,\mathrm{We}_l\,h/s$ represents the ratio of aerodynamic forces exerted on the liquid-gas interface to capillary forces. As a parameter relevant to the gas/liquid field governing equations, it does not contain any geometrical parameters with exception of the film thickness. Due to the different choices made for the characteristic velocities in the nondimensional equations for the gas and liquid phases, $u_{g;0}/u_s$ is another nondimensional parameter relevant to the problem. However, since $u_{g;0}/u_s$ can be expressed in terms of We_l, M, s/h and ρ_g/ρ_l, the density ratio ρ_g/ρ_l has been chosen as the second (geometry independent) nondimensional quantity relevant to the field equations. Note that, if $u_{g;0} \neq u_s$, the same nondimensional time-steps for the numerical procedures employed to solve the liquid- and gas-phase equations implies different physical time steps. Consequently, and since the capillary velocity u_s is in general smaller than the velocity $u_{g;0}$, subiteration for the solution of the liquid-phase equations is needed (if the same nondimensional time-step is used) or the nondimensional time-step for the liquid-phase analysis has to be adjusted to the one employed for the BEM solution of the gas phase. Note that parameters ρ_g/ρ_l and $\rho_g u^2_{g;0}/(\rho_l u^2_l)$ are essential to the problem or field equations, while other nondimensional parameters such as α, s/h and H/h depend on the particular atomizer configuration.

Model Validation and Numerical Accuracy

The various components of the numerical model employed within this analysis and discussed above have been benchmarked independently. Implementation of the boundary-

element method has been validated by predicting the flow across a cylinder and a NACA airfoil and by comparing the computed pressure distributions with analytical and experimental results, respectively. Here, the pressure across the different shapes has been evaluated by using the steady-state Bernoulli equation. The liquid-phase model (without gas-phase coupling) has been analyzed in detail within previous work, including an analysis on the accuracy of the employed thin film approximation or long wavelength assumption close to the point of film pinch-off where short wavelength contributions can be present. The latter has been accomplished by comparison of the computed results for an infinite periodically disturbed liquid film with solutions obtained from a two-dimensional discrete-vortex method.[37,43] Accuracy in the evaluation of the unsteady term within Eq. (7) has been established independently by comparing the pressure distribution along the surface of an object placed into a gas stream with the pressure distribution predicted for the same object now moving with the same relative velocity in the same but quiescent gas. With respect to the pressure evaluation within the gas-phase, the latter case is unsteady (due to the moving boundary) and $\partial\phi_g/\partial t \neq 0$, whereas in the former (steady) case, $\partial\phi_g/\partial t = 0$.

Note that the angled-derivative scheme[45] employed here and in Ref. 40 for the solution of the liquid film equations is second-order accurate in time and space. Numerical solutions for the pure convection equation showed that this scheme is superior to the Lax-Wendroff Method with Richtmyer splitting previously employed in Ref. 44, as it produces significantly less numerical diffusion for this test case. The latter feature is essential if details of the capillary wave propagation along the liquid film are to be predicted accurately. More information on the numerical method can be found in Ref. 45.

III. RESULTS

Base Case Analysis

Fig. 3 shows a dilationally distorting liquid film subject to the forcing conditions imposed onto the gas jet inlet velocities $u_{g;1}$ and $u_{g;2}$ according to Eq. (1) at the lower (1) and upper

(2) gas-inlet ports, respectively. Here, both lower and upper gas jet pulsations are in phase so that $n_{\theta,1} = n_{\theta,2} = 0$. This pulsing sequence, i.e. one gas pulse of time period T_p followed by a 'resting-period' T_p without gas flow is subsequently described as the base-case pulsation. Problem parameters for this case, subsequently referred to as base-case conditions are $M_{||} = M_{\perp} = 1$, $\rho = \rho_g/\rho_l = 0.0012$, $We_l = 10$ and $s/h = H/h = 10$. For all results presented in this analysis, grid-size and time-step independence has been verified by successive time-step reduction and mesh refinement (i.e., addition of computational nodes within the boundary-element analysis).

Fig. 4 shows the dilationally distorting liquid film for the similar case but a modified gas-jet modulation. Here, gas jet pulses of period T_p follow immediately upon each other without a 'resting-period.' As observed from Fig. 3, the energy provided by the impacting gas jets and base-case pulsation is insufficient to break the film, the latter being stabilized by surface tension. As more energy is transferred onto a given length of the moving film, this stabilizing effect is overcome and film rupture is predicted at a downstream location of $x/h = 106.5$ and at a nondimensional time $t^* = 25$.

Assuming base-case parameter conditions as well as base-case forcing conditions for both upper and lower gas jets, but allowing for a phase shift or time shift of period T_p between both jet pulses, i.e. $n_{\theta,1} = 0$ and $n_{\theta,2} = 1$, one obtains an initially sinuous distorting film as shown in Fig. 5. Note that changing the pulse shape from a $\sin^2$-function to a $(1 - \cos)$ distribution while keeping the pulse period T_p and the overall pulse energy constant does not significantly alter the resulting film distortion. Recall that, for all the simulations presented here, plug flow has been assumed at both gas jet outlets. The effect of start-up conditions has been studied for the sinuous case of Fig. 5. Fig. 6 displays the result for the case where the first gas-jet pulse (entering the discharge channel from the lower port) was specified according to $u'_{g;1} = (1 - \exp[-t/T_s])\, u_{g;1}(t)$ with $u_{g;1}$ from Eq. (1) and $T_s = 2.5$. As observed from Fig. 6, the downstream location where film rupture occurs does not change significantly although break-up times do vary. For the case shown in Fig. 6, the time until film rupture occurs increased from approximately $t^* = 16$ to $t^* = 21$. However, film pinch-off is still predicted

at $x/h \approx 45$, although the location of the pinch-off within the waveform differs. Variation of $n_{\theta;2}$ between 0 and 1 (with $n_{\theta;1} = 0$) produces mixed-mode film deformations (see Fig. 7). Due to the complexity in the resulting interface topology, the present work focused on the analysis of dilational and sinuous gas jet pulsations only.

For the cases shown in Figs. 5 and 6, strong nonlinear coupling between sinuous and dilational modes leads to film breakup close to the nozzle exit. Note that, on average, the same amount of energy is added to the system as previously for the case with in-phase pulsing of both jets (see Fig. 3). However with the given forcing frequency and atomizer configuration, film rupture is more readily obtained indirectly by sinuous forcing and nonlinear sinuous-dilational mode coupling rather than by forcing film pinch-off directly by dilational film modulation.

Comparison of Figs. 4 and 5 also shows that sinuous gas-jet pulsation under base-case conditions (and with base-case forcing) yields even shorter breakup times and lengths than the dilational case with modified forcing conditions, i.e. without 'resting-period;' despite the fact that, for the modified dilational case of Fig. 4, energy input into the system per unit time is, on average, twice that for the sinuous case illustrated in Fig. 5. Clearly, the greater amount of energy provided at the gas-jet inlet ports will not necessarily result in shorter film break-up times and lengths. More importantly, time history and absolute values of energy transfer rate from gas- to liquid-phase will determine the effectiveness with which the gas jets cause large amplitude dilational film distortions, which ultimately cause film rupture.

Sinuous (i.e. out-of-phase) gas-jet modulation will result in larger differences between the instantaneous gas-phase pressures on both sides of the liquid film. Consequently, more energy is transferred onto the liquid film than under dilational (i.e. in phase) forcing conditions for the two gas jets. If nonlinear sinuous-dilational mode coupling is strong (e.g., for low We_l values), sinuous gas-jet forcing conditions will consequently result in faster film break-up than dilational gas-jet forcing. The importance of nonlinear sinuous-dilational mode coupling as the determining mechanism for film break-up has already been discussed for annular liquid films discharging into a surrounding void.[40]

Weber Number Effect

Under conditions similar to those in Fig. 5 but larger Weber number We_l, film resistance to transverse distortion or deflection is reduced (see Fig. 8 for $We_l = 25$); however, at larger We_l-values, nonlinear sinuous-dilational mode coupling remains weak and the film does not rupture before it hits the walls of the discharge channel. Although impact of the film with the wall should result in rupture, the mechanism and the results will differ from those studied here. For our purposes, we will consider impact with the walls to be undesirable although it might have useful consequences in some technological applications.

Reduced mode coupling is manifested by stretched-band-like film distortion rather than the formation of fluid blobs (cylinders) as found for $We_l = 10$ (see Fig. 5) and as illustrated also in Fig. 9 for the case with $We_l = 5$. In the latter case, the smaller Weber number (e.g. larger surface tension at same discharge velocity and film thickness) stabilizes the film by reducing transverse film oscillations and consequently also gas-phase pressure variations along the film in the downstream direction. This results in larger break-up lengths and times for the smaller Weber number case despite the fact that, for a given sinuous wave (i.e. wavelength and disturbance amplitude), sinuous-dilational mode coupling is stronger for the smaller Weber number (i.e. $We_l = 5$) as illustrated by the underbraced terms in Eqs. (3,4).

Previous analyses of planar films in a zero ambient gas and with film modulations enforced locally onto the discharging film at the nozzle exit showed that, at a given imposed forcing frequency, up to two sinuous mode wavenumbers are observed downstream form the nozzle. In the parameter range of interest (i.e. large Weber number and low density ratio) both of these wavenumbers vary only little in magnitude so that the resulting film distortion shows a characteristic beat behavior.[37] Such a beat behavior could not be identified within the present configuration where film modulation is enforced via impacting and/or co-flowing gas streams. Note however that, in the present analysis, gas jets of a given finite width impact the moving film with a specified pulsation pattern and at a given frequency. In other words, the various disturbances generated by these jets and their specific wavelengths and

propagation velocities not only depend on the imposed gas-jet modulation frequency but also on the gas-jet geometry or gas-jet width; this is in contrast to the analysis of Ref. 37. For direct film modulation at the nozzle and zero density ambient gas (in Ref. 37), disturbances of various wavelengths result naturally from the harmonic modulation of the flow variables at the nozzle exit. The resulting wavelengths are affected by the imposed forcing frequency and the liquid Weber number (based on film thickness and film discharge velocity) only.

This raises the question, if film rupture via gas-jet modulation can be optimized by co-ordinating gas-jet width and frequency of gas-jet pulses (at a given nondimensional film discharge velocity or Weber number We_l). The difficulty here is that any modification of the pulsing frequency will not only alter film distortion directly by altering the film length exposed to the impacting gas jet during the pulse but also indirectly by modifying the overall gas-phase flowfield.

With respect to this study of Weber number effects on liquid film distortion, it should be noted that an increase in Weber number can be interpreted as a decrease in surface tension at the same value of h and u_l or as an increase of u_l at constant surface tension and h-value. In the latter case, the reference time within the solutions shown in Fig. 5 and 8 are the same, resulting in the same dimensional time frame. However, in the former case, $t_{ref} = l_{ref}/u_{ref}$ and $u_{ref} = \sqrt{\sigma/(2\rho_l h)}$; therefore an increase in the surface tension coefficient σ yields an increase in t_{ref} so that for the same nondimensional time, the elapsed physical time is larger in Fig. 8 than in Fig. 5. For constant liquid velocity u_l, we have $u_{ref} \sim \mathrm{We}^{-1/2}$, so that the dimensional time scale in Fig. 8 (with $\mathrm{We}_l = 25$) is stretched by a factor of $\sqrt{2.5}$ with respect to the dimensional time in Fig. 5 (with $\mathrm{We}_l = 10$).

Fig. 10 shows dilational film deformation for the same parameter configuration as used in Fig. 8, only now $n_{\theta,1} = n_{\theta,2} = 0$, whereas before $n_{\theta,1} = 0$ but $n_{\theta,2} = 1$. Figs. 8 and 10 suggest that, for larger Weber numbers (and film modulation via gas jet pulsing), film rupture can be effectively controlled by dilational gas-jet pulsations, particularly if constraints of the flow geometry are to be considered. In addition, for large Weber number flows, sinuous-dilational mode energy transfer becomes increasingly ineffective so that film rupture lengths for similar

dilational and sinuous mode forcing conditions become comparable.

In what follows, the discussion will focus on parametric studies for the sinuous mode case of Fig. 5. Sinuous mode film distortion has previously been considered to be the most relevant mode of film disintegration for practical atomization systems. This does not imply that the sinuous mode will be more effective in causing film rupture than the dilational mode under every possible operating condition (e.g., for high-pressure or large density ratio ρ_g/ρ_l applications). In the past, experimental studies have focused on the sinuous mode of film disintegration, while numerical models considered (with some exceptions) the analysis of the dilational mode only. Based on this observation, the present analysis is intended to provide some insight to film distortion under the mode least considered within previous numerical or analytical work on nonlinear liquid film distortion and disintegration.

Gas Momentum Effect

Several variations and combinations of gas-jet inlet momentum $M_{\parallel}$ and $M_{\perp}$ have been considered for the case shown in Fig. 5 where $M_{\parallel} = M_{\perp} = 1$. The result obtained for $M_{\perp} = 0.5$ is illustrated in Fig. 11. According to the reduced vertical momentum, the effect of the impacting gas jet onto the film is reduced, resulting in smaller initial sinuous film disturbances. Film break-up after downstream growth of these disturbances (possibly enhanced by capillary and/or Kelvin-Helmholtz instabilities) is delayed. A result similar to the one shown in Fig. 11 was obtained for the case where $M = \sqrt{M_{\parallel}^2 + M_{\perp}^2}$ is kept constant while α is reduced from 45 degrees (see Fig. 5) to 30 degrees (see Fig. 12). $M_{\perp} > 0.5$ and $M_{\parallel} > 1$ in these cases. However, despite the larger values of $M_{\perp}$ and $M_{\parallel}$, maximum amplitudes at a given time and downstream location remain somewhat smaller. Note that, the physical relevance of the short wavelength disturbances observed in Fig. 12 at $t^* = 27$ for $x/h > 75$ as predicted by the employed thin film model is uncertain. The accuracy and limitations of the current liquid-phase model with respect to short wavelength contributions, particularly close to the point of film breakup, has been discussed in detail in Ref. 44.

If α is decreased further (i.e. to $\alpha = 15°$), gas-jet normal momentum is further reduced in favor of an increase in gas momentum parallel to the undisturbed film. Fig. 13 shows that,

as a result, amplitudes of sinuous mode film disturbances are somewhat reduced compared to those found in Fig. 12 at the same time and downstream location. Results obtained for $\alpha = 75°$ varied only slightly from those computed for $\alpha = 45°$ shown in Fig. 5.

Figs. 14 and 15 illustrate cases where the vertical or parallel component of the gas-jet momentum was increased from 1 to 5 (at both inlet ports) while keeping all other parameters the same. In both instances, film pinch-off occurs close to the nozzle exit as a result of the pressure distribution generated by the impacting gas jets rather than through continuous wave growth, the latter being relevant for the case shown in Fig. 11 and 13, for example.

Note that continuous wave growth in Figs. 11 and 13 does not imply monotonic growth. The monotonic growth can be expected for steady gas-phase boundary conditions (i.e. zero or constant velocity at gas inlet ports). For gas-jet pulsations without underlying base flow, relative velocities between gas jets and liquid film vary significantly over time causing disturbance amplitudes to growth sporadically.

Density Effects

Changes in the density ratio ρ_g/ρ_l from the case shown in Fig. 5 have also been analyzed. Fig. 16 shows the result obtained for the similar parameter set as in Fig. 5 but with a five-fold increase in ρ_g/ρ_l. Due to the relative increase of gas-phase inertia, transverse film deflection is now larger (at the same gas-jet forcing conditions). Film distortion as illustrated in Fig. 16 resembles the prediction made in Fig. 8 for an increase in liquid Weber number We_l. However, in the present case, mode coupling is not altered and the film ruptures shortly before impacting on the channel walls. Also, for the larger density-ratio case, film deflection extends over a larger domain than shown in Fig. 8.

Pulse Period

The effect of variations in pulse period T_p on film distortion for the sinuous mode of Fig. 5 will now be summarized: 1) For large T_p-values (and constant jet width), the transverse displacement of the film becomes large before the counter-acting gas jet causes the deceleration and reversal of the displacement. Here, transverse film motion caused by an impacting gas-jet pulse might result in film impingement onto the channel walls (before re-

versal of the film dislocation due to gas-jet impact onto the film from the other side). 2) For small T_p-values (see Fig. 17), transverse film distortion remains small (due to more rapid appearance of the opposed gas jets) with only shorter wavelength disturbances appearing on the film. Note that the gas jet width is $s/h = 10$ and gas-jet impact changes from one side of the film to the opposite side at frequency $1/T_p$. Therefore, even though one gas jet generates an instantaneous film disturbance of approximate length $l = (s/h)\cos\alpha$, the only part of this disturbance not compensated by the action of the opposed jet has a length of $\lambda = u_l T_p$. In order to achieve an effective initial sinuous mode film distortion with gas-jets phased according to $n_{\theta,1} = 0$ and $n_{\theta,2} = 1$, the pulsing period T_p should be longer than the time needed for a liquid particle to travel across the length of the gas inlet ports, i.e. $T_p > s/(h\cos\alpha\, u_l)$. However, as mentioned above, for very large T_p values the film will tend to impact onto the walls of the discharge channel. In the present configuration, gas-jet impact is confined to the vicinity of the atomizer, whereas further downstream, amplitude growth of the liquid film disturbance will be increasingly influenced by Kelvin-Helmholtz effects. Therefore, the pulse period providing optimum wave growth will depend on 1) the generation of an optimum (to be defined) initial film disturbances in the vicinity of the atomizer (i.e., large amplitude and large initial dilational mode contribution or film straining) and 2) amplification of the initial disturbances through (sporadic) Kelvin-Helmholtz wave growth, where the wavelength of the disturbance with optimum growth rate will depend on the given parameter configuration, e.g. u_l, $u_{g,1/2}(t)$, We_l, ρ_g/ρ_l, and the dynamics of the unsteady gas streams.

Gas-Phase Continuous Flow

The previous discussion focused on liquid film distortion and disintegration resulting from time-periodic modulation of the gas-phase velocity on both sides of the liquid film. Forcing conditions onto the initially quiescent gas phase were imposed at the gas-jet outlets according to Eq. 1. Accordingly, gas-phase injection remained confined to pulse events of time-period T_p. Between these injection events, gas-phase velocities on both sides of the liquid film were determined by the dynamics of the deforming gas-liquid interfaces. In this paragraph, gas-

jet pulses are superimposed onto continuous gas streams discharging from the two gas-inlet ports. Figs. 18, 19 and 20 illustrate 3 cases with time-dependent forcing conditions similar to the sinuous mode case of Fig. 5 now superimposed onto steady gas streams entering from the two gas-inlet ports at constant velocity $u_{g;s}$. Steady inlet velocities are assumed to be the same at both gas-inlet ports in order to prevent continuous transverse film deflection, the latter being limited by the discharge chamber walls. Pulse period T_p in Figs. 18 through 20 is $T_p = 5, 8.75$ and 20, respectively; gas-stream steady base-flow velocity and amplitude of the gas-phase velocity modulation are fixed at $u_{g;s} = 0.25$ and $u_{g;0} = 0.5$. Therefore, the maximum injection velocity reached by the gas-jets in Figs. 5 and 18 is the same, while the average energy flux provided by the gas-jets in the latter case is larger, due to the underlying time-independent velocity component. The average energy flux for gas inlet ports 1 and 2 is given by

$$\dot{E}_{g;1,2} = \frac{1}{n} \int_{t=0}^{t=nT_p} \dot{m}_{1,2}(t) \frac{u_{g;1,2}(t)^2}{2} \, \mathrm{d}t \tag{9}$$

with the mass influx per unit width of the two-dimensional gas inlet ports $\dot{m}_{1,2}(t) = \rho_g \, s \, u_{g;1,2}(t)$. The integration in Eq. (9) is performed over a multiple number of pulse periods T_p (n = even integer). The time-independent component of the overall gas-jet momentum is equally distributed onto the gas jets on either side of the liquid film; consequently, the fluctuating part of the gas-jet momentum or gas pulse, which is reduced from its original value, will cause less deflection of the liquid film in the transverse direction. This results in an increase in breakup length and time (see Fig. 18), even though the underlying non-modulated gas-phase velocity allows for continuous energy transfer from gas-to liquid phase, i.e. continuous Kelvin-Helmholtz wave growth.

It is useful, in this context, to compare film distortion at $t^* = 32$ with the corresponding interface locations predicted for the case shown in Fig. 13, i.e. at $t^* = 27$. Note that, within the simulations of Figs. 18 through 20, gas-jet velocities on both sides of the liquid film were increased from zero to the specified $u_{g;s}$ value within a nondimensional start-up time of 5 units. After this time, gas-jet modulation was initiated beginning with the

lower gas jet. Also, in the case shown in Fig. 13, the maximum amplitude of the vertical gas-jet velocity component associated with the generation of the initial film disturbance is $u_{g;0} \sin(\pi/6)$, whereas in the former case it is $0.5\, u_{g;0} \sin(\pi/4)$. Comparison of the liquid film location for the two cases at the prescribed times, therefore illustrates that wave growth from intermediate gas-jet pulsing can result in larger overall amplitude disturbances than obtained via continuous wave growth from continuous gas-jets, the latter providing larger overall energy input into the system.

The effects of increasing pulse period T_p for the case with underlying base flow can be observed from Figs. 18, 19 and 20. As T_p is increased, transverse film deflection resulting from gas-jet impact is allowed to proceed further before being 'compensated' or counteracted by a gas-pulse from the opposite side of the film. Consequently, amplitudes in the centerline disturbance of the film increase as T_p is increased. On the other hand, larger values of T_p result in longer wavelength sinuous-mode film disturbances. However, at similar values for the disturbance amplitude, longer wavelength sinuous-mode waves result in reduced dilational mode wave amplitudes due to a reduction in nonlinear sinuous-dilational mode coupling with increases in the wavelength of the sinuous mode wave.

As for most of the results presented in earlier sections, the computational domain for the solutions in Figs. 18, 19 and 20 extended from $x/h = 0$ to $x/h = 125$, with prescribed static pressure in the gas-phase at the downstream location. Simulations for the similar cases but extended computational domain, i.e. $x/h = 250$ showed that, in the former case, the imposed pressure condition effectively suppresses long wavelength film disturbances generated during the start-up phase of the film modulation. Note that, this has not been observed for the cases without continuous gas-flow discussed earlier. (The importance of the start-up condition for the case without continuous gas jets has already been discussed earlier for the case illustrated in Fig. 5.)

Linear theory for continuous wave growth on thin films via the Kelvin-Helmholtz mechanism[43] shows that, for the base-case parameter set considered here, the described longer waves have significantly larger growth rates than the ones generated by the impact-

ing gas jets. This is illustrated by the growth rate plot shown in Fig. 21 for harmonic sinuous waves $\eta_{\pm} = \eta_0 \exp[i(kx - \omega t)]$ on a thin liquid film subject to two co-flowing gas streams in an infinite domain (here $\eta_{\pm}$ denotes the transverse deflection of the disturbed liquid interfaces). Since the longer wavelength contributions are not suppressed on the longer computational domain, transient effects characterized by growth of the longer wavelength disturbances generated during start-up will result in significant transverse deflection of the liquid film which is already being distorted at shorter wavelength due to the periodically impacting gas jets. See Fig. 22 for the case with $T_p = 5$. A similar observation has already been made for modulated thin annular liquid films in Ref. 40 where transient effects caused film collapse or fluid blob formation.

The longest wavelength suppressed on the shorter domain but present on the longer domain is of the order of the length of the longer domain; this implies that, for the case considered here (Figs. 20, 22), the nondimensional wavenumber kh suppressed on the shorter domain is of $O(0.01)$. From Fig. 21 we see that the corresponding nondimensional growth according to the linear analysis of Ref. 43 is about 0.035 which corresponds to a growth rate of 0.04 in terms of the nondimensionalization used in this work. This yields a threefold increase in the initial disturbance amplitude of the prescribed long-wavelength contribution after $t^* = 25$, if in fact this wavelength is not suppressed. (Compare Figs. 20 and 22.) From Fig. 20, one can estimate the dominant nondimensional disturbance wavenumber to be approximately $kh = 0.25$, the corresponding growth rate according to Fig. 21 is approximately six times smaller than for the described larger wavenumber contribution. It should be noted again that nonlinear sinuous-dilational mode coupling is reduced as the wavelength of the sinuous wave increases. Consequently, even though the longer sinuous waves will result in larger transverse film deflection, they will be less effective in causing film rupture or break-up than the shorter wavelength sinuous mode waves generated by the imposed periodic gas-jet pulses.

Direct Film Modulation

To this extend, liquid film distortions were generated by gas jets impacting onto the liquid film from either sides. An alternative method to generate initial film disturbances is to impose forcing conditions directly onto the liquid-phase flow variables at the slit nozzle where the liquid discharges from the atomizer. Practically, such a modulation can be achieved for example via piezoelectric actuators placed inside or adjacent to the liquid feeding channel. This has been analyzed for the case where gas density is negligible[37]. However, now gas density and motion will have an effect.

There are two important characteristics which distinguish the prescribed direct film modulation from the indirect modulation via impacting gas jets:

1) Only part of the energy used to modulate the gas jets is transferred into the liquid phase resulting in film distortion. Direct liquid-phase modulation, on the other hand, guarantees that all the energy invested in modulating one or more liquid-phase flow parameters will translate into film disturbances. Indeed, simulations similar to those shown in Figs. 3 and 5 but without gas jet modulation and time-dependent forcing conditions imposed onto the axial or transverse film velocities $\overline{u}$ and $\overline{v}$ at the nozzle, i.e.

$$\overline{w}(x=0,t) = \sum_{n=0}^{\infty} w_{l;0} \sin^2\left[\pi(\frac{t}{T_p} - 2n)\right] \quad \text{for} \quad 2n < \frac{t}{T_p} < (2n+1)$$
$$\text{and} \quad \overline{w}(x=0,t) = 0 \quad , \text{ otherwise} \tag{10}$$

where $w = \overline{u}$ or $w = \overline{v}$, resulted in nearly instantaneous film rupture if the energy invested into the modulation is assumed to equal the energy added to the gas-phase for the corresponding gas-phase modulated case shown in Figs. 3 and 5, respectively.

2) Direct liquid-phase modulation, as described above, imposes energy only locally on the film, i.e. at its discharge location from the atomizer. Indirect film modulation via impacting gas jets causes energy transfer onto the liquid film over a finite length of the discharging stream. In fact, a gas-jet pulse discharging from one of the gas-jet inlets shown in Fig. 1 will cause energy transfer or film modulation over the entire length of the disturbed liquid film; this is in contrast to the discussed direct film modulation which remains confined

to the film discharge plane throughout the entire simulated time frame. If, as considered later, the discharging film is modulated directly in the presence of continuous gas streams, energy transfer onto the film occurs both locally at the nozzle exit and globally through interaction of the disturbed liquid film interfaces with the "co-flowing" gas streams. Even if the surrounding gas-phase is quiescent, an originally localized film disturbance will have some non-local effect due to its interaction with the gas-phase. The latter has been assumed to be incompressible which implies an infinite value for the speed of sound or instantaneous propagation of information throughout the gas-phase.

Fig. 23 shows the case of a directly modulated liquid film with or without steady gas-jets and with modulation energy that equals 5 % of the energy previously added to the gas-phase in Fig. 5 in order to generate sinuous film distortions. In Fig. 23, modulations were enforced onto the transverse film velocity $\overline{v}$ at the nozzle exit $x = 0$ according to Eq. (10). In other words, the same time-dependent forcing function was used as previously employed for the gas-phase modulation in Fig. 5. Comparison of Figs. 5 and 23 shows that maximum transverse film deflection is comparable in both cases, even though energy input for the direct liquid-phase modulated case is significantly smaller than for the indirect gas-phase modulated film. On the other hand, as noted earlier, energy transfer onto the liquid via gas-jet modulation takes place along the entire disturbed interface. This results, as observed from Figs. 5 and 6 in stronger sinuous-dilational mode coupling or dilational film distortion which ultimately causes film rupture at approximately $x/h = 45$. Fig. 23 illustrates that mode coupling without significant gas-phase interaction is not strong enough (for the considered parameter configuration) to cause film rupture, even though disturbance amplitudes of the sinuous waves are comparable in both cases. The effect of continuous gas jets superimposed onto the liquid-phase-modulated discharging film is also demonstrated in Fig. 23. Comparison of the corresponding results shown in Fig. 23 indicates that the admission of continuous gas jets on both sides of the liquid film causes a 50 % reduction of the sinuous mode disturbance amplitudes generated by the imposed modulation of $\overline{v}$ at the nozzle. Furthermore, the dominant sinuous mode wavelength is reduced by a factor of 2

upon admission of equal velocity gas streams; at the same time, the amplitude of dilational mode film disturbances is increased. Using only 10 % of the energy admitted in the gas-phase modulated case of Fig. 5, direct liquid film modulation produced film rupture at approximately the same downstream location. However, as illustrated in Fig. 24, transverse film deflection is significantly larger in this case.

Direct liquid-phase modulation with or without adjacent gas streams has also been considered for the pure dilational mode of film distortion. Fig. 25 shows the distorting liquid film for the same parameter set as in Fig. 3 but now with modulation of the axial velocity component $\overline{u}$ according to Eq. (10) rather than gas-jet modulation as employed in Fig. 3. As for the previously discussed sinuous case, the amount of energy used to modulated the liquid film in Fig. 25 was only 5 % of the energy added in the case shown in Fig. 3. In contrast to the sinuous case of Fig. 23, where film rupture has not been observed within the simulated time frame, the film in Fig. 25 ruptures early at $t^* = 27$ at a downstream location of approximately $x/h = 68$. Clearly, for the considered parameter configuration, dilational modulation is preferred if film rupture is achieved by direct liquid-phase modulation. On the other hand, effective film breakup (characterized by small energy input and short breakup length) for gas-phase modulated films is achieved by forcing sinuous mode waves rather than dilational ones.

Comparison of Fig. 25 and 26 shows that time for film rupture from dilational liquid-phase modulation is reduced by the addition of surrounding gas streams; however, film breakup length is not influenced significantly. Also, the wavelengths of dilational mode disturbances generated by direct-liquid phase modulation is not significantly altered by the admission of gas streams on both sides of the discharging film.

From the previous discussion we find that, liquid film disintegration via gas-jet modulation is less effective than direct modulation of liquid-phase flow variables. However, this statement only refers to the initial film rupture process discussed here. Once liquid ligaments have been detached from the continuous liquid film, further breakup of these ligaments can only be achieved via energy transfer from the surrounding gas-phase onto the liquid-phase

ligaments or droplets. Here, large relative velocities between gas-phase and discrete liquid phase is expected to be essential to promote further breakup of ligaments and droplets.

Extended Quantitative Analysis

The previous sections have focused on the distortion and rupture characteristics of discharging liquid films impacted by gas jets. Quantitative data was only provided for film breakup lengths and times for the different configurations.

In order to allow qualitative and quantitative comparison of the computed results with future experimental observations of these films, we present the results from a quantitative analysis of the time-dependent variations in film thickness $\tilde{y}$ and film centerline location $\overline{y}$ at various positions downstream from the nozzle. The employed Fourier analysis and the consideration of phase diagrams for local values of $\tilde{y}$ and $\overline{y}$ follows the work by Ramos[46] who studied the drawing of annular liquid jets at low Reynolds numbers.

Figs. 27 through 30 illustrate phase plots obtained for the case shown in Fig. 11 at $x/h = 12.5$ and $x/h = 25$, respectively. Nearly time-periodic variations in film thickness $\tilde{y}(t^*)$ and centerline displacement $\overline{y}(t^*)$ occur close to the nozzle (Figs. 27 and 28). The centerline displacement becomes increasingly non-periodic, further downstream (Fig. 30). Deviation from periodic behavior at $x/h = 25$ is significantly less pronounced for $\tilde{y}(t^*)$ than for $\overline{y}(t^*)$. At $x/h = 12.5$ the phase of $\overline{y}(t^*)$ takes a dumbbell-like or hourglass-like shape whereas the orbit of $\tilde{y}(t^*)$ at the same location is circular with higher-harmonic contributions resulting in an additional inner heart-shaped loop. Fourier analysis of the signals $\tilde{y}(t^*)$ and $\overline{y}(t^*)$ shows that the dumbbell (hour-glass) shaped $\overline{y}$-orbit is generated mainly by the first and third harmonic of the sinuous modulation frequency, i.e. $f_m = 1/(2T_p)$. The phase of $\tilde{y}(t^*)$ is a result of the first, second, third and fourth harmonic in the film thickness variations, whereby according to the half-wavelength thinning of nonlinear sinuous distorting planar films, the value of the first harmonic in the thickness variation is twice that of the first harmonic in the centerline variation of the film. As the contribution of the fourth harmonic in $\tilde{y}$ decreases further downstream, the heart-shaped loop in the $\tilde{y}$-orbit changes to a simple inner loop without the "kink". As noted earlier, oscillations in film thickness at x/h = 25

are quasi-periodic whereas deviation from periodic behavior is already significant for $\overline{y}(t^*)$ at $x/h = 25$. However, Fourier analysis of the $\overline{y}$ signal shows that the energy contained in the sinuous film oscillation at that location is still found predominantly in the first and third harmonic of the modulation frequency f_m. It is noted here that the Fourier transform of $\tilde{y}$ or $\tilde{y} - h$ and $\overline{y}$ at a given downstream location x/h was taken within a time interval after the film oscillation at that particular location as been established or, in other words, after the initial film disturbance has passed the considered downstream location.

$\overline{y}$ and $\tilde{y}$ phases-plots for the cases illustrated in Figs. 6 and 12 are similar to those discussed above. For the reduced Weber number case of Fig. 9, the inner loop within the phase-plot for $\tilde{y}$ at $x/h = 12.5$ is very tight and without "kink". Fourier analysis of the time-dependent signal $\tilde{y}$ at that location shows that here, the fourth harmonic in the thickness variation is no longer important. For the corresponding phase-plot of $\overline{y}$, $\overline{y} = 0$ and $\partial\overline{y}/\partial t = 0$ are no longer general symmetry lines (as observed in Fig. 28), however the orbit still shows point-symmetry around $\partial\overline{y}/\partial t = \overline{y} = 0$.

It is noted here that the appearance or disappearance of the prescribed "kink" or heart-shaped inner loop in the phase plot of $\tilde{y}$ does not necessarily constitute the presence of a higher (in this case fourth) harmonic mode. It can also be the result of a variation in the phase-shift between the lower frequency modes.

In the presence of a non-zero constant gas flow superimposed onto the gas-jet pulsation of the base case (see Fig. 18) the hour-glass shaped orbit in the $\overline{y}$ phase-plot is still observed. However, the amplitudes in $\overline{y}$ and $\partial\overline{y}/\partial t$ increase with each completed orbit. Fourier analysis of the corresponding time-dependent signal for $\tilde{y}$ shows that as for the lower Weber number case discussed above, the fourth harmonic mode is no longer relevant here. The phase plot of $\tilde{y}$ at $x/h = 12.5$ does not exhibit the heart-shaped inner loop.

For the described gas-jet modulated liquid films, periodic behavior in the variation of $\tilde{y}$ and $\overline{y}$ deteriorates fast with increasing downstream distance. This is in contrast to a liquid film which is modulated within the liquid phase itself. For the sinusoidally modulated film in Fig. 23 without co-flowing gas streams, variations in film thickness and film centerline

location at fixed downstream location are highly periodic (after a certain start-up period) up to a downstream distance of $x/h = 50$. See Figs. 31 and 32 for $x/h = 12.5$. However, with co-flowing surrounding gas-streams re-occuring orbits (even close to the atomizer nozzle) are no longer observed.

Even though periodic behavior in the variation of $\tilde{y}$ and $\overline{y}$ deteriorates with increasing downstream distance (and in particular for gas-phase modulated films), analysis of the power-spectra for the oscillation in film thickness and/or film-centerline location shows that in the investigated cases, the majority of the film energy remains confined to the harmonic modes present close to the nozzle, latter being the first and third harmonic for the film centerline location and the first, second, third and fourth harmonic for the film thickness variation. Accordingly, and in an effort to provide as much significant quantitative data as possible, the included tables list real and imaginary parts of the Fourier transforms for the various dominant harmonic modes observed in the time-signals for the film thickness $\tilde{y}$ and film centerline location $\overline{y}$ at various downstream locations.

Fourier transforms $X(k)$ for length N input sequences $x(n)$ have been calculated by using MatLab^{TM} according to

$$X(k) = \sum_{n=1}^{N} x(n) \exp\left[-i2\pi(k-1)[(n-1)/N]\right] \qquad 1 \leq k \leq N$$

$$x(n) = \frac{1}{N} \sum_{k=1}^{N} X(k) \exp\left[i2\pi(k-1)[(n-1)/N]\right] \qquad 1 \leq n \leq N$$

where $x(n)$ is given by $x(n) = \tilde{y}(n\Delta t)$ or $x(n) = \overline{y}(n\Delta t)$ at a certain downstream location and within a certain time-interval, i.e. $n_s\Delta t < n\Delta t < n_e\Delta t$, whereby Δt is the time-step used within the simulation.

Since the input sequence $x(n)$ is real, the above equation for $x(n)$ can be rewritten in terms of a summation of sine and cosine functions with real coefficients

$$x(n) = \frac{1}{N} \sum_{k=1}^{N} a(k) \cos\left(\frac{2\pi(k-1)(n-1)}{N}\right) + b(k) \sin\left(\frac{2\pi(k-1)(n-1)}{N}\right) \qquad (11)$$

where

$$a(k) = \text{real}[X(k)] \quad , \quad b(k) = -\text{imag}[X(k)] \qquad , 1 \leq n \leq N \tag{12}$$

With the knowledge of the transforms $X(k_i)$ from Tables 1 through 4, the approximate phase plots for $\tilde{y}$ and $\overline{y}$ at the various downstream locations can be reconstructed and compared with the results obtained, for example, from experimental observations. Clearly, the energy contained in modes other than the ones described above and provided in the tables is small and justifies the omission of these modes in the present investigation.

Spray Angle

Liquid film atomization and spray formation is a three-dimensional phenomenon even for planar films and includes the formation of streamwise vortical structures leading (depending on operational conditions) to cellular film breakup or stretched streamwise ligament breakup.[7,8] Besides the importance of three-dimensional effects for the spray formation process, the resulting spray angle will greatly depend on the conditions (e.g. velocities) at which ligaments are shed continuously from the continuous liquid film. The present analysis, which applies only up to the point in time where film rupture first occurs, cannot address these issues (which are vital for an accurate determination of the spray angle).

In their experiment on liquid films discharging from a planar twin-fluid atomizer, Mansour and Chigier[6] considered the envelope of the transversely distorting liquid film as a measure for the spray angle. However, for modulated liquid films Asare, Takahashi and Hoffman[23] showed that following linear stability theory, the amplitude of the envelope grows exponentially up to a point where it saturates due to nonlinear effects. The authors also showed (for certain operational conditions) good agreement of their experimental results with theoretical predictions from a simplified trajectory theory. Accordingly, a prediction of spray angle based on the slope of the envelope at the point of film rupture greatly depends on the film rupture point and cannot be very reliable.

Nevertheless, based on the envelope growth observed for the different configuration, indications are that an increase in spray angle (with respect to the base case of Figs. 5 and 6) is expected with an increase in Weber number (see Fig. 8) and with an increase in gas-

to-liquid density ratio (see Fig. 16). Naturally, the most significant increase in spray angle is expected for an increase in vertical gas-jet momentum ratio. See Fig. 14, where liquid ligaments are expected to be shed periodically from the highly deflecting film. Furthermore, based on the film envelope, a reduction in spray angle can be expected for a decrease in Weber number (see Fig. 9), a reduction of vertical gas-jet momentum (see Fig. 11), and a reduction in gas-jet impact angle (see Figs. 12 and 13). For liquid films modulated at the nozzle exit, Fig. 23 indicates that the addition of constant co-flowing gas streams will result in a decrease in the spray angle, if indeed this angle is based on the envelope behavior of the distorting film.

IV. SUMMARIZING REMARKS

The flowfield in the vicinity of a twin-fluid atomizer has been analyzed numerically. Considered is a thin two-dimensional inviscid incompressible liquid film discharging from the atomizer centerline surrounded on both sides by gas jets which impact symmetrically onto the discharging film. Initial film distortion is enforced actively by: 1) modulation of the impacting gas jets (indirect or gas-phase modulation) with gas momentum components parallel and normal to the liquid stream, 2) modulation in the liquid-phase at the atomizer exit (direct or liquid-phase modulation) or 3) direct liquid film modulation with superposition of continuous gas streams. The investigation focused on gas-phase modulated films. Effects of different flow parameters on film breakup characteristics were studied by varying one of the flow parameters from a given base-case configuration.

For direct (i.e., gas-phase) modulated films, energy input at the gas-inlet ports was found to be inadequate in identifying effective film rupture conditions, the latter being characterized by short break-up length and times at minimum energy input into the system. For the parameter domain surrounding the considered base case, film rupture was obtained more effectively by sinuous forcing and subsequent nonlinear sinuous-dilational mode coupling rather than by dilational forcing at the same average energy flux into the system. Also, it

was observed that intermediate gas-jet pulsing (without underlying continuous gas flow) can yield the same or larger amplitude disturbances than obtained through continuous disturbance wave growth from continuous jets at the same overall energy input into the system.

Direct modulation of liquid phase flow-parameters, i.e. axial or transverse film velocity, at the nozzle exit is more effective than gas-jet modulation, the latter transferring only a portion of the modulation energy onto the film. Computational results also indicate that for direct liquid phase forcing, dilational modulation (i.e. modulation yielding dilational film distortion) is more effective in causing film rupture than sinuous modulations, while, as noted earlier, the opposite is true for gas-jet modulated liquid films. Also, for liquid-phase modulated films admission of nonzero ambient gas streams significantly reduces sinuous mode wavenumbers whereas influence on wavelengths remains small for dilationally distorting films.

For gas-phase modulated films, variations of Weber number, gas jet to liquid film momentum ratio, gas-to-liquid density ratio and pulse period were considered and their effect on film distortion was analyzed. An increase in Weber number from its base-case value (i.e. from 10 to 25) resulted in stretched band-like films and a delay in film rupture due to reduced sinuous-dilational mode coupling. On the other hand, reduction in Weber number (i.e. from 10 to 5) resulted in smaller disturbance amplitudes and larger break-up time and length despite stronger nonlinear mode coupling manifested by the contraction of the film into fluid cylinders connected by thinner fluid films. Transverse deflection of the film centerline for a five-fold increase in density ratio was similar to the one observed for the increased Weber number case; however, fluid blob formation was still observed.

A five-fold increase in vertical or parallel gas-jet-to-liquid-film-momentum ratio resulted in "immediate" film rupture caused by the dynamics of the impacting gas jets rather than by continuous growth of film disturbances downstream with energy transfer from the adjacent gas-streams.

Variation in pulse period affects film distortion in two ways: It changes the amplitude of the initial film disturbances generated by the pulsed gas-jets, since increasing the pulse period

provides more time for transverse film movement (due to one-sided gas-jet impact) before being counter-acted by an opposed gas jet. On the other hand, it alters the wavelengths of the disturbances generated on the film and therefore the gas-to-liquid energy transfer downstream from Kelvin-Helmholtz-type wave growth.

ACKNOWLEDGEMENT

This research has been supported by the U.S. Army Research Office through Grant No. DAAD19–99–1–0204 with Dr. David Mann as the program manager.

REFERENCES

[a)] Present address: Department of Mechanical and Aerospace Engineering, 3101 Engineering Gateway, University of California, Irvine, CA 92697.

[1] A. H. Lefebvre, *Atomization and Sprays* (Hemisphere Publishing Corp., New York, 1989).

[2] T. Arai, and H. Hashimoto, "Disintegration of a thin liquid sheet in a cocurrent gas stream," in *Proc. 3rd Int. Conf. Liquid Atom. Spray Sys.*, pp. V1B/1/1-7.

[3] T. Arai, and H. Hashimoto, "Behavior of gas-liquid interface on a liquid film jet (Instability of a liquid film jet in a co-current gas stream)," *Bulletin of JSME* **28**, 2652 (1985).

[4] H. Hashimoto, and T. Suzuki, "Experimental and theoretical study of fine interfacial waves on thin liquid sheet," *JSME Int. J., Ser. II* **34**, 277 (1991).

[5] A. Mansour, and N. Chigier, "Disintegration of liquid sheets," *Phys. Fluids A* **2**, 706 (1990).

[6] A. Mansour, and N. Chigier, "Dynamic behavior of liquid sheets," *Phys. Fluids A* **3**, 2971 (1991).

[7] B.E. Stapper, and G.S. Samuelsen, "An experimental study of the breakup of a two-dimensional liquid sheet in the presence of co-flow air shear," AIAA Paper No. 90-0461, Reno, NV, 1990.

[8] B.E. Stapper, and G.S. Samuelsen, "An experimental study of the effects of liquid properties on the breakup of a two-dimensional liquid sheet," *J. of Eng. for Gas Turbines and Power* **114**, 39.

[9] E.C. Fernandes, M.V. Heitor, and V. Sivadas, *Towards controlled liquid atomization*, Internal Report, Center for Innovation Technology and Policy Research, Technical University of Lisbon, Portugal (2001).

[10] E.A. Ibrahim, and E.T. Akpan, "Three-dimensional instability of viscous liquid sheets,"

Atomization and Sprays **6**, 649 (1996).

[11] S. Kawano, H. Hashimoto , H. Togari, A. Ihara, T. Suzuki, and T. Harada, "Deformation and breakup of an annular liquid sheet in a gas stream," *Atom. Sprays* **7**, 359 (1997).

[12] P. Berthoumieu, G. Lavergne, H. Carentz, and A. Muller, "Liquid sheet breakup: Comparison between planar and annular geometries," in *Proc. 16th Ann. Conf. Liquid Atom. Spray Systems*, ILASS Europe, pp. VI.4.1–VI.4.6.

[13] P. Berthoumieu, and G. Lavergne, "Video techniques applied to the characterization of liquid sheet breakup," *J. of Visualization* **4**, 267 (2001).

[14] R.H. Rangel, and W.A. Sirignano, "The linear and nonlinear shear instability of a fluid sheet," *Phys. Fluids A* **3**, 2392 (1991).

[15] N. Dombrowski, and P.C. Hooper, "The effect of ambient density on drop formation in sprays," *Chem. Eng. Sci.* **17**, 291 (1962).

[16] S.A. Jazayeri, and X. Li, "Nonlinear breakup of liquid sheets," in *Proc. 9th Ann. Conf. Liquid Atom. Spray Sys.*, ILASS North America, pp. 114–119.

[17] A. Lozano, C.J. Call, C. Dopazo, and A. Garcia-Olivares, "Experimental and numerical study of the atomization of a planar liquid sheet," *Atomization and Sprays* **6**, 77 (1996).

[18] A. Lozano, A. Garcia-Olivares, and C. Dopazo, "The instability growth leading to a liquid sheet breakup," *Phys. Fluids* **10**, 2188 (1998).

[19] W.D. Bachalo, "Spray diagnostics for the twenty-first century," *Atom. Sprays* **10**, 439 (2000).

[20] G.D. Crapper, N. Dombrowski, and G.A.D. Pyott, "Large amplitude Kelvin-Helmholtz waves on thin liquid sheets," *Proc. R. Soc. London, Ser. A, Math. Phys. Sci.* **342**, 209 (1975).

[21] W.W. Hagerty, and J.F. Shea, "A study of the stability of plane fluid sheets,"

J. Appl. Mech. **22**, 509 (1955).

[22] H.B. Squire, "Investigation of the instability of a moving liquid film," *Br. J. Appl. Phys.* **4**, 167 (1953).

[23] H.R. Asare, R.K. Takahashi, and M.A. Hoffman, "Liquid sheet jet experiments: comparison with linear theory," *Trans. ASME, J. Fluids Eng.* **103**, 595 (1981).

[24] G.D. Crapper, N. Dombrowski, W.P. Jepson, and G.A.D. Pyott, "A note on the growth of Kelvin-Helmholtz waves on thin liquid sheets," *J. Fluid Mech.* **57**, 671 (1973).

[25] G.D. Crapper, and N. Dombrowski, "A note on the effect of forced disturbances on the stability of thin liquid sheets and on the resulting drop size," *Int. J. Multiphase Flow* **10**, 731 (1984).

[26] C.J. Clark, and N. Dombrowski, "Aerodynamic instability and disintegration of inviscid liquid sheets," *Proc. R. Soc. London, Ser. A, Math. Phys. Sci.* **329**, 467 (1972).

[27] I.-P. Chung, C. Presser, and J.L. Dressler, "Effect of piezoelectric transducer modulation on liquid sheet disintegration," *Atom. Sprays* **8**, 479 (1998).

[28] S.K. Mitra, X. Li, and M. Renksizbulut, "On the breakup of viscous liquid sheets by dual-mode linear analysis", *J. Prop. Power* **17**, 728 (2001).

[29] M. Gaster, "A note on the relation between temporally-increasing and spatially-increasing disturbances in hydrodynamic stability," *J. Fluid Mechanics* **14**, 222 (1962).

[30] S.A. Jazayeri, and X. Li, "Structures of liquid-sheet sprays," *Particle and Particle System Characterization* **17**, 56 (2000).

[31] S.A. Jazayeri, and X. Li, "Nonlinear instability of plane liquid sheets," *J. Fluid Mechanics* **406**, 281 (2000).

[32] W.T. Pimbley, "Drop formation from a liquid jet: A linear one-dimensional analysis considered as a boundary value problem," *IBM J. Res. Develop.* **20**, 148 (1976).

[33] W.T. Pimbley, and H.C. Lee, Satellite Droplet Formation in a Liquid Jet. *IBM J. of Res. and Develop.* **21**, 21 (1977).

[34] D.B. Bogy, "Use of one-dimensional Cosserat theory to study instability in a viscous liquid jet," *Phys. Fluids* **21**, 190 (1978).

[35] J.H. Hilbing, and S.D. Heister, "Droplet size control in liquid jet breakup," *Phys. Fluids* **8**, 1574 (1996).

[36] C. Mehring, and W.A. Sirignano, "Planar-liquid-stream distortion from Kelvin-Helmholtz and Capillary Effects," in *Proc. 8th Int. Conf. on Liquid Atom. Spray Systems*, ICLASS, available on CD-rom.

[37] C. Mehring, and W.A. Sirignano, "Nonlinear capillary wave distortion and disintegration of thin planar liquid sheets," *J. Fluid Mech.* **388**, 69 (1999).

[38] C.A. Brebbia, *The Boundary Element Method for Engineers* (Pentech Press, London, 1980).

[39] C. Mehring, *Nonlinear distortion of thin liquid sheets.* Ph.D. Thesis, University of California, Irvine, 1999.

[40] C. Mehring, and W.A. Sirignano, "Axisymmetric capillary waves on thin annular liquid sheets. Part II: Spatial development," *Phys. Fluids* **12**, 1440 (1999).

[41] J.H. Hilbing, S.D. Heister, and K.M. Rump, "Recent advances in nonlinear modeling of atomization processes," *Proc. 9th Ann. Conf. Liquid Atom. Spray Systems*, ILASS North America, pp. 104–108.

[42] C.A. Spangler, J.H. Hilbing, and S.D. Heister, "Nonlinear modeling of jet atomization in the wind-induced regime," *Phys. Fluids* **7**, 964 (1995).

[43] W.A. Sirignano, and C. Mehring, " Review of theory of distortion and disintegration of liquid streams", *Progr. Eng. and Comb. Science* **26**, 609 (2000).

[44] C. Mehring, and W.A. Sirignano, "Axisymmetric capillary waves on thin annular liquid sheets. Part I: Temporal stability," *Phys. Fluids* **12**, 1417 (1999).

[45] R.D. Richtmyer, and K.W. Morton, *Difference Methods for Initial-Value Problems* (Wiley, New York, 2nd edition, 1967).

[46] J.I. Ramos, "Drawing of annular liquid jets at low Reynolds numbers," *Comp. Theor. Polymer Sci.* **11**, 429 (2001).

Table 1: Complex Fourier coefficients determined for nondimensional frequencies $f = 0, 0.2, 0.4, 0.6, 0.8$ of $\tilde{y}(t^*)$ and frequencies $g = 0, 0.1, 0.3$ of $\overline{y}(t^*)$ at various downstream locations x/h. Data taken from cases shown in Fig. 6, Fig. 9 and Fig. 18. (t^*_{int} denotes the sampling interval.)

case	Fig.6	Fig.9	Fig.18	
x/h	12.5	12.5	12.5	25
t^*_{int}	11 - 20.9	8 - 17.9	11 - 31.5	16.25 - 26.25
f_0	-1.7425	0.1243	-3.6091	-1.1409
$f_{0.2}$	-2.4001 -i 3.5750	0.6519 -i 8.5912	-2.2346 -i 3.2005	4.9988 +i 2.6593
$f_{0.4}$	-0.3777 -i 5.7013	-0.0560 -i 3.4911	0.2596 -i 2.8377	-3.3047 -i 1.3497
$f_{0.6}$	-0.3274 -i 1.8957	-0.9075 +i 0.8650	0.1585 -i 0.4658	0.2757 -i 1.2830
$f_{0.8}$	-0.6983 +i 0.4870	-0.0686 -i 0.1412	0.0080 +i 0.0422	0.0847 -i 0.0845
g_0	9.67	-4.9318	46.92	-63.8480
$g_{0.1}$	-126.48 -i 66.94	81.5998 +i 83.3471	117.45 +i 170.43	-11.3874 +i 80.3349
$g_{0.3}$	-10.37 -i 27.69	-11.1639 -i 11.2677	-16.95 +i 10.15	0.7101 +i 22.4862

Table 2: Complex Fourier coefficients determined for nondimensional frequencies $f = 0, 0.2, 0.4, 0.6, 0.8$ of $\tilde{y}(t^*)$ and frequencies $g = 0, 0.1, 0.3$ of $\overline{y}(t^*)$ at various downstream locations x/h. Data taken from cases shown in Fig. 11 and Fig. 12. (t^*_{int} denotes the sampling interval.)

case	Fig.11		Fig.12		
x/h	12.5	25	12.5	25	50
t^*_{int}	8 - 18	11.5 - 21.5	6 - 26	11.5 - 21.5	17 - 27
f_0	-1.1274	-0.2904	-2.2123	-0.3252	-0.1413
$f_{0.2}$	2.1313 +i 0.1244	5.2311 +i 4.6508	-3.0126 -i 2.7513	4.5862 +i 4.4771	8.0436 +i 12.3251
$f_{0.4}$	-2.6680 -i 0.2732	-4.4851 -i 5.4008	-0.4646 -i 4.7289	-3.4008 -i 5.0893	-15.8212 +i 7.7273
$f_{0.6}$	0.7068 -i 0.5327	1.9118 -i 2.8906	-0.1792 -i 1.5370	1.9544 -i 1.9449	-3.4856 +i 4.5756
$f_{0.8}$	0.3036 -i 0.2878	0.6632 +i 0.0905	-0.2280 +i 0.5580	0.4152 +i 0.2162	-0.0874 +i 0.6210
g_0	-5.3221	-16.7992	4.68	-17.8351	5.01
$g_{0.1}$	-18.4821 +i 75.7047	-32.4973 +i 75.9395	133.87 +i 93.26	-40.7346 +i 78.6269	-29.20 -i 100.29
$g_{0.3}$	5.1482 -i 14.6942	-14.3083 +i 30.8077	3.72 +i 30.94	-15.5162 +i 25.3493	7.14 -i 32.95

Table 3: Complex Fourier coefficients determined for nondimensional frequencies $f = 0, 0.2, 0.4, 0.6, 0.8$ of $\tilde{y}(t^*)$ and frequencies $g = 0, 0.1, 0.3$ of $\overline{y}(t^*)$ at various downstream locations x/h. Data taken from cases shown in Fig. 23. (t^*_{int} denotes the sampling interval.)

case	Fig.23 (dash,solid)			Fig.23 (dot,dash-dot)
x/h	12.5	25	50	12.5
t^*_{int}	8 - 38	10 - 40	20 - 40	7 - 27
f_0	1.0959	2.6197	0.8649	-3.7106
$f_{0.2}$	5.0258 -i 0.3302	-12.3063 -i 15.3748	4.1233 +i 44.0686	-0.8199 -i 3.9278
$f_{0.4}$	-1.2484 +i 5.7662	-1.0425 -i 16.3421	-26.9334 +i 3.7302	2.4076 -i 3.7397
$f_{0.6}$	-0.4002 -i 0.6104	1.1145 -i 5.6337	-5.6068 -i 4.2925	0.8231 +i 0.2940
$f_{0.8}$	1.5359 +i 1.1584	0.1498 +i 0.2117	0.2417 +i 1.1853	-0.2590 +i 1.4226
g_0	0.21	-12.7	1.93	63.36
$g_{0.1}$	12.85 +i 536.95	580.55 +i 657.35	-391.44 -i 31.04	226.70 +i 231.71
$g_{0.3}$	-9.86 -i 55.09	25.25 -i 33.98	-29.35 +i 12.68	-10.70 +i 19.00

Table 4: Complex Fourier coefficients determined for nondimensional frequencies $f = 0, 0.2, 0.4, 0.6, 0.8$ of $\tilde{y}(t^*)$ at various downstream locations x/h. Data taken from cases shown in Fig. 3 and Fig. 4. (t_{int} denotes the sampling interval.)

case	Fig.3			Fig.4		
x/h	12.5	25	50	12.5	25	50
t^*_{int}	7 - 37	10 - 40	15.5 - 45.5	5 - 25	9.5 - 24.5	15 - 25
f_0	-1.0487	-1.1002	-1.0912	-1.4044	-1.0758	-0.7213
$f_{0.1}$	-0.6770 - i 1.0303	-1.8518 - i 1.9126	-4.6015 -i 3.4093	-0.0004 +i 0.0003	-0.0008-i 0.00115	0.0045 +i 0.0009
$f_{0.2}$	0.8751 - i 0.9734	2.4318 - i 2.0079	4.3950 -i 4.8127	-1.6982 +i 0.3701	0.8970 -i 2.9529	1.0881 -i 4.6293
$f_{0.3}$	0.8444 + i 0.4398	1.4058 + i 1.2092	2.7260+i 0.9146	0.0026 -i 0.0002	0.0015 -i 0.00285	-0.0016 +i 0.0095
$f_{0.4}$	0.0424 + i 0.3450	-0.0645 + i 0.1913	-0.0625 -i 0.4539	-0.4588 +i 0.1487	0.4805+i 0.2696	0.2182 +i 0.0205
$f_{0.5}$	0.0512 - i 0.0836	0.0737 - i 0.2080	0.1080 -i 0.4961	-0.0027 -i 0.0049	-0.0041 -i 0.00185	0.0136 +i 0.0303
$f_{0.6}$	0.0322 + i 0.0066	0.0178 + i 0.1015	0.1618 -i 0.0052	0.0465 -i 0.0973	0.0743 -i 0.1839	-0.4138 -i 0.3860

Figure captions

Figure 1: Schematic of Twin-Fluid Atomizer Configuration

Figure 2: Solution procedure for dilational mode film forcing ($\overline{y} = 0$, $\overline{v} = 0$; $h = \tilde{y}$, $u = \overline{u}$, $\phi = \phi_{g;1}$, $p_g = p_{g;1}$, $\Gamma = \Gamma_1$, $y_- = -\tilde{y}/2$, p_c = capillary pressure along lower interface).

Figure 3: Dilationally distorting gas-jet-modulated semi-infinite planar film under base-case forcing conditions according to Eq. (1) and for base-case parameter set: $s/h = H/h = 10$, $\rho_g/\rho_l = 0.0012$, $\mathrm{We}_l = 10$, $\mathrm{M}_\perp = \mathrm{M}_{||} = 1$. $T_p = 5$, $n_{\theta;1,2} = 0$.

Figure 4: Dilationally distorting gas-jet-modulated film with base-case parameter configuration and modified pulse characteristics.

Figure 5: Sinusoidally distorting gas-jet-modulated film under base-case forcing conditions according to Eq. (1) and for base-case parameter set: $s/h = H/h = 10$, $\rho_g/\rho_l = 0.0012$, $\mathrm{We}_l = 10$, $\mathrm{M}_\perp = \mathrm{M}_{||} = 1$. $T_p = 5$, $n_{\theta;1} = 0$, $n_{\theta;2} = 1$.

Figure 6: Discharging sinusoidally distorting gas-jet-modulated liquid film according to Fig. 5 with modified start-up conditions.

Figure 7: Discharging gas-jet-modulated liquid film according to Fig. 5 under mixed-mode forcing conditions ($n_{\theta;1} = 0, n_{\theta;2} = 0.5$).

Figure 8: Effect of Weber number increase ($\mathrm{We}_l = 25$) on discharging sinusoidally distorting gas-jet-modulated liquid film.

Figure 9: Effect of Weber number decrease ($\mathrm{We}_l = 5$) on discharging sinusoidally distorting gas-jet-modulated liquid film.

Figure 10: Effect of Weber number increase ($\mathrm{We}_l = 25$) on discharging dilationally distorting gas-jet-modulated liquid film.

Figure 11: Effect of decreased vertical gas-jet momentum ($\mathrm{M}_\perp = 0.5$ on discharging sinusoidally distorting gas-jet-modulated liquid film. $\mathrm{M}_{||} = 1$).

Figure 12: Effect of decreased gas-jet injection angle α ($\alpha = 30°$, $M = \sqrt{M_{\parallel}^2 + M_{\perp}^2} = \sqrt{2}$) on discharging sinusoidally distorting gas-jet-modulated liquid film.

Figure 13: Effect of decreased gas-jet injection angle ($\alpha = 15°$) on discharging sinusoidally distorting gas-jet-modulated liquid film.

Figure 14: Effect of increased vertical gas-jet momentum ($M_{\perp} = 5$) on discharging sinusoidally distorting gas-jet-modulated liquid film.

Figure 15: Effect of increased parallel gas-jet momentum ($M_{\parallel} = 5$) on discharging sinusoidally distorting gas-jet-modulated liquid film.

Figure 16: Effect of increased gas-to-liquid density ratio ($\rho_g/\rho_l = 0.006$) on discharging sinusoidally distorting gas-jet-modulated liquid film.

Figure 17: Effect of decreased pulse period ($T_p = 2.5$) on discharging sinusoidally distorting gas-jet-modulated liquid film.

Figure 18: Effect of non-zero time-independent gas-jet velocity on discharging sinusoidally distorting gas-jet-modulated liquid film ($T_p = 5$; $u'_{g;0} = 0.5u_{g;0}, u_{g;s}(t) = 0.25$).

Figure 19: Effect of increased pulse period ($T_p = 8.75$) on on discharging sinusoidally distorting gas-jet-modulated liquid film with underlying non-zero gas-jet velocity $u_{g;s}$.

Figure 20: Effect of increased pulse period ($T_p = 20$) on discharging sinusoidally distorting gas-jet-modulated liquid film with underlying non-zero gas-jet velocity $u_{g;s}$.

Figure 21: Dimensionless growth rate $\mathrm{Im}[\omega/(kU_0)]$ as function of $kh = 2\pi h/\lambda$ for planar liquid film with co-flowing gas streams (at relative velocity U_0) and $\mathrm{We} = \rho_l U_0^2 h/\sigma = 971$ and $\rho_g/\rho_l = 0.0012$.

Figure 22: Influence of domain length ($x_{max}/h = 250$) on discharging sinusoidally distorting gas-jet-modulated liquid film with underlying non-zero gas-jet velocity $u_{g;s}$.

Figure 23: Sinusoidally distorting liquid-phase-modulated film according to Eq. (10), with or without adjacent constant velocity gas streams and under base-case parameter conditions: $s/h = H/h = 10$, $\rho_g/\rho_l = 0.0012$, $\mathrm{We}_l = 10$, $\mathrm{M}_\perp = \mathrm{M}_\parallel = 1$, $T_p = 5$. $u_{g;s} = 0$: $t^* = 9$ (dashed), 19 (solid); $u_{g;s} = 0.45$: $t^* = 9$ (dotted), 19 (dash-dot). Without continuous gas jets, energy input is 5% of that in Fig. 5.

Figure 24: Sinusoidally distorting liquid-phase-modulated film according to Eq. (10), without adjacent constant velocity gas streams and under base-case parameter conditions: $s/h = H/h = 10$, $\rho_g/\rho_l = 0.0012$, $\mathrm{We}_l = 10$, $\mathrm{M}_\perp = \mathrm{M}_\parallel = 1$, $T_p = 5$. Energy input is twice that of Fig. 23.

Figure 25: Dilationally distorting liquid-phase-modulated film according to Eq. (10) injected into a quiescent ambient gas under base-case parameter conditions: $s/h = H/h = 10$, $\rho_g/\rho_l = 0.0012$, $\mathrm{We}_l = 10$, $\mathrm{M}_\perp = \mathrm{M}_\parallel = 1$, $T_p = 5$. Energy input is 5% of that in Fig. 5.

Figure 26: Dilationally distorting liquid-phase-modulated film according to Eq. (10) with adjacent constant velocity gas streams and under base-case parameter conditions: $s/h = H/h = 10$, $\rho_g/\rho_l = 0.0012$, $\mathrm{We}_l = 10$, $\mathrm{M}_\perp = \mathrm{M}_\parallel = 1$, $T_p = 5$. Energy input from direct film modulation equals that in Fig. 25.

Figure 27: Phase plot for $\tilde{y}(t^*)$ at $x/h = 12.5$ according to the case shown in Fig. 11. (Nondimensional time t^* progresses in the clockwise direction.)

Figure 28: Phase plot for $\overline{y}(t^*)$ at $x/h = 12.5$ according to the case shown in Fig. 11.

Figure 29: Phase plot for $\tilde{y}(t^*)$ at $x/h = 25$ according to the case shown in Fig. 11.

Figure 30: Phase plot for $\overline{y}(t^*)$ at $x/h = 25$ according to the case shown in Fig. 11.

Figure 31: Phase plot for $\tilde{y}(t^*)$ at $x/h = 12.5$ according to the case shown in Fig. 23 without co-flowing gas streams.

Figure 32: Phase plot for $\overline{y}(t^*)$ at $x/h = 12.5$ according to the case shown in Fig. 23 without co-flowing gas streams.

FIGURES

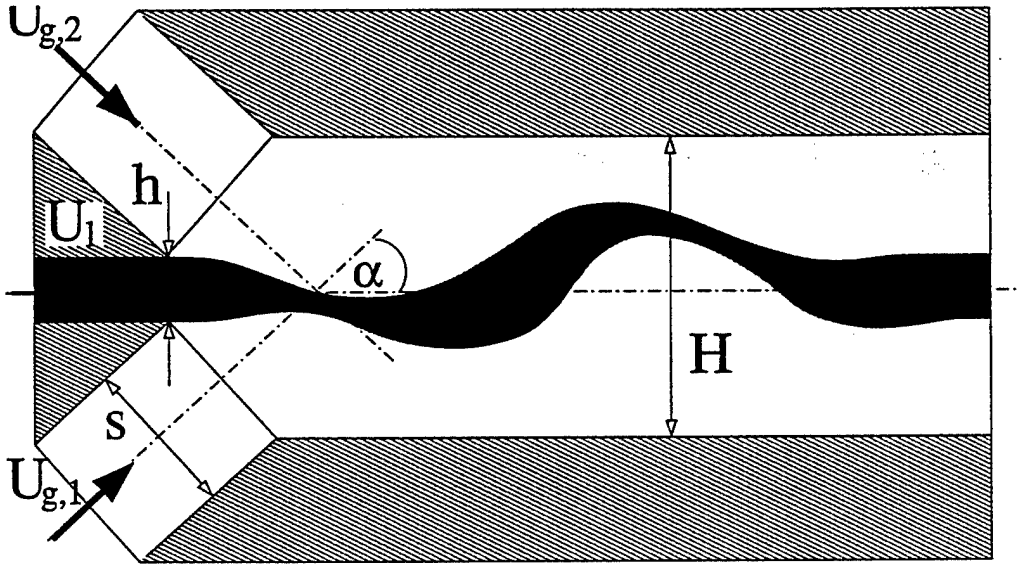

FIG. 1. Mehring, Phys. Fluids

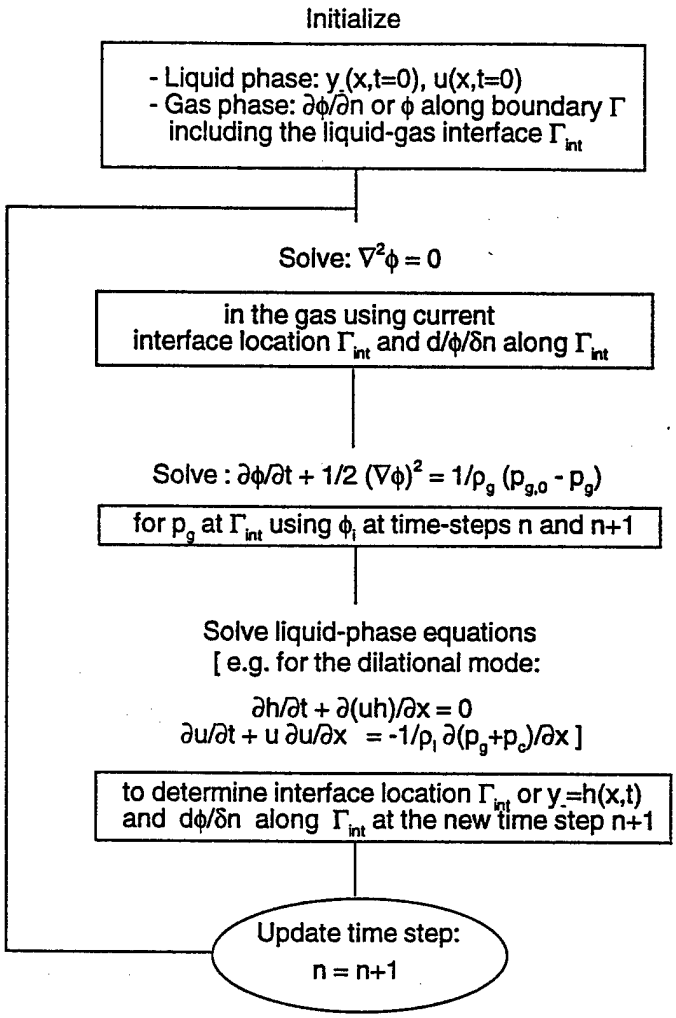

FIG. 2. Mehring, Phys. Fluids

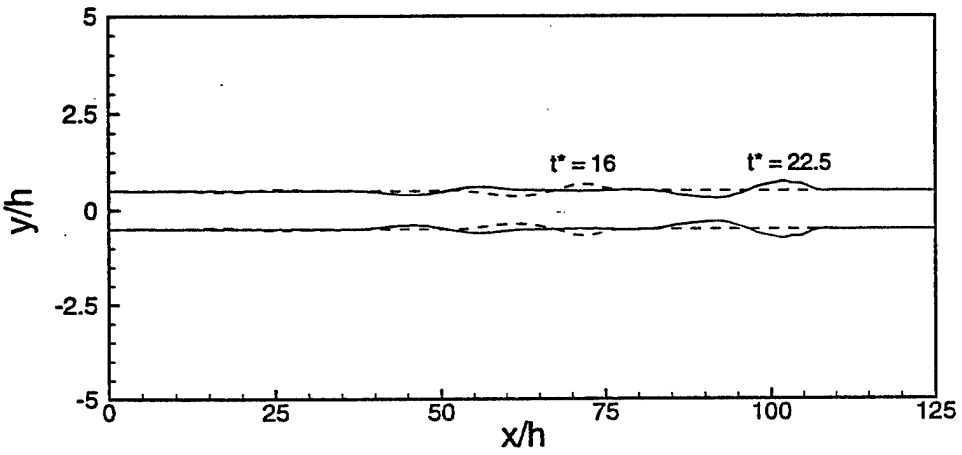

FIG. 3. Mehring, Phys. Fluids

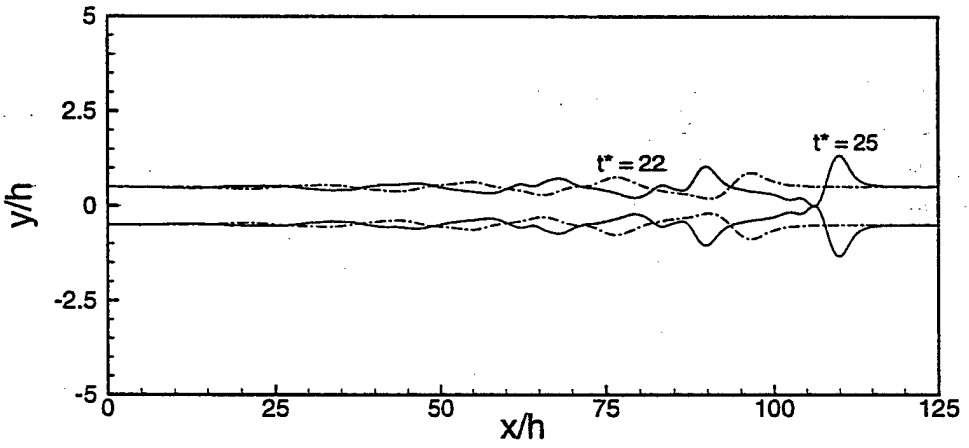

FIG. 4. Mehring, Phys. Fluids

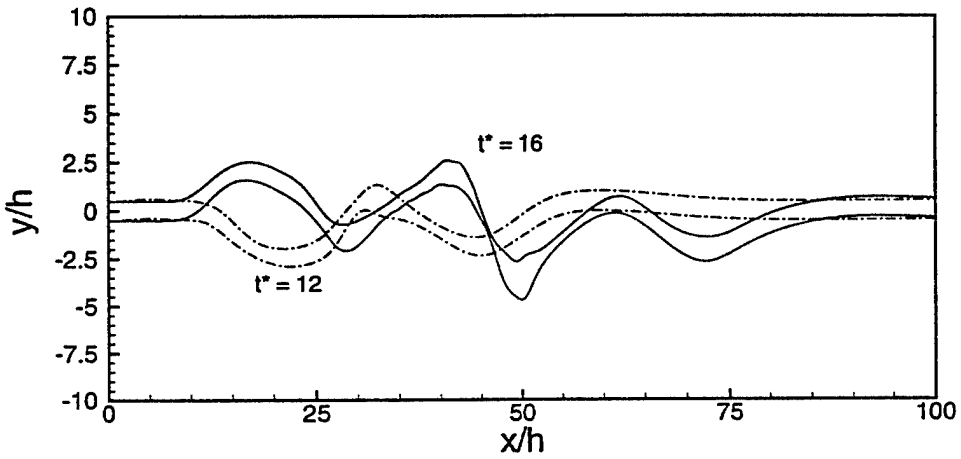

FIG. 5. Mehring, Phys. Fluids

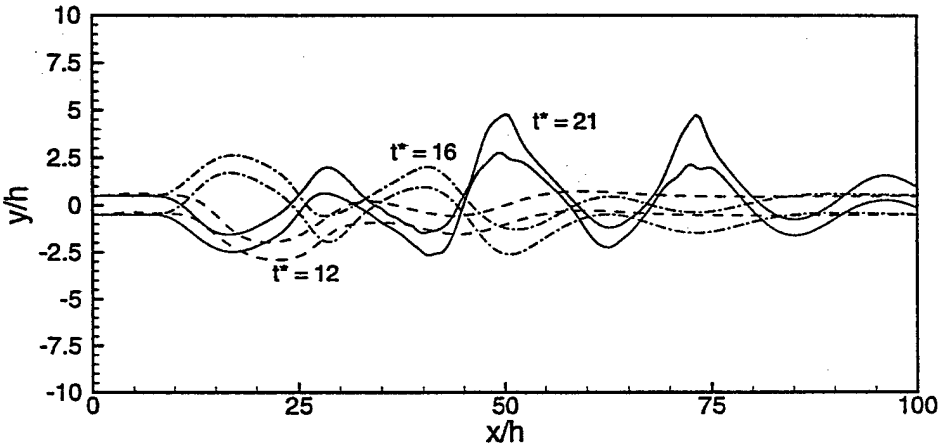

FIG. 6. Mehring, Phys. Fluids

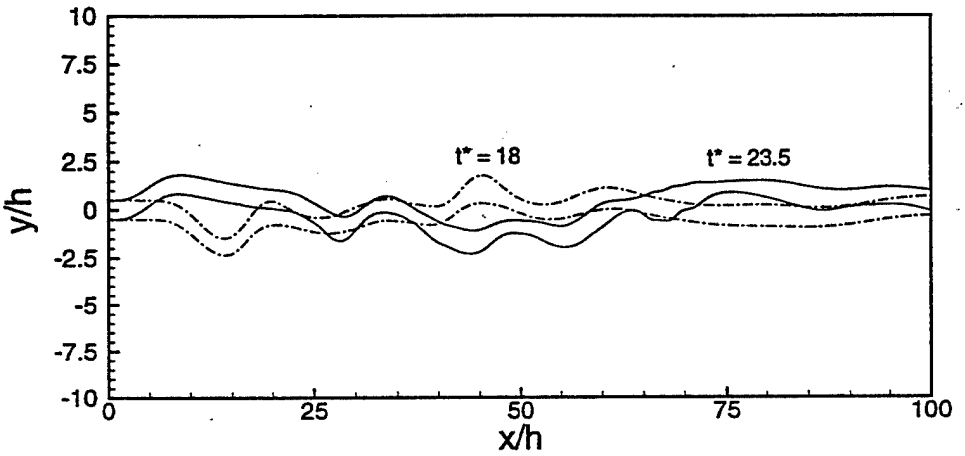

FIG. 7. Mehring, Phys. Fluids

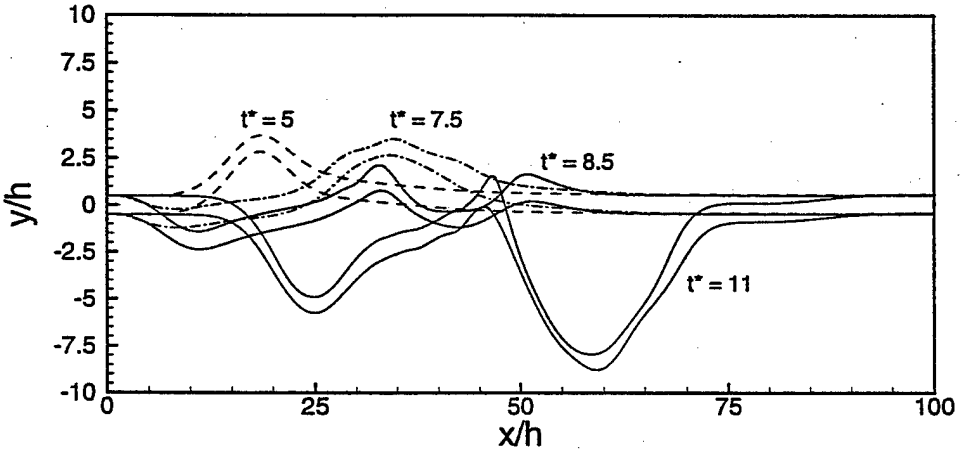

FIG. 8. Mehring, Phys. Fluids

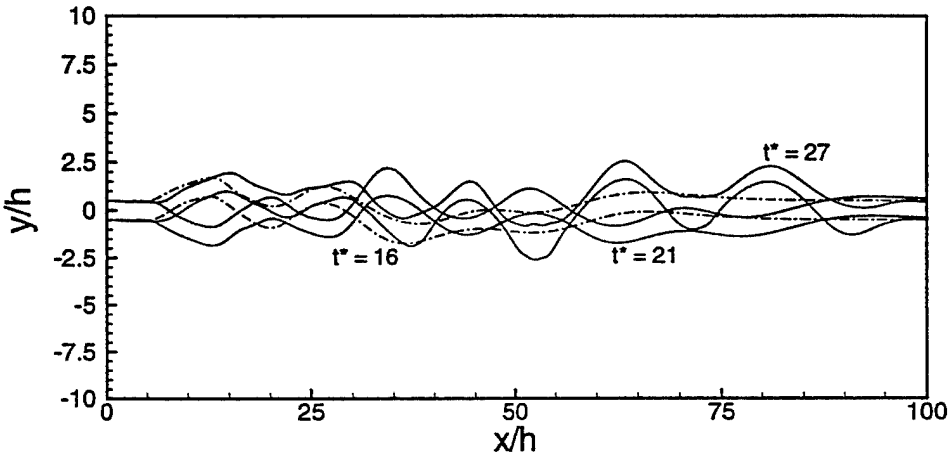

FIG. 9. Mehring, Phys. Fluids

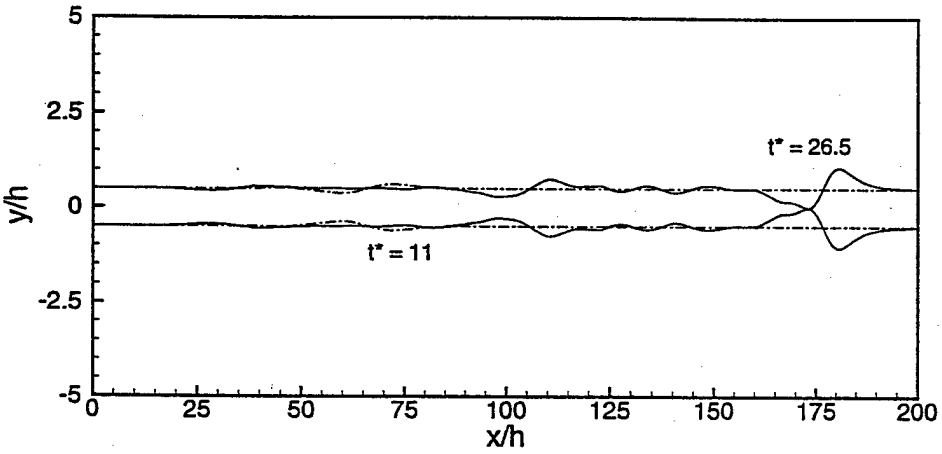

FIG. 10. Mehring, Phys. Fluids

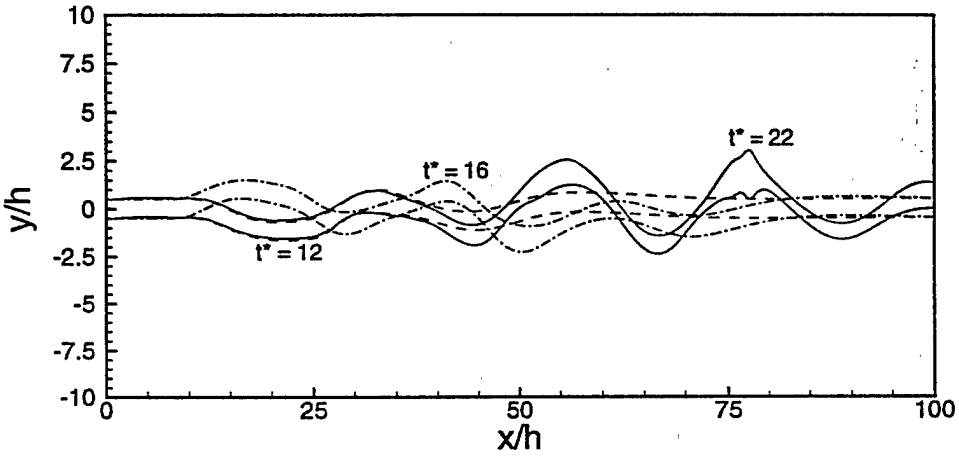

FIG. 11. Mehring, Phys. Fluids

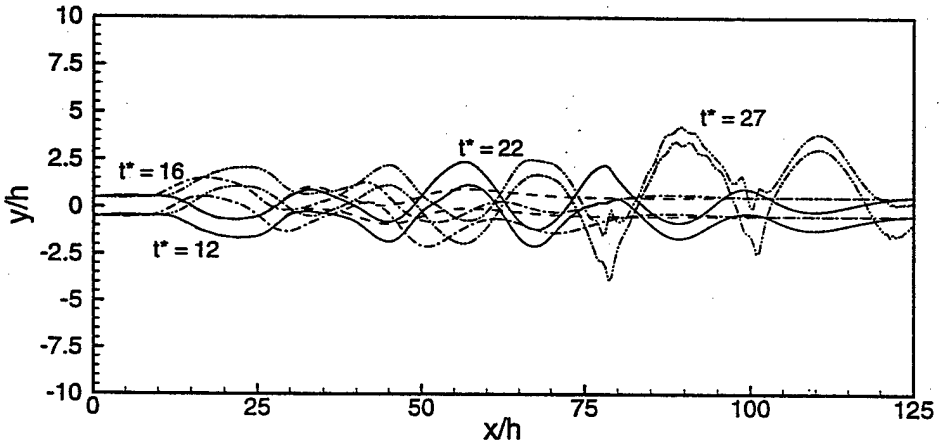

FIG. 12. Mehring, Phys. Fluids

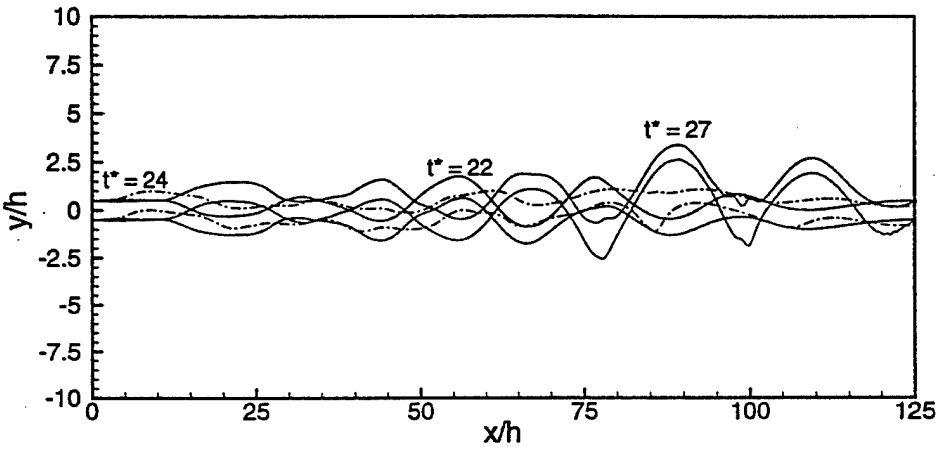

FIG. 13. Mehring, Phys. Fluids

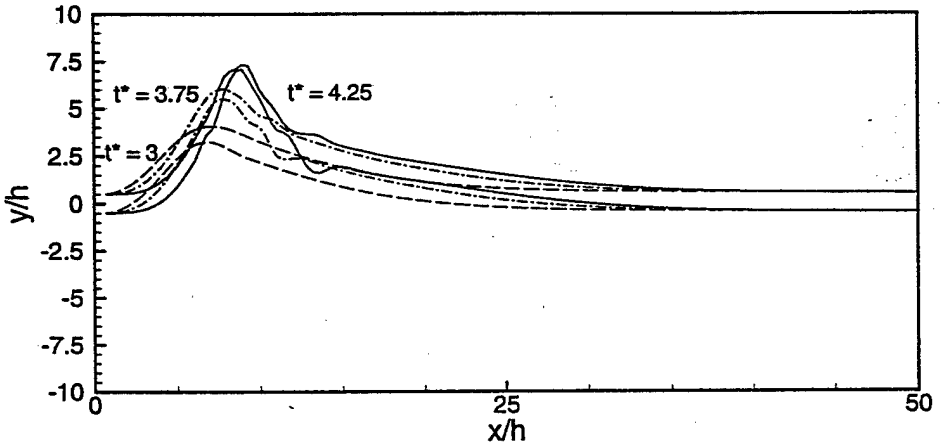

FIG. 14. Mehring, Phys. Fluids

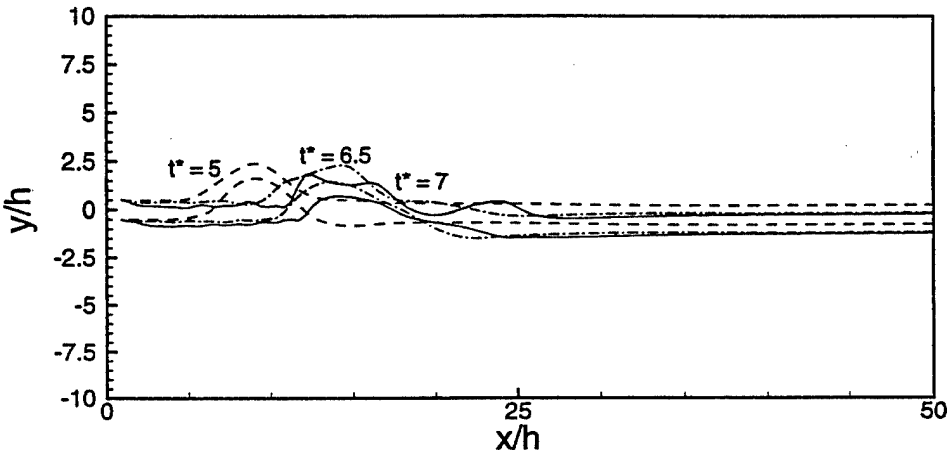

FIG. 15. Mehring, Phys. Fluids

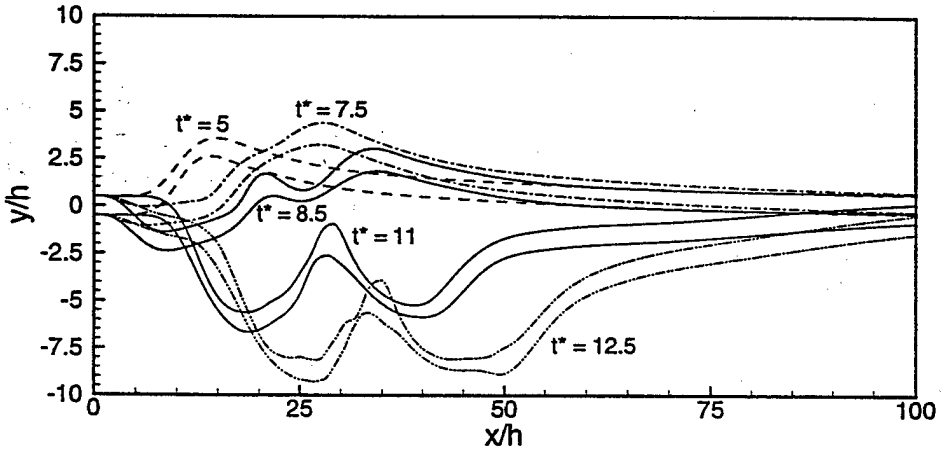

FIG. 16. Mehring, Phys. Fluids

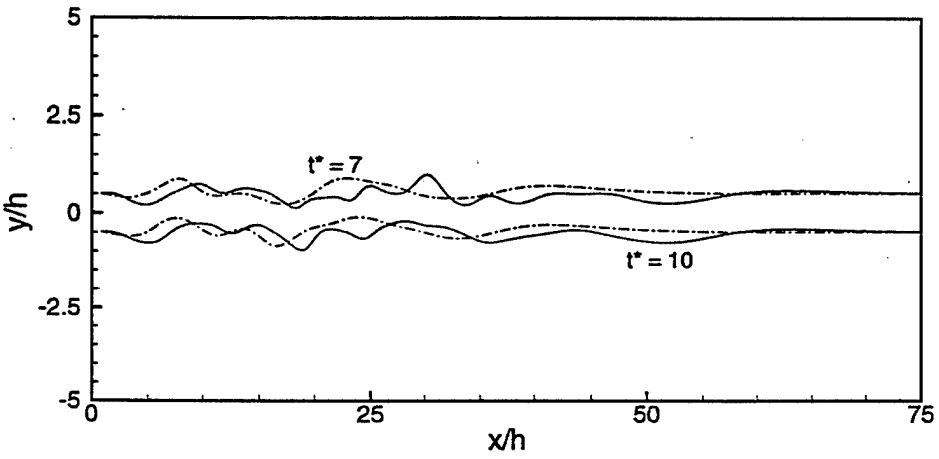

FIG. 17. Mehring, Phys. Fluids

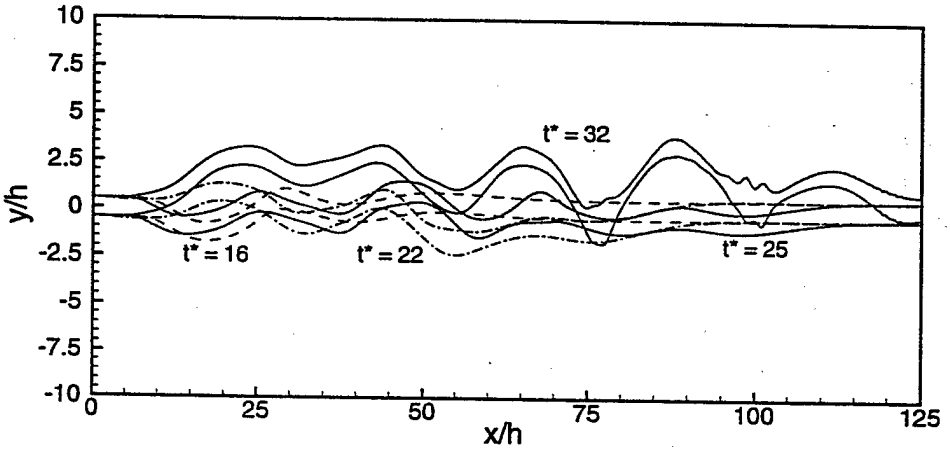

FIG. 18. Mehring, Phys. Fluids

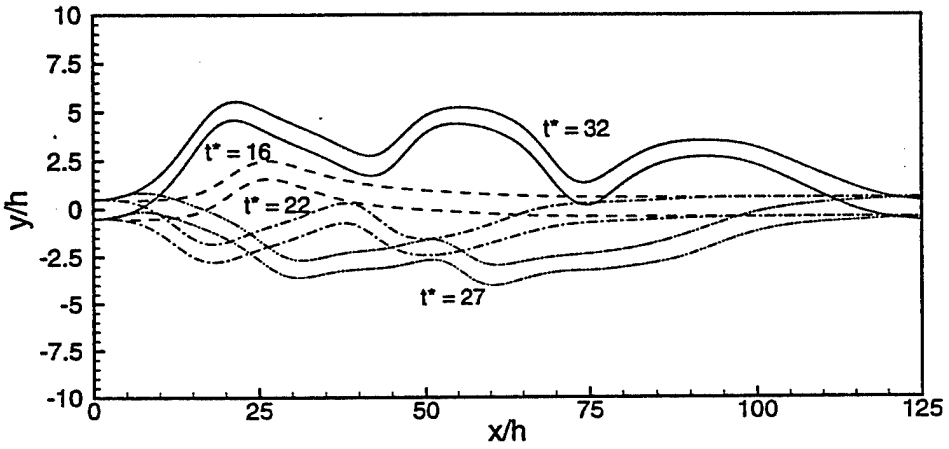

FIG. 19. Mehring, Phys. Fluids

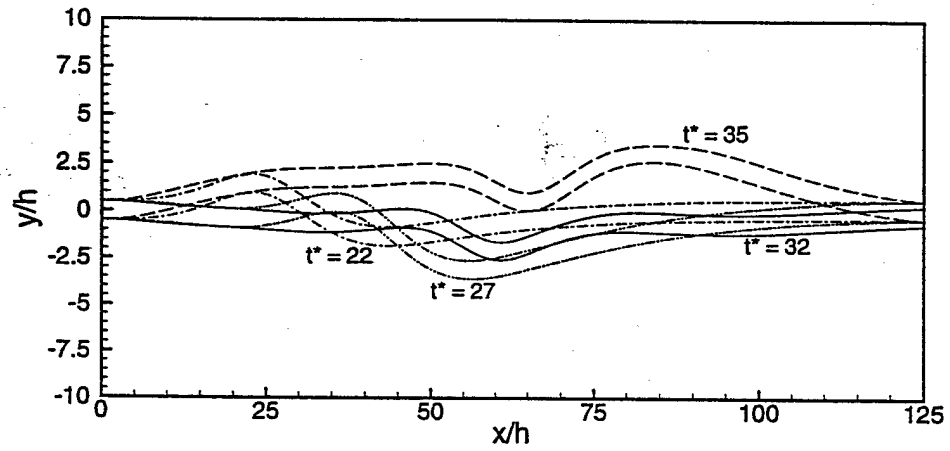

FIG. 20. Mehring, Phys. Fluids

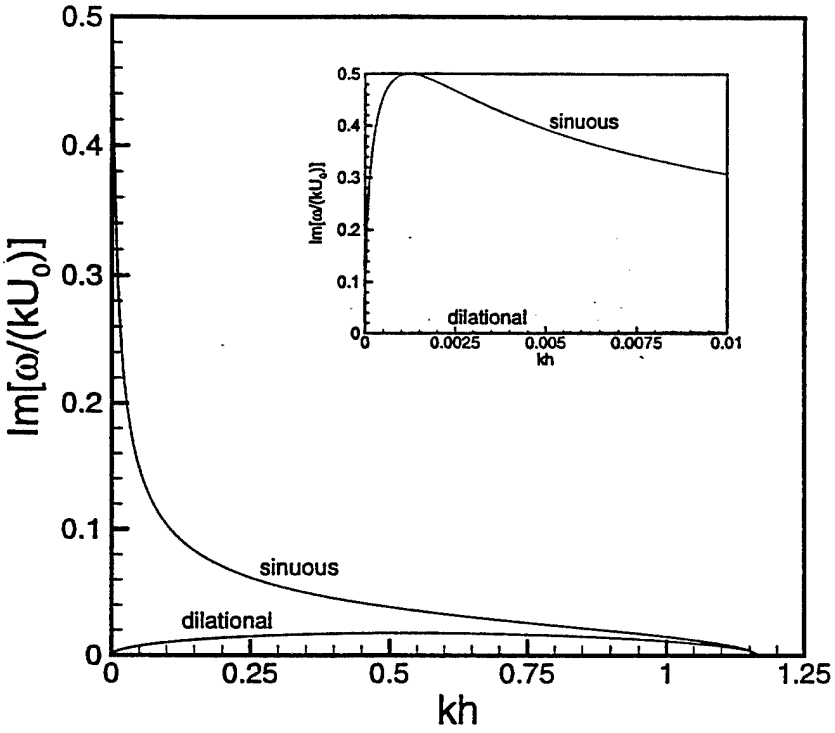

FIG. 21. Mehring, Phys. Fluids

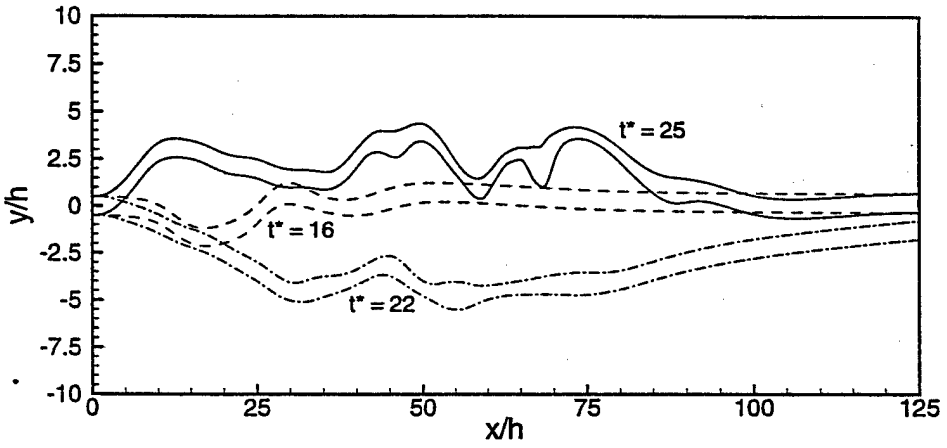

FIG. 22. Mehring, Phys. Fluids

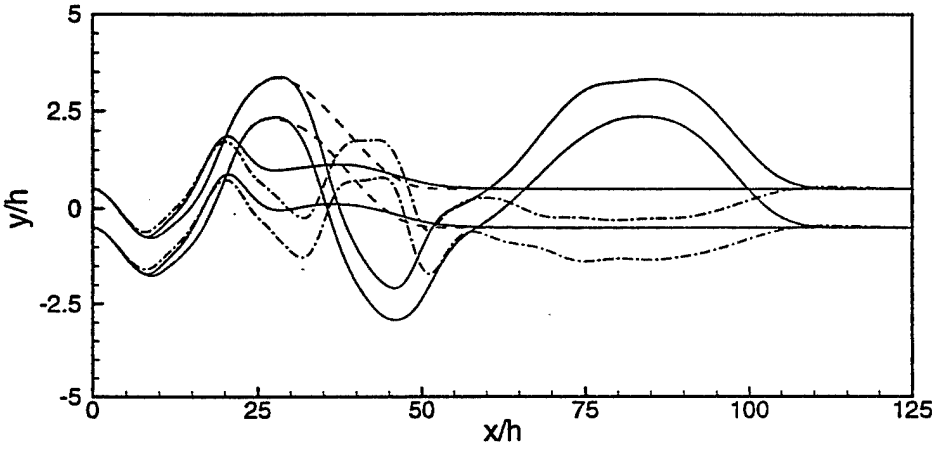

FIG. 23. Mehring, Phys. Fluids

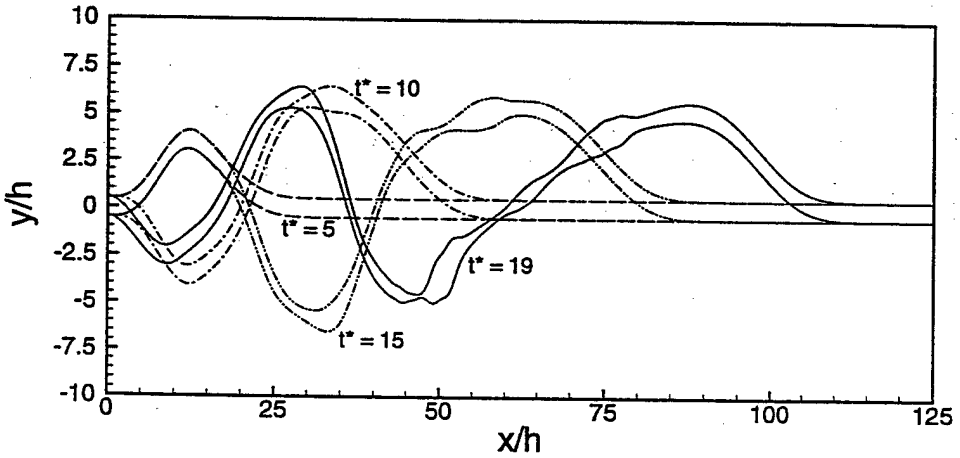

FIG. 24. Mehring, Phys. Fluids

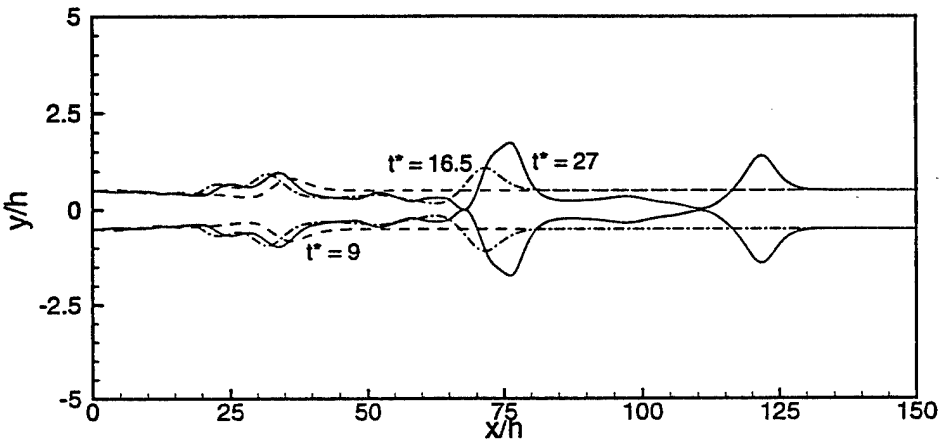

FIG. 25. Mehring, Phys. Fluids

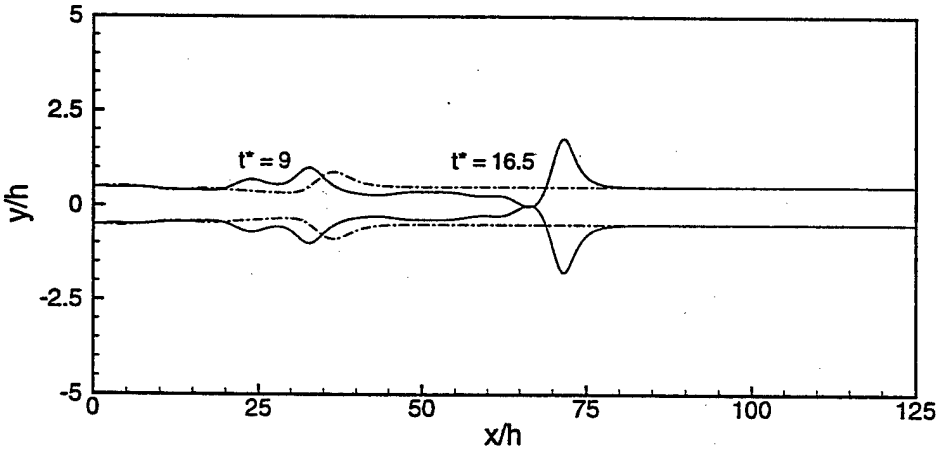

FIG. 26. Mehring, Phys. Fluids

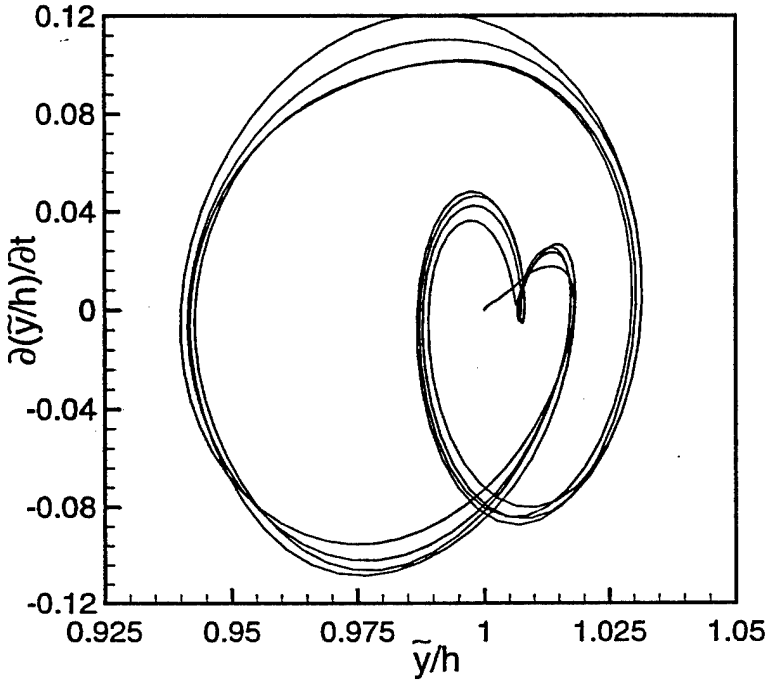

FIG. 27. Mehring, Phys. Fluids

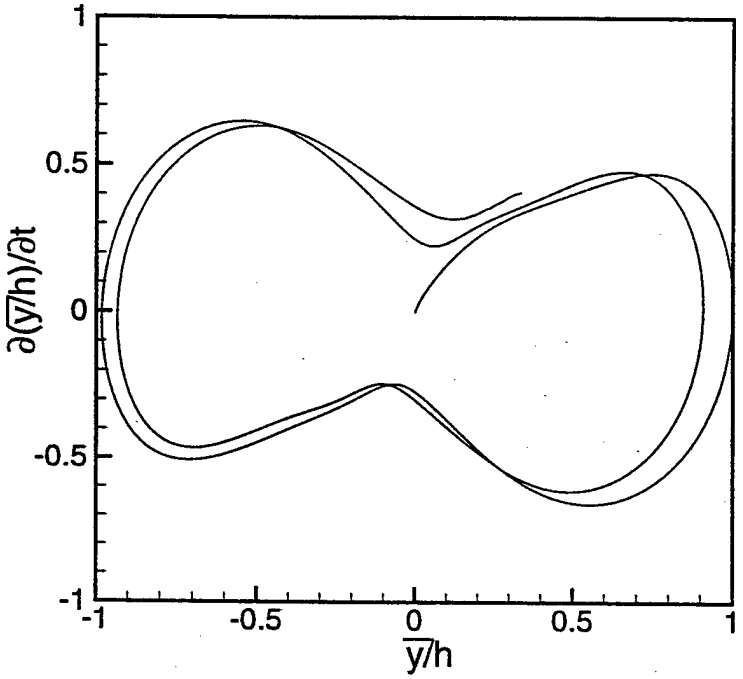

FIG. 28. Mehring, Phys. Fluids

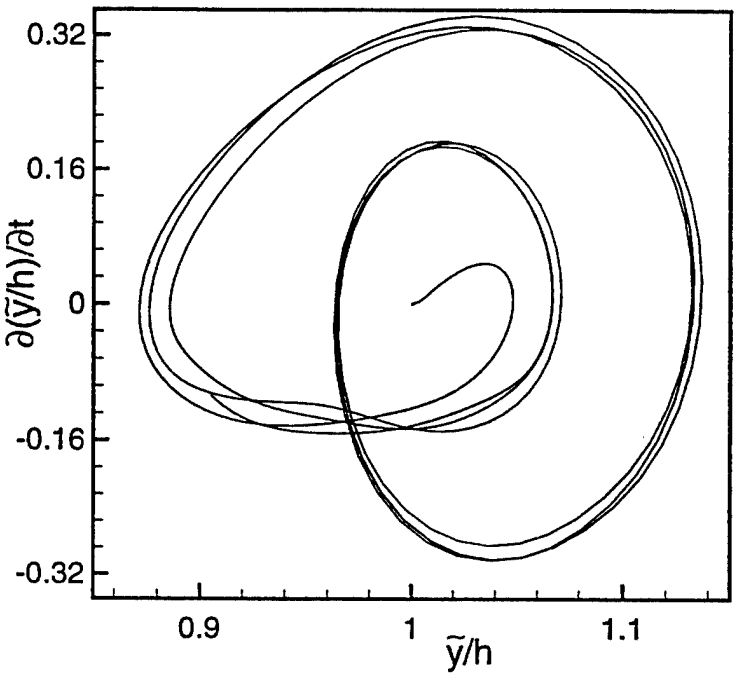

FIG. 29. Mehring, Phys. Fluids

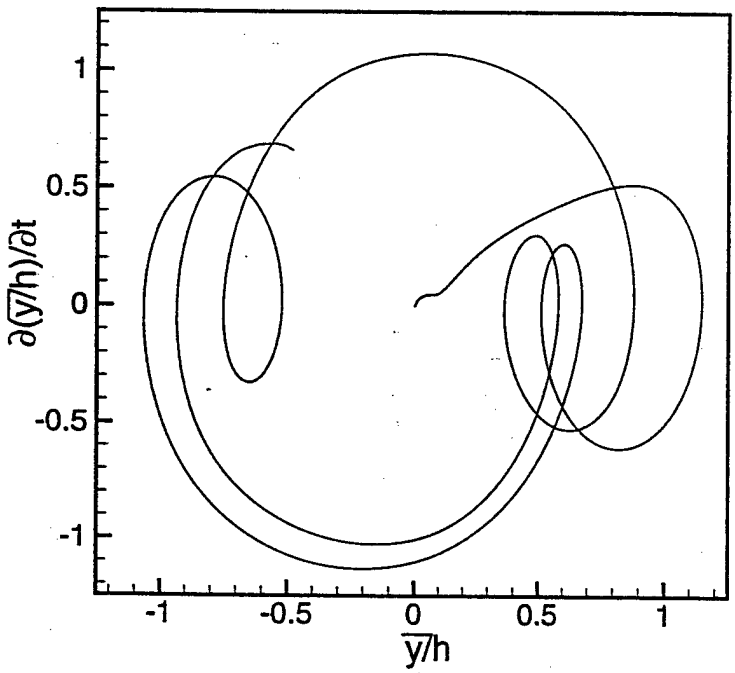

FIG. 30. Mehring, Phys. Fluids

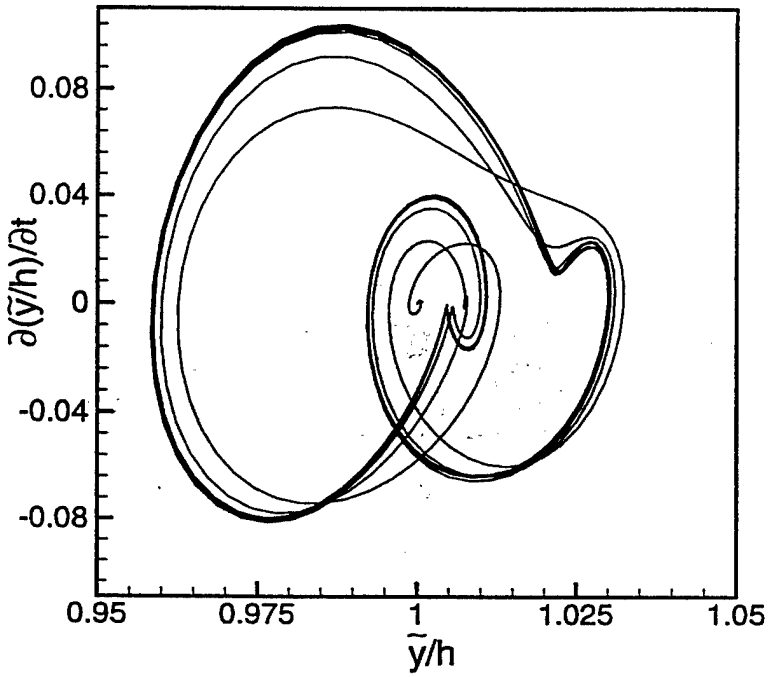

FIG. 31. Mehring, Phys. Fluids

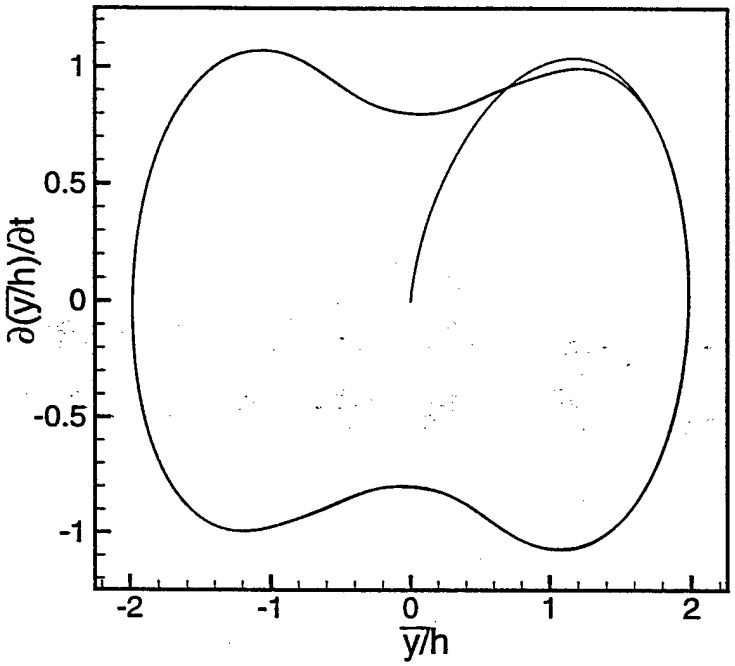

FIG. 32. Mehring, Phys. Fluids

Capillary Stability of Modulated Swirling Liquid Films

C. Mehring and W.A. Sirignano

Department of Mechanical and Aerospace Engineering

University of California, Irvine

Irvine, CA 92697

Abstract

The linear and nonlinear distortion and breakup of three-dimensional swirling or non-swirling annular and swirling conical thin inviscid liquid films are analyzed by means of a reduced-dimension approach. The films discharge from an annular slit nozzle or atomizer into a gas of negligible density at negligible gravity conditions. Nonlinear numerical simulations describe film distortion up to the time when film rupture first occurs. Linear and nonlinear solutions are presented and discussed for various configurations and with either dilational or sinuous three-dimensional modulations imposed onto the films at the nozzle exit. Nonlinear growth rates can be significantly larger than predicted by linear theory. Initially axisymmetric disturbances remain axisymmetric and fluctuations in the circumferential direction generated by numerical error are not amplified for the considered cases. Overall film topology at the time of film rupture suggests that single dilational or sinuous oblique waves will result in

spiraling filaments detaching from the continuous film. Combination of clockwise and counter-clockwise travelling dilational waves results in an approximately rectangular array of larger ligaments interspaced by thin fluid films indicating subsequent cellular-type breakup for both annular and conical configurations. Results for similar sinuous mode modulations suggest film disintegration via shedding of continuous annular rings from swirling annular films and filament shedding from swirling conical films.

Introduction

The stability of liquid sheets plays an important role in various technological applications including spray combustion of liquid fuels in furnaces, internal combustion piston engines, jet engine combustion chambers and rocket motors [?]. The combustion of liquid fuels in the described applications is frequently achieved through the generation and disintegration of swirling conical liquid films [2]. The stability of annular films is of relevance in applications such as film shell encapsulation or shell formation, film blowing, as well as in the use of collapsing annular films as chemical reactors for toxic waste incineration.

Experimental observations of disintegrating conical liquid sheets have already been described by various authors. See Ref. [3] for a more detailed review. Theoretical analyses of the phenomenon of liquid-film breakup were in general limited to linear planar or annular sheet configurations; the latter with or without swirl [4]. In particular, linear three-dimensional analyses of planar or swirling annular sheets were only presented by Ibrahim and Akpan [5], Ponstein [6] and Panchagnula, Sojka and Santangelo [4]. A linear analysis of swirling conical sheets poses a variable coefficient problem, and has not, to the knowledge of the authors,

been presented in the literature. The few nonlinear analyses presented on the subject were also limited to the planar geometry [7, 8, 9, 10, 11], annular sheets, or liquid bells without swirl [12, 13, 14, 15]. A nonlinear analysis of truly three-dimensionally distorting (swirling or non-swirling) annular and swirling conical films discharging from a nozzle or atomizer and subject to dilational or sinuous modulations at the nozzle exit has not been presented so far, even though the prescribed configurations (in particular swirling conical liquid films) are of importance in practical atomization systems, such as swirl-cup atomizers or pre-filming atomizers.

Linear and nonlinear analyses of discharging, modulated, pressure-stabilized, thin annular liquid films were presented in Ref. [17]. The linear analysis predicted that, in general, film modulation generates four dilational and two sinuous mode wavenumbers. Group velocity analysis (with terms of $O(R^{-3})$ neglected) and consideration of the Sommerfeld radiation condition downstream lead to the conclusion that only two dilational mode wavenumbers will appear on the discharging film (k_2 and k_3 in Ref. [17]). For sufficiently large forcing frequencies ω or Weber numbers We (based on liquid density, undisturbed film thickness and undisturbed liquid velocity at the nozzle exit), wavenumber k_3 resulted in an exponentially growing dilational mode wave whereas k_2 (its complex conjugate value) resulted in an exponentially decaying disturbance downstream. Linearly unstable sinuous mode waves are predicted only for Weber numbers We > 2 at forcing frequencies $\omega < (1/R)\sqrt{1 - 2/\mathrm{We}}$, i.e. where wavenumber l_2 resulted in an exponentially growing wave and l_1 (the complex conjugate of l_2) produced an exponentially decaying disturbance downstream. For small Weber numbers, i.e. We ≤ 5, nonlinear and linear numerical simulations of the initial and boundary-value problem were dominated by transient effects. In particular, film collapse and

bubble formation was observed to occur near the wavefront as the initial film disturbance propagated into the undisturbed film. In Ref. [3] axisymmetric, swirl-stabilized annular film were analyzed. According to linear analysis and in contrast to the pressure-stabilized case, no pure dilational mode is found on swirl-stabilized annular films. For swirl-stabilized films, collapse of the undisturbed annular configuration is prevented by the centrifugal forces resulting from the swirling motion; for pressure-stabilized (non-swirling) annular films, a constant positive pressure difference is maintained between the inner core and the surrounding of the annulus in order to prevent the film from collapsing on itself due to surface tension. In the pressure-stabilized case, linear mode-coupling occured solely from the sinuous to the dilational mode via the conservation-of-mass equation. Nevertheless, for large enough Weber numbers and low forcing frequencies, linear dilational or predominantly dilational mode waves behave qualitatively the same on both pressure- and swirl-stabilized films. However, the instability range and unstable growth rate for linear "dilational" waves is significantly larger for swirl-stabilized films in comparison to pressure-stabilized ones, i.e. $\omega_{l,s} > \omega_{l,p}$ with ω_l being the forcing frequency at the stability limit and subscripts s and p denoting swirl- and pressure-stabilized films, respectively. A significantly larger growth rate of "dilational" mode waves on swirling axisymmetric annular films has also been observed in the comparison of a dilationally modulated nonlinear swirl-stabilized film and a similar pressure-stabilized films [3]. Qualitative differences between linear "dilational" mode waves on swirl- and pressure-stabilized annular films were found at increased forcing frequencies, e.g. $\omega > 0.6$ (for large Weber numbers), and even at lower forcing frequencies if the Weber numbers were small enough. However, in the parameter and comparative numerical studies of Ref. [3], cases with large modulation frequencies were not considered due to the limitations of the em-

ployed thin film model. Small Weber number cases were also excluded from the analysis, due to the dominance of transient effects in the corresponding numerical simulations. In strong contrast to pressure-stabilized films, where linear theory predicts that unstable sinuous waves are only found for Weber numbers We > 2, predominantly sinuous-mode unstable waves on swirl-stabilized films are only observed for We < 2. However, as in Ref. [17] and due to the dominant behavior of transient effects within the numerical analysis, swirling annular (or conical) films at small Weber numbers were not studied in Ref. [3]. Rather, the parameter studies of Ref. [3] (analyzing the effect of Weber number, modulation amplitude and swirl number on breakup time and breakup length) were conducted around four annular (e.g. swirl number $k = 1$) base cases with modulations of the axial or transverse film velocity at the nozzle exit at We $= 100$ and forcing frequencies $\omega < 0.42$. The linear analysis of Ref. [3] was constrained to swirling axisymmetric annular films. Initial conditions for the numerical simulations of axisymmetric swirling conical films in Ref. [3] were obtained by integrating the nonlinear steady-state equations from the nozzle exit with appropriate boundary conditions at the nozzle and a 4th-order Runge-Kutta integrator. Modulation of the axial and/or transverse film velocity were of the form $\overline{v}^*_{z,r} = A_{z,r}\left[1 - e^{-t^*/T_s}\right]\sin\left(2\pi t^*/T_p\right)$ with the nondimensional time-period of the harmonic forcing T_p and the nondimensional forcing amplitudes of the axial or transverse velocity modulation $A_{z,r}$.

A brief discussion on three-dimensionally modulated swirling annular and conical films was included in Ref. [3]. However, this discussion was limited to the numerical solution of initially axisymmetric film modulations or axisymmetric modulations with superimposed small-amplitude circumferential disturbances. Three-dimensional solutions, for sheets with axisymmetric modulations only, remained axisymmetric throughout the simulations, indi-

cating that small perturbations due to numerical error do not result in a three-dimensional capillary instability. For the considered annular and conical films with harmonic forcing of the axial or transverse velocity, the characteristics of the film distortion remained predominantly axisymmetric.

The present analysis extends the three-dimensional discussion of Ref. [3] by considering film modulations which result in truly three-dimensional film distortion and rupture, as well as by incorporating a detailed description of the three-dimensional model. In addition, the present analysis includes a three-dimensional linear spatial analysis of swirling annular films. In analogy to the axisymmetric analysis of Ref. [3], the linear analysis 1) identifies the appropriate number of boundary conditions for the numerical simulations and 2) identifies the magnitude and importance of nonlinear effects by comparison between linear analytical and nonlinear numerical results. Analogous to previous work by the authors [3, 7, 17, 18, 19], group velocities of the capillary waves emanating from the modulated nozzle and from downstream are obtained from the linear analysis and are used to identify the number of boundary conditions to be specified at the atomizer exit and the number at downstream infinity for both linear and nonlinear analyses.

In the analysis of thin liquid sheets or films presented here, only capillary and inertia effects are considered. Subsequently, the term 'annular' refers to thin-walled cylindrical liquid columns with approximately ring-shaped cross-sectional area of constant time-averaged radius along the axial direction. Sheets or films which roughly resemble hollow cones, i.e., thin-walled liquid columns with monotonically increasing or decreasing annular radius of the ring-shaped cross-sectional area, are named 'conical' sheets. Clearly, sheets or films discharging from an annular nozzle and with a monotonically increasing or decreasing annular

radius within the region near the atomizer are still described as being 'conical' even if the annular radius undergoes oscillations further downstream. The latter phenomenon might occur due to the dynamic exchange of translational or rotational kinetic energy and potential or surface energy.

Problem Formulation

The present work extends previous work by the authors on non-swirling annular and swirling conical sheets. [3, 16, 17, 18, 21]. Considered are semi-infinitely-long thin swirling (or non-swirling) liquid films exiting from an annular nozzle or atomizer as shown in Fig. 1.

Three-dimensional dilational and sinuous disturbances are considered. Liquid viscosity is neglected and the sheet is exiting into a void under negligible gravity. The assumption of thin sheets allows the reduction of the dimensionality of the problem by integrating across the thickness of the sheet. This approach, also referred to as the lubrication approximation, has been employed by Ramos [14] and by the authors [3, 7, 16, 17, 20] for the analyses of thin planar and axisymmetric annular sheets without swirl, as well as axisymmetric swirling conical sheets.

Only spatial film stability or film distortion will be of interest here. The spatially periodic temporal film distortion and film stability is not relevant to the conical sheet with its varying radius. The temporal instability can apply to the annular cylindrical sheet and for the radially expanding sheet.

Governing Equations

The governing equations, describing the unsteady motion in an incompressible, inviscid three-dimensionally distorting liquid sheet under zero gravity and in a cylindrical coordinate system, are given by

$$\frac{\partial v_z}{\partial z} + \frac{\partial v_r}{\partial r} + \frac{v_r}{r} + \frac{1}{r}\frac{\partial v_\theta}{\partial \theta} = 0 \tag{1}$$

$$\frac{\partial v_z}{\partial t} + v_z\frac{\partial v_z}{\partial z} + v_r\frac{\partial v_z}{\partial r} + \frac{1}{r}v_\theta\frac{\partial v_z}{\partial \theta} = -\frac{1}{\rho}\frac{\partial p}{\partial z} \tag{2}$$

$$\frac{\partial v_r}{\partial t} + v_z\frac{\partial v_r}{\partial z} + v_r\frac{\partial v_r}{\partial r} + \frac{1}{r}v_\theta\frac{\partial v_r}{\partial \theta} - \frac{v_\theta^2}{r} = -\frac{1}{\rho}\frac{\partial p}{\partial r} \tag{3}$$

$$\frac{\partial v_\theta}{\partial t} + v_z\frac{\partial v_\theta}{\partial z} + v_r\frac{\partial v_\theta}{\partial r} + \frac{1}{r}v_\theta\frac{\partial v_\theta}{\partial \theta} + \frac{v_r\, v_\theta}{r} = -\frac{1}{\rho r}\frac{\partial p}{\partial \theta} \tag{4}$$

where v_z, v_r and v_θ are the velocity components in the axial (z-), radial (r-) and circumferential (θ-) directions, respectively. See Fig. 1. p and ρ_l denote the pressure and the density of the liquid.

Indicating the outer and inner location of the sheet by $r_+(z,t)$ and $r_-(z,t)$, we define the radial centerline position and the thickness of the sheet by $\bar{r}(z,t) = (r_+ + r_-)/2$ and $\Delta r(z,t) = r_+ - r_-$. The pressure and the radial velocity component at the fluid interfaces $(p_\pm, v_{r,\pm})$ are given by the following kinematic and dynamic boundary conditions,

$$v_{r,\pm} = \frac{\partial r_\pm}{\partial t} + v_{z,\pm}\frac{\partial r_\pm}{\partial z} + \frac{1}{r}v_{\theta\pm}\frac{\partial r_\pm}{\partial \theta} \tag{5}$$

$$p_{\pm} = p_{g,\pm} \pm \sigma\kappa_{\pm} \tag{6}$$

where the local curvature $\kappa_{\pm}$ is given by the divergence of the unit normal vector at the particular location of the outer (+) or inner (−) sheet interface, i.e. $\kappa_{\pm} = \nabla \cdot \vec{n}_{\pm}$. In the previous equation p_g is the pressure of the surrounding gas and σ denotes the surface tension coefficient of the liquid. For non-swirling annular sheets $p_{g,+} = 0$ but $p_{g,-} \neq 0$ in order to stabilize the annular sheet in its undisturbed configuration. The latter is also referred to as 'pressure stabilization'. See Ref. [17] in this context. This contrasts with 'swirl-stabilized' annular or conical sheets, where $p_{g,\pm} = 0$ and stabilization of the undisturbed (unmodulated) sheet is obtained by balancing surface tension forces with the centrifugal forces due to swirl. Clearly, gas-phase effects are not included in the present analysis. The pressure in the gas surrounding the considered liquid films is assumed constant because at atmospheric pressure, the gas density is negligible compared to the liquid density. The influence of a gas-phase flow field surrounding discharging planar liquid films has been analyzed by the authors for the case of a two-dimensional twin-fluid atomizer [20].

Expanding the dependent variables in terms of $r - \bar{r}(x,t)$ and employing a similar expansion for $1/r$, one obtains the following system of equations for $\bar{r}$, Δr and the leading-order expansion terms of the velocity components v_z, v_r, v_θ, i.e. u_0, v_0 and w_0, respectively.

$$\frac{\partial \Delta r}{\partial t} + \frac{\partial (u_0 \Delta r)}{\partial z} + \frac{\Delta r}{\bar{r}} v_0 + \frac{1}{\bar{r}} \frac{\partial (\Delta r w_0)}{\partial \theta} = 0 \tag{7}$$

$$v_0 = \frac{\partial \overline{r}}{\partial t} + u_0 \frac{\partial \overline{r}}{\partial z} + w_0 \frac{1}{\overline{r}} \frac{\partial \overline{r}}{\partial \theta} \tag{8}$$

$$\frac{\partial u_0}{\partial t} + u_0 \frac{\partial u_0}{\partial z} + \frac{1}{\overline{r}} w_0 \frac{\partial u_0}{\partial \theta} = -\frac{1}{\rho} \left[\frac{\partial \overline{p}}{\partial z} - \Delta p \left(\frac{1}{\Delta r} \frac{\partial \overline{r}}{\partial z} + \frac{1}{4\overline{r}} \frac{\partial \Delta r}{\partial z} \right) \right] \tag{9}$$

$$\frac{\partial v_0}{\partial t} + u_0 \frac{\partial v_0}{\partial z} + \frac{w_0}{\overline{r}} \frac{\partial v_0}{\partial \theta} - \frac{w_0^2}{\overline{r}} = -\frac{1}{\rho} \frac{\Delta p}{\Delta r} \tag{10}$$

$$\frac{\partial w_0}{\partial t} + u_0 \frac{\partial w_0}{\partial z} + \frac{w_0}{\overline{r}} \frac{\partial w_0}{\partial \theta} + \frac{w_0 v_0}{\overline{r}} = -\frac{1}{\rho \overline{r}} \left[\frac{\partial \overline{p}}{\partial \theta} - \frac{\Delta p}{\Delta r} \frac{\partial \overline{r}}{\partial \theta} \right] \tag{11}$$

with

$$\begin{aligned} \overline{p} &\equiv \frac{p_+ + p_-}{2} = \frac{\sigma}{2} \left[\nabla \cdot \vec{n}_+ - \nabla \cdot \vec{n}_- \right] \\ \Delta p &\equiv p_+ - p_- = \sigma \left[\nabla \cdot \vec{n}_+ + \nabla \cdot \vec{n}_- \right] \end{aligned}$$

whereby the divergence of the normal vector at the outer and inner interfaces at a specific location (θ_0, z_0) is evaluated from

$$\nabla \cdot \vec{n} = \left(1 - \frac{1}{r} r_{\theta\theta} - r_z^2 - r r_{zz} \right) \left[r_\theta^2 + \Omega \right]^{-1/2} \tag{12}$$

$$+ \frac{r_\theta}{2r} \left[r_\theta^2 + \Omega \right]^{-3/2} \left[2 r_\theta r_{\theta\theta} + \frac{2 r_\theta}{r} \Omega + 2 r^2 r_z r_{z\theta} \right]$$

$$+ \frac{r r_z}{2} \left[r_\theta^2 + \Omega \right]^{-3/2} \left[2 r_\theta r_{\theta z} + \frac{2 r_z}{r} \Omega + 2 r^2 r_z r_{zz} \right] \tag{13}$$

whereby $\Omega = r^2\,(1 + r_z^2)$ and $r = \bar{r} \pm \Delta r/2$.

Equations (7) through (11) form a closed system of partial differential equations which together with appropriate boundary and initial conditions govern the three-dimensional nonlinear distortion of thin swirling liquid films exiting from a nozzle or atomizer into a void. For the subsequent analyses, the above equations have been nondimensionalized by using the undisturbed film thickness and film discharge velocity at the nozzle exit, i.e. Δr_0 and $\overline{v_z}_{,0}$, as characteristic length and velocity, respectively. The Weber number in the resulting nondimensional equations is given by $\mathrm{We} = \rho_l \overline{v_z}_{,0}^2 \Delta r_0/\sigma$.

Governing equations for the nondimensional linearized problem have been obtained by introducing

$$\Delta r^* = 1 + h,\ \bar{r}^* = R + \eta,\ u_0^* = 1 + u^*,\ v_0^* = V + v^*,\ w_0^* = W + w^*$$

into the nondimensional form of Eqns. (7) through (11). In the above equations, h and η denote nondimensional fluctuations in the film thickness and transverse film centerline location, respectively. u^*, v^* and w^* represent nondimensional fluctuations in the axial, transverse and circumferential velocity components. We define $\varepsilon = 1/\sqrt{2\mathrm{We}}$. Within the present analysis, $V = 0$ and $W = 2\varepsilon R\,(R^2 - 0.25)^{-0.5} \approx 2\varepsilon$; the latter represents the nondimensional swirl-velocity which stabilized the undisturbed annular film with nondimensional radius R.

The linearized system of equations becomes

$$\frac{\partial h}{\partial t^*} + \frac{\partial h}{\partial z^*} + \frac{\partial u^*}{\partial z^*} = -\frac{1}{R}\,v^* - \frac{1}{R}\left\{W\frac{\partial h}{\partial \theta} + \frac{\partial w^*}{\partial \theta}\right\} \tag{14}$$

$$\frac{\partial u^*}{\partial t^*} + \frac{\partial u^*}{\partial z^*} + \frac{W}{R}\frac{\partial u^*}{\partial \theta} = \varepsilon^2 \left\{ \frac{\partial^3 h}{\partial z^{*3}} + \frac{1}{R^2}\left(\frac{\partial h}{\partial z^*} + \frac{\partial^3 h}{\partial \theta^2 \partial z^*} \right) + \frac{4}{R}\frac{\partial \eta}{\partial z^*} \right\} \quad (15)$$

$$\frac{\partial v^*}{\partial t^*} + \frac{\partial v^*}{\partial z^*} + \frac{W}{R}\frac{\partial v^*}{\partial \theta} - \frac{2}{R}W w^* + \frac{W^2}{R^2}\eta = 4\varepsilon^2 \left\{ \frac{\partial^2 \eta}{\partial z^{*2}} + \frac{1}{R^2}\left(\eta + \frac{\partial^2 \eta}{\partial \theta^2} \right) + \frac{1}{R}h \right\} \quad (16)$$

$$\frac{\partial w^*}{\partial t^*} + \frac{\partial w^*}{\partial z^*} + \frac{W}{R}\frac{\partial w^*}{\partial \theta} = -\frac{W}{R}v^* + \frac{\varepsilon^2}{R}\left\{ \frac{\partial^3 h}{\partial z^{*2}\partial \theta} + \frac{4}{R}\frac{\partial \eta}{\partial \theta} \right\} \quad (17)$$

$$\frac{\partial \eta}{\partial t^*} + \frac{\partial \eta}{\partial z^*} + \frac{W}{R}\frac{\partial \eta}{\partial \theta} = v^* \quad (18)$$

where terms of $O(R^{-3})$ have been neglected and where t^* denotes nondimensional time and z^* represents the nondimensional axial coordinate. Note that, the radiant θ is already nondimensional. Eqns. (14) to (18) apply in the pressure range where gas density is negligibly small and the effects of gas inertia can be neglected. Solutions to Eqs. (14) – (18) are assumed to be of the form

$$\begin{aligned} h &= A_h e^{i(kz^* + n\theta - \omega t^*)} \\ u^* &= A_u e^{i(kz^* + n\theta - \omega t^*)} \\ \eta &= A_\eta e^{i(kz^* + n\theta - \omega t^*)} \\ v^* &= A_v e^{i(kz^* + n\theta - \omega t^*)} \\ w^* &= A_w e^{i(kz^* + n\theta - \omega t^*)} \end{aligned} \quad (19)$$

Substitution of Eqns. (19) into Eqns. (14) - (18) provides the dispersion relation governing the propagation of capillary waves on the modulated film, i.e.

$$
\begin{aligned}
&(a^2 - b\,g)\,[2\,c\,e - (g + e\,(f - e/4))\,(2f - e)] \\
&+ c\,n\,k^2\,\left[c^{1/2}\left(a^2 + 4g\right) + n\,a\,(g + e\,(f - e/4))\right] \\
&\qquad - c\,a\,\left[2\,f\,e + (2f - e)^2 + 4\,g\right] \;=\; 0
\end{aligned}
\tag{20}
$$

with

$$
\begin{aligned}
a &= \frac{2\varepsilon}{R}n - (\omega - k) \\
b &= k^2 - \frac{1}{R^2}(1 - n^2) \\
c &= \frac{\varepsilon^2}{R^2} \\
e &= \omega - k \\
f &= \frac{\varepsilon}{R}n \\
g &= \varepsilon^2 k^2
\end{aligned}
$$

Note that k and n denote the wavenumbers of capillary waves propagating in the axial and circumferential direction, respectively. ω represents the angular frequency at which modulations are forced onto the discharging film at the atomizer exit.

Analogous to previous work by the authors, evaluation of the group velocity for wavenumbers k_i, i.e. $C(k_i) = \mathrm{d}\omega/\mathrm{dRe}[k_i]$ can now be used to determine which disturbances generated by the nozzle modulation at frequency ω will be found downstream. In particular, if the group

velocity for a particular axial wavenumber is positive, then that wavenumber will be found further downstream, if the particular wavenumber has negative group velocity, then the corresponding disturbance will not be found downstream from the nozzle since no modulation is applied downstream. The latter is effectively a representation of the Sommerfeld radiation condition which implies that no energy is propagated upstream from infinity [7, 17]. Note that after film rupture the discharging film will have finite length which necessitates a reconsideration of the downstream boundary condition. In that case, the rejection of wavenumber solutions with negative group velocity based on the application of the Sommerfeld radiation condition is no longer valid.

Equation (20) is the dispersion relation for linear three-dimensional capillary waves on thin swirling annular films discharging into a void and in a reference frame fixed to the nozzle exit.

Assuming exponential solutions for h, η, u^*, v^* and w^* according to Eq. (19), the general solution to the boundary-value problem for a given forcing frequency ω and circumferential wavenumber n is given by

$$\begin{aligned} h(z^*,t^*) &= \sum_{j=1}^{5} A_{h,j} e^{i(kz^*+n\theta-\omega t^*\omega t^*)} \\ \eta(z^*,t^*) &= \sum_{j=1}^{5} A_{\eta,j} e^{i(kz^*+n\theta-\omega t^*\omega t^*)} \\ u^*(z^*,t^*) &= \sum_{j=1}^{5} A_{u^*,j} e^{i(kz^*+n\theta-\omega t^*\omega t^*)} \\ v^*(z^*,t^*) &= \sum_{j=1}^{5} A_{v^*,j} e^{i(kz^*-n\theta-\omega t^*\omega t^*)} \end{aligned} \tag{21}$$

$$w^*(z^*,t^*) \;=\; \sum_{j=1}^{5} A_{w^*,j} e^{i(kz^*+n\theta-\omega t^*\omega t^*)} \tag{22}$$

where the index $j = 1,\ldots 5$ refers to the 5 wavenumber solutions to the dispersion relation for a given forcing frequency ω and circumferential wavenumber n which have to be considered within the present analysis according to the employed parameter range and the discussion of the previous paragraph. These wavenumber solutions are k_2, k_3 and $k_5 - k_7$, respectively. The unknown coefficients within the above solutions depend on each other according to

$$\underbrace{\begin{bmatrix} ip_j & 0 & ik_j & R^{-1} & inR^{-1} \\ i\varepsilon^2 k_j\left[q_j-\frac{1}{R^2}\right] & -i\frac{4\varepsilon^2}{R}k_j & ip_j & 0 & 0 \\ -\frac{4\varepsilon^2}{R} & 4\varepsilon^2 q_j & 0 & ip_j & -\frac{4\varepsilon}{R} \\ 0 & ip_j & 0 & -1 & 0 \\ i\frac{\varepsilon^2}{R}n\left[q_j-\frac{1}{R^2}\right] & -i\frac{4\varepsilon^2}{R^2}n & 0 & \frac{2\varepsilon}{R} & ip_j \end{bmatrix}}_{M} \begin{bmatrix} A_{h,j} \\ A_{\eta,j} \\ A_{u^*,j} \\ A_{v^*,j} \\ A_{w^*,j} \end{bmatrix} = \begin{bmatrix} 0 \\ 0 \\ 0 \\ 0 \\ 0 \end{bmatrix} \tag{23}$$

with $p_j = [\frac{2\varepsilon}{R}n - (\omega - k_j)]$ and $q_j = [k_j^2 s + \frac{1}{R^2}n^2]$ for $j = 1,\ldots,5$. The above system of equations is obtained after substituting Eqs. (21) into Eqs. (14)–(18). Eqs. (23) are linearly dependent since $\det[M] = 0$ and can be reduced to

$$\frac{A_{h,j}}{A_{\eta,j}} = -\frac{s_j + 4\varepsilon^3 k_j^2/[Rp_j]}{\varepsilon p_j/2 - \varepsilon^3 k_j^2/p_j[q_j - R^{-2}]} \tag{24}$$

$$\frac{A_{u^*,j}}{A_{\eta,j}} = -\frac{1}{\varepsilon k_j}\left[\varepsilon p_j/2\frac{s_j + 4\varepsilon^3 k_j^2/[Rp_j]}{\varepsilon p_j/2 - \varepsilon^3 k_j^2/p_j[q_j - R^{-2}]} + s_j\right] \tag{25}$$

$$\frac{A_{v^*,j}}{A_{\eta,j}} = i\,p_j \tag{26}$$

$$\frac{A_{w^*,j}}{A_{\eta,j}} = \frac{n[q_j - R^{-2}][\varepsilon^2 k^2 + \varepsilon n/R(\omega - k_j) - (\omega - k_j)^2/4] - 2\varepsilon(\omega - k_j)/R}{\varepsilon n/R[q_j - R^{-2}] - p_j} \tag{27}$$

with p_j and q_j as defined above and $s_j = n\varepsilon^2(k_j^2+2R^{-2})-(\varepsilon/R)(\omega-k_j)(1-n)-(n/4)(\omega-k_j)^2$. This provides four independent equations for the five unknown coefficients of each index $j = 1,\ldots,5$. Altogether, this yields twenty independent equations for twenty-five unknown coefficients. The remaining five conditions needed in order to determine fully the unknown coefficients are given by the boundary conditions specified at the nozzle exit, i.e. one condition for each of the five wavenumbers $k_{2,3}$ and k_{5-7} with positive group velocities.

Results and Discussion

Linear Analysis

Relevant Wavenumber Solutions / Wave Character

Eq. (20) has been solved for wavenumbers k_i at given values of Weber number We or ε and circumferential wavenumber n. Solutions to the dispersion relation were obtained numerically by using Mathematica^{TM}. Evaluation of the corresponding group velocities $C(k_i) = \mathrm{d}\omega/\mathrm{dRe}[k_i]$ predicts that for $\omega \leq 0.6$ and small n-values (< 8 for We $= 5 - 1000$ and beyond), information travels in the same direction as in the axisymmetric case: Five wavenumbers correspond to waves that originate at the nozzle and send information in the downstream direction (later denoted by $k_{2,3}$ for dilational mode waves and k_{5-7} for sinuous

mode waves) and two (dilational mode) wavenumbers correspond to waves which originate at downstream infinity that send information upstream (later denoted by k_1, k_4), according to their positive and negative group velocities, respectively. The subscript i is an integer index that indicates the particular wave number. Previous analyses of non-swirling axisymmetric discharging annular films indicated the existence of only four wavenumbers with positive group velocity [17]. In the present case, modulation of the swirl velocity allows for the existence of one additional wavenumber solution with positive group velocity.

Figs. 2, 3 and 4 illustrate the solutions to Eq. (20) obtained by Mathematica^{TM} plotted over n and ω for $\varepsilon = 1/\sqrt{10}$ and $R = 10$. Each of the various computed solutions might represent a different wavenumber in a different parameter range (ω, n). After combination of the various branches from the different solutions in order to represent the seven wavenumber solutions $k_i (i = 1, \ldots, 7)$, one observes that, wavenumber plots $k_i(\omega)$ for non-axisymmetric cases with $n \leq 5$ will resemble the axisymmetric result $(n = 0)$ qualitatively. The described collection of branches into the different wavenumber solutions was guided by comparison with the wavenumber solutions previously determined for non-swirling annular films (see Figs. 3 and 4 of Ref. [17]). Fig. 5 displays wavenumbers k_i as a function of ω for the $n = 3$ case. For $\omega \leq 0.7$ dashed and solid lines illustrate predominantly dilational mode waves (k_{1-4}), whereas dotted and dash-dotted lines denote predominantly sinuous mode waves ($k_{5,6}$ and k_7). For larger Weber number cases (e.g. We = 1000) and $n \leq 8$ the functional dependence of wavenumbers k_i on forcing frequency is similar to the We = 5 case illustrated here, even though absolute values might be quite different. Note that pure dilational or sinuous waves only appear as the planar film limit $R \to \infty$ is approached. Prediction of the wave-character (i.e., dilational or sinuous) is made via evaluation of the amplitude ratio h_i^0/η_i^0 which is

independent of the imposed upstream (or nozzle) boundary conditions, i.e.

$$\frac{h_i^0}{\eta_i^0} = R\left[\frac{2}{R^2} + k_i^2 - \frac{(\omega - k_i)^2}{4\varepsilon^2}\right] \tag{28}$$

Evaluation of $\mathrm{Im}[k_i]$ and consideration of $C(k_i) = \mathrm{d}\omega/\mathrm{dRe}[k_i]$ shows that for the case illustrated in Fig. 5 no sinuous mode wavenumber (dotted and dash-dotted lines) is to be rejected (i.e. $C(k_{5-7}) > 0$) and no unstable "sinuous" mode wavenumber exists. The same is true for the axisymmetric mode and non-axisymmetric modes (with $n \leq 8$) of the similar case (i.e. $R = 10$, $\varepsilon = 1/\sqrt{10}$ or $\mathrm{We} = 5$) (see Figs. 2 – 4). Only one of the four "dilational" mode wavenumbers, namely k_3, produces exponentially growing solutions in the downstream direction. In Fig. 5, this wavenumber case is indicated by the solid line.

Fig. 6 illustrates the growth rate for the described unstable predominantly dilational wave k_3 as a function of modulation frequency and circumferential wavenumber n for the particular case of $\mathrm{We} = 1000$ (or $\varepsilon = 1/\sqrt{2000}$) and $R = 10$. From Fig. 6 and similar results for various other combinations of We and R, we observe that for large Weber numbers, the instability range of the unstable dilational mode wave decreases with increasing n-values. For unstable behavior and large ω values, the growth rate decreases with increasing n values. In fact, for large enough n-values, no film instability might exist. However, for unstable behavior at small ω values, the growth rate is found to increase with increasing values of n until for large enough n-values, the growth rate drops down to zero.

As the Weber number is decreased (at fixed R-values), the maximum growth rate of the unstable dilational-mode wave is increased. Compare Fig. 6, Fig. 7 and Fig. 8 for We = 1000, 50 or 5 and $R = 10$, respectively. Fig. 8 also illustrates that for small Weber numbers,

and small enough n-values, the instability range of non-axisymmetric modes ($n \neq 0$) is larger than for the $n = 0$ case. However, as in Figs. 6 and 7, for a given parameter set R and We, the maximum growth rate is still observed for the axisymmetric ($n = 0$) case.

For the same case as depicted in Fig. 7, Fig. 9 shows the dependence of the wave angle $\mathrm{d}\theta_i/\mathrm{d}z = -k_i/n$ for the unstable predominantly dilational wave ($i = 3$) on the circumferential wavenumber n. The magnitude of the wave angle is found to decrease with increasing n-values and at fixed ω-values, except for small values of ω. Also, $|\mathrm{d}\theta/\mathrm{d}z|$ increases essentially linearly with ω at fixed n, except for small ω values. In the latter case, the considered unstable dilational-mode wave has negative wave velocity but positive group velocity, so that the winding of the helical structure generated by the wave changes from clockwise to counter-clockwise. This behavior has also been observed within the numerical analysis of the corresponding initial-and-boundary-value problem.

Linear Field Solutions

Solutions to the linear boundary-value problem discussed earlier were obtained for the case where the five boundary conditions at $z^* = 0$ are given by harmonic variations imposed onto variables h, η, u^*, v^* and w^* according to $e^{i(n\theta - \omega t^*)}$ with complex forcing amplitudes denoted by h^0, η^0, u^0, v^0 and w^0. For the purpose of validating the numerical analysis presented below and for the purpose of identifying the influence of nonlinear effects on the growth of unstable waves (via comparison between linear analytical and nonlinear numerical results), the linear problem was solved for the case where only the unstable dilational mode wavenumber k_3 is being generated at the nozzle through modulation of the film thickness, i.e. $h(z^* = 0, t^*) = h^0 \cos(n\theta - \omega t^*)$. Accordingly, the above equations are solved

for the complex forcing amplitudes η^0, u^0, v^0 and w^0. In particular, coefficients pertaining to wavenumbers other than k_3, i.e. $A_{h,j\neq 2}, A_{\eta,j\neq 2}, A_{u^*,j\neq 2}, A_{v^*,j\neq 2}$ and $A_{w^*,j\neq 2}$, are zero and $A_{h,2} = h^0$. Coefficients $A_{\eta,2}, A_{u^*,2}, A_{v^*,2}$ and $A_{w^*,2}$ are readily determined from Eqns. (24) through (27). Table 1 lists the various nonzero coefficients (normalized by h^0) for the cases which have been used to compare linear analytical and nonlinear numerical solutions.

Nonlinear Analysis

The governing equations for the nonlinear three-dimensional distortion of swirling annular or conical liquid sheets have been solved numerically by using the Law-Wendroff Method with Richtmyer splitting [22]. Initial conditions for the transient simulations of swirling and non-swirling annular films are trivial ($\Delta r(z, t = 0) = \Delta r_0, \overline{r}(z, t = 0) = \overline{r}_0$). The initial film shape for swirling conical films (discharging from the nozzle with more swirl than needed to stabilize the film in its annular positions) was obtained by integrating the nonlinear axisymmetric film equations in the downstream direction starting at the nozzle exit. See Ref. [3] for more details. Modulations of the dependent variables $\Delta r^*, \overline{r}^* r, u_0^*, v_0^*$ and w_0^* were imposed at the nozzle exit ($z^* = 0$) in order to generate: 1) The unstable "dilational" mode wave predicted by linear theory (annular case only) and 2) a system of standing and/or travelling waves (annular and conical case). The former provides a dynamically simple system, which eases the comparison between linear and nonlinear theories. The latter case has been considered in context with the active control of the film disintegration process; it represents a dynamically complex system.

For both swirl-stabilized annular and 'conical' sheets, the number of boundary conditions

at the nozzle exit was chosen according to the number of wavenumbers k_i with associated positive group velocities, relevant to the linear boundary-value-problem analysis presented earlier for swirl-stabilized annular films, i.e. five boundary conditions were imposed at $z^* = 0$. Analogous to the analysis of swirling axisymmetric films [3], boundary conditions at the nozzle exit for nondimensional sheet thickness Δr^*, radial sheet-centerline location $\overline{r}^*$, and the velocity components in the axial, radial and circumferential direction u_0^*, v_0^* and w_0^* were chosen according to the described steady-state solutions, but with additional harmonic variations of the film thickness or the axial, circumferential and transverse velocity components generating axisymmetric or three-dimensional standing and/or travelling sinuous or dilational mode waves.

As in Ref. [3], additional numerical boundary conditions (required to solve the unsteady problem) were specified for $\partial^2 \Delta r^* / \partial z^{*2}$ and $\partial^2 \overline{r}^* / \partial z^{*2}$ with values corresponding to the imposed steady-state initial conditions.

In summary, for the analysis of the considered unsteady problem, five boundary conditions and two numerical conditions were specified at the nozzle exit.

Parameter Range and Forcing Conditions

Analogous to previous work by the authors, and in order to omit the dominance of transient effects in the majority of the nonlinear numerical simulations, the present numerical study was limited to large Weber number flows, i.e. We = 50 or We = 1000. Values for the radius-to-thickness ratio of the discharging films, as well as values for the imposed circumferential wavenumber and forcing frequencies (determining downstream and circumferential disturbances) were chosen small enough to guarantee film rupture and/or the appearance of

significant nonlinear three-dimensional effects within a computationally feasible time frame. In addition the same parameters were chosen large enough so that the assumptions of the employed lubrication model are not violated. For all the results presented here, the nondimensional annular radius has been fixed at $R = 10$. Results computed for cases with $n = 1$ have not been included due to the delayed appearance of three-dimensional effects even at circumferential wave amplitudes comparable to those of the downstream-propagating waves. The analysis of conical films was limited to cases with swirl number $k = 10$, indicating that the liquid exits the annular slit nozzle with ten times the amount needed to stabilize it in the annular configuration. The steady-state cone angle in this case is approximately 44 degrees.

Disturbance amplitudes in the various flow variables were chosen over a wide range. Small amplitude values were used in order to benchmark the numerical model by allowing direct comparison between linear analytical and numerical results for a given set of boundary or forcing conditions. Larger amplitude values were chosen in order to predict the appearance of nonlinear effects and possibly film rupture near the nozzle exit. As noted before, early appearance of nonlinear effects and film rupture were essential in order to perform the numerous nonlinear quasi-three-dimensional numerical simulations in a reasonable time frame and at reasonable computational costs. Note that, in general, practical liquid film atomizers are designed (among other things) to achieve film rupture, disintegration and atomization at short distances from the atomizer nozzle. The latter being an important requirement in the design of more compact, i.e. shorter and lighter, combustion systems.

Here, we focus on 1) a comparison of linear and nonlinear unstable dilational mode waves on swirling annular films and 2) a description of film topology and film rupture under a variety of forcing conditions resulting in standing and/or travelling sinuous and/or dilational waves

via modulation of various different flow variables, i.e. $\phi = \eta, u_0^*, v_0^*, w_0^*$. The general forcing condition for one of the flow variables ϕ employed here is given by

$$\phi = \Phi + \phi' \left[1 - e^{(-t^*/T_e)}\right] \left[f_1(\frac{2\pi t^*}{T_p} + \phi'' f_2(n\theta - j\,\frac{2\pi t^*}{T_{tr}} t)\, f_3(\frac{2\pi t^*}{T_p})\right] \tag{29}$$

Here, Φ represents the steady-state value of the particular flow variable. f_1, f_2 and f_3 denote either sine or cosine functions. The parameter j takes the value 0 or 1 in order to model a standing or a travelling wave, respectively. The exponential term $[1 - e^{(-t^*/T_e)}]$ assures a smooth start-up of the transient simulation preventing the film distortion process from being dominated by the dynamics of the initial wave-front propagating into the undisturbed semi-infinite film [23]. T_e denotes the characteristic time for the described start-up process. The various parameter combinations and forcing conditions which have been analyzed are summarized in Tables 2 through 8, together with data on film break-up time and length for the various cases. If film rupture did not occur within the computational time frame, minimum film thickness and corresponding downstream location (at the end of the simulation) are tabulated instead.

Single "Dilational" Wave Modulation

Figs. 10 and 11 show the instantaneous film thickness as a function of downstream distance for a swirling annular film with We = 1000, $R = 10$ and $n = 0$ or $n = 3$, respectively. The forcing frequency in both cases was $\omega = 0.26$ with $h_0 = 0.35$. Boundary conditions have been specified in order to generate the previously discussed unstable dilational wave only. For the axisymmetric case illustrated in Fig. 10 the nondimensional film breakup length (i.e. length measured from the nozzle exit to the first point of film rupture) is $l_b^* = 390$. The

rupture occurs at $t_b^* = 422.85$ measured in nondimensional terms. Comparison with linear analysis shows that the nonlinear growth rate (at $z^* = 300$) is about 56 % larger than predicted by linear theory. For the non-axisymmetric mode shown in Fig. 11, breakup length and time were predicted as $l_b^* = 245$ and $t_b^* = 275.55$, respectively. Here, the increase of the film thickness Δr_{max} is approximately the same as for the $n = 0$ case. On the other hand, the decrease of Δr_{min} in the downstream direction is larger for the $n = 3$ case resulting in shorter film break-up time and length. Wave angle measurements obtained from the the nonlinear numerical simulation shown in Fig. 11 agree very well with the wave angle prediction $\mathrm{d}\theta/\mathrm{d}z = -k/n$ obtained from linear theory. In other words, constant film-thickness values are found along $z = -(n/k)\theta$ lines.

Figs. 12 and 13 demonstrate film distortion and rupture for a a lower Weber number case, i.e. We = 50, at the same annular radius, forcing frequency and circumferential wavenumber as in Fig. 11 ($R = 10$, $\omega = 0.26$, $n = 3$). The disturbance amplitude in the film thickness for this case was $h_0 = 0.15$. The lower Weber number results in an increased growth rate of the modulated unstable "dilational" wave. Consequently, breakup length and time are significantly smaller than for the similar larger Weber number case. In particular, $l_b^* = 95$ and $t_b^* = 115.2$ for the case shown in Figs. 12 and 13. Observed growth of Δr_{max} and decrease of Δr_{min} in the downstream direction correspond to the observation previously described for the larger Weber number case (Fig. 11). Also, distortion characteristics are not different from the larger Weber number case. It is noted here that, for the similar axisymmetric case ($n = 0$), film rupture does not occur within the simulated time frame ($0 < t^* < 150$).

The present nonlinear analysis considers an initial- and boundary-value problem. Film modulation is started at $t^* = 0$ after which the front of the film disturbance is propagated

downstream into the undisturbed flowing film. As discussed earlier, the temporal growth of the propagating initial wave-front might dominate over the spatial wave growth; the latter resulting from continuous modulation at a prescribed forcing frequency. Comparisons of the corresponding film rupture lengths and times with predictions from linear spatial theory are not appropriate. The dominant behavior of the described transient effect is observed in Figs. 14, 15 and 16. for $n = 0$ or $n = 3$ with $R = 10$, $\omega = 0.06$, We $= 50$ and $\Delta r^{*0} = 0.15$. Even as transient effects dominate the film distortion process, non-axisymmetric disturbances provide shorter break-up length and break-up time. For the axisymmetric case in Fig. 14, film rupture does not occur within the simulated time frame, i.e. $0 < t^* < 250$. For the non-axisymmetric $n = 3$ case illustrated in Figs. 15 and 16, film breakup (dominated by "start-up" effects) is observed at $l_b^* = 117.5$ adn $t_b^* = 127.2$. At the time of rupture, film distortion is highly nonlinear, particularly close to the propagating wave front.

Multiple Dilational Wave Modulation / Wave System

In order to investigate the feasibility of actively controlling the film disintegration process, film distortion and film rupture were investigated for the case where multiple superimposed waves are generated at the nozzle exit.

Non-swirling Annular Films

Fig. 17 illustrates the case of a dilationally modulated non-swirling (pressure-stabilized) annular film with a harmonic forcing imposed at $z^* = 0$ according to

$$u_0^*(t^*) = 1 + A\left[1 - \exp\left(\frac{-t^*}{T_e}\right)\right]\cos(n\theta)\sin\left(\frac{2\pi t^*}{T_p}\right) \tag{30}$$

$$w_0^*(t^*) = B\left[1 - \exp\left(\frac{-t^*}{T_e}\right)\right] \sin(n\,\theta) \sin\left(\frac{2\pi t^*}{T_p}\right) \tag{31}$$

where t^* denotes the nondimensional time variable, and θ is measured in radians. For non-swirling annular sheets, stabilization of the undisturbed film is achieved by a nonzero constant pressure difference across the film, i.e. $p_{g,-} - p_{g,+} = \sigma(1/r_{0,+} + 1/r_{0,-}) = 2\sigma r_0/(r_0^2 - \Delta r_0^2/4)$, where the subscript '0' denotes undisturbed values at the nozzle exit. The Weber number for this case is We = 1000, the undisturbed annular film radius $\overline{r}_0^* = 10$, $T_p = T_e = 10$ and $A = B = 0.04$. Five (standing) waves have been imposed in the circumferential direction, i.e. $n = 5$. As observed from Fig. 17, the imposed film modulation results in the development of a regular cellular structure on the film in the downstream direction from the nozzle exit. As the amplitude of the film distortion increases, a system of fluid ligaments forms. The ligaments are elongated in the circumferential direction and are connected by a thinner film of liquid. Local maxima and minima in the film thickness alternate in the circumferential direction and also in the downstream direction at constant θ-value. Points where the film breaks first (i.e. where it reaches zero thickness) are found at the same downstream location z^* and located near the transitions between the thin film regions and the thicker ligaments resulting in the simultaneous formation of larger stretched free liquid ligaments inter-spaced by thinner fluid films. Both larger ligaments and thinner fluid fluid films are expected to contract towards a spherical shape due to surface tension (after being generated from the continuous film) and oscillate, due to the absence of viscous damping, around their spherical equilibrium shapes. A simple theoretical analysis considering the aspect of viscous dissipation in liquid atomization systems can be found in Ref. [24]. Note that the current implementation does not allow for continuation of the simulation beyond the point when the

film breaks at some location(s).

Fig. 18 illustrates the similar (pressure-stabilized) case as shown in Fig. 17 but now with a three-dimensional sinuous modulation enforced at the nozzle. The behavior is generated by harmonic variations of the transverse film velocity according to

$$v_0^*(t^*) = C\left[1 - \exp\left(\frac{-t^*}{T_e}\right)\right]\cos(n\theta)\,\sin\left(\frac{2\pi t^*}{T_p}\right) \tag{32}$$

with $C = 0.1, T_p = T_e = 10$ and $n = 5$. In this case, the initially regular three-dimensional sinuous disturbance flattens in the downstream direction, generating thicker fluid rings (with circumferential thickness fluctuations) which are connected by thin films of liquid. The observed change from a three-dimensional sinuous to a more or less axisymmetric dilational structure results from the development of nonlinear sinuous-dilational mode coupling downstream, but is also related to the presence of multiple downstream propagating waves resulting in an envelope behavior for film thickness and film centerline location in the downstream direction. The latter has already been described for non-swirling axisymmetric annular films [17] and was observed, for example, also in cases 2 and 3 of Table 6. As in the dilationally modulated case, film rupture is observed first between the larger fluid rings. The fluid rings themselves can be expected to break due to the dominance of the most unstable wavelength analogously to the Rayleigh instability mechanism for straight liquid jets [25, 26].

Swirling Annular Films

Fig. 19 illustrates the film thickness distribution for a non-swirling pressure-stabilized annular liquid film, when the front of the disturbance generated by the modulation has propagated to about $z^* = 35$ in the downstream direction. Problem parameters for this case

are the same as for the case illustrated in Fig. 18. The film was modulated according to the forcing conditions prescribed in Eq. (32). Fig. 20 shows the instantaneous thickness distribution at the same time for the corresponding swirl-stabilized case. Comparison of the film distortion for pressure-stabilized and swirl-stabilized films shows no significant differences in the particular film thickness distribution. However, as already observed for axisymmetric films [3], disturbance amplitudes are significantly larger in the swirl-stabilized case, reducing the length between nozzle exit and downstream position where film rupture first occurs.

Swirling Conical Films

Fig. 21 shows the outer film surface location for the case of a swirling conical sheet generated by liquid which exits the annular slit nozzle with ten times the amount of swirl needed to stabilize the film in its annular configuration when exiting the nozzle. In other words, the swirl velocity for this case is ten times larger than for the case illustrated in Fig. 20.

Initial conditions for this case were obtained by solving the nonlinear steady-state axisymmetric equations as described in Ref. [3]. The liquid film is modulated sinusoidally at the nozzle ($z^* = 0$) according to Eq. (32). The Weber number for this case is We = 1000, $R = 10$ and $T_p = T_e = 10$. As in the previous case, 5 standing waves were imposed at the nozzle exit, i.e. $n = 5$, with $C = 0.1$.

For the same case and at the same time, Fig. 22 shows the instantaneous film thickness distribution. Interestingly, areas of the film with a local maximum of the film thickness at the nozzle exit develop into areas with two local maxima in the film thickness. The latter is not found for the similar swirling annular sheet of Fig. 20 and results from the film divergence in

the conical case. Film divergence due to excess swirl also causes the regular cellular structure observed at the nozzle to stretch forming a net-like or web-like configuration of thicker fluid ligaments imposed onto a thinner layer of liquid (see Fig. 23). As previously described for non-swirling annular films, film rupture first occurs in the transition regions between the thinner liquid layers and the thicker ligaments. For both non-swirling and swirling annular films described earlier, initial film break-up points are located at the same downstream position and more or less symmetrically on both sides of the thin films or thicker ligaments. In the swirling conical case, this symmetry is lost and initial rupture points are found only on one side of the thin film regions, whereas the other side still remains connected to the neighboring larger liquid mass. Depending on the flow conditions, the fluid within the thin films might be subsequently re-absorbed into the larger ligaments. Note that, for the annular films of Figs. 19 and 20, the continuous liquid film is expected to disintegrate initially into thinner liquid layers located between larger fluid ligaments. However, recombination of the larger fluid masses with the smaller ones is still possible due to different relative velocities of their center of gravity. The latter is analogous to the recombination of main and satellite droplets observed in liquid jet atomization processes such as ink-jet printing [27].

For larger disturbance amplitudes, film breakup occurs close to the nozzle exit (see Fig. 24) with film distortion being highly nonlinear prior to breakup. For the case shown in Fig.24 fluid accumulates into spike-like structures with the possibility of drop generation before film breakup into larger ligaments occurs. It is conceivable that droplets ejected into the inner region of the conical film will impact onto the film causing film rupture and atomization at the downstream location where they have impacted. The relevance of the impingement of droplets onto discharging liquid films near the nozzle exit has already been

considered by other authors [28].

Clearly, in order to investigate liquid-film dynamics after initial break-up of the continuous film is predicted, the current model has to be extended to describe the dynamics of the newly generated free film edges. At the film edges, lubrication equations cannot be employed. Rather, the authors envision a combination of a dynamic-film-edge model in combination with the current lubrication model away from the edges. Limitations of this combined model are reached when the thickness-to-length ratio of the retracting free liquid ligaments is of $O(1)$. Also, as noted earlier, rejection of boundary conditions at the nozzle exit on the basis of the Sommerfeld radiation condition can no longer be employed after rupture of the semi-infinite film generates free ligaments and a finite-length continuous film is discharging from the nozzle exit.

Summary

Linear and nonlinear analyses of modulated three-dimensionally distorting thin inviscid free liquid films discharging into a gas of negligible density are presented. The nonlinear numerical analysis uses a lubrication model reducing the three-dimensional problem to a system of two-dimensional unsteady equations. Linear theory for swirling annular films predicts that for We > 2 only one unstable wave is generated on the film due to its modulation at the nozzle exit. Depending on Weber number and film radius, linear growth rates for this unstable dilational mode wave might be larger for non-axisymmetric modes than for the corresponding axisymmetric case. However, for the considered parameter range, maximum growth rates for a given Weber number and annular radius are still observed for the ax-

isymmetric case. Modulation of multiple dilational mode waves at the nozzle exit allows for uniform breakdown of swirling and non-swirling annular films indicated by the generation of uniformly sized liquid volumes which are uniformly spaced and connected by thinner liquid layers. Film topology and break-up of three-dimensionally modulated conical films are discussed. Comparison with the corresponding swirling annular film shows that for sinuous film modulation, film divergence causes the separation of initially formed larger fluid blobs into a pair of smaller fluid volumes connected by an even thinner liquid layer.

Within the considered large Weber number and low forcing frequency range, wave angle measurements from the nonlinear numerical simulations agree very well with predictions $\mathrm{d}\theta/\mathrm{d}z = -k/n$ obtained from linear theory for both sinuous and dilational waves on swirling annular films. On clockwise swirling conical films, spiraling dilational and sinuous waves moving in the clock-wise direction increase in slope as the film thins out in the downstream direction. The slope of counter-clockwise propagating waves decreases with downstream distance. The described changes in slope can be attributed to a decrease in swirl velocity with increase in annular film radius downstream that results from the conservation-of-angular-momentum principle. Based on the location of the initial film rupture points and the thickness distribution at the time of film rupture, Figs. 25 through 29 illustrate projected break-up patterns characteristic for the cases with pure standing or travelling dilational or sinuous mode waves modulated at the nozzle. For mixed standing/travelling and sinuous/dilational wave modulation, the resulting break-up pattern are modified or mixed versions of the patterns illustrated in Figs. 25 - 29. Here, filled circles indicate locations of local maxima in the film thickness, solid lines are perpendicular to the directions along which the various modulated waves (two in the standing-wave cases, one in the travelling-wave cases) are prop-

agating. Dashed lines represent predictions for the free film edges generated after the initial rupture of the film. The illustrated break-up pattern (dashed lines) are derived from the assumption that after the initial local rupture of the film , the free liquid edge(s) propagates mainly along the direction where the film thickness is the smallest. This assumption is based on the observation that the velocity of a free liquid-film edge is given by $u_e = \sqrt{2\sigma/(\rho t)}$, where σ, ρ and t denote surface tension coefficient, density and thickness of the uniform film [29]. For the investigated cases with travelling dilational or sinuous mode circumferential waves (wavenumber n), superposition with the imposed axial wave (wavenumber k) results in an oblique wave spiraling clock-wise downstream on the annular or conical film. Here, initial film breakup occurs simultaneously at various z = constant points. The perforations are expected to expand along the line of minimum film thickness (see dashed lines in Fig. 25 for the annular case) which results in the formation of liquid filaments spiraling downstream in the counter-clockwise direction ("filament beak-up"). On swirling annular films with superimposed dilational standing-wave modulations in the circumferential direction, film rupture first occurs after the formation of larger fluid blobs and upstream just behind these larger fluid masses. Again, initial film rupture will take place simultaneously at various z =constant positions. Subsequent expansion of the film perforations can be expected to generate a more or less circular pattern within each cell formed by neighboring fluid blobs. This type of film rupture can be characterized as "cellular break-up" and is illustrated in Fig. 26. The same break-up pattern can also be observed for non-swirling (pressure-stabilized) annular films and for swirling conical films with similar forcing conditions (see Fig. 27). However, due to film divergence the "cells" will stretch in the conical case and film thickness within the cells will be reduced. Therefore, expansion of the film perforation is expected to occur sig-

nificantly faster than in the corresponding annular case. Note, however, that initial rupture of the film in the conical case is delayed. Fig. 28 illustrates the break-up pattern expected for the considered swirling annular cases with a standing sinuous circumferential wave imposed at the nozzle exit. As for the dilational case discussed earlier, initial film perforation takes place just behind the larger fluid blobs. However, in this case the perforations are expected to propagate (more or less) along z = constant lines in the circumferential direction (see Fig. 28), ultimately resulting in the detachment of fluid rings with pronounced thickness fluctuations in the circumferential direction ("ring break-up"). The similar standing wave sinuous mode modulation imposed onto the conical film geometry yields the "filament break-up" pattern shown in Fig. 29. For the investigated cases, the filaments are spiraling clock-wise in the downstream direction. In contrast to the single wave modulation of Fig. 25, breakup of the filaments in Fig. 29 will be greatly influenced by the existing non-uniform mass distribution along the filaments.

Acknowledgments

This research has been supported by the U.S. Army Research Office through Grant/ Contract No. DAAH04-96-1-0055 and DAAD19-99-1-0204 with Dr. David Mann as the program manager.

References

[1] A.H. Lefebvre, *Atomization and Sprays*, Hemisphere, New York, NY, 1989.

[2] R.P. Fraser, Liquid Fuel Atomization, *Sixth International Symposium on Combustion*, Yale University, New Haven, pp. 687–701, 1956.

[3] C. Mehring, and W.A. Sirignano, Nonlinear Capillary Waves on Swirling, Axisymmetric Free Liquid films, *Int. J. Multiphase Flow*, vol. 27, pp. 1707–1734, 2001.

[4] M.V. Panchagnula, P.E. Sojka, and P.J. Santangelo, On the Three–Dimensional Instability of a Swirling, Annular, Inviscid Liquid Sheet subject to Unequal Gas Velocities, *Phys. Fluids*, vol. 8, no. 12, pp. 3300–3312, 1996.

[5] E.A. Ibrahim, and E.T. Akpan, Three-Dimensional Instability of Viscous Liquid Sheets, *Atomization and Sprays*, vol. 6, pp. 649-665, 1996.

[6] J. Ponstein, Instability of Rotating Cylindrical Jets, *Appl. Sci. Res. A*, vol. 8, pp. 425–456, 1959.

[7] C. Mehring, and W.A. Sirignano, Nonlinear Capillary Wave Distortion and Disintegration of Thin Planar Liquid Sheets, *J. Fluid Mech.*, vol. 388, pp. 69–113, 1999.

[8] I. Kim, and W.A. Sirignano, Three–Dimensional Wave Distortion and Disintegration of Thin Planar Liquid Sheets, *J. Fluid Mech.*, vol. 410, pp. 147–183, 2000.

[9] A. Lozano, A. Garcia-Olivares, and C. Dopazo, The Instability Growth Leading to a Liquid Sheet Breakup, *Phys. Fluids*, vol. 10, no. 9, pp. 2188-2197, 1998.

[10] R.H. Rangel, and W.A. Sirignano, Nonlinear Growth of Kelvin-Helmholtz Instability: Effect of Surface Tension and Density Ratio, *Phys. Fluids*, vol. 31, no. 7, pp. 1845–1855, 1988.

[11] R.H. Rangel, and W.A. Sirignano, The Linear and Nonlinear Shear Instability of a Fluid Sheet, *Phys. Fluids*, vol. 3, no. 10, pp. 2392-2400, 1991.

[12] C.P. Lee, and T.G. Wang, A Theoretical Model for the Annular Jet Instability, *Phys. Fluids* , vol. 29, no. 7, pp. 2076–2085, 1986.

[13] C.P. Lee, and T.G. Wang, The Theoretical Model for the Annular Jet Instability - Revisited, *Phys. Fluids A*, vol. 1, no. 6, pp. 967–974, 1989.

[14] J.I. Ramos, Annular Liquid Jets: Formulation and Steady–State Analysis, *Z. Angew. Math. Mech.*, vol. 72, no. 11, pp. 565–589, 1992.

[15] M.V. Panchagnula, P.E. Sojka, and A.K. Bajaj, The Non–Linear Breakup of Annular Liquid Sheets, *Proc. 11th Ann. Conf. Liquid Atom. Spray Sys.*, pp. 170–174, ILASS North and South America, 1998.

[16] C. Mehring, and W.A. Sirignano, Axisymmetric Capillary Waves on Thin Annular Liquid Sheets. Part I: Temporal Stability, *Phys. Fluids* , vol. 12, no. 6, pp. 1417–1439, 2000.

[17] C. Mehring, and W.A. Sirignano, Axisymmetric Capillary Waves on Thin Annular Liquid Sheets. Part II: Spatial Development, *Phys. Fluids* , vol. 12, no. 6, pp. 1440–1460, 2000.

[18] W.A. Sirignano, and C. Mehring, Review of Theory of Distortion and Disintegration of Liquid Streams, *Progr. Eng. Comb. Sci.*, vol.26, pp. 609–655, 2000.

[19] W.A. Sirignano, and C. Mehring, Disintegration and Distortion of Liquid Streams, AIAA Progress Series, *Liquid Rocket Thrust Chambers: Aspects of Modeling, Analysis, and Design*, Chap. 6, 2002.

[20] C. Mehring, and W.A. Sirignano, Disintegration of Planar Liquid Film Impacted by Two-Dimensional Gas Jets, submitted for publication in *Phys. Fluids*.

[21] C. Mehring, and W.A. Sirignano, Three-Dimensional Capillary Stability of Modulated Swirling Liquid Films, *Proc. 14th Ann. Conf. Liquid Atom. Spray Sys.*, available on CD rom, ILASS North and South America, 2001.

[22] J.H. Ferziger, *Numerical Methods for Engineering Applications*, Wiley, New York, NY, 1981.

[23] M.J. Lighthill, Group Velocity, *J. Inst. Math. Appl.*, vol. 1, pp. 1–27, 1965.

[24] W.A. Sirignano, and C. Mehring, Comments on Energy Conservation in Liquid-Stream Disintegration, *Proc. 8th Int. Conf. on Liquid Atom. Sys.*, available on CD rom, 2000.

[25] R.P. Fraser, P. Eisenklam, N. Dombrowski, and D. Hasson, Drop Formation from Rapidly Moving Sheets, *AIChE J.*, vol. 8, no. 5, pp. 672–680, 1962.

[26] N. Dombrowski, and P.C. Hopper, The Effect of Ambient Density on Drop Formation in Sprays, *Chem. Eng. Sci.*, vol. 17, pp. 291–305, 1962.

[27] J.H. Hilbing, and S.D. Heister, Droplet Size Control in Liquid Jet Breakup, *Phys. Fluids*, vol. 8, pp. 1574–1581, 1995.

[28] N. Dombrowski, and G. Munday, Spray Drying, in *Biochemical and Biological Engineering Science*, Chap. 16, Academic Press, London, 1968.

[29] G.I. Taylor, The Dynamics of Thin Sheets of Fluid, III. Disintegration of Fluid Sheets, *Proc. Royal Soc. London A*, vol. 253, pp. 296–312, 1959.

Table 1: Nonzero normalized coefficients within Eqs. 21 if only the unstable dilational mode wave with wavenumber k_3 is modulated at the nozzle exit.

case	We = 1000				We = 50, ω = 0.26	
	$n = 0$		$n = 3$		$n = 0$	$n = 3$
	$\omega = 0.06$	$\omega = 0.26$	$\omega = 0.06$	$\omega = 0.26$		
$\mathrm{Re}[k_3]$		0.259998		0.247686	0.259957	0.205644
$\mathrm{Im}[k_3]$		-0.00336706		-0.00241779	-0.0150983	-0.0122502
$\mathrm{Re}[A_{\eta,2}/h^0]$	4.07431	1.07193	-2.35187	1.31047	1.06706	1.85022
$\mathrm{Im}[A_{\eta,2}/h^0]$	0.158797	0.0202575	1.91089	0.102595	0.0903446	0.819221
$\mathrm{Re}[A_{u^*,2}/h^0]$	-0.00383658	-0.000203372	-0.0102061	0.00577779	-0.00406128	-0.000287701
$\mathrm{Im}[A_{u^*,2}/h^0]$	0.151768	0.0143359	0.00764552	0.0169967	0.0640431	0.107195
$\mathrm{Re}[A_{v^*,2}/h^0]$	-0.0814861	-0.00479382	-0.117893	-0.00604028	-0.0213412	-0.0679461
$\mathrm{Im}[A_{w^*,2}/h^0]$	-0.003167593	-0.0000905945	-0.13906	0.0121581	-0.00180689	0.0833378
$\mathrm{Re}[A_{w^*,2}/h^0]$	0.0262353	0.0036093	-0.0459605	0.00305534	0.0161147	0.0180419
$\mathrm{Im}[A_{w^*,2}/h^0]$	-0.00143516	0.0000660645	0.00966504	0.00169273	0.00131817	0.0204783

Table 2: Dilational travelling wave modulation on swirling annular films generated via harmonic oscillations of axial film velocity u^* [$R = 10$, $T_p = 15$, We $= 1000$, $f_1 = f_3 = \sin$, $f_2 = \cos$, $j = 1$, $u_0^* = 0.025$, $\eta = v^* = u^* = w^* = 0$].

case	n	T_{tr}	u_{3d}	k	$t_{b,m}$	$l_{b,(m)}$
0	1	2π	0	1	120	100
1	1	2π	0.1	1	100	80.1 (0.2)
2	3	2π	0.1	1	117.9	98
3	3	$2\pi/3$	0.1	1	122.1	102
4	3	$20\pi/3$	0.1	1	117.6	97.5
5	3	2π	0.1	10	114.6	94.8

Table 3: Dilational travelling or standing wave modulation on swirling annular films generated via harmonic oscillations of axial film velocity u^* [$R = 10$, $T_p = 15$, We $= 1000$, $f_1 = \sin$, $f_3 = 1$, $f_2 = \cos$, $n = 3$, $T_{tr} = 2\pi$, $u_0^* = 0.025$, $\eta = v^* = u^* = w^* = 0$].

case	u_{3d}^*	j	k	$t_{b,m}$	l_b
0	0.1	1	1	118.1	97.8
1	1.0	1	1	105.7	87.1
2	0.1	0	1	119.4	99.5
3	0.5	0	10	116.9	97.8

Table 4: Sinuous travelling wave modulation on swirling annular films generated via harmonic oscillations of transverse film velocity v^* [$R = 10$, $T_p = 25$, We $= 1000$, $f_1 = f_3 = \cos$, $f_2 = \cos$, $T_{tr} = 2\pi$, $v_0^* = 0.1$, $\eta = u^* = w^* = 0$].

case	n	v_{3d}^*	k	$t_{b,m}$	$l_{b,m}$
0	3	0.1	1	142.6	113.7
1	3	0.5	1	131.7	102.6
2	0	0.1	1	145.1	116.2
3	3	0.5	10	181.7	153

Table 5: Sinuous standing and travelling wave modulation on swirling annular films generated via harmonic oscillations of transverse film velocity v^* [$R = 10$, $T_p = 25$, We $= 1000$, $f_1 = \cos$, $f_3 = 1$, $f_2 = \cos$, $n = 3$, $T_{tr} = 2\pi$, $v_0^* = 0.1$, $\eta = u^* = w^* = 0$].

case	v_{3d}^*	j	k	$t_{b,m}$	$l_{b,m}$
0	0.5	1	1	139.2	85.2
1	0.5	0	1	107.1	78.9
2	0.5	0	10	145.6	118.1

Table 6: Sinuous or mixed sinuous/dilational standing wave modulation on non-swirling annular films generated via harmonic oscillations of transverse film velocity v^* or both film thickness η and v^*. [$R = 10$, $T_p = 10$, We $= 1000$, $k = 1$, $f_3 = 1$, $j = 0$, $n = 5$, $u^* = w^* = 0$].

case	f_1	f_2	η ('), v^* (")	$t_{b,m}$	$l_{b,(m)}$
0	sin	cos	0.1"	75	39.8 (0.4)
1	sin	1	0.5"	65	50.3 (0.15)
	0	cos	0.2'		
2	sin	sin	0.5"	100	48.2 (0.23)
	sin	cos	0.5'		
3	sin	sin	0.4"	75	46.8 (0.05)
	sin	cos	0.4'		

Table 7: Sinuous or dilational travelling or standing wave modulation on swirling films generated via harmonic oscillations of either u^*, v^* or w^*. [$R = 10$, $T_p = T_x = 10$, We $= 1000$, $f_2 = \cos$, $f_1 = 0$, $\eta = 0$].

case	f_3	j	u ('), v^* ("), w^* ( )	n	k	$t_{b,m}$	$l_{b,(m)}$
0	sin	0	0.25"	5	1	37.5	23.1 (0.14)
1	sin	0	0.25"	5	10	36.4	23.4
2	sin	0	0.15"	5	10	56.3	33.1
3	sin	0	0.1"	5	10	78	57.5 (0.1)
4	1	1	2	2	10	70	52.4 (0.015)
5	1	1	0.05'	2	10	77.5	55 (0.019)
6	sin	0	0.05'	2	10	75	52.5
7	sin	0	0.5	4	10	27.6	18.5

Table 8: Modulation of single unstable dilational mode wave onl Dilational travelling wave modulation on swirling annular films generated via harmonic oscillations of axial film velocity u^* [$R = 10$, $T_p = 15$, We $= 1000$, $f_1 = f_3 = \sin$, $f_2 = \cos$, $j = 1$, $u_0^* = 0.025$, $\eta = v^* = u^* = w^* = 0$].

case	n	T_{tr}	u_{3d}	k	$t_{b,m}$	$l_{b,(m)}$
0	1	2π	0	1	120	100
1	1	2π	0.1	1	100	80.1 (0.2)
2	3	2π	0.1	1	117.9	98
3	3	$2\pi/3$	0.1	1	122.1	102
4	3	$20\pi/3$	0.1	1	117.6	97.5
5	3	2π	0.1	10	114.6	94.8

Figure Captions

Figure 1: Schematic depictions of the investigated semi-infinite annular and conical swirling sheet configurations: (a) dilational modulation, (b) sinuous modulation.

Figure 2: Solutions 1-3 to Eq. (20) obtained via Mathematica^{TM}.

Figure 3: Solutions 4 and 5 to Eq. (20) obtained via Mathematica^{TM}.

Figure 4: Solutions 6 and 7 to Eq. (20) obtained via Mathematica^{TM}.

Figure 5: Solutions to Eq. (20) for wavenumbers $k_i (i = 1, \ldots, 7)$ [We $= 5, R = 10, n = 3$]. For $\omega < 0.7$, k_{1-4} are predominantly dilational mode waves and k_{5-7} are predominantly sinuous mode waves.

Figure 6: Growth rates for unstable dilational mode wave k_3 [We $= 1000, R = 10$]: $\circ : n = 0$, $\square : n = 1$, $\diamond : n = 2$, $\triangle : n = 3$, $\triangledown : n = 4$.

Figure 7: Growth rates for unstable dilational mode wave k_3 [We $= 50, R = 10$]: $\circ : n = 0$, $\square : n = 1$, $\diamond : n = 2$, $\triangle : n = 3$, $\triangledown : n = 4$.

Figure 8: Growth rates for unstable dilational mode wave k_3 [We $= 5, R = 10$]: $\circ : n = 0$, $\square : n = 1$, $\diamond : n = 2$, $\triangle : n = 3$, $\triangledown : n = 4$.

Figure 9: Wave angle $\mathrm{d}\theta/\mathrm{d}z^* = k/n$ for unstable dilational mode wave k_3 [We $= 50, R = 10$]: $\square : n = 1$, $\diamond : n = 2$, $\triangle : n = 3$, $\triangledown : n = 4$.

Figure 10: Instantaneous film thickness distribution for swirling annular axisymmetric liquid film ($n = 0$) with modulation of the film thickness at the nozzle exit in order to generate the unstable dilational mode wave predicted by linear theory [$R = 10$, $\omega = 2\pi T_p = 0.26$, We $= 1000$, $A_{\Delta r^*} = 0.35$; $l_b^* = 390$, $t_b^* = 422.85$].

Figure 11: Instantaneous three-dimensional film thickness distribution for swirling annular liquid film ($n = 3$) with modulation of the film thickness at the nozzle exit in order to generate the unstable dilational mode wave predicted by linear theory [$R = 10$, $\omega = 2\pi T_p = 0.26$, We $=$ 1000, $A_{\Delta r^*} = 0.35$; $l_b^* = 245$, $t_b^* = 275.55$].

Figure 12: Instantaneous film three-dimensional thickness distribution for swirling annular liquid film ($n = 3$) with modulation of the film thickness at the nozzle exit in order to generate the unstable dilational mode wave predicted by linear theory [$R = 10$, $\omega = 2\pi T_p = 0.26$, We $= 50$, $A_{\Delta r^*} = 0.15$].

Figure 13: Instantaneous film interface locations for the swirling annular liquid film of Fig. 12. Film break-up length and time are $l_b^* = 95$ and $t_b^* = 115.2$, respectively.

Figure 14: Instantaneous film thickness distribution for swirling annular axisymmetric liquid film ($n = 0$) with modulation of the film thickness at the nozzle exit in order to generate the unstable dilational mode wave predicted by linear theory [$R = 10$, $\omega = 2\pi T_p = 0.06$, We $= 50$, $A_{\Delta r^*} = 0.15$; $t_b^* > 225$].

Figure 15: Instantaneous three-dimensional film thickness distribution for swirling annular liquid film ($n = 3$) with modulation of the film thickness at the nozzle exit in order to generate the unstable dilational mode wave predicted by linear theory [$R = 10$, $\omega = 2\pi T_p = 0.06$, We $= 50$, $A_{\Delta r^*} = 0.15$; $l_b^* = 117.5$, $t_b^* = 127.2$].

Figure 16: Slices through the distorting liquid film of Fig. 15 at various downstream locations. Nozzle exit located at $z^* = 0$.

Figure 17: Instantaneous film-interface locations for non-swirling (pressure-stabilized) annular liquid film dilationally modulated at the nozzle exit $z^* = 0$ according to Eqns. (30) and (31)

$[R = 10,\ \mathrm{We} = 1000,\ T_p = T_e = 10,\ n = 5,\ A = B = 0.04]$.

Figure 18: Instantaneous film-interface locations for non-swirling (pressure-stabilized) annular liquid film sinusoidally modulated at the nozzle exit $z^* = 0$ according to Eq. (32) $[R = 10,\ \mathrm{We} = 1000,\ T_p = T_e = 10,\ n = 5,\ C = 0.1]$.

Figure 19: Instantaneous non-dimensional film thickness distribution for the non-swirling (pressure-stabilized) annular liquid film of Fig. 18, subject to three-dimensional sinuous forcing at the nozzle exit $z^* = 0$ according to Eq. (32) $[R = 10,\ \mathrm{We} = 1000,\ T_p = T_e = 10,\ n = 5,\ C = 0.1]$.

Figure 20: Instantaneous non-dimensional film thickness distribution for swirling annular liquid film subject to three-dimensional sinuous forcing at the nozzle exit $z^* = 0$ according to Eq. (32) $[R = 10,\ \mathrm{We} = 1000,\ T_p = T_e = 10,\ n = 5,\ C = 0.1]$.

Figure 21: Instantaneous outer interface topology for swirling conical liquid film with three-dimensional sinuous modulation enforced at the nozzle exit $z^* = 0$ according to Eq. (32) $[R = 10,\ \mathrm{We} = 1000,\ T_p = T_e = 10,\ n = 5,\ C = 0.1$, swirl number $k = 10]$.

Figure 22: Instantaneous non-dimensional film thickness distribution for swirling conical liquid film of Fig. 21.

Figure 23: Disturbed and undisturbed outer film interface for the swirling conical liquid film of Fig. 21.

Figure 24: Instantaneous film-interface locations for swirling conical liquid film with three-dimensional sinuous modulation enforced at the nozzle exit $z^* = 0$ according to Eq. (32) $[R = 10,\ \mathrm{We} = 1000,\ T_p = T_e = 10,\ n = 5,\ C = 0.25$, swirl number $k = 10]$.

Figure 25: Sketch of general film break-up pattern for swirling annular liquid film in (z, θ) plane at instant in time with one dilational or sinuous travelling wave modulated at the nozzle. Solid

lines: maximum thickness contour lines (local line thickness = measure of maximum local film thickness). Dashed lines: film perforation pattern.

Figure 26: Sketch of general film break-up pattern for swirling annular liquid film in (z, θ) plane at instant in time with standing dilational circumferential wave modulated at the nozzle. Solid line: maximum thickness contour line for single oblique wave. Dashed line: instantaneous free film edge. Shaded area: void. Solid circle: local film-thickness maximum.

Figure 27: Sketch of general film break-up pattern for swirling conical liquid film in (z, θ) plane at instant in time with standing dilational circumferential wave modulated at the nozzle. Solid line: maximum thickness contour line for single oblique wave. Dashed line: instantaneous free film edge. Shaded area: void. Solid circle: local film-thickness maximum.

Figure 28: Sketch of general film break-up pattern for swirling annular liquid film in (z, θ) plane at instant in time with standing sinuous circumferential wave modulated at the nozzle. Solid line: maximum thickness contour line for single oblique wave. Dashed line: instantaneous free film edge. Solid circle: local film-thickness maximum.

Figure 29: Sketch of general film break-up pattern for swirling conical liquid film in (z, θ) plane at instant in time with standing sinuous circumferential wave modulated at the nozzle. Solid line: maximum thickness contour line for single oblique wave. Dashed line: instantaneous free film edge. Solid circle: local film-thickness maximum.

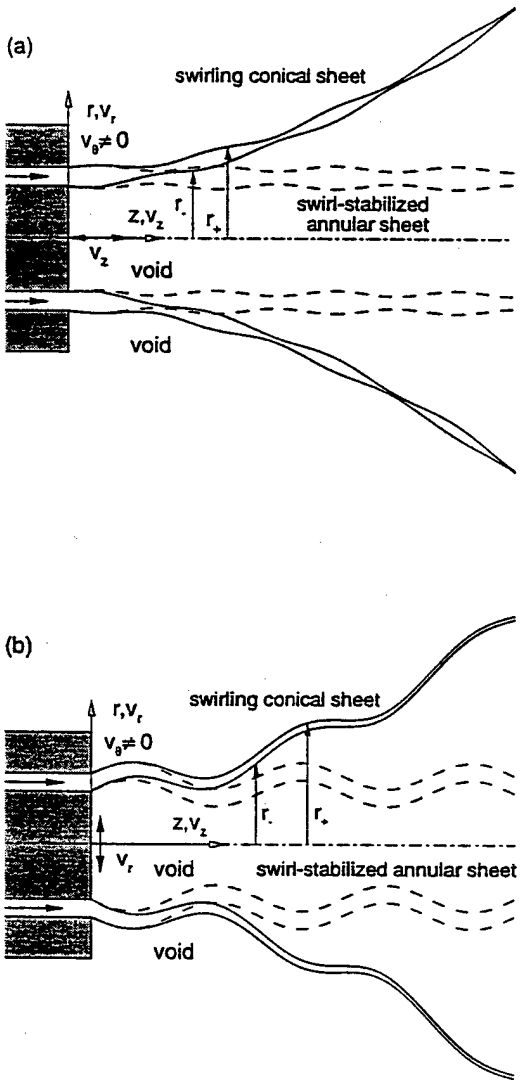
(a)
swirling conical sheet
r,v_r
v_θ≠0
z,v_z
r_-
r_+
swirl-stabilized
annular sheet
v_z
void
void
(b)
swirling conical sheet
r,v_r
v_θ≠0
z,v_z
r_-
r_+
v_r
void
swirl-stabilized annular sheet
void

Figure 1:

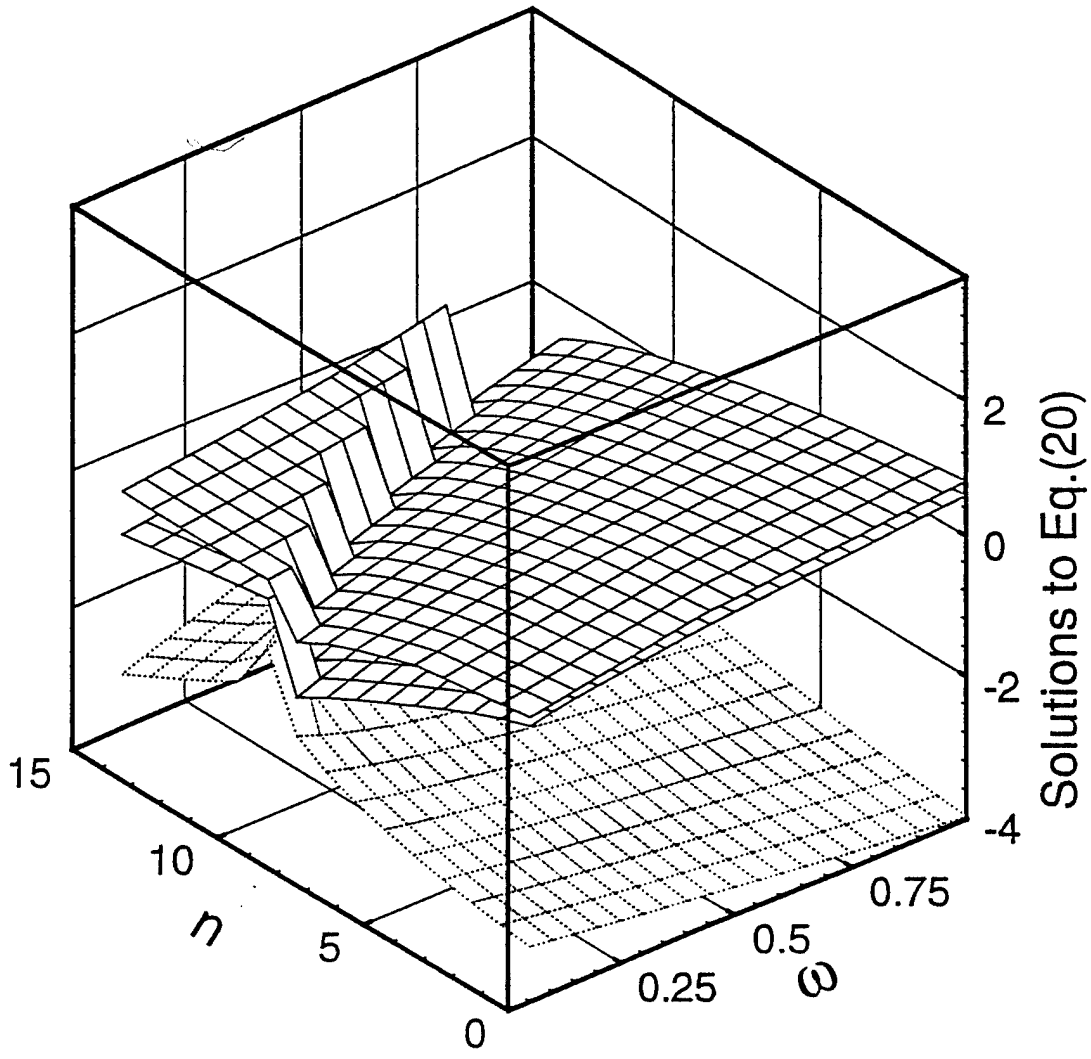

Figure 2:

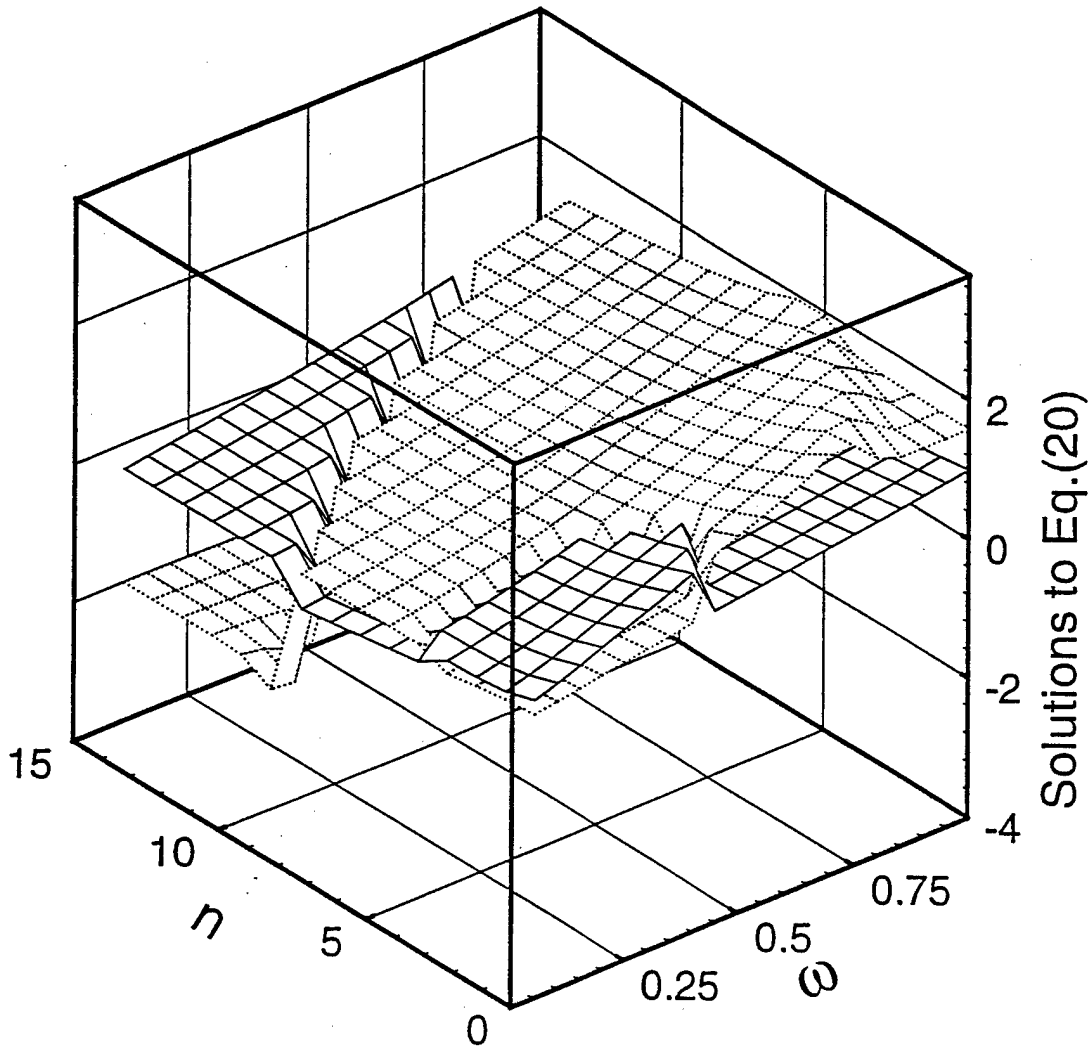

Figure 3:

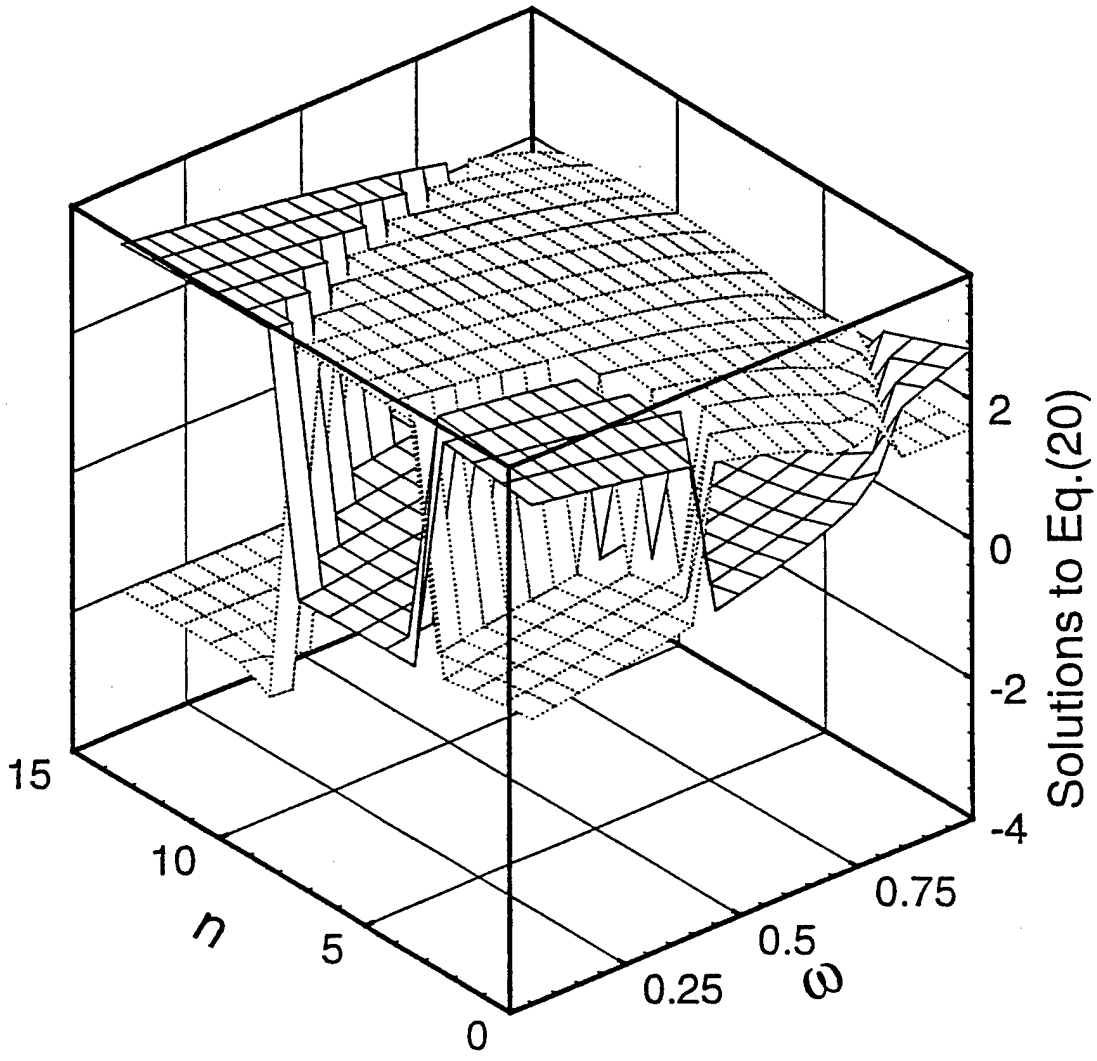

Figure 4:

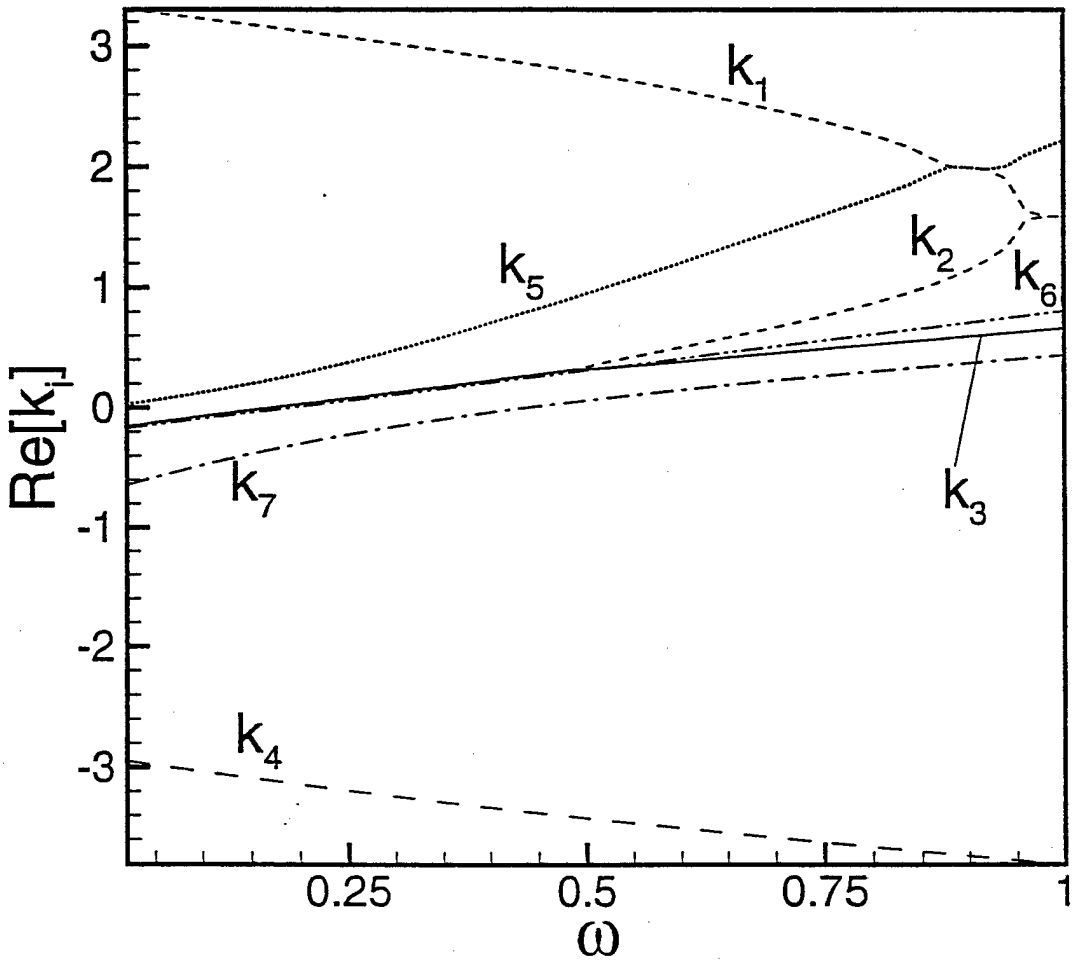

Figure 5:

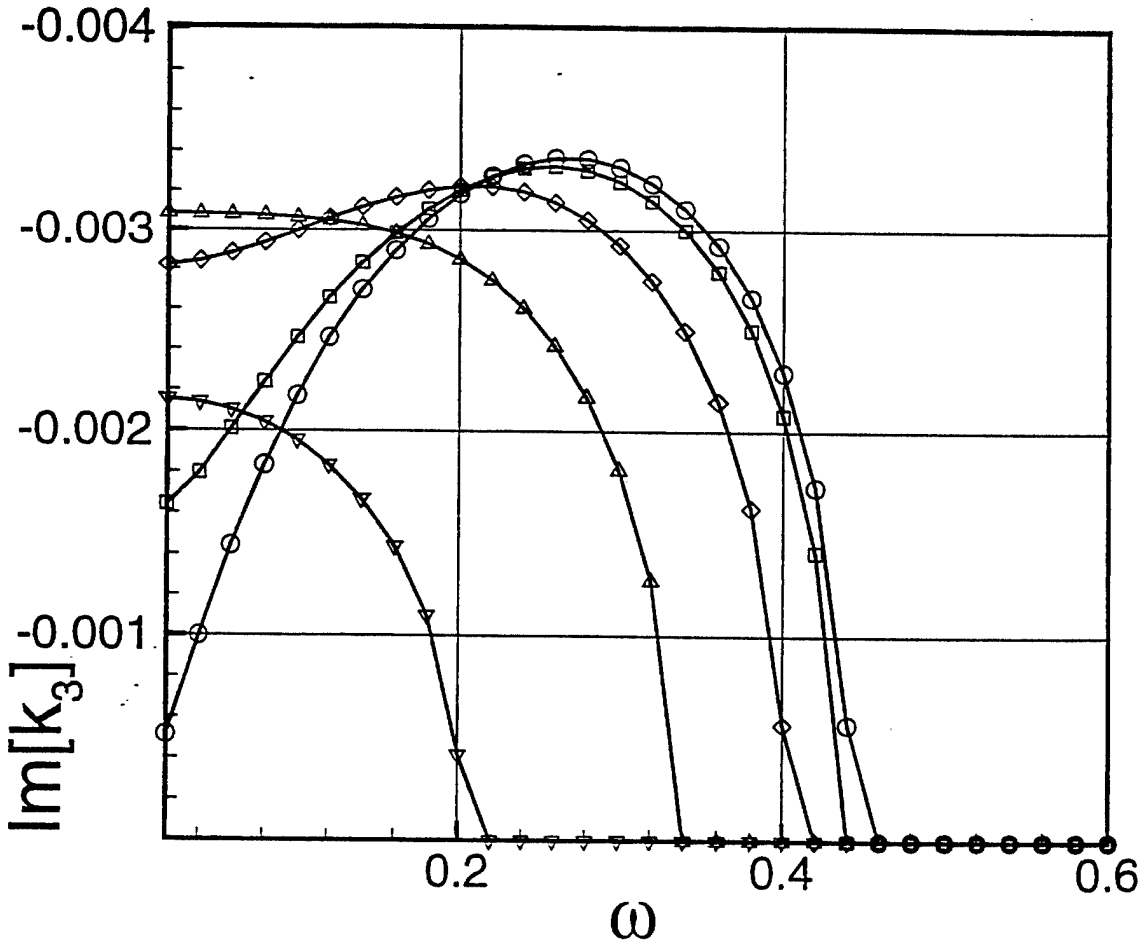

Figure 6:

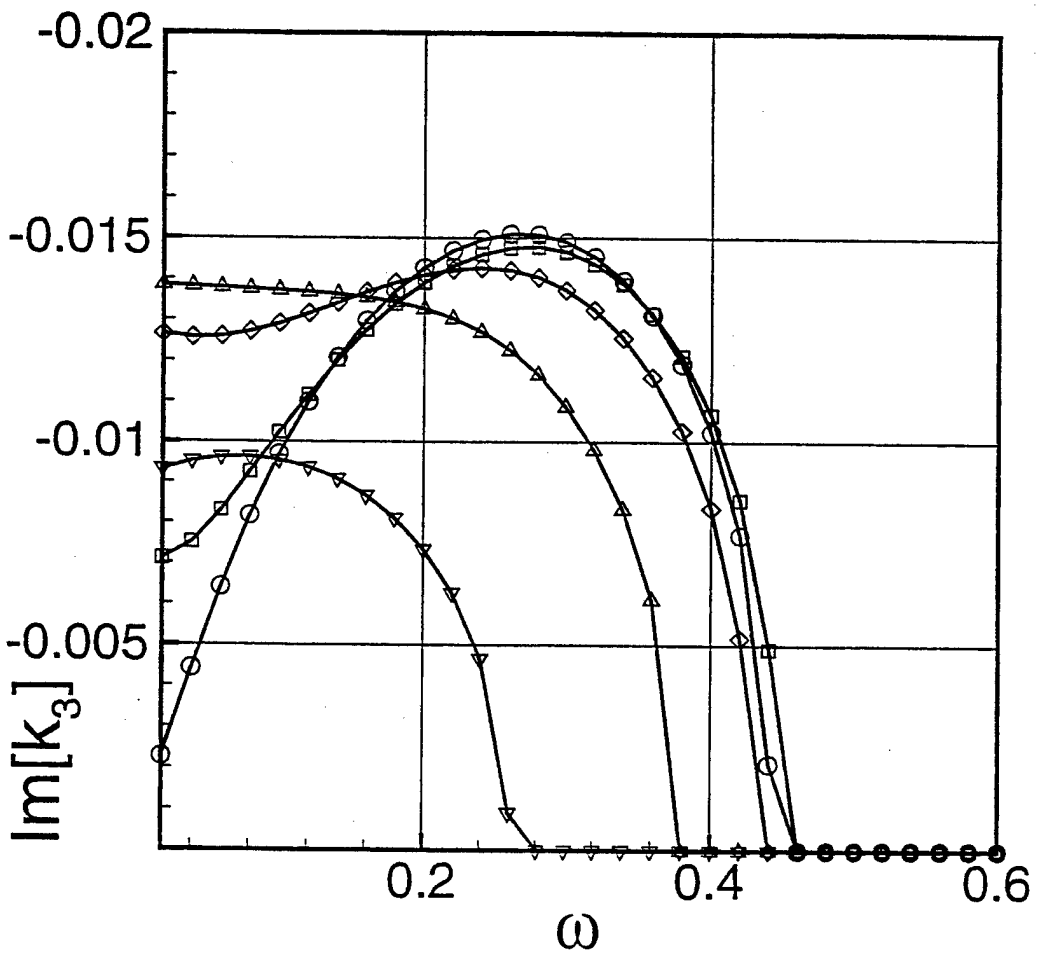

Figure 7.

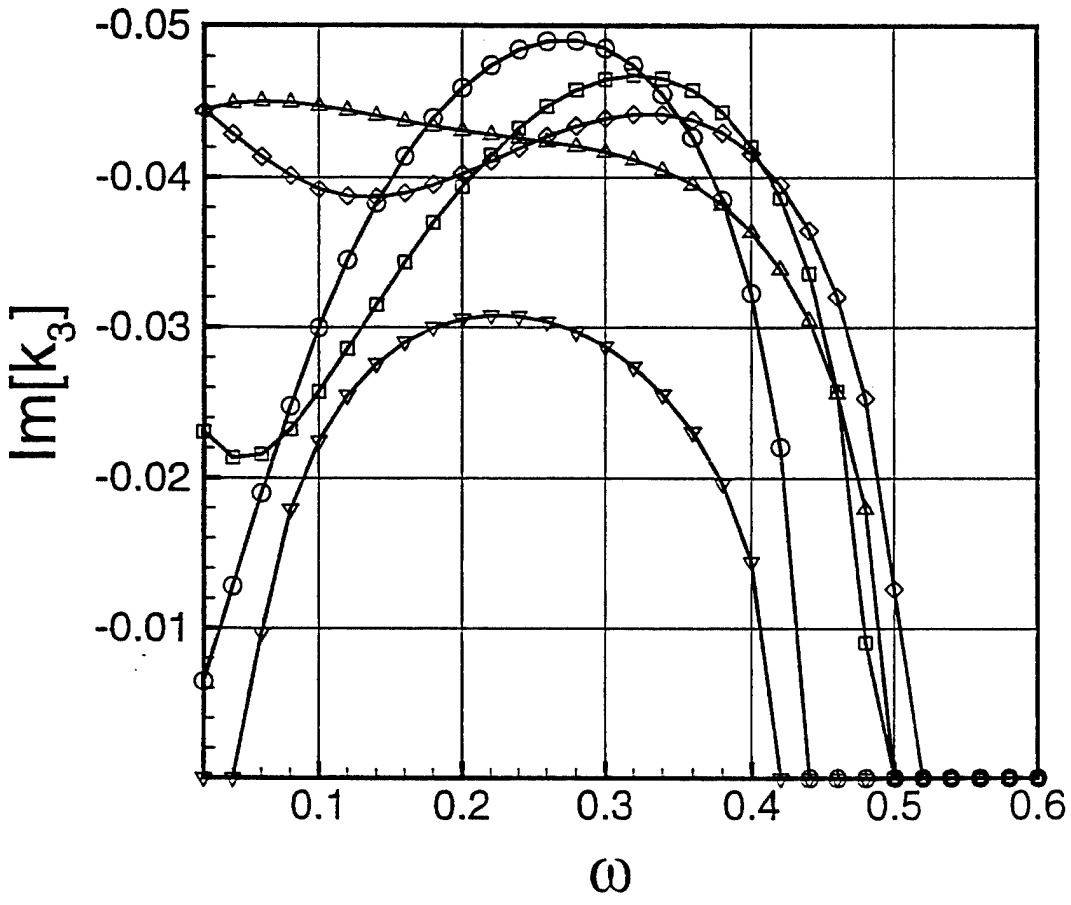

Figure 8:

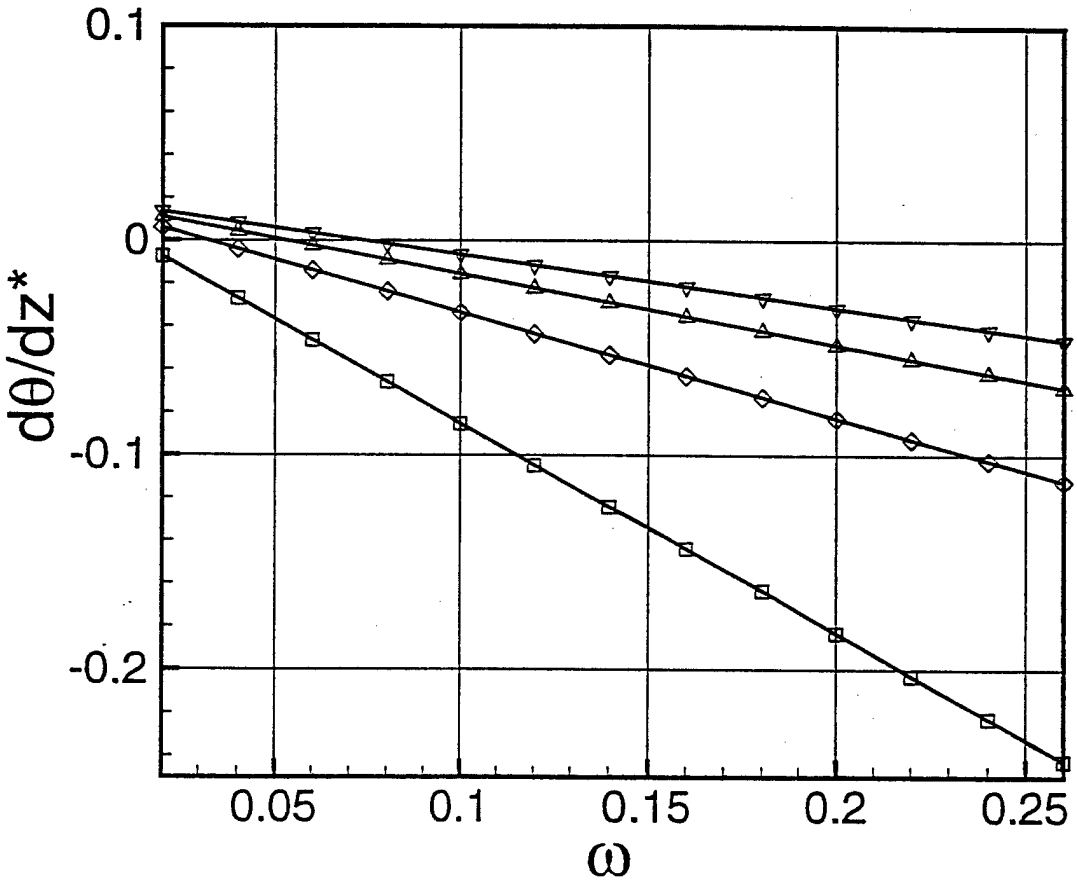

Figure 9:

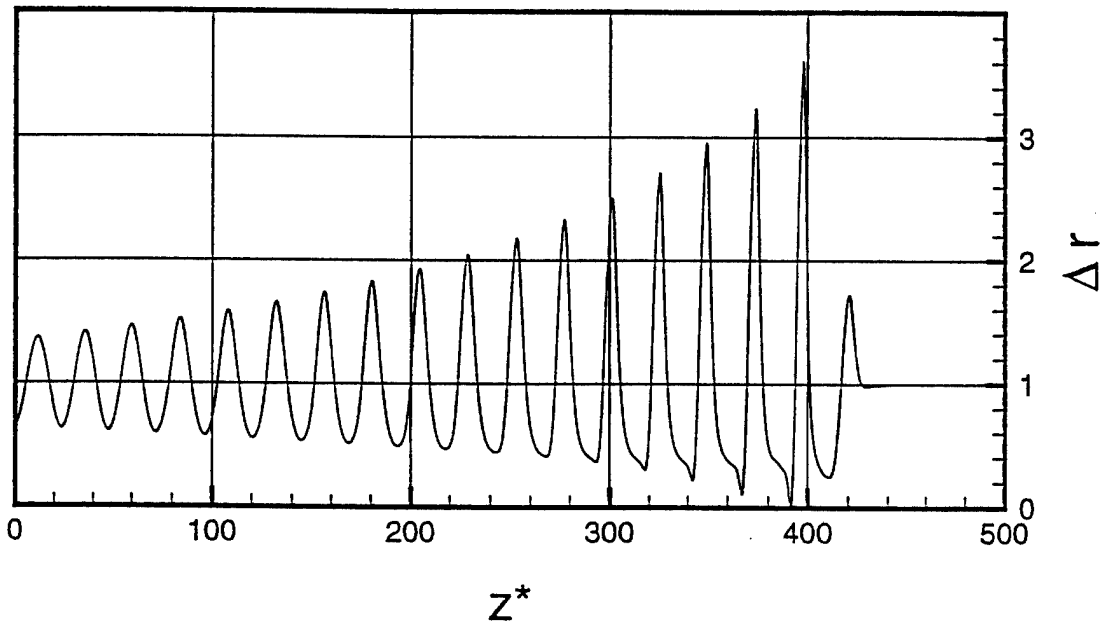

Figure 10:

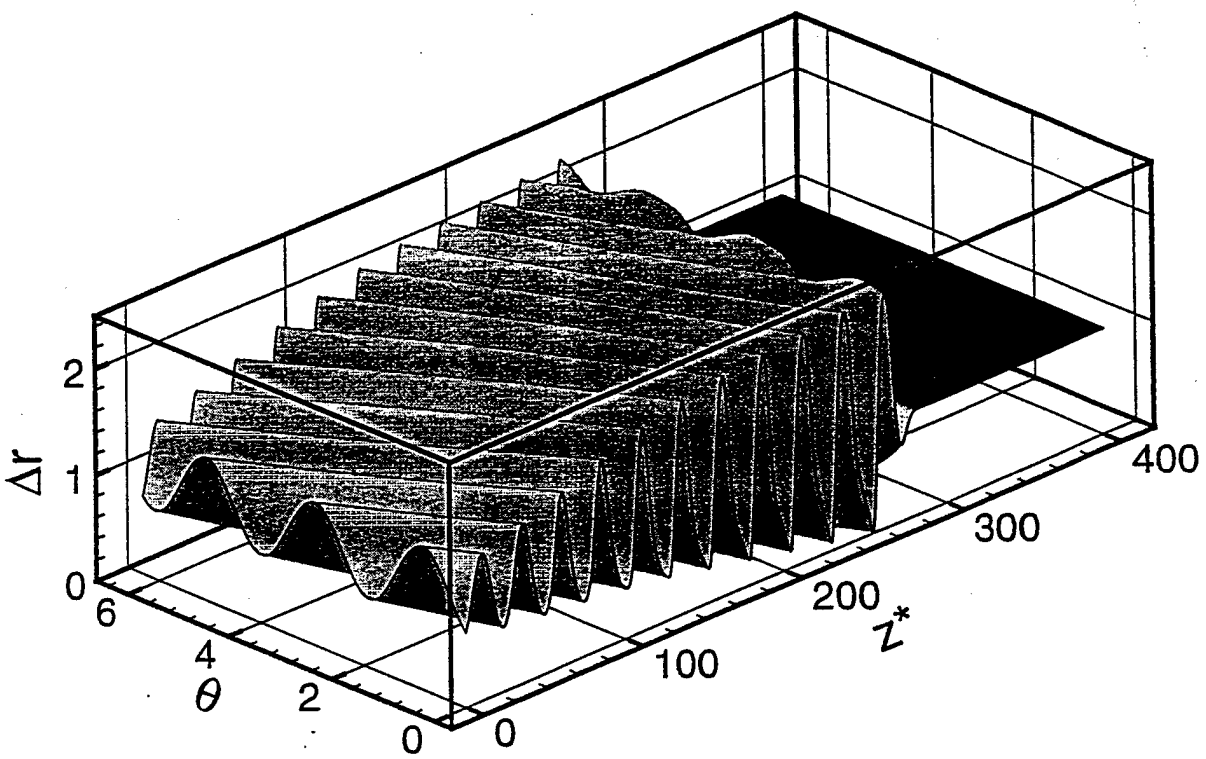

Figure 11:

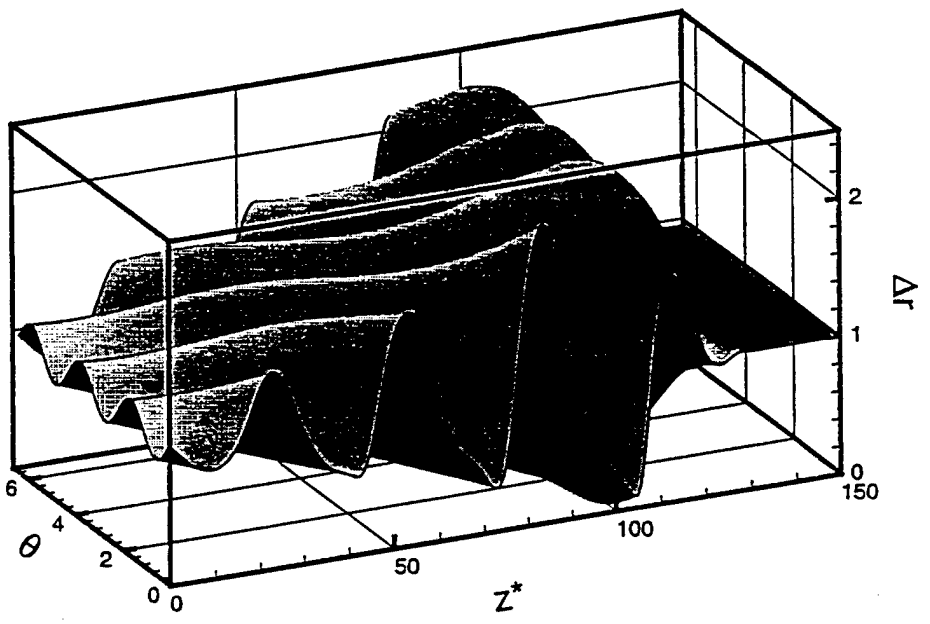

Figure 12:

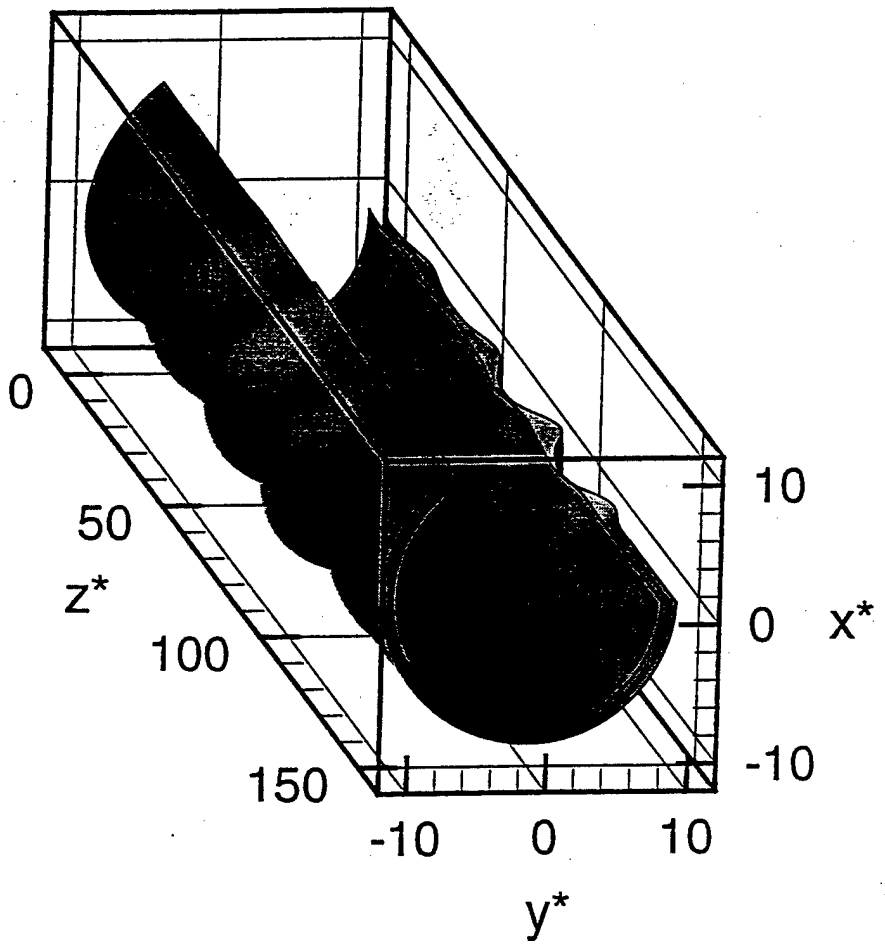

Figure 13:

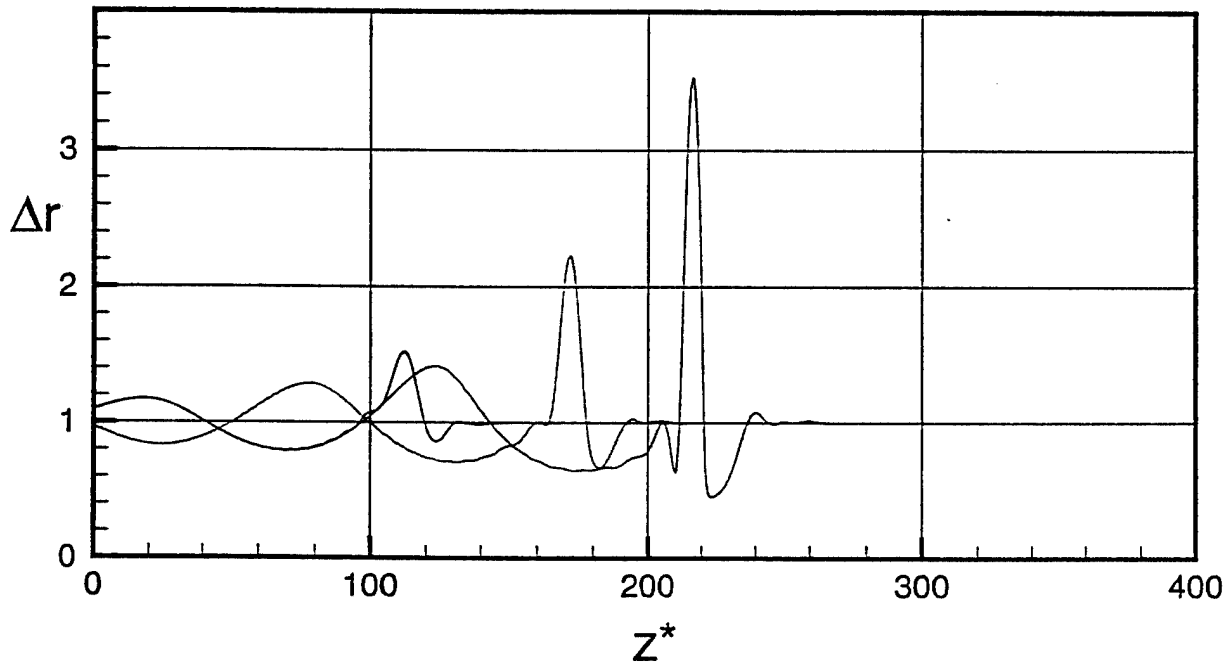

Figure 14:

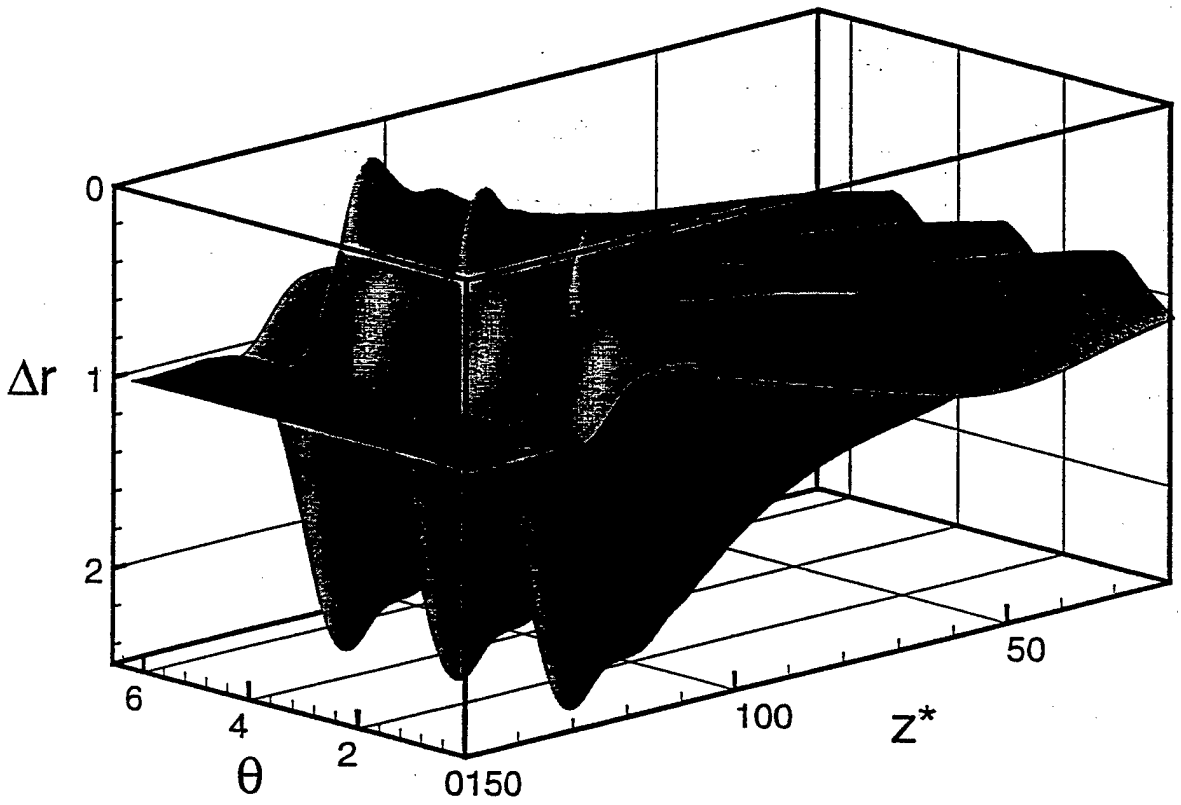

Figure 15:

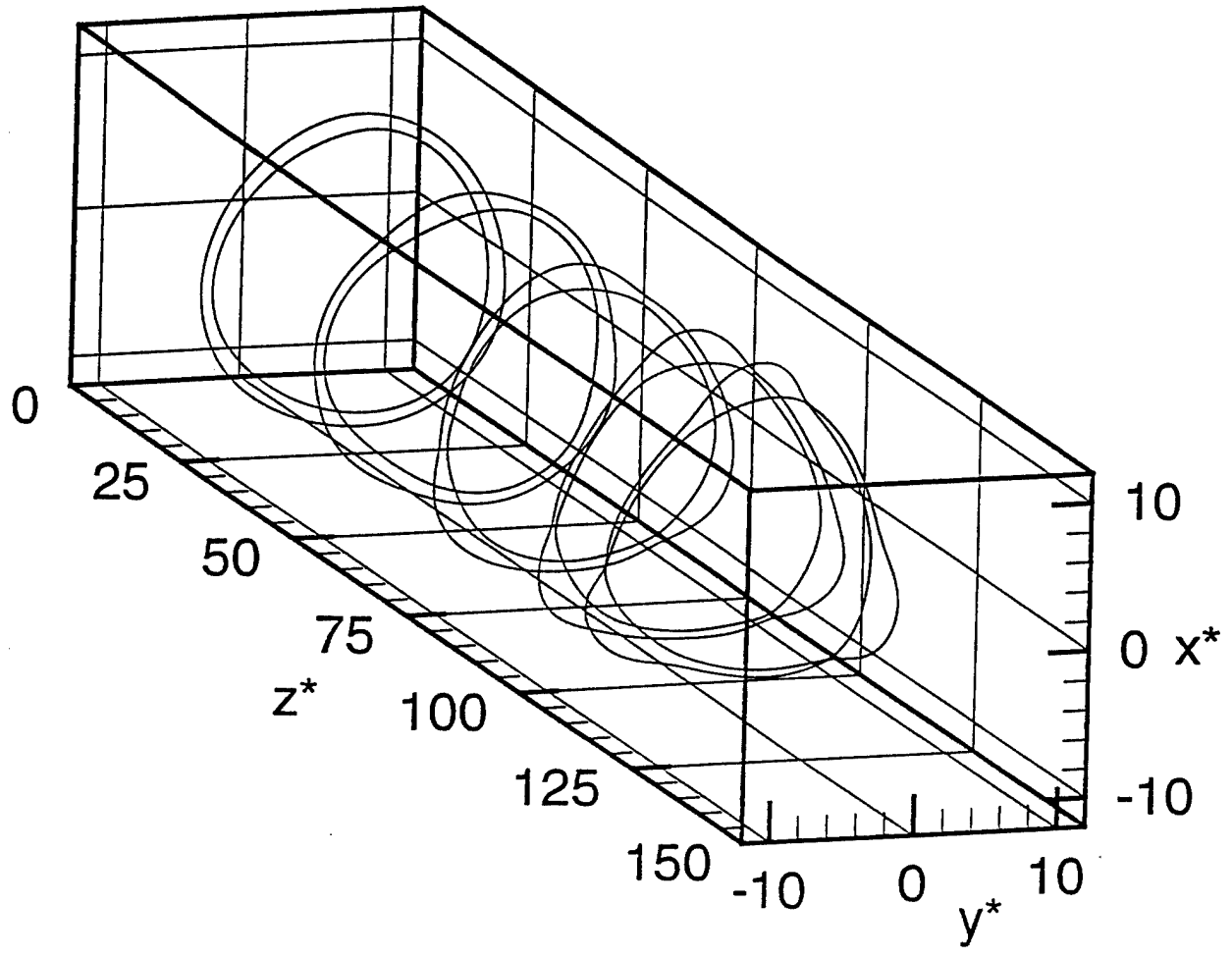

Figure 16:

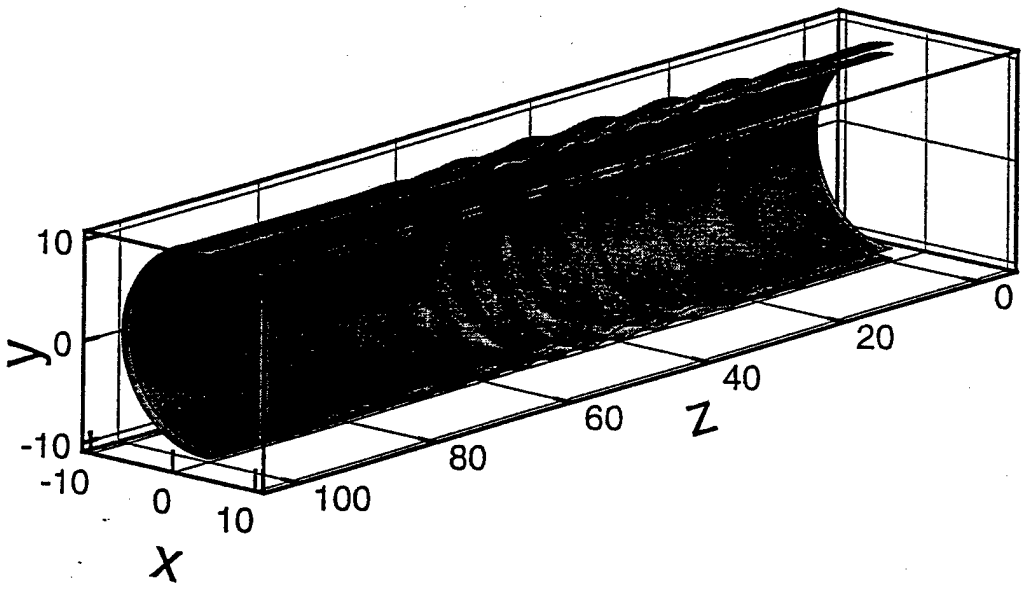

Figure 17:

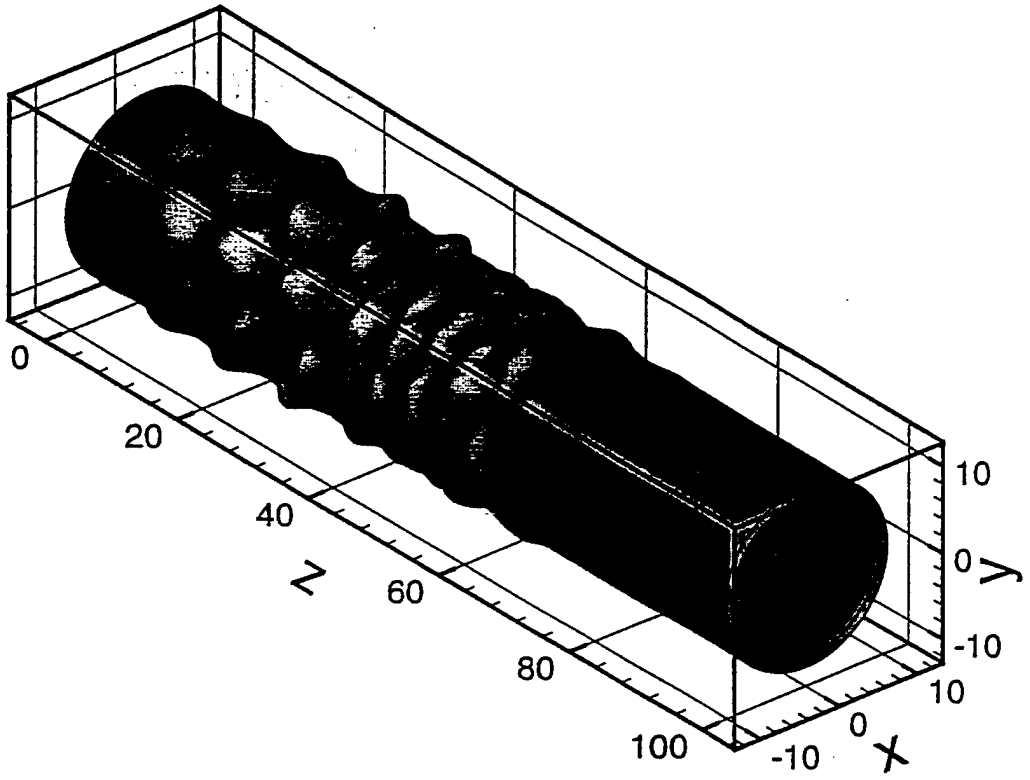

Figure 18:

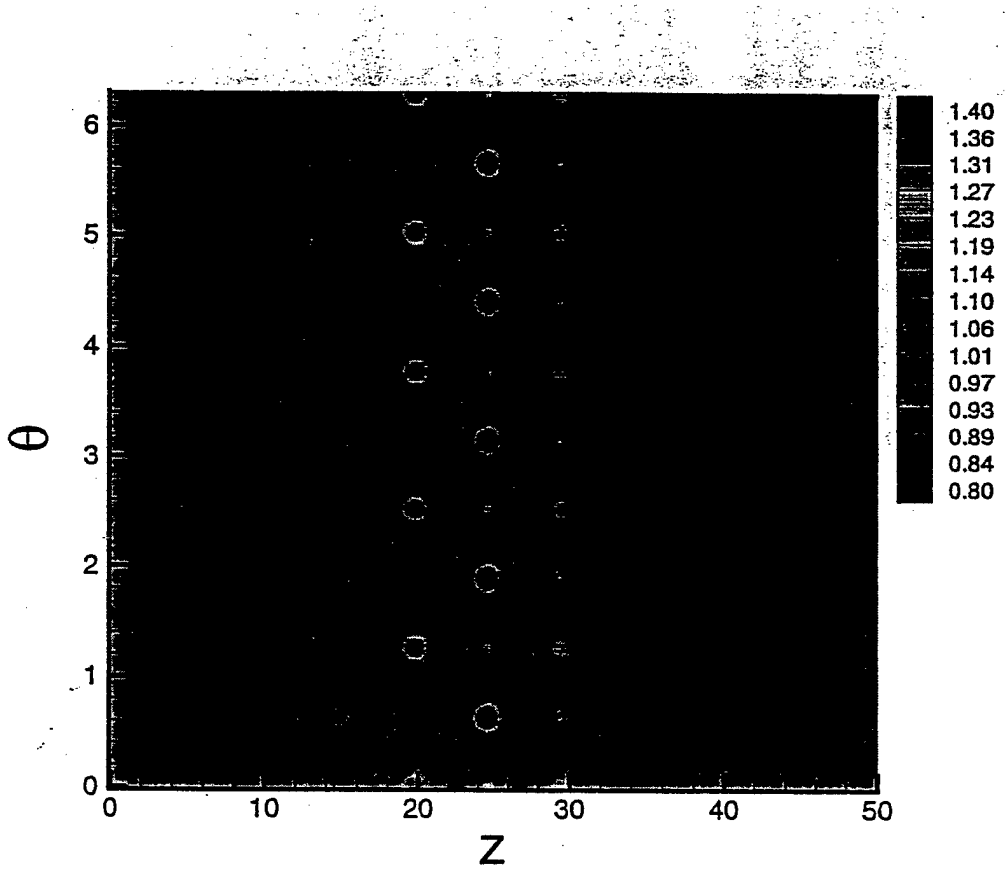
1.40
1.36
1.31
1.27
1.23
1.19
1.14
1.10
1.06
1.01
0.97
0.93
0.89
0.84
0.80
θ
0
1
2
3
4
5
6
0
10
20
30
40
50
Z

Figure 19:

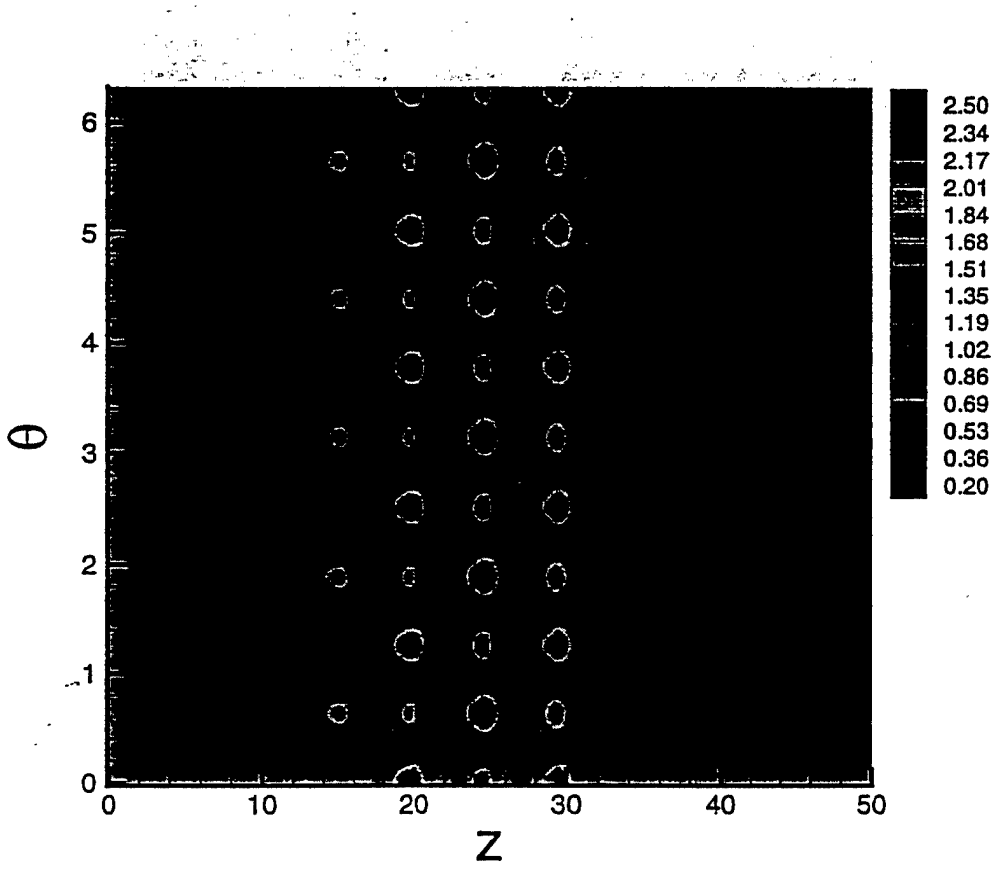
θ
Z
0
1
2
3
4
5
6
0
10
20
30
40
50
2.50
2.34
2.17
2.01
1.84
1.68
1.51
1.35
1.19
1.02
0.86
0.69
0.53
0.36
0.20

Figure 20:

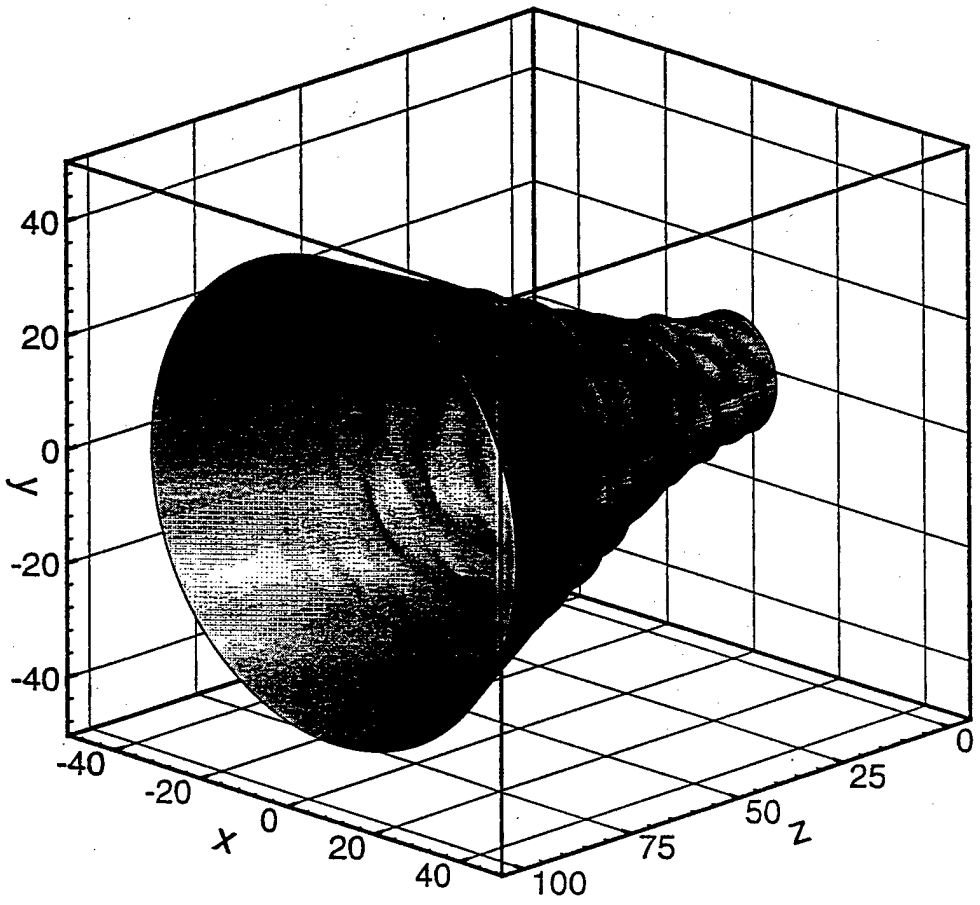

Figure 21:

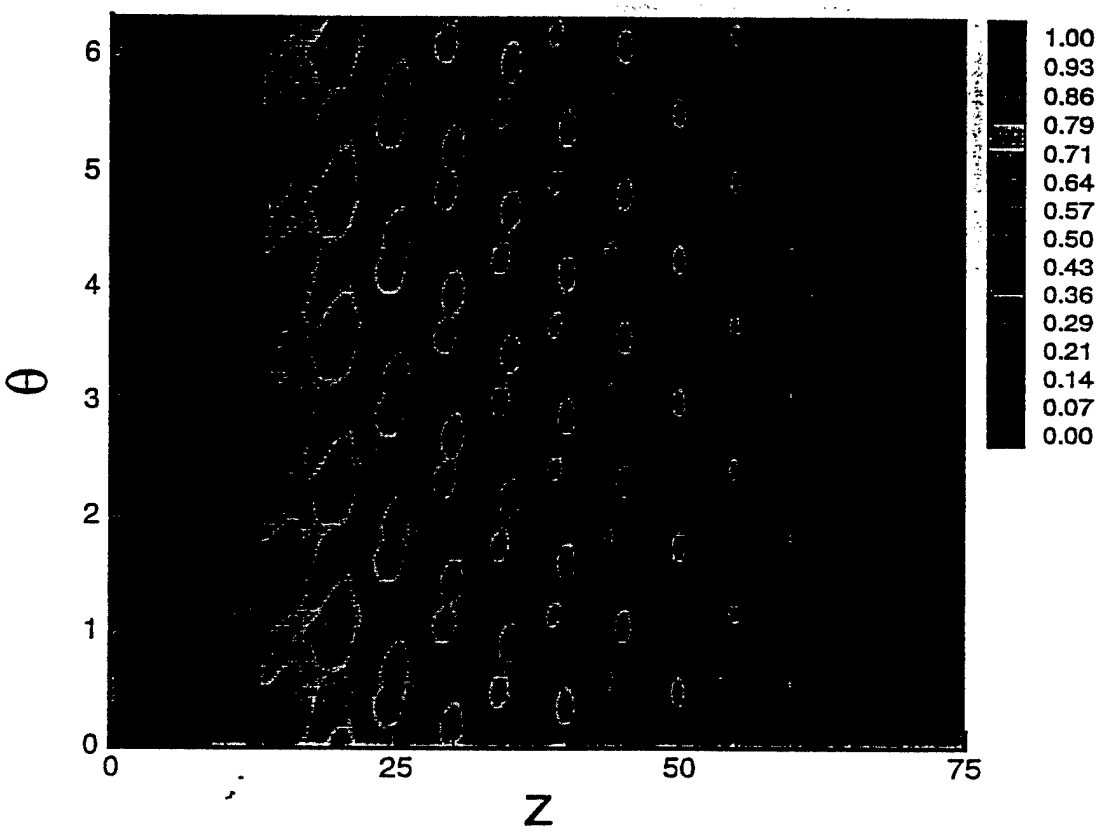
θ
6
5
4
3
2
1
0
0
25
50
75
Z
1.00
0.93
0.86
0.79
0.71
0.64
0.57
0.50
0.43
0.36
0.29
0.21
0.14
0.07
0.00

Figure 22:

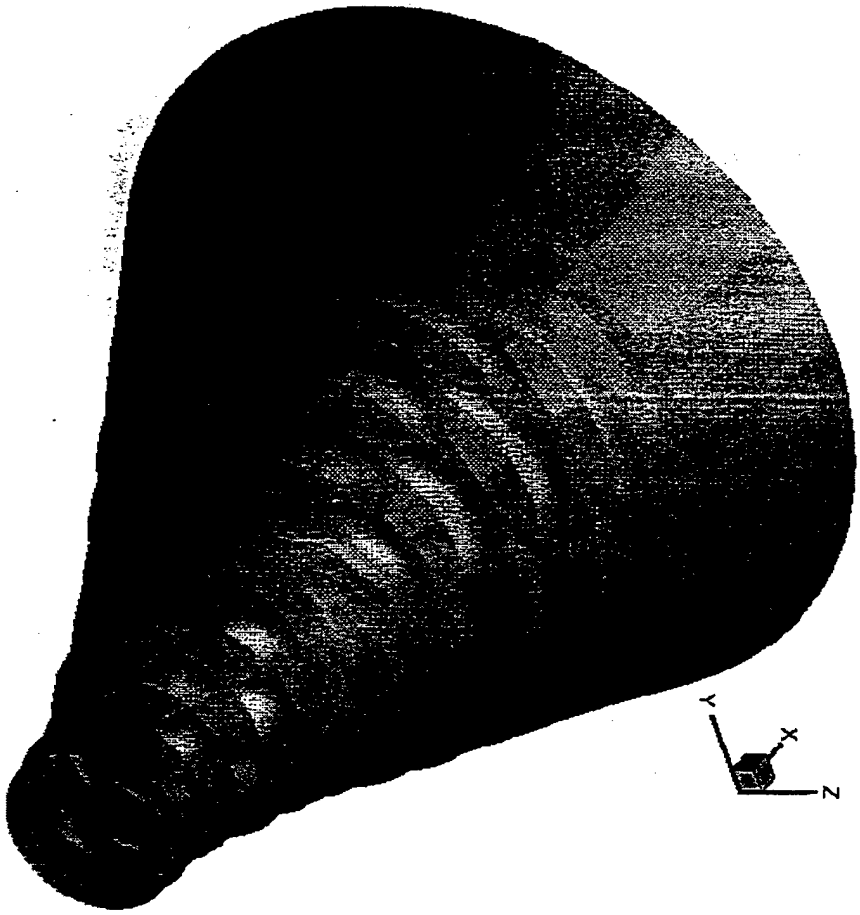

Figure 23:

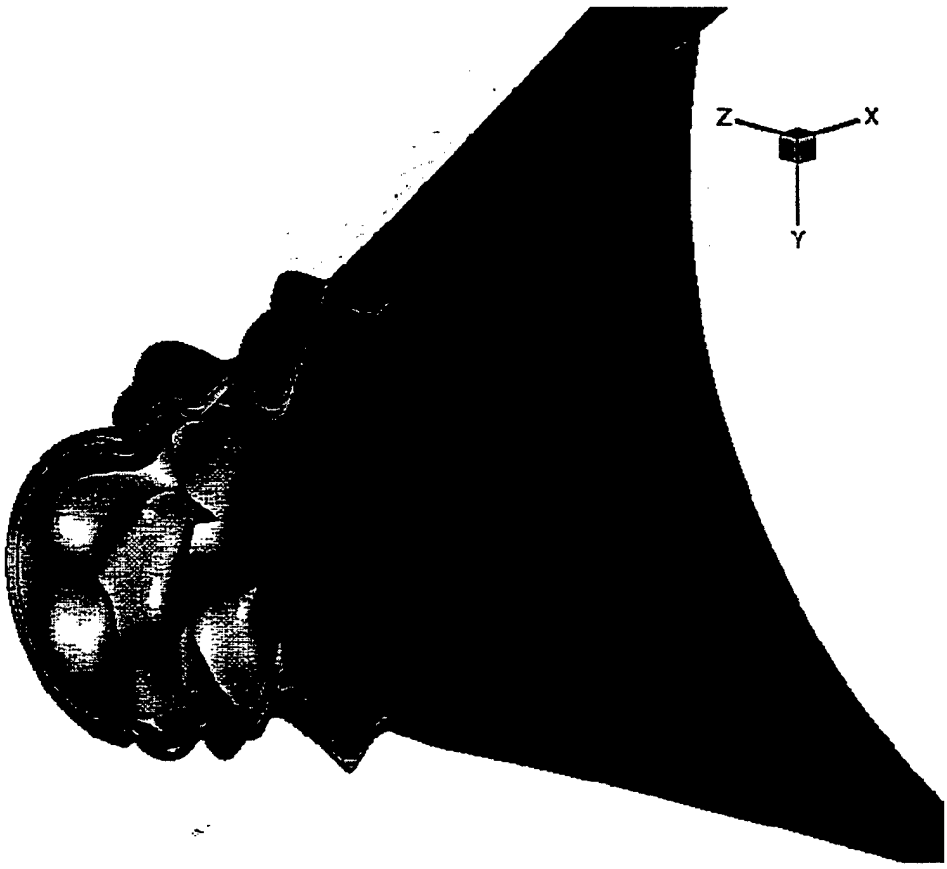

Figure 24:

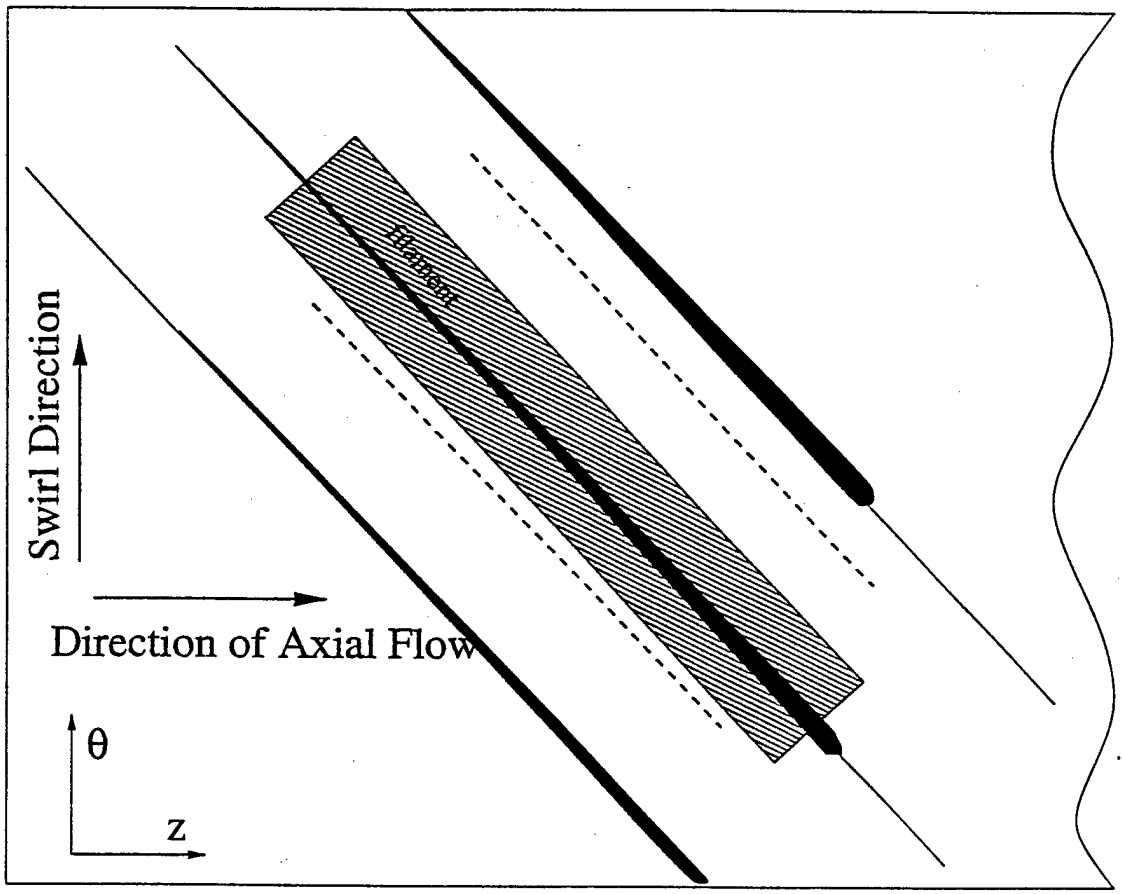

Figure 25:

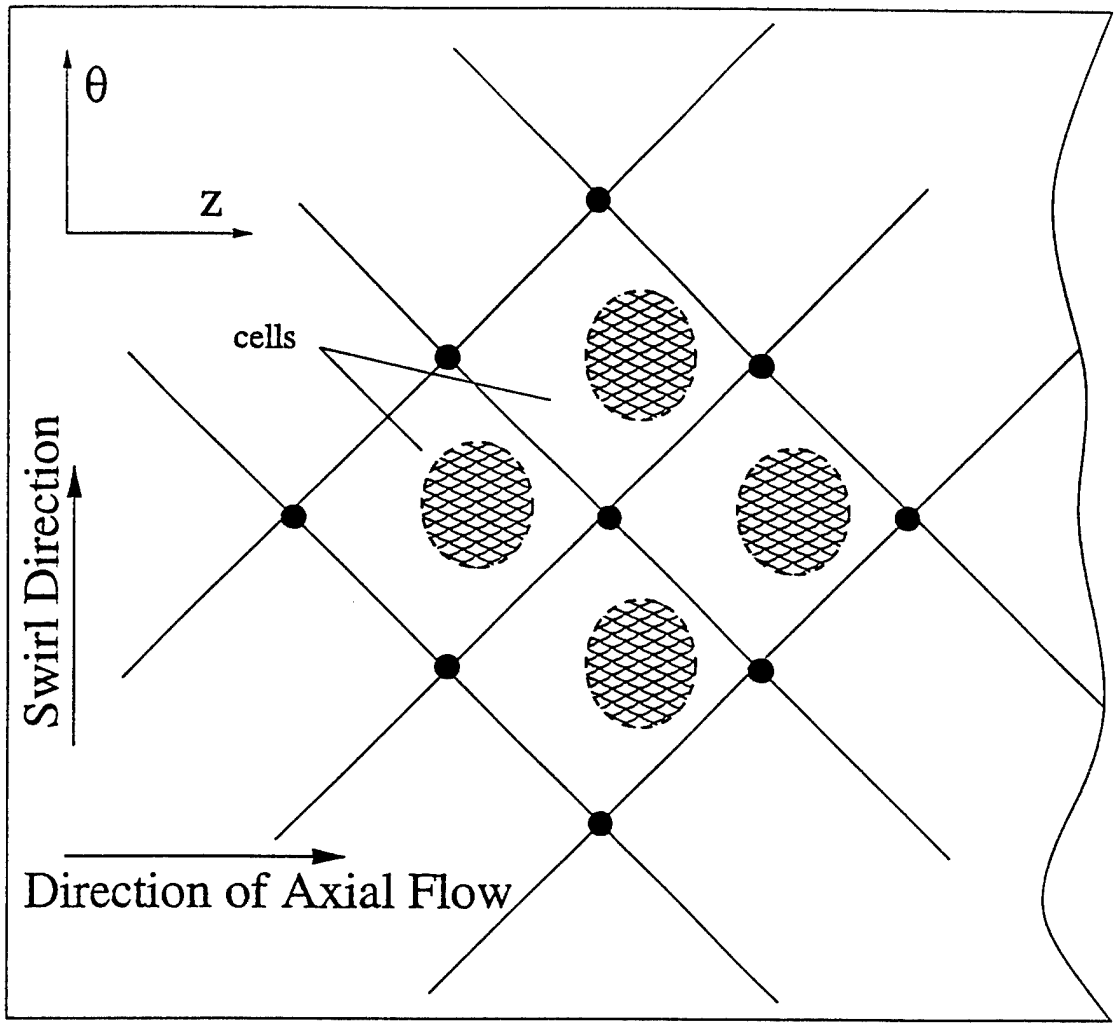

Figure 26:

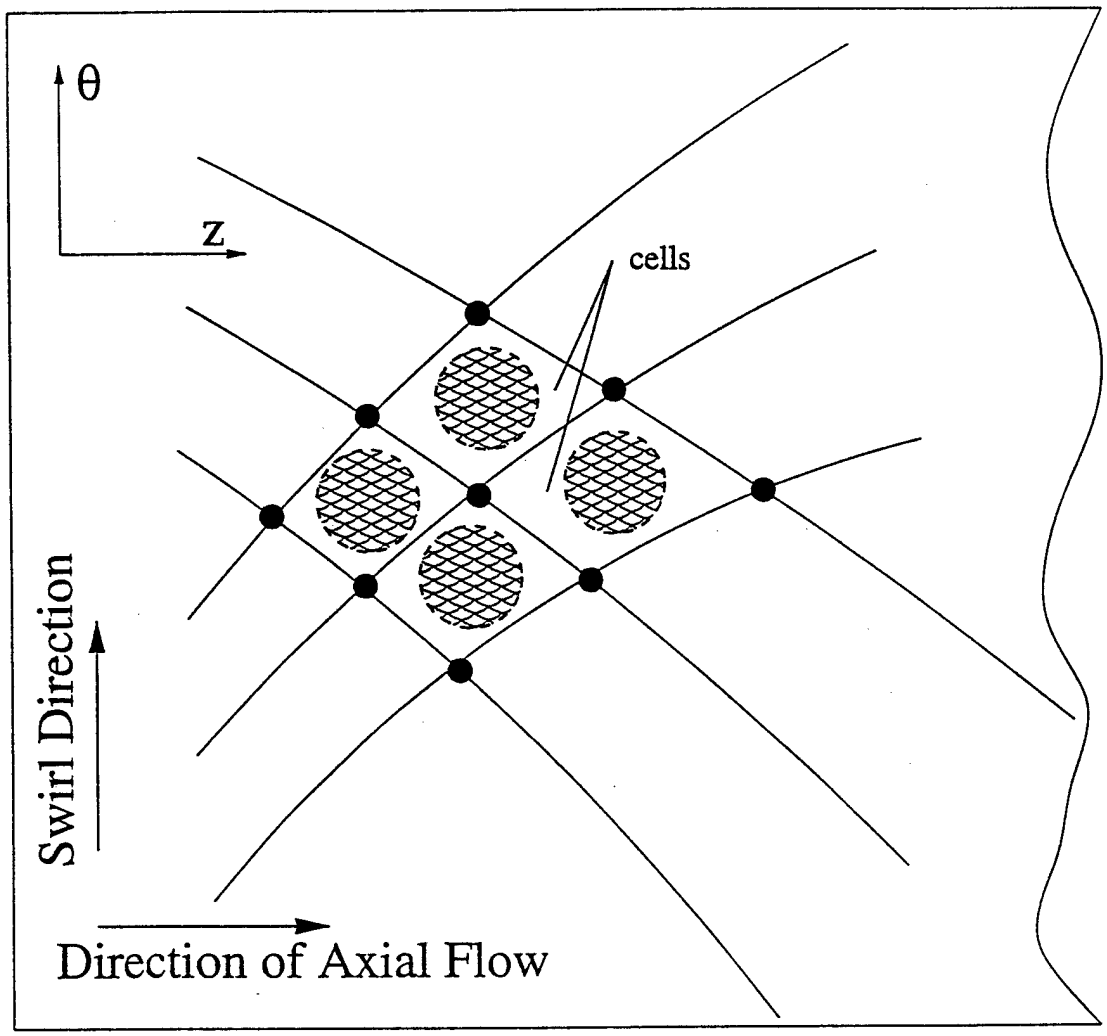

Figure 27:

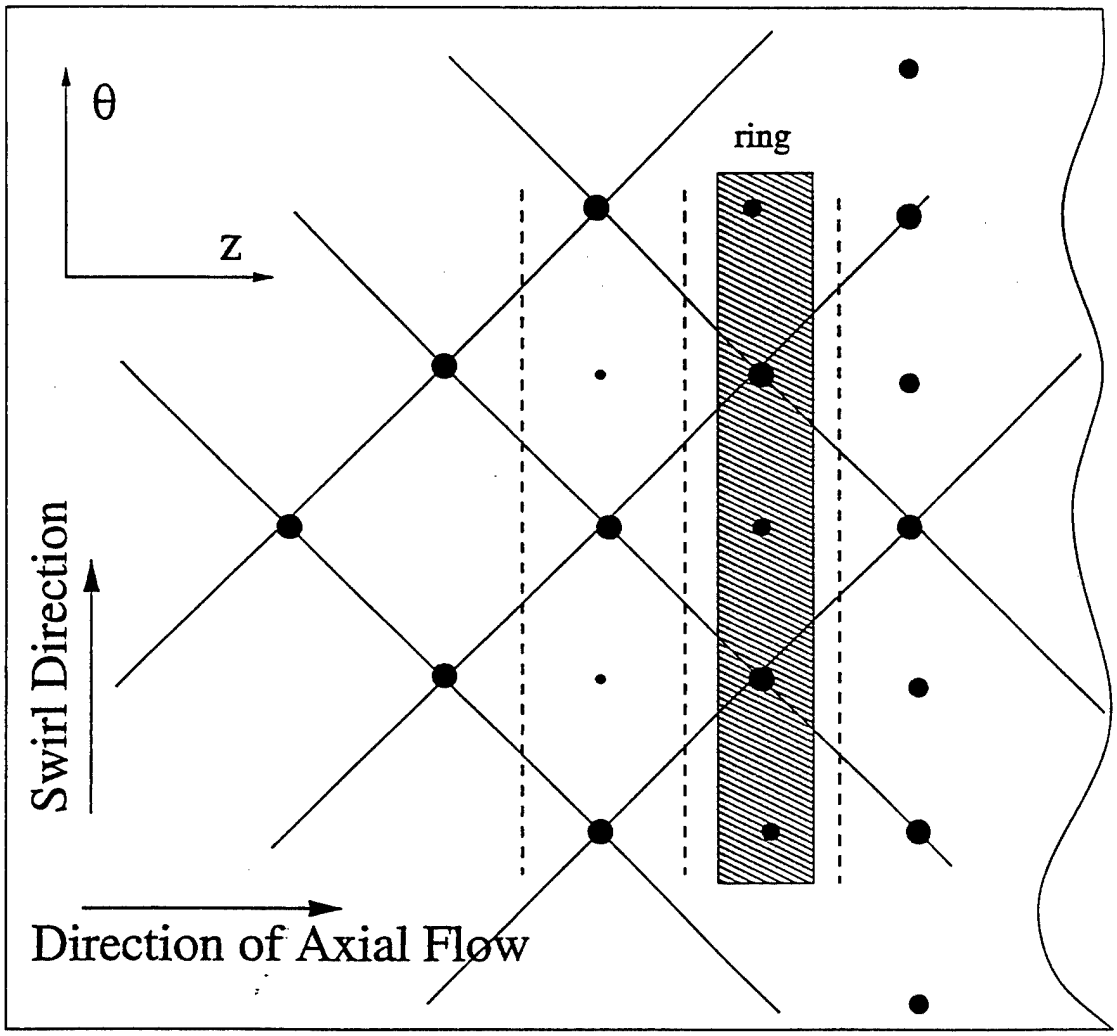

Figure 28:

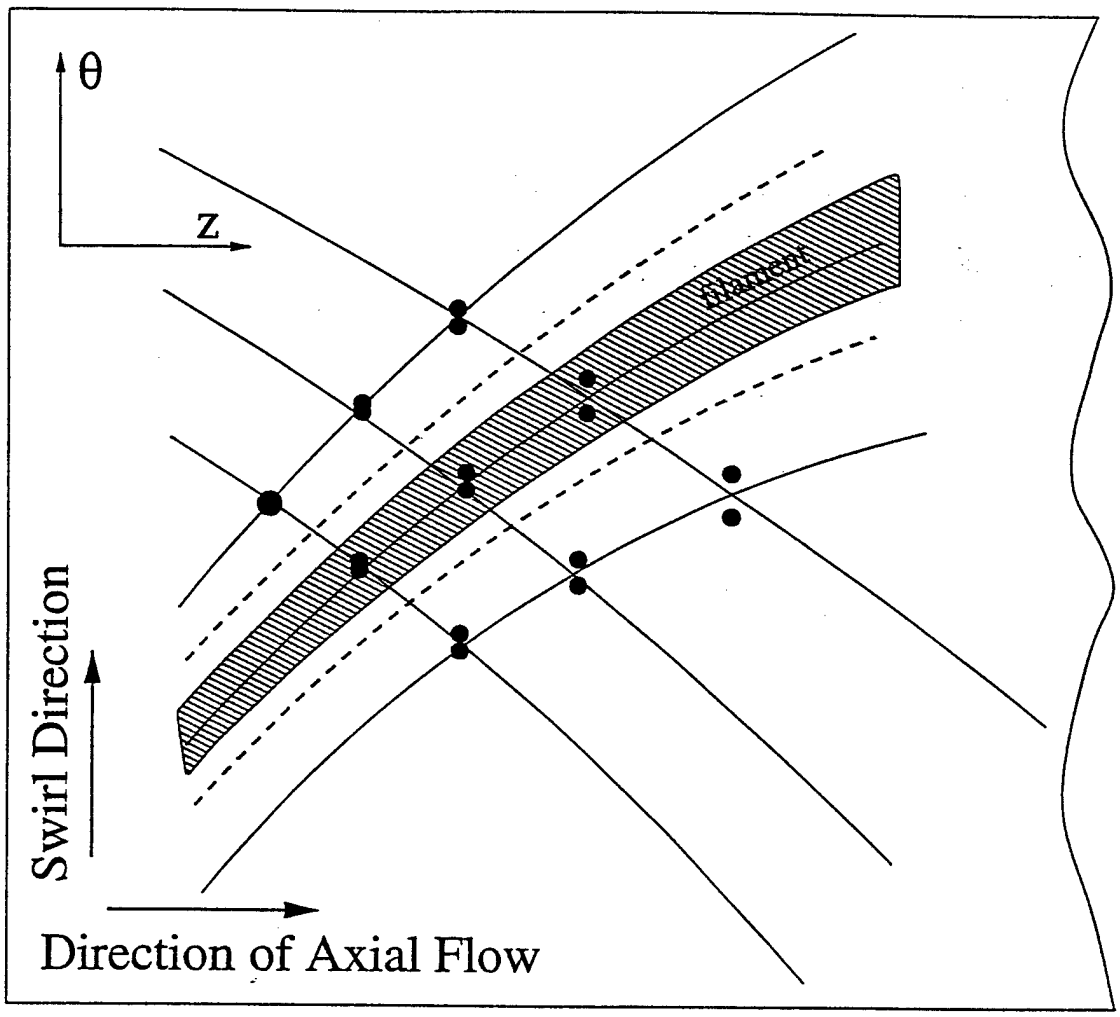

Figure 29:

PF # ?

Dynamic Stretching of A Planar Liquid Bridge

C. Mehring[a)] and W. A. Sirignano[a)]

Department of Mechanical and Aerospace Engineering, University of California, Irvine

(February 18, 2003)

Abstract

A thin incompressible viscous planar free liquid film in a void and under zero gravity is analyzed by means of a reduced-dimension (lubrication) approach. Linear analysis focuses on films with harmonic modulations in the axial film velocity enforced at the ends of the planar bridge. Effect of changes in the problem parameters on the overall distortion characteristics of the film are discussed. Nonlinear film distortion and break-up is investigated for the case of temporally increasing velocity at the end of the film resulting in continuous film stretching eventually leading to film rupture. Implementation of the employed numerical model is validated for the linear limit by comparison with the analytical linear solutions and for harmonically modulated film-end velocities.

Within the nonlinear analysis of the continuously stretched film bridge, several distinct film topologies are identified depending on liquid Weber number and Reynolds number, i.e., the magnitude of the stretching rate (end velocity) compared to signal propagation rates through the liquid via capillary waves and viscous action. That is, the Weber number is the square of the ratio of stretching rate to capillary wave velocity while Reynolds number is the ratio of stretching rate to the characteristic viscous velocity. Here, film

topology is typically characterized by three distinct regions, i.e. a film wedge forming at the pulling end(s), the film center region and a transition region. The size and shape of these regions greatly depends on the particular case under investigation.

Film distortion characteristics observed for continuously compressed planar films conform with observations made by other authors for the similar case of contracting free liquid films.

I. INTRODUCTION

Written reports on the analysis of thin films originate as far back as Leonardo da Vinci[1] who described the formation of a liquid film when pulling a reed out of soapy water. Today, liquid films are found in a wide variety of engineering applications including novel concepts such as liquid film space radiators,[2,3] liquid lithium films for inertial fusion reactors,[4] liquid bells employed as toxic waste incinerators[5] and modulated injected fuel films for actively controlled fuel spray formation in the combustion chambers of advanced gas turbine engines.[6]

Previous work by the authors has focused on the initial distortion and disintegration of continuously discharging films (or periodically disturbed infinite films) with relevance to the described actively controlled fuel atomization process.[7–10] In an effort to understand the dynamics of the larger fluid ligaments initially shed from the discharging continuous film, a finite length continuously stretched or compressed two-dimensional planar liquid film in a void (also referred to as liquid bridge) has been analyzed. The avoidance of considering a finite-length film with free ends allows the use of lubrication equations (previously derived by the authors) without additional modelling needs at the film ends. Those equations become invalid for a freely contracting or stretching film whose ends are characterized by a radius of curvature of the film interface that becomes as small as the film thickness.

Thin planar films in a surrounding void and subject to two-dimensional symmetric (or antisymmetric) disturbances are well known to be linearly stable.[11] However, nonlinear theory has shown that the superposition of multiple symmetric disturbances on a periodically disturbed infinite film can produce nonlinear film instability.[12,13] Furthermore, for very thin films, long-range molecular forces (acting between the two film interfaces) can also result in film instability, even by linear theory. There have been various linear and nonlinear analyses on this subject. For a detailed review the reader is referred to Ref. 11 and 14.

Previous work focused on periodically disturbed films with zero or constant "base flow" velocity. Previous analyses of finite length liquid bridges focused on cylindrical fluid columns or annular liquid/soap films rather than two-dimensional films.[15,16] The proposed analysis a

dynamically stretched or compressed planar liquid bridge has not, to the knowledge of the authors, been reported in the literature.

A brief nonlinear analysis of a contracting two-dimensional free liquid film was presented in Ref. 17. The authors described topological changes in the interface distortion with changes in Reynolds number and Weber number. The present work focuses on the interface dynamics of the stretching film for various Weber numbers, Reynolds numbers, film-thickness-to-length ratios and the acceleration period (time over which the film ends are accelerated from zero velocity to the maximum pull velocity).

In this context, it is worthwhile to note that in the spray formation application described earlier, stretching of the initially formed liquid ligaments proceeds the contraction process, the latter taking place once a sufficiently stretched ligament has ruptured.

II. GOVERNING EQUATIONS AND PROBLEM SET-UP

The governing equations within the liquid phase of an incompressible viscous planar free liquid film at zero gravity are given by:

$$\frac{\partial u}{\partial x} + \frac{\partial w}{\partial z} = 0 \tag{1}$$

$$\frac{\partial u}{\partial t} + u\frac{\partial u}{\partial x} + w\frac{\partial u}{\partial z} = -\frac{1}{\rho}\frac{\partial (p+\Phi)}{\partial x} + \nu\left(\frac{\partial^2 u}{\partial x^2} + \frac{\partial^2 u}{\partial z^2}\right) \tag{2}$$

$$\frac{\partial w}{\partial t} + u\frac{\partial w}{\partial x} + w\frac{\partial w}{\partial z} = -\frac{1}{\rho}\frac{\partial (p+\Phi)}{\partial z} + \nu\left(\frac{\partial^2 w}{\partial x^2} + \frac{\partial^2 w}{\partial z^2}\right) \tag{3}$$

where x is the direction along the film, z is the transverse direction, u and w are the respective velocity components, p is pressure, ν is kinematic viscosity, and Φ denotes the potential energy function per unit volume which accounts for the presence of long-range molecular forces and which depends on the thickness of the free film.[18,19] When the film thickness is large, the effect of the Van der Waals (long-range molecular) forces is well represented through the Navier-Stokes equations with the use of surface tension in the

interface conditions and the Φ-term is negligible. However, Φ becomes important and can even dominate film dynamics as the film thickness drops below 100–1000 Angströms.[14] The present analysis will focus on film dynamics at fairly large film thicknesses so that here, Van der Waals forces are included in the governing equations only to illustrate their potential relevance as film thinning progresses, i.e. before film rupture occurs. The majority of results presented here neglect the effects through the Φ-term of the described intermolecular forces; rather, their integrated effect appears in the continuum representation.

Boundary conditions at the film interfaces $z = h(x,t)_{\pm}$ are given by the following kinematic and dynamic conditions.

Kinematic condition:

$$w = \frac{\partial h_{\pm}}{\partial t} + u_{\pm}\frac{\partial h_{\pm}}{\partial x} \tag{4}$$

Dynamic condition:

$$\vec{\vec{\Upsilon}}_{\pm} \cdot \vec{n}_{\pm} = -\kappa_{\pm}\sigma\vec{n}_{\pm} \tag{5}$$

where $+$ and $-$ refer to the upper and lower interface, respectively. In Eq. (5), $\vec{\vec{\Upsilon}}$ denotes the stress tensor, κ represents the interface curvature and $\vec{n}$ is the outward pointing unit normal vector at the interface. Eq. (5) has a tangential and a normal component. The tangential component, i.e. the total shear stress on the interface, is identical to zero since externally imposed surface forces, as well as surface gradients of surface tension σ have been neglected here.

The stress tensor is given by

$$\vec{\vec{\Upsilon}} = \begin{bmatrix} -\mathrm{p} + 2\mu\frac{\partial u}{\partial x} \\ \mu\left(\frac{\partial u}{\partial z} + \frac{\partial w}{\partial x}\right) \\ \mu\left(\frac{\partial u}{\partial z} + \frac{\partial w}{\partial x}\right) \\ -\mathrm{p} + 2\mu\frac{\partial w}{\partial z} \end{bmatrix} \tag{6}$$

and

$$\vec{n}_{\pm} = \frac{(\mp \partial h_{\pm}/\partial x, \pm 1)}{\sqrt{1 + (\partial h_{\pm}/\partial x)^2}} \tag{7}$$

$$\kappa_{\pm} = -\vec{\nabla} \cdot \vec{n} = \pm \frac{\partial^2 h_{\pm}/\partial x^2}{[1 + (\partial h_{\pm}/\partial x)^2]^{3/2}} \tag{8}$$

Accordingly, the components of the dynamic condition Eq. (5) in the axial and transverse directions can be written as:

$$\left[1 - \left(\frac{\partial h_{\pm}}{\partial x}\right)^2\right] \left[\frac{\partial u_{\pm}}{\partial z} + \frac{\partial w_{\pm}}{\partial x}\right] - 4 \frac{\partial h_{\pm}}{\partial x} \frac{\partial u_{\pm}}{\partial x} = 0 \tag{9}$$

$$-p_{\pm} + \frac{2\mu}{e_{1\pm}} \left[e_{2\pm} \frac{\partial w_{\pm}}{\partial z} - \frac{\partial h_{\pm}}{\partial x} \left(\frac{\partial u_{\pm}}{\partial z} + \frac{\partial w_{\pm}}{\partial x}\right)\right] = \sigma \kappa_{\pm} \tag{10}$$

with $e_{1\pm} = [1 + (\partial h_{\pm}/\partial x)^2]$ and $e_{2\pm} = [1 - (\partial h_{\pm}/\partial x)^2]$. Since the film thickness is small compared to the length of the film, we employ a polynomial expansion of the dependent variables $\theta = u, w, p$, or Φ in terms of z, i.e.

$$\theta = \theta_0(x,t) + \theta_1(x,t)\, z + \theta_2(x,t)\, z^2 + \ldots \tag{11}$$

analogous to the one presented in Ref. [5] for inviscid films.

Considering zero- and first-order terms in the series expansion for u and w within the kinematic condition (4) yields,

$$\begin{aligned} w_+ &= \frac{\partial h_+}{\partial t} + u_0 \frac{\partial h_+}{\partial x} + u_1 \frac{\delta}{2} \frac{\partial h_+}{\partial x} \\ w_- &= \frac{\partial h_-}{\partial t} + u_0 \frac{\partial h_-}{\partial x} - u_1 \frac{\delta}{2} \frac{\partial h_-}{\partial x} \end{aligned} \tag{12}$$

and

$$\begin{aligned} w_+ &= w_0 + w_1 \frac{\delta}{2} \\ w_- &= w_0 - w_1 \frac{\delta}{2} \end{aligned} \tag{13}$$

where δ denotes the film thickness $\delta(x,t) = h_+ - h_-$ and $h_{\pm} = \pm\delta/2$, respectively. The summation $w_+ + w_-$ and subtraction $w_+ - w_-$ then provides

$$w_0 = u_1 \frac{\delta}{4} \frac{\partial \delta}{\partial x}$$
$$w_1 = \frac{1}{\delta} \left(\frac{\partial \delta}{\partial t} + u_0 \frac{\partial \delta}{\partial x} \right) \tag{14}$$

The leading-order approximation to the continuity equation Eq. (1) is given by

$$\frac{\partial u_0}{\partial x} + w_1 = 0 \tag{15}$$

which after consideration of Eqs. (14 yields

$$\frac{\partial \delta}{\partial t} + \frac{\partial (u_0 \delta)}{\partial x} = 0 \tag{16}$$

The lowest-order approximation to the axial ($x-$) momentum equation is obtained analogously (i.e. by replacing u, v and p by the appropriate series expansions) and is given by

$$\frac{\partial u_0}{\partial t} + u_0 \frac{\partial u_0}{\partial x} = -\frac{1}{\rho} \frac{\partial (p_0 + \Phi_0)}{\partial x} + \nu \frac{\partial^2 u_0}{\partial x^2} + 2\nu u_2 \tag{17}$$

where expressions for p_0, Φ_0 and u_2 remain to be determined (see below).

Employing a similar procedure, one obtains the lowest-order approximation to the transverse (z-) momentum equation, i.e.

$$\frac{\partial w_0}{\partial t} + u_0 \frac{\partial w_0}{\partial x} = -\frac{1}{\rho} (p_1 + \Phi_1) \tag{18}$$

Note that, the forces driving the transverse motion of the fluid are of first order (i.e. p_1 and Φ_1). Therefore, the transverse fluid motion in the considered dilational case, the transverse fluid motion can be neglected in this analysis. Nevertheless, substituting w_0 from Eqs. (14) into Eq. (18), one obtains an equation relating the first-order expansion coefficients u_1, p_1 and Φ_1.

Eqs. (16) and (17) represent the leading-order equations considered within the present analysis. In order to close the lowest-order system of equations and proceed with its (numerical) solution, p_0, Φ_0 and u_2 remain to be expressed in terms of known quantities or quantities for which governing equations are given, i.e. δ and u_0.

An approximation for u_2 is obtained by employing the second-degree polynomial expansion of u in the evaluation of $\partial^2 u/\partial z^2$. This yields $\partial^2 u/\partial z^2 = 2u_2$ or after integration from the lower to the upper interface boundaries,

$$u_2 = \frac{1}{2\delta}\left[\left(\frac{\partial u}{\partial z}\right)_+ - \left(\frac{\partial u}{\partial z}\right)_-\right] \tag{19}$$

The right-hand-side of Eq. (19) can be expressed by means of the shear-stress boundary condition Eq. (9) solved for $(\partial u/\partial z)_\pm$, i.e.

$$\left(\frac{\partial u}{\partial z}\right)_\pm = -\left(\frac{\partial w}{\partial x}\right)_\pm + 4\left[1-\left(\frac{\partial h_\pm}{\partial x}\right)^2\right]^{-1}\frac{\partial h_\pm}{\partial x}\frac{\partial u_\pm}{\partial x} \tag{20}$$

where an expression for $(\partial w/\partial x)_\pm$ is obtained by taking the derivative of Eq. (1) in $x-$direction and subsequent integration in $z-$direction. The result of this procedure yields

$$\begin{aligned}
-\left[\left(\frac{\partial w}{\partial x}\right)_+ - \left(\frac{\partial w}{\partial x}\right)_-\right] &= \int_{h_-}^{h_+}\frac{\partial^2 u}{\partial x^2}\,\mathrm{d}z = \frac{\partial}{\partial x}\int_{h_-}^{h_+}\frac{\partial u}{\partial x}\,\mathrm{d}z - \frac{\partial h_+}{\partial x}\frac{\partial u_+}{\partial x} + \frac{\partial h_-}{\partial x}\frac{\partial u_-}{\partial x} \\
&= \frac{\partial}{\partial x}\left[\frac{\partial}{\partial x}\int_{h_-}^{h_+} u\mathrm{d}z - \frac{\partial h_+}{\partial x}u_+ + \frac{\partial h_-}{\partial x}u_-\right] - \frac{\partial \delta}{\partial x}\frac{\partial \overline{u}}{\partial x} \\
&= \frac{\partial}{\partial x}\left[\frac{\partial}{\partial x}(\overline{u}\delta) - \overline{u}\frac{\partial \delta}{\partial x}\right] - \frac{\partial \delta}{\partial x}\frac{\partial \overline{u}}{\partial x} = \frac{\partial}{\partial x}\left[\delta\frac{\partial \overline{u}}{\partial x}\right] - \frac{\partial \delta}{\partial x}\frac{\partial \overline{u}}{\partial x} = \delta\frac{\partial^2 \overline{u}}{\partial x^2}
\end{aligned} \tag{21}$$

where $\overline{u} = \int_{h_-}^{h_+} u\mathrm{d}z/\delta = u_0 + \delta^2/2\,u_2 + h.o.t.$ Introducing Eq. (21) into Eq. (20) yields the integral form of the shear stress boundary condition,

$$\left[\left(\frac{\partial u}{\partial z}\right)_+ - \left(\frac{\partial u}{\partial z}\right)_-\right] = \delta\frac{\partial^2 u_0}{\partial x^2} + 4\frac{\partial \delta}{\partial x}\frac{\partial u_0}{\partial x}\left[1-\left(\frac{1}{2}\frac{\partial \delta}{\partial x}\right)^2\right]^{-1} + O(\delta^3, \delta^2\frac{\partial \delta}{\partial x}) \tag{22}$$

if only the two lowest-order terms in the expansion of u are considered. Therefore,

$$u_2 = \frac{1}{2}\frac{\partial^2 u_0}{\partial x^2} + \frac{2}{\delta}\frac{\partial \delta}{\partial x}\frac{\partial u_0}{\partial x} + O(\delta^2, \delta\frac{\partial \delta}{\partial x}) \tag{23}$$

The lowest-order approximation for the interface pressures $p_\pm$ is obtained by considering only terms up to order one in the series expansion for p, i.e.

$$p_\pm = p_0 \pm p_1\frac{\delta}{2} \tag{24}$$

This yields $p_0 = (p_+ + p_-)/2$ whereby p_+ and p_- are taken from the normal stress boundary condition Eq. (10). The result is

$$p_0 = -\frac{\sigma}{2}\frac{\partial^2\delta}{\partial x^2}\left[1+\frac{1}{4}\left(\frac{\partial\delta}{\partial x}\right)^2\right]^{-3/2} - 2\mu\frac{\partial u_0}{\partial x}\left[1+\frac{1}{2}\left(\frac{\partial\delta}{\partial x}\right)^2\left(1-\frac{1}{4}\left(\frac{\partial\delta}{\partial x}\right)^2\right)^{-1}\right] + O(\delta^2, \delta\frac{\partial\delta}{\partial x}) \tag{25}$$

where again only the two lowest-order terms in the approximation to u have been considered in Eq. (10).

Note that, when evaluating u_2 and p_0 in Eq. (17), the employed lower-order approximation to the normal stress and shear stress boundary conditions Eqs. (9) and (10) have not employed any simplifications with respect to the interface geometry; in particular, the full curvature term is retained in the evaluation of the surface tension within Eq. (10).

Using Eqs. (22) and Eq. (25), Eqs. (16) and (17) can be rewritten to obtain the leading-order equations for symmetric film distortion governing the film thickness $\delta = (h_+ - h_-)$ and the axial velocity u_0

$$\frac{\partial\delta}{\partial t} + \frac{\partial(u\delta)}{\partial x} = 0 \tag{26}$$

$$\begin{aligned}\frac{\partial u}{\partial t} + u\frac{\partial u}{\partial x} = \nu\frac{\partial^2 u}{\partial x^2}\left[4+2(f-1)\,g\right] + 4\nu\frac{1}{\delta}\frac{\partial\delta}{\partial x}\frac{\partial u}{\partial x}\,g \\ +2\nu\frac{\partial u}{\partial x}\frac{\partial\delta}{\partial x}\frac{\partial^2\delta}{\partial x^2}\,g^2 + \frac{\sigma}{2\rho}\frac{\partial^3\delta}{\partial x^3}\,f^{-3/2} \\ -\frac{3}{8}\frac{\sigma}{\rho}\frac{\partial\delta}{\partial x}\left(\frac{\partial^2\delta}{\partial x^2}\right)^2 f^{-5/2} + \frac{3A}{\rho\delta^4}\frac{\partial\delta}{\partial x}\end{aligned} \tag{27}$$

where the subscript '0' in u_0 has been omitted and

$$f = 1+\left(\frac{1}{2}\frac{\partial\delta}{\partial x}\right)^2,\; g = \left[1-\left(\frac{1}{2}\frac{\partial\delta}{\partial x}\right)^2\right]^{-1}$$

Furthermore, the last term in Eq. (27) represents $-(\partial\Phi_0/\partial x)/\rho$ where Φ_0 has been expressed by

$$\Phi_0 = A\,\delta^{-3} \tag{28}$$

according to Ref. 18, with $A = A^\circ/(6\pi)$ where A° is the Hamaker constant $A^\circ = 10^{-13}$ erg, but without an additive constant.[20,21] If the denominators in Eqs. (7 , 8) are approximated

by 1 (i.e. considering $(\partial h_{\pm}/\partial x)^2 \ll 1$), then Eqs. (26 , 27) reduce to the equations presented by Erneux and Davis in Ref. 21 for long wavelength disturbances on thin films, i.e.

$$\frac{\partial \delta}{\partial t} + \frac{\partial (u\delta)}{\partial x} = 0$$
$$\frac{\partial u}{\partial t} + u\frac{\partial u}{\partial x} = 4\nu\frac{\partial^2 u}{\partial x^2} + 4\frac{\nu}{\delta}\frac{\partial \delta}{\partial x}\frac{\partial u}{\partial x} + \frac{\sigma}{2\rho}\frac{\partial^3 \delta}{\partial x^3} + \frac{3A}{\rho\delta^4}\frac{\partial \delta}{\partial x} \tag{29}$$

Here we have a parameter 4 in the viscous term to which viscous forces inside the liquid contribute one, shear stress at the interface contributes one, and normal stress contributes two. The second term on the right-hand-side is a viscosity correction term which results from the shear stress at the interface.

In the present analysis, no approximations are made in the formulation of the interface conditions. In particular, the full curvature term is retained in Eq. (10). This "ad-hoc" assumption in an otherwise lower-order one-dimensional model follows the analyses and observations by Ruckenstein and Jain,[18] Eggers[22] and Eggers and Dupont,[23] who studied the dynamics of drop formation from cylindrical liquid jets or columns. Similar considerations were made by Mehring and Sirignano[7,8] who analyzed capillary waves on thin planar and annular free liquid films.

Eqs. (26) and (27) have been used to study the dynamic stretching of a thin liquid film subject to equal but opposite pulling velocities at both ends. Due to the symmetry, it is sufficient to analyze only one half of the film. The configuration considered within the present work is shown in Fig. 1, with the plane of symmetry located at $x = 0$. The film is assumed to be initially undisturbed with $\delta(x,0) = \delta_i$ and $u(x,0) = 0$ for $0 \le x \le l_i$ where $(2l_i)$ is the initial total length of the film. Boundary conditions in the plane of symmetry at $x = 0$ for $t \ge 0$ are given by $(\partial\delta/\partial x) = 0$ and $u = 0$. The pulling velocity $u_p(t)$ at $x = l(t) = \int_0^t u_p(t')\,dt' + l_i$ was assumed to increase smoothly from 0 to a maximum steady value U according to

$$u[l(t),t] = u_p(t) = U/2\,[1 - \cos(2\pi t/T_p)] \qquad \text{for} \qquad 0 \le t \le T_p/2 \quad \text{and}$$
$$u_p(t) = U \qquad \text{for} \qquad t > T_p/2 \tag{30}$$

The film thickness δ at the pulling end was assumed to be fixed, i.e. $\delta[l(t), t] = \delta_i$.

With the prescribed initial and boundary conditions, Eqs. (26) and (27) have been solved numerically after nondimensionalization and after introducing the following coordinate transformation:

$$\eta = \frac{x}{l(t)} \quad , \quad \tau = t \tag{31}$$

where $2\,l(t)$ denotes the instantaneous total film length.

With this change of variables, the problem becomes a fixed-boundary-value problem, which greatly simplifies its numerical analysis. Note that, with increasing film length $l(t)$, the fixed spatial resolution in η used within the subsequent numerical analysis, corresponds to a continuously decreasing resolution in x, i.e. physical space. Therefore, predictions for film lengths at breakup and time until breakup have to be considered with some caution. It is noted here that, the present work is focused on a description of film dynamics in the course of film stretching (or compression) prior to film rupture and not on an exact prediction of film length at rupture or time until film rupture.

For the non-dimensionalization, the following non-dimensional variables have been employed,

$$\delta^* = \frac{\delta}{\delta_i}\,,\; u^* = \frac{u}{U}\,,\; l^* = \frac{l}{l_i}\,,\; \tau^* = \frac{\tau}{l_i/u_c}\,,\; \zeta = \frac{\delta_i}{l_i} \tag{32}$$

where δ_i, l_i and U denote the initial film thickness, initial film length and maximum pull velocity, as introduced earlier. The capillary velocity u_c is given by $u_c = \sqrt{\sigma/(\rho\delta_i)}$. Introducing the prescribed transformation and non-dimensionalization, Eqs. (26) and (27) are given by:

$$\frac{\partial\delta^*}{\partial\tau^*} + \sqrt{We}\frac{\left[u^* - \eta u_p^*\right]}{l^*}\frac{\partial\delta^*}{\partial\eta} + \sqrt{We}\frac{\delta^*}{l^*}\frac{\partial u^*}{\partial\eta} = 0 \tag{33}$$

$$\frac{\partial u^*}{\partial\tau^*} + \sqrt{We}\frac{\left[u^* - \eta u_p^*\right]}{l^*}\frac{\partial u^*}{\partial\eta} = \tag{34}$$

$$\frac{\zeta}{l^{*2}}\,Oh\,\left[4 + 2(f^* - 1)g^*)\right]\,\frac{\partial^2 u^*}{\partial\eta^2} + \frac{4\zeta}{l^{*2}\delta^*}\,Oh\,g^*\,\frac{\partial\delta^*}{\partial\eta}\frac{\partial u^*}{\partial\eta}$$

$$+\frac{2\zeta^3}{l^{*4}} Oh\, g^{*2} \frac{\partial u^*}{\partial \eta}\frac{\partial \delta^*}{\partial \eta}\frac{\partial^2 \delta^*}{\partial \eta^2} + \frac{3A^*}{\delta^{*4} l^* \sqrt{We}}\frac{\partial \delta^*}{\partial \eta}$$

$$+\frac{\zeta^2}{2l^{*3}\sqrt{We}} f^{*-3/2}\frac{\partial^3 \delta^*}{\partial \eta^3} - \frac{3\zeta^4}{8l^{*5}\sqrt{We}} f^{*-5/2}\frac{\partial \delta^*}{\partial \eta}\left(\frac{\partial^2 \delta^*}{\partial \eta^2}\right)^2$$

with

$$f^* = 1 + \left(\frac{\zeta}{2l^*}\frac{\partial \delta^*}{\partial \eta}\right)^2 , \; g^* = \left[1 - \left(\frac{\zeta}{2l^*}\frac{\partial \delta^*}{\partial \eta}\right)^2\right]^{-1}$$

and Ohnesorge number, Weber number and nondimensional 'modified' Hamaker constant A^* given by

$$Oh = \frac{\sqrt{We}}{Re} , \; We = \frac{\rho U^2 \delta_i}{\sigma} , \; A^* = \frac{A}{\sigma \delta_i^2} \tag{35}$$

where the Reynolds number Re is defined as $Re = U\,\delta_i/\nu$.

Linear Analysis

We now consider a linear analysis of the described planar liquid film with its ends harmonically modulated 180° out of phase keeping the symmetry . The average mean axial velocity of the film is zero in this case and the average half-length is L. Therefore, here the capillary velocity $u_c = \sqrt{\sigma/\rho\delta_i}$ has been employed in order to nondimensionalize Eqs. (26) and (27).

Replacing variables δ^*, u^* and l^* (now nondimensionalized using u_c and δ_i) by their mean and fluctuating values, i.e.

$$\delta^* = 1 + \delta' \quad , \quad u^* = u' \quad , \quad l^* = L + l'$$

linearization of Eqs. (33) and (34) yields

$$\frac{\partial \delta'}{\partial \tau^*} + \frac{1}{L}\frac{\partial u'}{\partial \eta} = 0 \tag{36}$$

$$\frac{\partial u'}{\partial \tau^*} = \frac{4}{Re}\frac{1}{L^2}\frac{\partial^2 u'}{\partial \eta^2} + 3A'\frac{1}{Re^2}\frac{1}{L}\frac{\partial \delta'}{\partial \eta} + \frac{1}{2}\frac{1}{L^3}\frac{\partial^3 \delta'}{\partial \eta^3} \tag{37}$$

with $A' = A/(\rho\nu^2\delta_i)$ and now $\eta = x/L$. Note that, in contrast to the nonlinear analysis of the continuously stretched or compressed liquid bridge, the Reynolds number within this linear analysis is based on the initial (undisturbed) film thickness δ_i and the capillary velocity $u_c = \sqrt{\sigma/\rho\delta_i}$. A modal analysis of the above equations is conducted by assuming wavelike solutions of the form

$$\delta' = a \cdot e^{i(\omega\tau^* - k\eta)} \tag{38}$$

$$u' = b \cdot e^{i(\omega\tau^* - k\eta)} \tag{39}$$

$$\tag{40}$$

where ω is the non-dimensional oscillation frequency at a particular location along the film and $k = 2\pi\delta_i/\lambda$ is the wavenumber characterizing the disturbances appearing on the film.

Introducing the above equations for δ' and u' into the linear equations Eq. (36) and Eq. (37) yields the characteristic equation which determines the dependence of the disturbance wavenumbers k on the forcing frequency ω.

$$\omega^2 - i\left(\frac{4}{Re}\kappa^2\right)\omega + \frac{3A'}{Re^2}\kappa^2 - \frac{1}{2}\kappa^4 = 0 \tag{41}$$

with $\kappa = k/L$ and $\omega = \sqrt{\sigma/(\rho\delta_i^3)}\,\Omega$ where Ω denotes the dimensional forcing frequency.

In order to clearly illustrate the effects of viscosity, surface tension and intermolecular forces on the stability of the liquid film, Eq. (41) is solved for forcing frequency ω in dependence of real wavenumber κ, i.e.

$$\omega_{1,2} = \frac{1}{2}\left\{\underbrace{i\,\frac{4}{Re}\kappa^2}_{\text{viscous}} \pm i\left[\underbrace{\frac{16}{Re^2}\kappa^4}_{\text{viscous}} + \underbrace{12A^*\kappa^2}_{\text{molecular}} \quad \underbrace{-\,2\,\kappa^4}_{\text{surface tension}}\right]^{-1/2}\right\} \tag{42}$$

where $A^* = A'/Re^2 = A/(\sigma\delta_i^2)$ as already introduced earlier. In Eq. (42), the first term in curly brackets and the first term in square brackets account for viscous effects. Note that, the combined effect of both terms will always act stabilizing on the distorting film, i.e. result in real values for ω. The second and third terms on the right-hand-side of Eq. (42) account for intermolecular forces and surface tension, respectively. While the former might result in

film instability due to the production of a complex ω-value with negative imaginary part; the latter, by itself, will always produce real ω-values indicative of a stable film. While the surface tension represents the effect of intermolecular forces for larger thickness, it acts in opposite manner to the Φ-term which is intended to represent intermolecular forces in the very thin film situation. That is, when the intermolecular forces act primarily on neighboring molecules in the same surface layer as happens for thicker films, the effect is stabilizing and is well represented by the surface tension formulation. However, when the intermolecular forces act significantly upon molecules in the other surface layer of a very thin film, the effect is destabilizing and is represented through the Φ-term.

Eq. (42) show that, for $\kappa^2 < 6A^*$, ω will take only positive or negative imaginary values ω_1 and ω_2. The latter will result in an exponentially growing solution while the former will produce a solution which decays exponentially in time. Note that the unstable growth rate ω_2 will be smaller than the decay rate ω_1. For $6A^* < \kappa^2 < 6A^*/(1-8/Re^2)$, the square-root term in Eq. (42) will be positive but smaller than $4\kappa^2/Re$. In this case, Eq. (42) will produce solely exponentially decaying solutions. If $\kappa^2 > 6A^*/(1-8/Re^2)$, the square-root term in Eq. (42) will be complex and the resulting frequencies $\omega_{1,2}$ will contain an exponentially decaying part (due to viscous damping) and a travelling-wave part.

If the effect of intermolecular forces is neglected in the analysis, no film instability exists and ω has a double root at $Re = 2\sqrt{2}$, i.e. $\omega_{1,2} = 2i\kappa^2/Re$ with exponentially decaying solutions only. Exponentially decaying solutions are also found for $Re < 2\sqrt{2}$, however here the decay rates associated with each solution of ω are different. For Reynolds numbers above $2\sqrt{2}$ each solution for ω is associated with an exponentially decaying solution and a travelling-wave-type solution. Consider the linear boundary-value problem of a planar liquid film bridge (i.e., a free liquid film bounded at both ends by a solid vertical surface) with harmonic forcing of its ends at frequency ω. Here, Eq. (41) has to be solved for wavenumbers k dependent upon ω. The prescribed modulation will result in a film distortion composed of four wavenumbers since Eqs. (36) and (37) form a fourth-order system. If intermolecular forces are neglected, k_1 through k_4 are given by

$$\kappa_{1,2} = k_{1,2}/L = \pm 2\left[-i\,\omega\left(Re^{-1} - \sqrt{Re^{-2} - 1/8}\right)\right]^{1/2}$$
$$\kappa_{3,4} = k_{3,4}/L = \pm 2\left[-i\,\omega\left(Re^{-1} + \sqrt{Re^{-2} - 1/8}\right)\right]^{1/2} \qquad (43)$$

where the ' + ' or ' - ' sign relates to k_1 and k_2 or k_3 and k_4, respectively. Note that k_i ($i = 1$ through 4) are always complex. No film instability exists if intermolecular forces can be neglected. Using the four solutions obtained for wavenumbers k_i in (43), the general solution to the described linear boundary-value problem is given by:

$$\delta' = \sum_{i=1}^{4} a_i \cdot e^{i\,(\omega\tau^* - k_i\eta)} \quad , \quad u' = \sum_{i=1}^{4} b_i \cdot e^{i\,(\omega\tau^* - k_i\eta)}\,, \qquad (44)$$

where, according to Eq. (36), the eight coefficients a_i and b_i are linearly dependent on each other according to four relations

$$\frac{a_i}{b_i} = \frac{k_i}{\omega\,L} \qquad (45)$$

The remaining four unknown coefficients are determined by four boundary conditions imposed at the ends of the liquid bridge. For the present analysis, these boundary conditions have been specified as

$$u'(\tau^*, \eta = \pm L) = \pm U_0 \cos(2\pi f\,\tau^*)$$
$$\delta'(\tau^*, \eta = \pm L) = 0 \qquad (46)$$

The prescribed boundary-value problem has been solved for a variety of Reynolds numbers Re, forcing frequencies $f = \omega/(2\pi)$ and thickness-to-length ratios, i.e. L-values.

III. RESULTS

A. Linear Analysis

We now describe the analytical results obtained for the linear boundary-value problem specified in the previous section. Some figures also contain the corresponding numerical solutions obtained by using the numerical scheme employed to solve the nonlinear distortion

of a continuously stretched or compressed film discussed later. The excellent agreement between linear analytical and numerical solutions illustrates the proper implementation of the lubrication equations Eqs. (26) and (27), at least in the linear limit.

Effect of Changes in Reynolds number:

For large Reynolds numbers Re, viscous damping of the capillary waves generated by the modulation at the film ends is very small and the instantaneous envelope in the film thickness distribution is essentially uniform along the film. See Fig. 2. As the Reynolds number decreases, capillary waves are subject to viscous damping and the maximum disturbance amplitude in the film thickness is decreased and the amplitude of the instantaneous envelope in δ' along the film decreases towards the film center; see Fig. 3. As the Reynolds number is decreased further, the decay rate of the described envelope towards the film center increases. At low enough Re-values, no wave phenomena is observed. However, for the case shown in Fig. 4, information on the film modulation still reaches the film center resulting in a time-varying local extremum in δ'. Variations in δ' are smallest at the film center. At very low Reynolds numbers, information propagation is dominated by viscous effects; see Fig. 5. We observed that, whereas the overall maximum disturbance amplitude in δ' (at a particular time) decreases, its amplitude at the film center is increased. Spatial variations in δ' are moderate at very low Reynolds numbers, approaching uniform instantaneous film thickness along the film, with exception close to the film ends where $\delta' = 0$ has been enforced. For the same case, the axial velocity profile along the film is nearly linear as the velocity at the film ends reaches its maximum values (positive or negative).

Effect of Changes in Thickness-to-Length Ratio $1/L$:

Comparison amongst Figs. 3, 4, 5 and Figs. 6, 7, 8 illustrates that, the characteristics of film topology and film dynamics (including instantaneous maximum disturbance amplitudes) at the film ends do not change with decreasing film thickness-to-length ratio. However, at larger L-values the decay rate of the envelope in δ' along the film towards the film center is

increased so that the center region remains essentially undisturbed. For very larger L-values, decay rates of the envelope in the film thickness disturbance do not change significantly with changes in L. This can be observed by comparing Fig. 7 and 9, for example.

Effect of Changes in Forcing Frequency f:

Changes in film distortion characteristics with increases in modulation frequency f (at constant Re- and L-values), such as those observed in Figs. 4 and 10 or Figs. 5 and 11, resemble those observed for the similar case but larger L-value if results are plotted over an axial coordinate normalized by the nondimensional film length L. See Figs. 10 and 7 or Figs. 11 and 8. Note however that maximum thickness disturbances are significantly smaller for the case with increased forcing frequency. Also, recall that maximum disturbance amplitudes did not notably change with changes in the thickness-to-length ratio (i.e. $1/L$-value) of the film.

B. Nonlinear Analysis

The nonlinear analysis has focused on films which are continuously stretched or compressed at their ends. Numerical solutions of the nondimensional nonlinear evolution equations were obtained explicitly by employing central differencing for the spatial derivatives in combination with one-sided spatial differencing for the evaluation of the highest-order spatial derivative at the pulling end. Time step $\Delta\tau^*$ and mesh size $\Delta\eta$ were fixed throughout each simulation and have been chosen in order to guarantee stability of the numerical solution and in order to provide an accurate prediction of film topology and film dynamics in the course of film stretching. The latter has been demonstrated by comparison with results using reduced time-steps and/or mesh sizes. It is noted here once more that, predictions of film break-up length and break-up time for significantly stretched films have to be considered with some caution due to the deteriorating spatial resolution resulting from the transformation of the stretching-film problem to a fixed boundary-value problem. Figs. 12 through 17 illustrate

results for various combinations of Reynolds number Re and Weber number We at fixed thickness-to-length ratio ζ and constant T_p-value, i.e. $\zeta = 0.1$ and $T_p = 1$, respectively.

Figs. 12 and 13 show the variation of film thickness and axial film velocity with time for the case with $We = 1$ and $Re = 100$. Note that $We = 1$ implies that the maximum pulling velocity U equals the capillary wave velocity $u_c = \sqrt{\sigma/(\rho\delta_i)}$. Precisely, u_c represents the capillary wave speed for sinuous mode waves and not dilational waves as considered here; the latter have been shown to be dispersive with wave velocity inversely proportional to wavelength. For dilational waves of wavelength greater than $2\pi\delta_i$, the wave speed is less than u_c.[7] The nondimensional length $l_b^* = l_b/l_i$ at which the film ruptures is 2.42, with rupture occuring after nondimensional time $\tau_b^* = \tau_b/(l_i/U) = 1.92$. In this analysis, film rupture is assumed to take place if the value of the film thickness δ reaches zero or drops below zero value locally.

From Fig. 12, we observe the formation of a liquid wedge at the pulling end. Also, capillary waves initially generated at the pulling end propagate into the film leading to an absolute maximum in the film thickness at $\eta = x/l = 0$ before and at the time of film break-up. For the same case as shown in Fig. 12, Fig. 13 illustrates the formation of a singularity in the axial velocity at the point of film rupture, the latter being located close to the pulling end dividing the film into a wedge-shaped region and a stretched film region.

Fig. 14 shows the similar case as in Fig. 12 but with a decrease in Weber number from $We = 1$ to 0.01 (at fixed Reynolds number). Since $We = (\rho U^2\delta_i)/\sigma = U^2/u_c^2$, where u_c denotes the capillary velocity, the lower Weber number indicates that the pulling velocity is significantly smaller than the velocity at which the longer wavelength dilational capillary waves propagate along the film. Accordingly, the time scale for the exchange of information along the liquid film is significantly smaller than the time scale associated with the generation of film disturbances due to the accelerating film. Consequently, a distinct liquid wedge at the pulling end is no longer formed. As the film stretches over a longer period of time without rupture, the film thickness at $\eta = 0$ continuously decreases at later times and its maximum value is reached at the pulling end. The overall film length at breakup is increased,

i.e. $l_b^* = 4.36$ with film rupture taking place at a significantly later time $\tau_b^* = 35.75$ than for the case shown in Figs. 12 and 13.

Fig. 15 displays numerical results obtained for the case with $Re = 100$ and $We = 100$. In this case, the maximum pulling velocity is significantly larger than the capillary wave speed. Accordingly, the effects of film thinning by film stretching are not communicated fast enough towards the film center such that, at the point of film rupture, the center of the film remains essentially undisturbed with film thickness $\delta^*(\eta = 0, \tau_b^*)$ close to 1. Due to the significant increase in stretching/pulling velocity, the film breaks very early after only $\tau_b^* = 0.79$. However, due to the large value of U the film has already stretched significantly at the time of rupture, i.e. $l_b^* = 3.98$. Note that this value is larger than the one predicted for the case with decreased Weber number, whereas the opposite is true for the observed break-up time τ_b^*. Fig. 15 illustrates that an increase in maximum pulling velocity also results in a narrower film wedge (both in the transformed and the original spatial coordinates), i.e. thinner thickness boundary-layer at the pulling end, and film breakup closer to the pulling end. It is also interesting to note that for the case shown in Fig. 15, a singular behavior in the axial velocity at the point of film rupture is no longer observed (not illustrated). Notable differences between the results illustrated in Fig. 15 and the similar case with long-range molecular forces considered, only appeared for film thicknesses below $\delta^* = 0.01$.

Fig. 16 illustrates a case for small Weber number and Reynolds number, i.e. $We = 0.01$ and $Re = 1$. This can reflect a hundred-fold decrease in velocity from the case of Fig. 15. Comparison with Fig. 14 shows that break-up time and film length at rupture increase as the Reynolds number is decreased from 100 to 1 (i.e. $l_b^* = 16.8$ at $\tau_b^* = 162.64$). The break-up time and length are also much greater here than for the case of Fig. 15. A long thin liquid filament or band of "uniform" thickness is formed with a film wedge located at the pulling end. Filament pinching occurs at its transition into the film wedge. Furthermore, in comparison to the case shown in Fig. 12 and Fig. 13, the amplitude of the velocity singularity which is forming at the pinch-point is greatly reduced.

The influence of a reduction in Reynolds number from Re = 100 to 1 for a larger Weber

number case, i.e. We = 100, can be observed by comparing Fig. 15 and Fig. 17. For the larger Re number case in Fig. 15, information is propagated into the film mainly due to capillary waves, however, since the pulling velocity in this case is significantly larger than the capillary wave velocity, the center of the film at $\eta = 0$ remained virtually undisturbed by the pulling of its ends. On the other hand, for the same value of Weber number but smaller Reynolds number, propagation of information from the pulling end into the film is greatly determined by viscous diffusion. Consequently, the film thickness in Fig. 17 has a local maximum at the centerline whose value continuously decreases as time progresses. At the same time, film length at breakup and breakup time (i.e. $l_b^* = 3.77$ and $\tau_b^* = 0.77$) remain close to the values predicted for the larger Reynolds number case of Fig. 15. This result, and the observation that the thickness boundary layer in Fig. 17 at the pulling end is slightly smaller than that displayed in Fig. 15, shows that viscous diffusion results in a more uniform film thickness in the stretched film region outside of the thickness boundary-layer, i.e. away from the film wedge at the pulling end. Also, whereas for the smaller Reynolds number case film thickness is more uniform away from the thickness boundary layer, film pinching in the vicinity of the liquid wedge is more pronounced than for the corresponding larger Reynolds number case at the same time (e.g. $\tau^* = 0.7$). In other words, the local minimum in film thickness at the transition from film wedge to the outer stretched-film region is more distinct in Fig. 17 than in Fig. 15. In fact, for the larger Reynolds number case film distortion might be characterized as 'film tearing' rather than 'film pinching.'

Comparison of Fig. 17 with Fig. 16 also illustrates that for small Reynolds numbers, an increase in Weber number results in a decrease in the size of the film thickness boundary-layer. Note that such a layer was not observed for the case in Fig. 14 with smaller viscous diffusion in comparison to the case of Fig. 16. This indicates, of course, that viscous diffusion not only serves the propagation of information, but it also is effective in damping wave amplitudes (via viscous dissipation) and in delaying film rupture, the latter occuring at $\tau_b^* = 35.75$ and $l_b^* = 4.36$ in Fig. 14, whereas $\tau_b^* = 16.80$ and $\tau_b^* = 162.64$ for the case in Fig. 16.

Fig. 18 illustrates a case with $Re = 1$ and $We = 1$. Analogous to the similar case with larger Weber number shown in Fig. 17, a distinct maximum in the film thickness develops at the film center with its maximum value continuously decreasing. However, the stabilizing effect of surface tension prevents film rupture in the lower Weber number case so that film stretching progresses over a much longer time-period resulting in more significant film stretching before film rupture ($l_b^* = 8.63, \tau_b^* = 8.13$). In this context, the results of Fig. 18 for $We = 1$ resemble those of Fig. 16 for $We = 0.01$ (both for $Re = 1$), even though in the latter case the film stretches over a longer distance resulting in a nearly uniform very thin film region near the film center.

Comparison of Figs. 12, 18 and 19 illustrates the effect of changes in Reynolds number at low Weber number (i.e. $We = 1$). As the Reynolds number is decreased from $Re = 100$ to 1, capillary waves are damped by viscous action, film rupture is delayed and film stretching is enhanced. Fig. 19 shows that for a very viscous film (i.e. very small Re-values), the film thickness essentially decreases uniformly over the entire film as film stretching progresses. Film rupture eventually occurs in the immediate vicinity of the pulling ends where $\delta^* = 1$ is enforced. The prescribed observation has also been made for the case of a compressed highly viscous film (see below). It remains to be noted that, break-up length and time for the case shown in Fig. 19 (i.e., $l_b^* = 5.52$ and $\tau_b^* = 5.22$) are not very different from those observed for the case shown in Fig. 18.

Effect of Changes in ζ or T_p

The various cases discussed in the previous section have been analyzed with respect to changes in thickness-to-length ratio of the film ζ as well as with respect to changes in the time interval T_p over which the films ends are accelerated from zero velocity to the maximum pull velocity U, in particular, ζ was decreased from 0.1 to 0.01 and T_p was increased from 1 to 10, respectively. Note that, a smaller ζ value corresponds to a longer film assuming the film thickness is kept constant.

Figs. 20 through 24 illustrate instantaneous film thickness distributions for the various

cases (characterized by We and Re values) near the time of film rupture. Solid lines represent results for the "base" cases discussed earlier, dashed and dot-dashed lines denote the results for the corresponding cases (i.e., with same We- and Re-values) but with decreased ζ-value or increased T_p-value, respectively. Fig. 23 contains an additional result for the case of $\zeta = 0.025$. Note that the results are plotted versus x/l_i so that for direct comparison between the $\zeta = 0.1$ results (solid and dash-dotted lines) and the $\zeta = 0.01$ result (dashed lines), the latter has to be stretched by a factor of ten to give the dimensional length comparison, assuming that the film thickness is the same in all three cases. Also, the characteristic time used in the nondimensionalization is $\tau_{ref} = l_i/u_c$. This implies that, for direct comparison between the $\zeta = 0.01$ and the $\zeta = 0.1$ results in one particular figure, the time associated with the $\zeta = 0.01$ result has to be multiplied by a factor of ten to yield the same dimensional time, again assuming the initial film thickness is the same in all 3 cases.

The figures illustrate that, for a particular combination of We and Re, nondimensional film length, i.e. l/l_i at the point of rupture is significantly smaller for the $\zeta = 0.01$ case. That is, the initially thinner sheet requires a smaller fractional increase in length in order to break. However, dimensional time until break-up and dimensional break-up length will be significantly larger for the lower ζ-value. Recall in this context, that $\tau_{ref} = l_i/u_c$. The prescribed observation is particularly obvious in Figs. 20 and 22 through 24. For $\zeta = 0.01$ with Re =100 and We = 1 or 100 (Figs. 20 and 22), the center region of the film remains essentially undisturbed throughout the simulation. However, for small Weber numbers (i.e. We=0.01 at Re = 1 or 100), capillary waves from one end of the film are able to reach the film center prior to film rupture resulting in a disturbed film center region. (See Figs. 21 and 23.) The similar observation is made for smaller Reynolds numbers but larger Weber numbers (i.e. Re=1 at We = 100). Here, the viscous forces cause the film thickness to decrease in the center region even for the smaller ζ-value case.

If the acceleration of the film ends is reduced by increasing T_p from 1 to 10, the films stretch further before rupture occurs. This is particularly obvious from Figs. 20, 22 and 24. As the films are stretched over a longer time interval (prior to rupture), the film thickness in

the film center region will be significantly smaller at the time of film rupture (in comparison to the similar cases but smaller T_p value). See Figs. 20, 22, 24. The prescribed observation is less pronounced in the low Weber number, low Reynolds number case, where the film stretches significantly even in the $T_p = 1$, $\zeta = 0.1$ "base" case. Due to the delay in film rupture the maximum film thickness in the film center at the time of rupture will be smaller for larger T_p value. However, due to the decreased film acceleration in this case, the film thickness in the film center region at a given nondimensional time will be larger for smaller T_p values. See Fig. 21 in this context.

Table 1 summarizes the various parameter configurations analyzed within the present study including predictions of break-up length l_b^*, break-up time τ_b^*/ζ and film thickness in the film center at the time of film rupture $\delta^*(\tau_b^*, \eta = 0)$ for the various cases. Note that, τ_b^*/ζ is proportional to the dimensional break-up time and $\delta^*(\tau_b^*, \eta = 0)$ indicates the extent to which the propagation of disturbances towards the center has proceeded at the time of film rupture.

Film Compression

In order to illustrate how the dynamics of a planar film bridge can relate to the dynamics of a free planar film, the present analysis was extended to include negative film end-velocities, effectively leading to film compression. Fig. 25a illustrates a film compression case with velocity boundary conditions according to Eq. (30) but with $-U/2$ instead of $U/2$. The Weber number and Reynolds numbers in this case were 1 and 100, respectively. A fluid blob (i.e. a liquid cylinder) forms at the compression end(s) with capillary waves proceeding the cylinder and propagating towards the film center. Figure 25b shows the predictions obtained for the similar case but Re = 1 instead of 100. Here, a liquid rim is still formed at the film ends. Due to increased viscous damping, however, no capillary waves proceed the rim. As the Reynolds number is further decreased, information from the film ends is rapidly propagated to the film center via viscous forces. Consequently, the film thickness increases more or less uniformly across the entire film except near the film ends due to the prescribed

boundary condition $\delta * (\tau^*) = 1$.

Figures 26a-c illustrate computational results presented by Brenner and Gueyffier[17] for a freely contracting film and for Weber numbers and Reynolds numbers comparable to those shown in Figs. 25a-c, respectively. The observations made in Ref. 17 for the freely contracting film are essentially the same as those described earlier for the compressed film bridge.

Neglect of Intermolecular Force Term

Figure 27 illustrates results for the same case as in Fig. 12 but with the effect on intermolecular forces (modelled via the potential Φ) neglected. Comparison between Figs. 12 and 27 shows that omission of the destabilizing effect of long-range intermolecular forces can prevent film rupture and produce non-physical global flow features, such as the continuous shedding of smaller ligaments from the pulling end. The ligament shedding has not been observed for any of the other cases discussed in this work. However, it illustrates that the consideration of a continuum model alone for the analysis of film rupture can produce misleading results.

IV. CONCLUDING REMARKS

The dynamic stretching (and compression) of a thin viscous liquid film in a void has been analyzed by means of reduced-dimension or lubrication approach. The numerical implementation of the nonlinear governing equations has been validated for the linear limit by comparison with analytical linear results for a film bridge with harmonic modulations of the axial film-end velocities. Nonlinear solutions for the continuously stretching film have been presented for various Weber number and Reynolds number combinations, for two different initial film-thickness-to-film-length ratios and at two different acceleration conditions for the film ends. Consistent results are found from both the linear and nonlinear analyses. The importance of the film stretching rate in comparison to either the capillary wave velocity or the characteristic viscous velocity has been demonstrated. If the stretching rate is large, the distortion signals are slow in reaching large distances from the forced end; so distortion

is confined to a smaller portion of the sheet. For small stretching rates, the distortion is significant over a larger portion of the film.

For films with an initial length-to-thickness ratio of $O(10)$ and with a time-scale for film-end acceleration (from zero to maximum pull velocity) comparable to the propagation time of capillary waves from film end through film center, various distinct film topologies were observed, depending on Weber number and Reynolds number. For cases with length-to-thickness ratio of $O(100)$ information on the acceleration of the film ends does not reach the film center region. Here, evolution of film topology is similar for all the considered Weber number and Reynolds number combinations; with a more or less undisturbed film center region smoothly transitioning into a narrow liquid wedge at the pulling end. For cases with low film-end acceleration, film rupture is significantly delayed resulting (in all the considered cases) in a significantly stretched film prior to rupture with or without significant amounts of fluid remaining in the film center region.

Nonlinear film distortion has also been investigated for the continuously compressed planar film bridge, illustrating the relevance of the film bridge analysis for the contracting and stretching of a free planar film such as those found in the atomization process of liquid fuels in typical gas turbine combustors.

ACKNOWLEDGMENT

This research has been supported by the U.S. Army Research Office through Grant No. DAAD19–99–1–0204 with Dr. David Mann as the program manager. The authors would also like to thank Professor Michael Brenner for permission to reprint Fig. 26.

REFERENCES

[a] Present address: Department of Mechanical and Aerospace Engineering, 3101 Engineering Gateway, University of California, Irvine, CA 92697.

[1] Codex Leicester, 1506-1510.

[2] D.L. Chubb, F.D. Calfo, M.W. McConley, M.S. McMaster, and A.A. Afjeh, "Geometry of thin liquid sheet flows," *AIAA J.* **32**, 6, 1325 (1993).

[3] S.G. Bankoff, M.J. Miksis, and H. Kim, "Control of flowing liquid films by electrostatic fields in space," *3rd Microgravity Fluid Physics Conference*, NASA Lewis Research Center, Cleveland, OH, CP3338, pp. 701-710, 1996.

[4] J.A. Maniscalco, W.R. Meier, M.J. Monsler, "Conceptual design of a laser fusion power-plant," UCRL-79652, Lawrence Livermore Laboratory, 1997.

[5] J.I. Ramos, "Inviscid, slender, annular liquid jets," *Chem. Eng. Sci.* **51**, 6, 981 (1996).

[6] W.D. Bachalo, "Spray diagnostics for the twenty-first century," *Atom. Sprays* **10**, 439 (2000).

[7] C. Mehring, and W.A. Sirignano, "Nonlinear capillary wave distortion and disintegration of thin planar liquid sheets," *J. Fluid Mech.* **388**, 69 (1999).

[8] C. Mehring, and W.A. Sirignano, "Axisymmetric capillary waves on thin annular liquid sheets. Part I: Temporal stability," *Phys. Fluids* **12**, 1417 (1999).

[9] C. Mehring, and W.A. Sirignano, "Axisymmetric capillary waves on thin annular liquid sheets. Part II: Spatial development," *Phys. Fluids* **12**, 1440 (1999).

[10] C. Mehring, and W.A. Sirignano, "Disintegration of Planar Liquid Film Impacted by Two-Dimensional Gas Jets," *Phys. Fluids*, in press.

[11] W.A. Sirignano, and C. Mehring, " Review of theory of distortion and disintegration of liquid streams", *Progr. Eng. and Comb. Science* **26**, 609 (2000).

[12] K. Matsuuchi, "Modulational instability of nonline2yyar capillary waves on thin liquid sheets," *J. Phys. Soc. Japan* **37**, 6, 1680 (1974).

[13] K. Matsuuchi, "Instability of thin liquid sheet and its break-up," *J. Phys. Soc. Japan* **41**, 4, 1410 (1976).

[14] A. Oron, S.H. Davis, and S.G. Bankoff, "Long-scale evolution of thin liquid films," *Rev. Mod. Phys.* **69**, 3, 931(1997).

[15] I. Martinez, and J.M. Perales, "Mechanical behavior of liquid bridges in microgravity," *Physics of Fluids in Microgravity*, (ed.) R. Monti, Taylor & Francis, pp. 21-45.

[16] Y.-J. Chen, and P.H. Steen, "Dynamics of inviscid capillary breakup: collapse and pinchoff of a film bridge," *J. Fluid Mech.* **341**, 245 (1997).

[17] M.P. Brenner, and D. Gueyffier, "On the bursting of viscous films," *Phys. Fluids* **11**, 3, 737 (1999).

[18] E. Ruckenstein, and R.K. Jain, "Spontaneous rupture of thin liquid films," *Chem. Soc. Faraday Trans.* **270**,132 (1974).

[19] A. Sharma, C.S. Kishore, and S. Salaniwai, "Nonlinear stability and rupture of ultrathin free films," *Phys. Fluids* **7**, 8, 1832 (1995).

[20] M.B. Williams, and S.H. Davis, "Nonlinear theory of film rupture," *J. Col. Intf. Sci.* **90**, 1, 220 (1982).

[21] T. Erneux, and H. Davis, "Nonlinear rupture of free films," *Phys. Fluids A* **5**, 5, 1117 (1993).

[22] J. Eggers, "Nonlinear dynamics and breakup of free-surface flows," *Rev. Mod. Phys* **69**, 3, 865 (1997).

[23] J. Eggers, and T.F. Dupont, "Drop formation in a one-dimensional approximation of the Navier-Stokes equation," *J. Fluid Mech.* **262**, 205 (1994).

Tables

We	Re	ζ	T_p	l_b^*	τ_b^*/ζ	$\delta^*(\tau_b^*, \eta = 0)$	Figure No.
1	100	0.1	1	2.42	19.2	1.25	12, 20 (solid)
1	100	0.01	1	1.52	102	1	20 (dashed)
1	100	0.1	10	6.45	104.4	0.44	20 (dash-dotted)
100	100	0.1	1	3.98	7.9	0.98	15, 22 (solid)
100	100	0.01	1	2.04	53	1	22 (dashed)
100	100	0.1	10	12.32	54.2	0.68	22 (dash-dotted)
0.01	1	0.1	1	16.80	1626.4	0.01	16, 23 (solid)
0.01	1	0.025	1	6.14	2074.4	0.35	23 (dot-dot-dashed)
0.01	1	0.01	1	3.03	2080	1.14	23 (dashed)
0.01	1	0.1	10	16.31	1628.1	0.02	23 (dash-dotted)
0.01	100	0.1	1	4.36	357.5	0.03	14, 21 (solid)
0.01	100	0.01	1	1.50	552	1.07	21 (dashed)
0.01	100	0.1	10	4.11	373.8	0.08	21 (dash-dotted)
100	1	0.1	1	3.77	7.7	0.49	17, 24 (solid)
100	1	0.01	1	2.08	53	0.96	24 (dashed)
100	1	0.1	10	7.65	44.7	0.22	24 (dash-dotted)
1	1	0.1	1	8.63	81.3	0.29	18
1	0.01	0.1	1	5.52	52.2	0.17	19
1	100	0.01	5	0.83	176	1	26 (a)
1	1	0.01	5	0.70	215	1	26 (b)
1	0.01	0.01	5	0.56	247	1.65	26 (c)

Table 1: Summary of parameter survey including results for nondimensional values of break-up length l_b^*, break-up time τ_b^*/ζ and film thicknes at the film center during film rupture $\delta^*(\tau_b^*, \eta = 0)$.

Figure captions

Figure 1: Schematic of investigated free stretching film configuration ($h = \delta$).

Figure 2: Solid: Linear analytical solution for $U_0 = 0.01, Re = 100, f = 0.1, L = 10$. Dashed: Numerical solution for the same case.

Figure 3: Solid: Linear analytical solution for $U_0 = 0.01, Re = 10, f = 0.1, L = 10$. Dashed: Numerical solution for the same case.

Figure 4: Solid: Linear analytical solution for $U_0 = 0.01, Re = 1, f = 0.1, L = 10$. Dashed: Numerical solution for the same case.

Figure 5: Linear analytical solution for $U_0 = 0.01, Re = 0.2, f = 0.1, L = 10$.

Figure 6: Linear analytical solution for $U_0 = 0.01, Re = 10, f = 0.1, L = 100$.

Figure 7: Linear analytical solution for $U_0 = 0.01, Re = 1, f = 0.1, L = 100$.

Figure 8: Linear analytical solution for $U_0 = 0.01, Re = 0.2, f = 0.1, L = 100$.

Figure 9: Linear analytical solution for $U_0 = 0.01, Re = 1, f = 0.1, L = 250$.

Figure 10: Linear analytical solution for $U_0 = 0.01, Re = 1, f = 0.5, L = 10$.

Figure 11: Linear analytical solution for $U_0 = 0.01, Re = 0.2, f = 0.5, L = 10$.

Figure 12: Film thickness δ^* as a function of time τ^* and normalized spatial coordinate η for $We = 1$ and $Re = 100$ $[l_b^* = 2.42, \tau_b^* = 1.92]$.

Figure 13: Axial film velocity u^* as a function of time τ^* and normalized spatial coordinate η for $We = 1$ and $Re = 100$ $[l_b^* = 2.42, \tau_b^* = 1.92]$.

Figure 14: Film thickness δ^* as a function of time τ^* and normalized spatial coordinate η for $We = 0.01$ and $Re = 100$ $[l_b^* = 4.36, \tau_b^* = 35.75]$.

Figure 15: Film thickness δ^* as a function of time τ^* and normalized spatial coordinate η for $We = 100$ and $Re = 100$ [$l_b^* = 3.98$, $\tau_b^* = 0.79$].

Figure 16: Film thickness δ^* as a function of time τ^* and normalized spatial coordinate η for $We = 0.01$ and $Re = 1$ [$l_b^* = 16.80$, $\tau_b^* = 162.64$].

Figure 17: Film thickness δ^* as a function of time τ^* and normalized spatial coordinate η for $We = 100$ and $Re = 1$ [$l_b^* = 3.77$, $\tau_b^* = 0.77$].

Figure 18: Film thickness δ^* as a function of time τ^* and normalized spatial coordinate η for $We = 1$ and $Re = 1$ [$l_b^* = 8.63$, $\tau_b^* = 8.13$].

Figure 19: Film thickness δ^* as a function of time τ^* and normalized spatial coordinate η for $We = 1$ and $Re = 0.01$ [$l_b^* = 5.52$, $\tau_b^* = 5.22$].

Figure 20: Film thickness δ^* at various times τ^* plotted versus normalized spatial coordinate x/l_i for $We = 1$ and $Re = 100$. Solid: δ_i/l_i=0.1, $T_p = 1$, dashed: δ_i/l_i=0.01, $T_p = 1$, dash-dotted: δ_i/l_i=0.1, $T_p = 10$.

Figure 21: Film thickness δ^* at various times τ^* plotted versus normalized spatial coordinate x/l_i for $We = 0.01$ and $Re = 100$. Solid: δ_i/l_i=0.1, $T_p = 1$, dashed: δ_i/l_i=0.01, $T_p = 1$, dash-dotted: δ_i/l_i=0.1, $T_p = 10$,

Figure 22: Film thickness δ^* at various times τ^* plotted versus normalized spatial coordinate x/l_i for $We = 100$ and $Re = 100$. Solid: δ_i/l_i=0.1, $T_p = 1$, dashed: δ_i/l_i=0.01, $T_p = 1$, dash-dotted: δ_i/l_i=0.1, $T_p = 10$.

Figure 23: Film thickness δ^* at various times τ^* plotted versus normalized spatial coordinate x/l_i for $We = 0.01$ and $Re = 1$. Solid: δ_i/l_i=0.1, $T_p = 1$, dashed: δ_i/l_i=0.01, $T_p = 1$, dash-dotted: δ_i/l_i=0.1, $T_p = 10$, dash-dot-dotted: δ_i/l_i=0.025, $T_p = 1$.

Figure 24: Film thickness δ^* at various times τ^* plotted versus normalized spatial coordinate x/l_i for $We = 100$ and $Re = 1$. Solid: δ_i/l_i=0.1, $T_p = 1$, dashed: δ_i/l_i=0.01, $T_p = 1$,

dash-dotted: δ_i/l_i=0.1, $T_p = 10$,

Figure 25: Film compression for $We = 1$ and $Re = 100$ (a), 1 (b) and 0.01 (c).

Figure 26: Film compression for $We = 1, Re = 1$. Results presented in Ref. 17 for contracting free planar liquid film and Weber and Reynolds numbers comparable to those presented in Fig. 25.

Figure 27: Film thickness δ^* as a function of time τ^* and normalized spatial coordinate η for $We = 1$ and $Re = 100$ and without the consideration of intermolecular forces, i.e. $A^* = 0$.

FIGURES

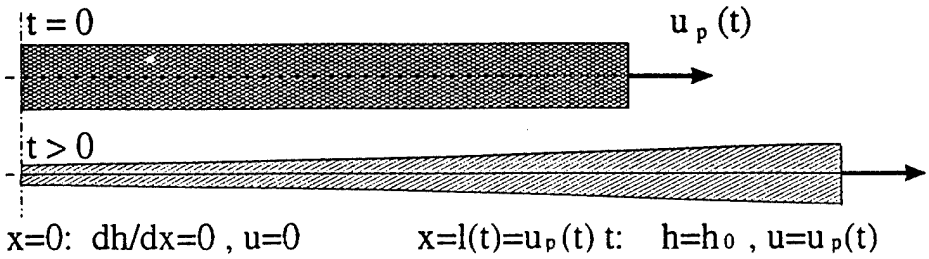

FIG. 1. Mehring, Phys. Fluids

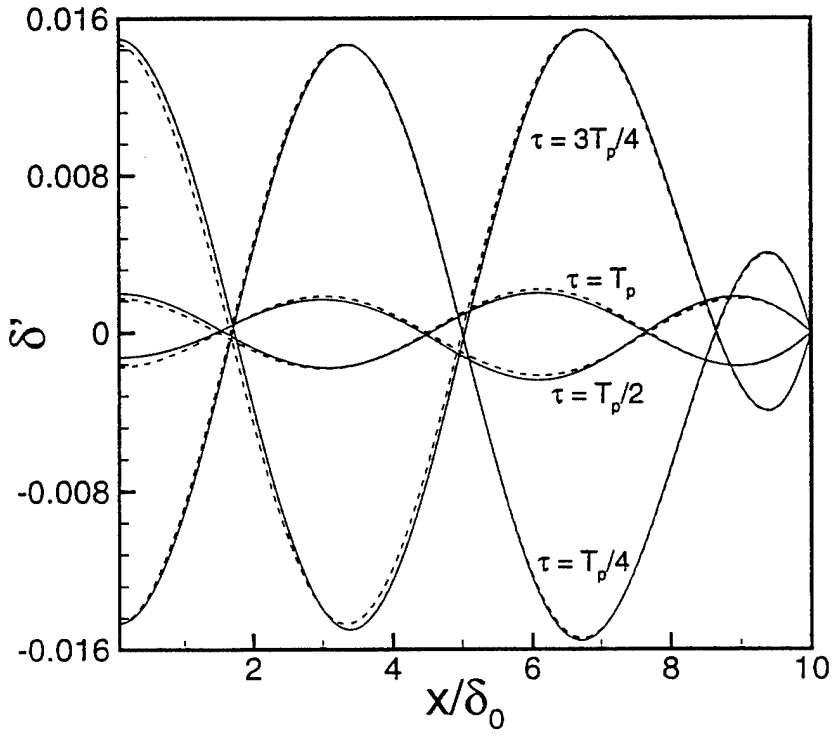

FIG. 2. Mehring, Phys. Fluids

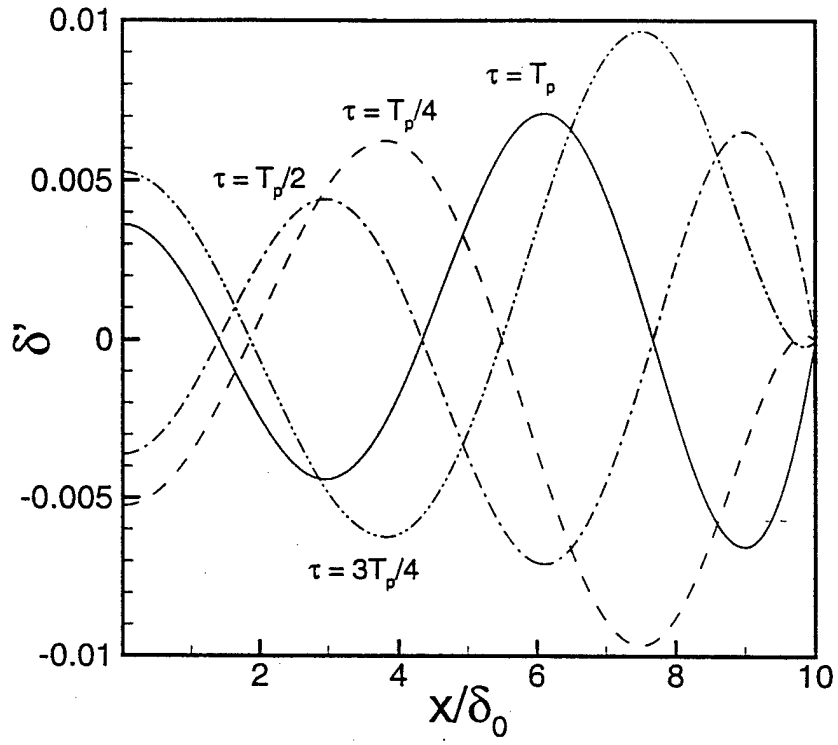

FIG. 3. Mehring, Phys. Fluids

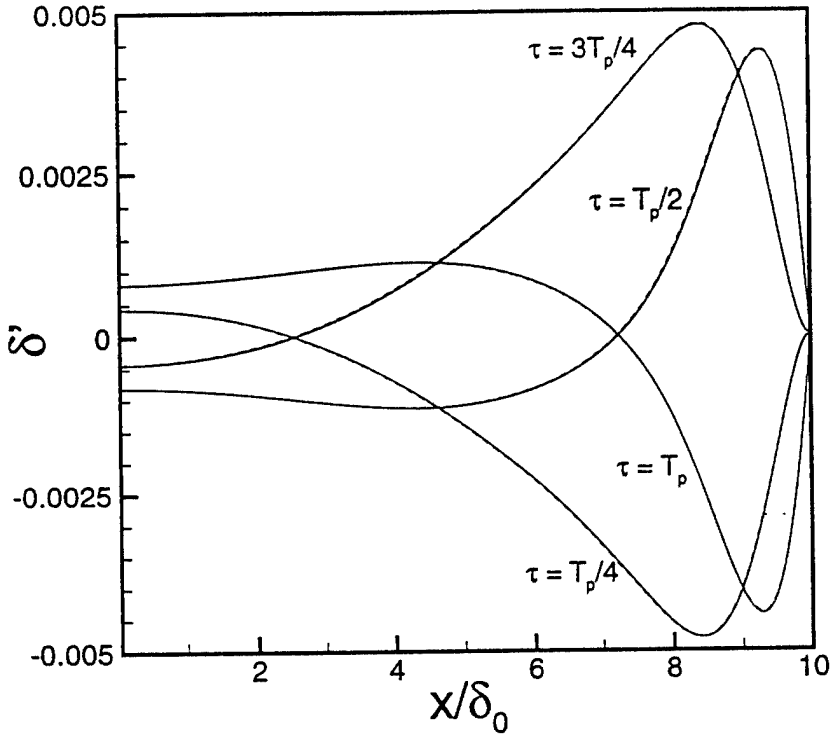

FIG. 4. Mehring, Phys. Fluids

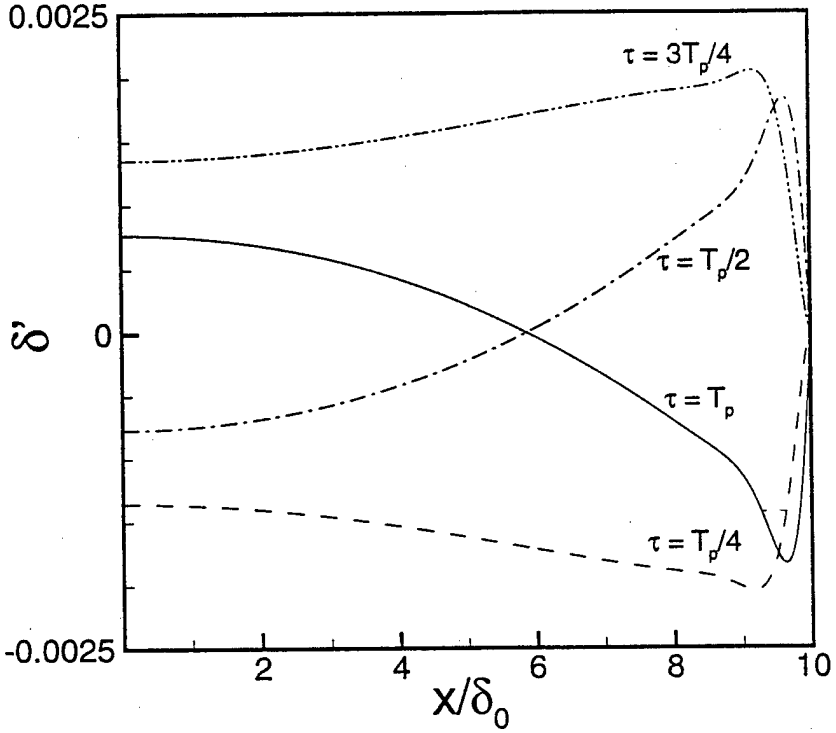

FIG. 5. Mehring, Phys. Fluids

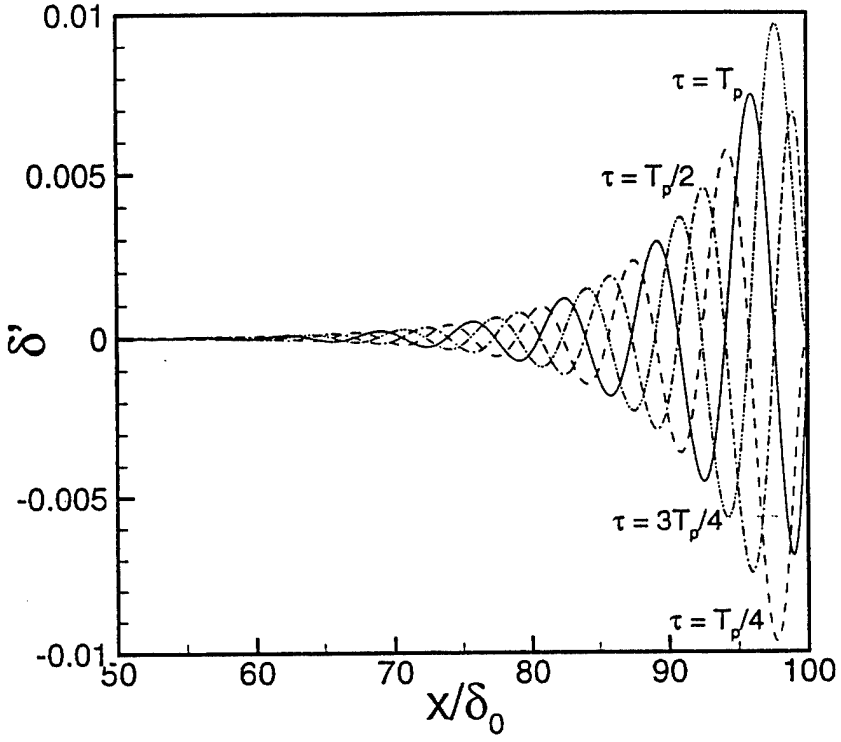

FIG. 6. Mehring, Phys. Fluids

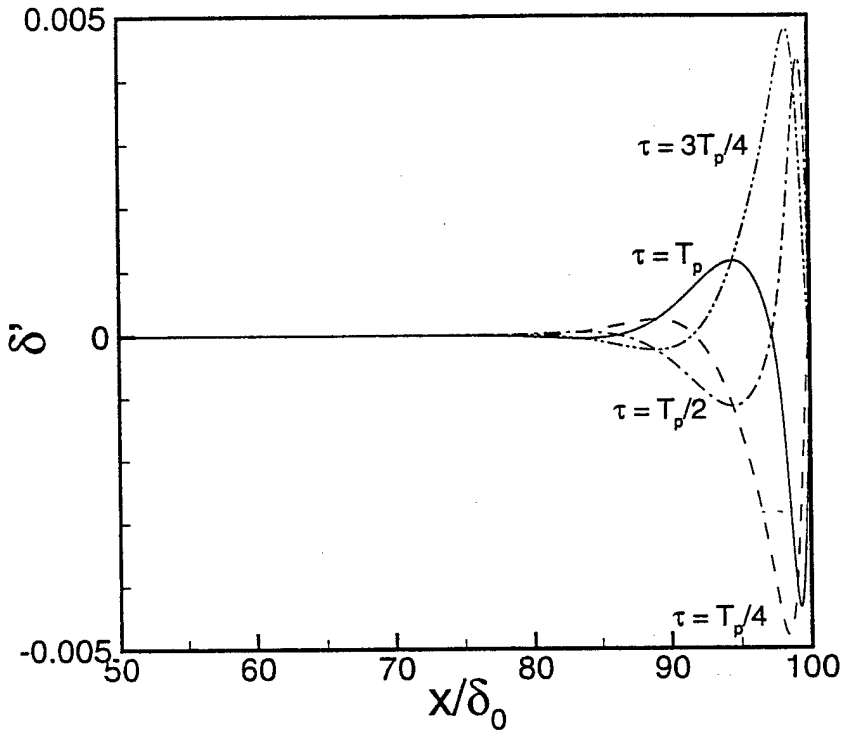

FIG. 7. Mehring, Phys. Fluids

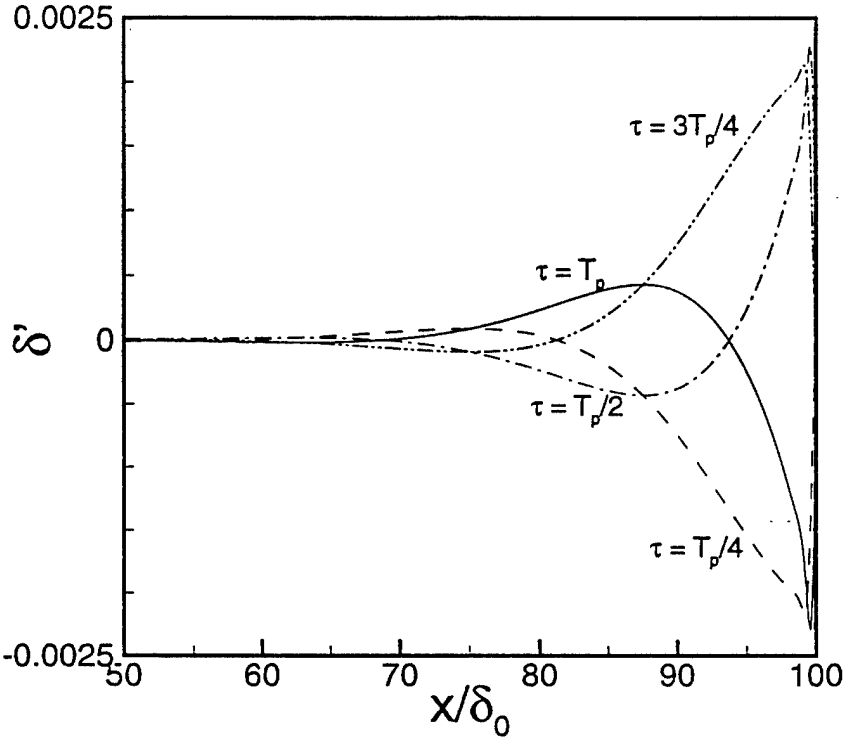

FIG. 8. Mehring, Phys. Fluids

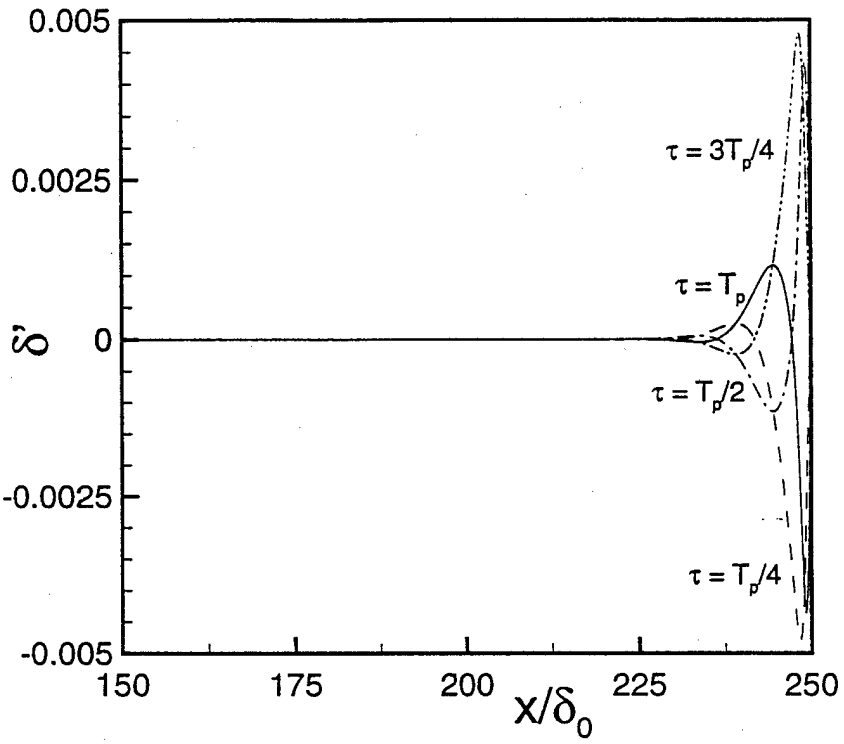

FIG. 9. Mehring, Phys. Fluids

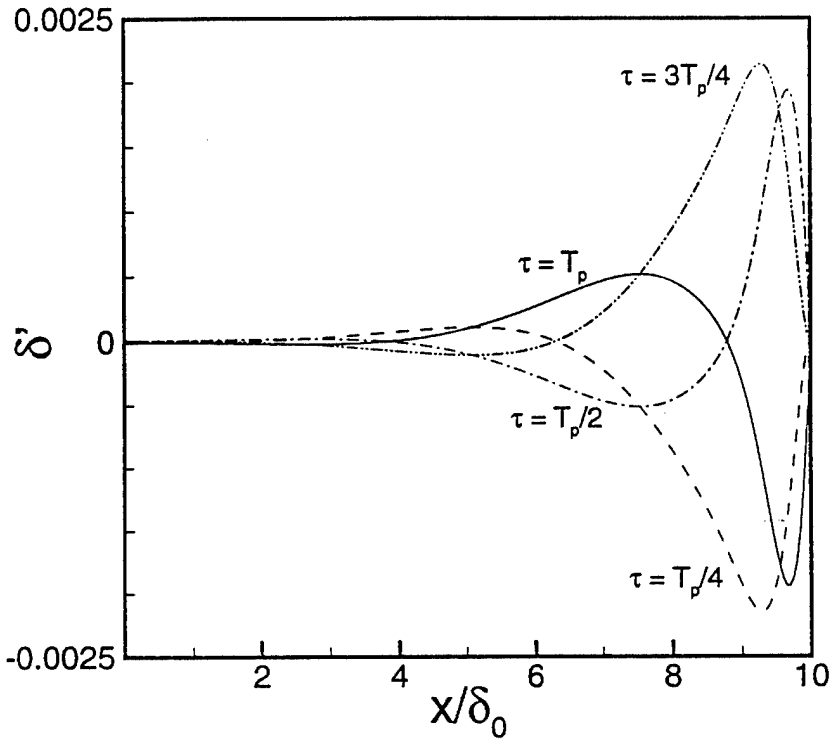

FIG. 10. Mehring, Phys. Fluids

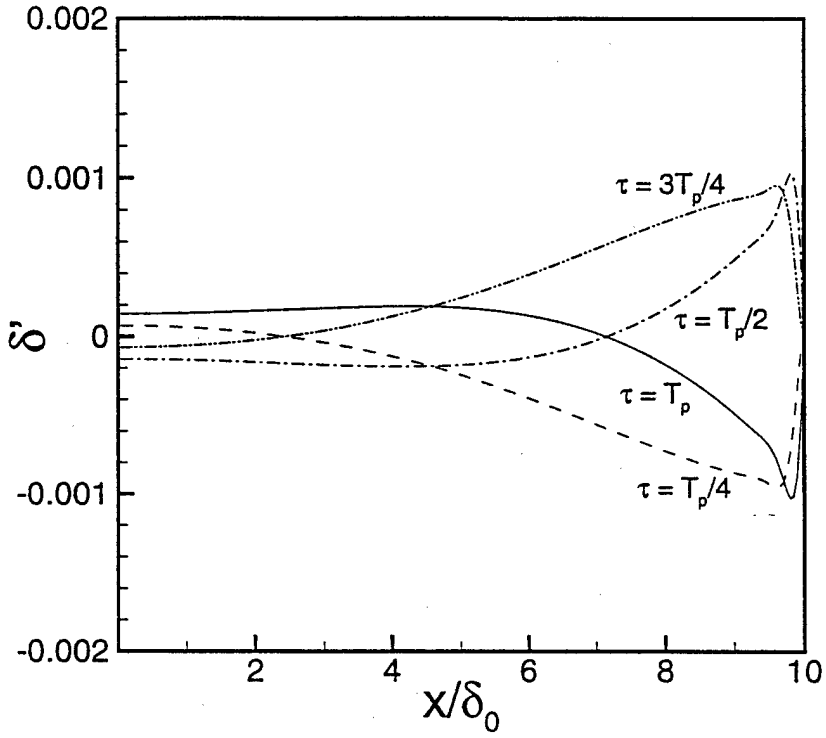

FIG. 11. Mehring, Phys. Fluids

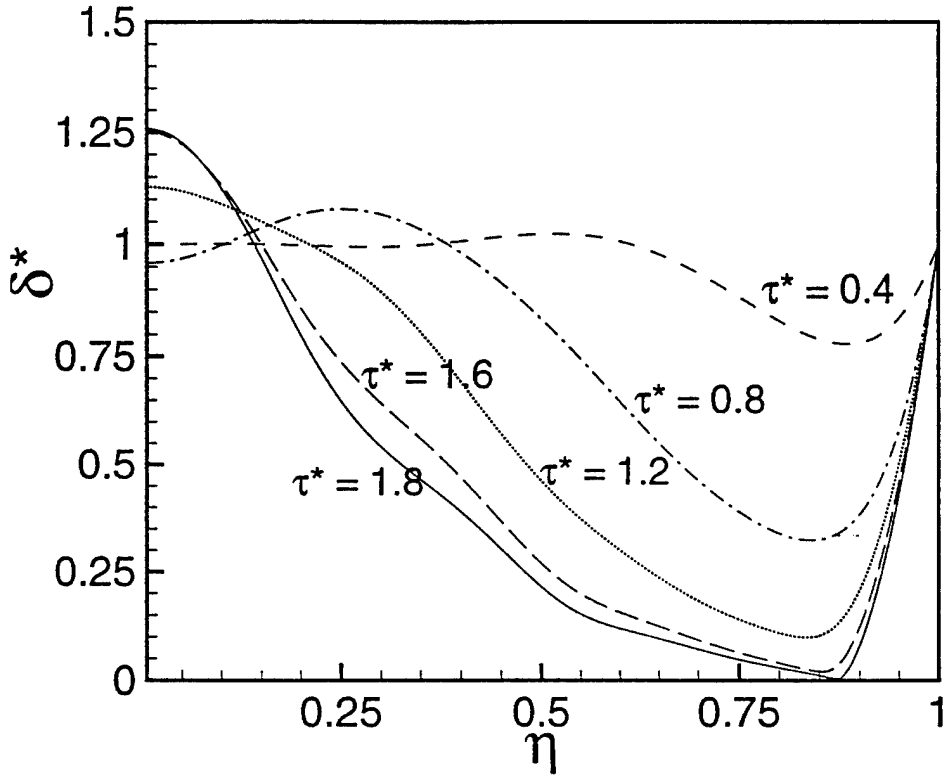

FIG. 12. Mehring, Phys. Fluids

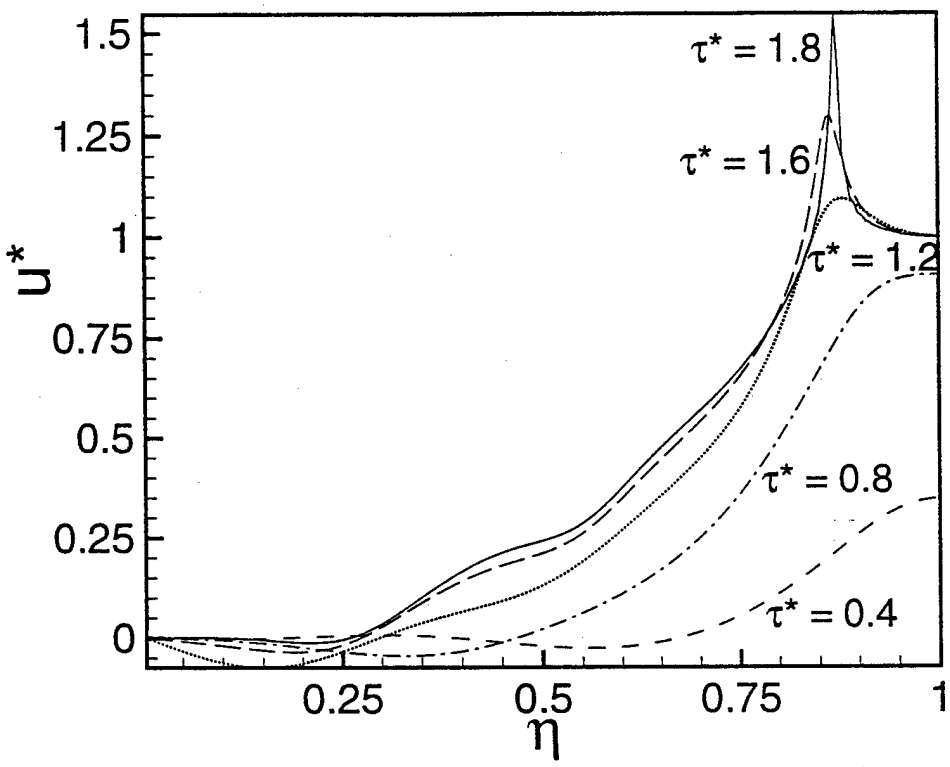

FIG. 13. Mehring, Phys. Fluids

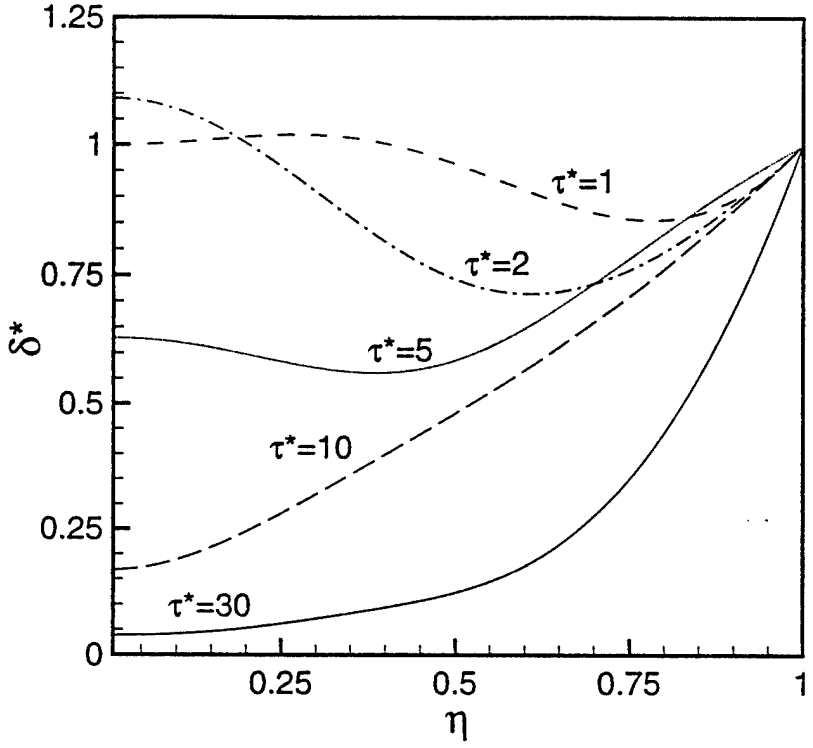

FIG. 14. Mehring, Phys. Fluids

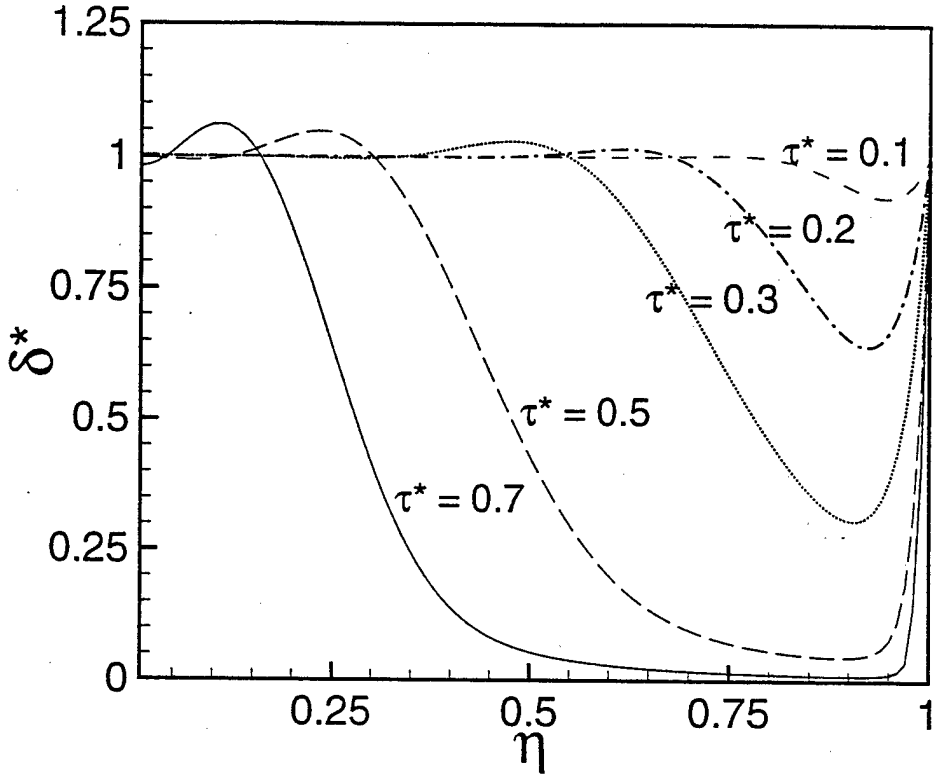

FIG. 15. Mehring, Phys. Fluids

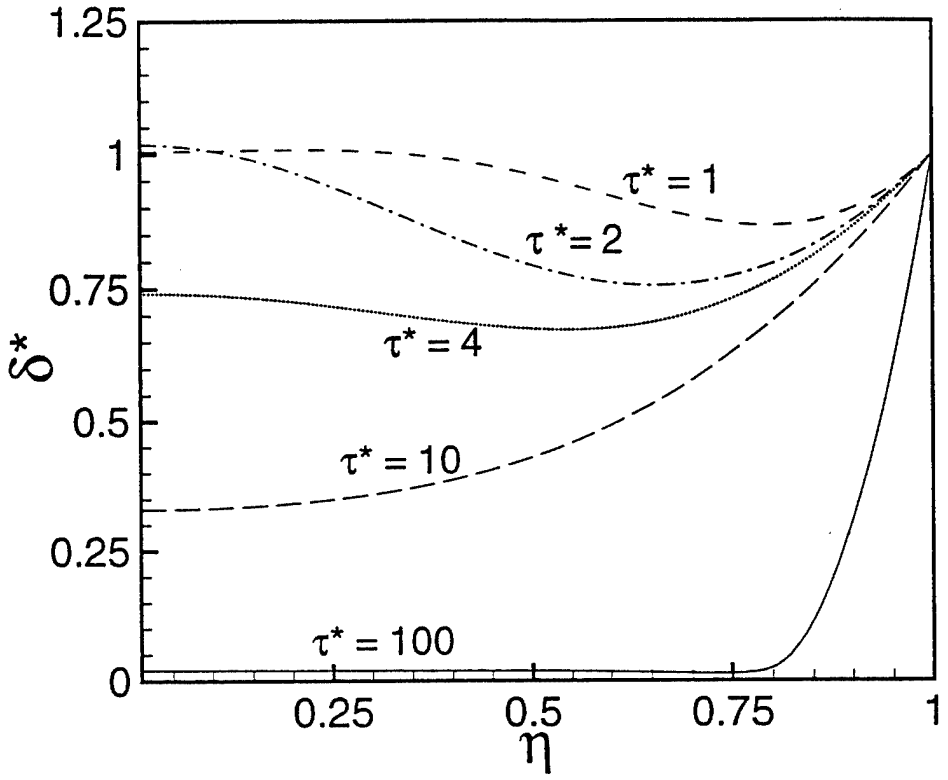

FIG. 16. Mehring, Phys. Fluids

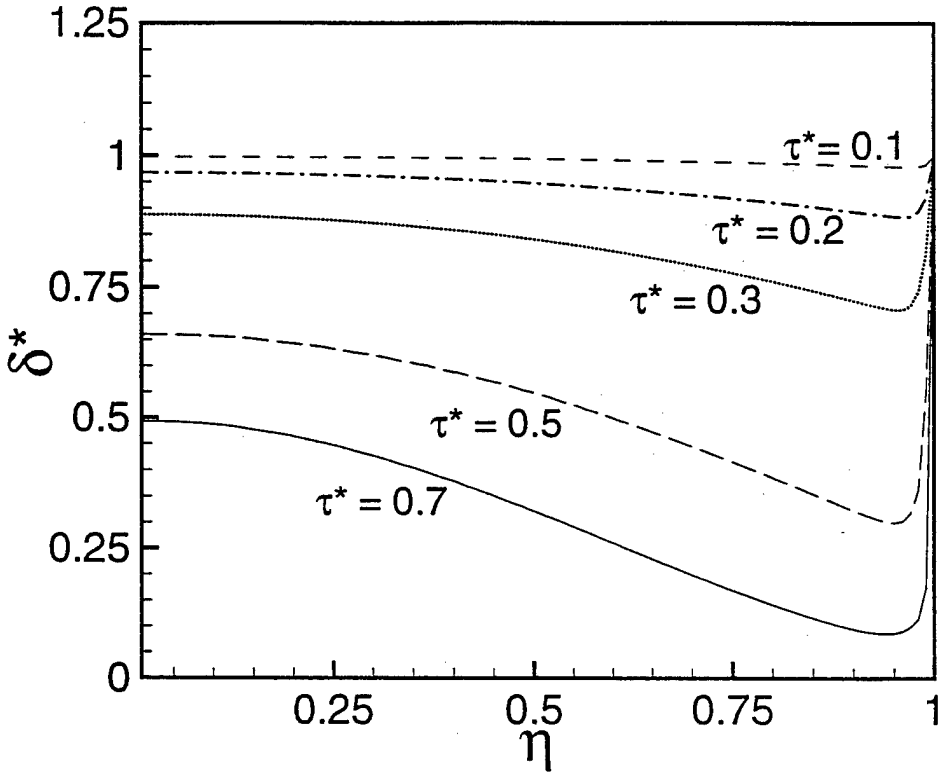

FIG. 17. Mehring, Phys. Fluids

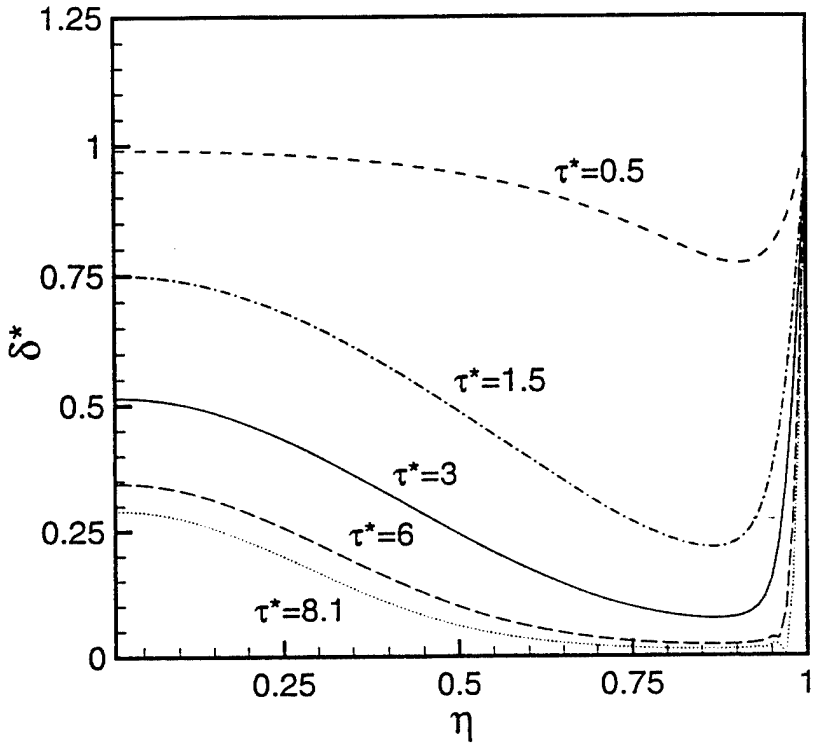

FIG. 18. Mehring, Phys. Fluids

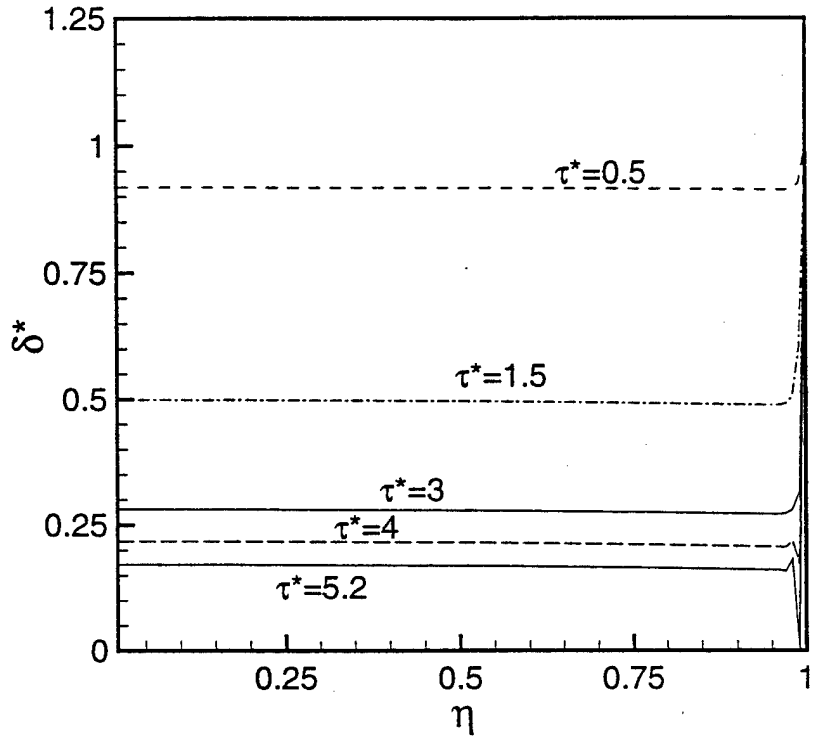

FIG. 19. Mehring, Phys. Fluids

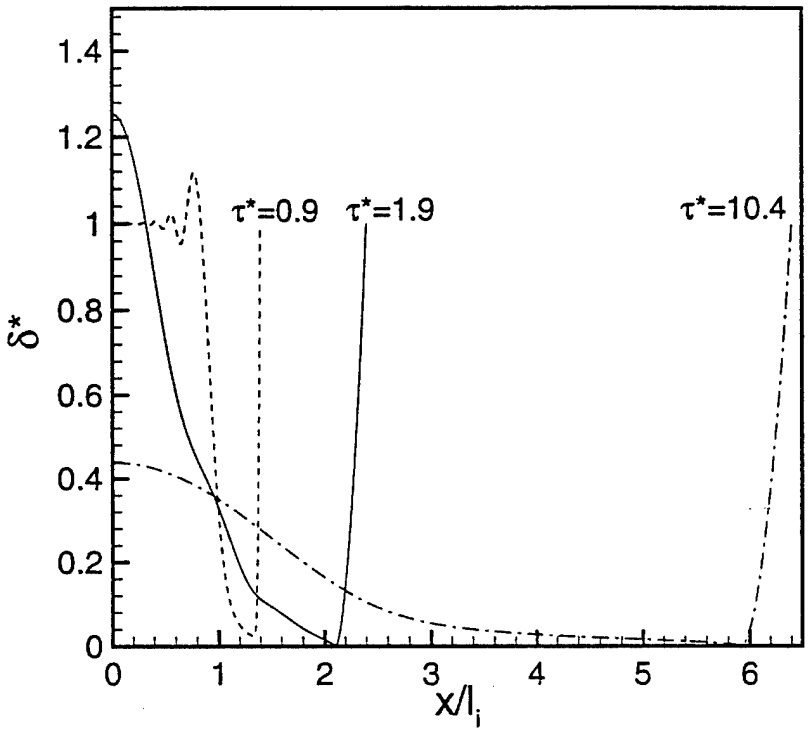

FIG. 20. Mehring, Phys. Fluids

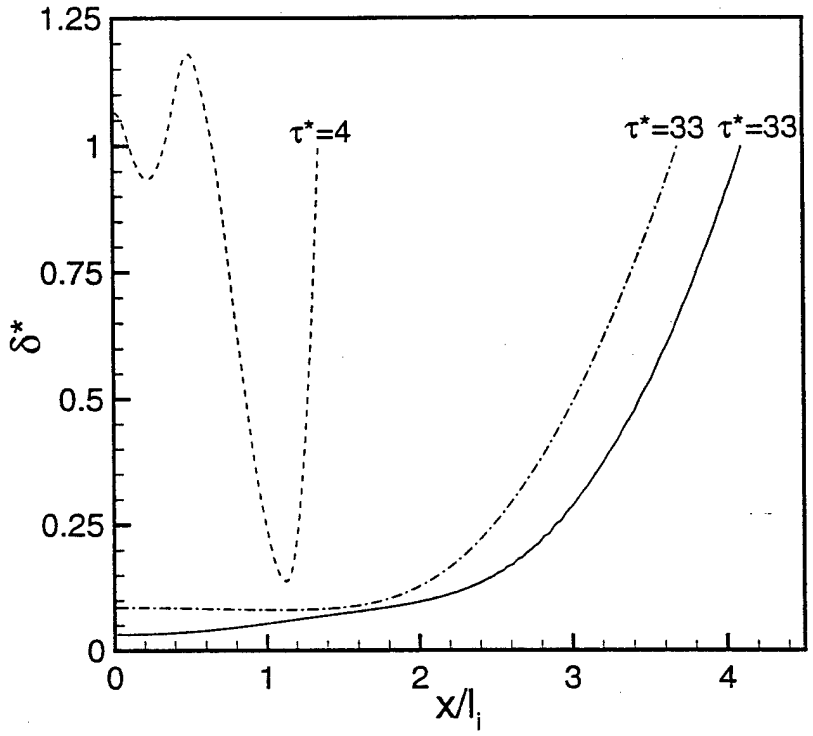

FIG. 21. Mehring, Phys. Fluids

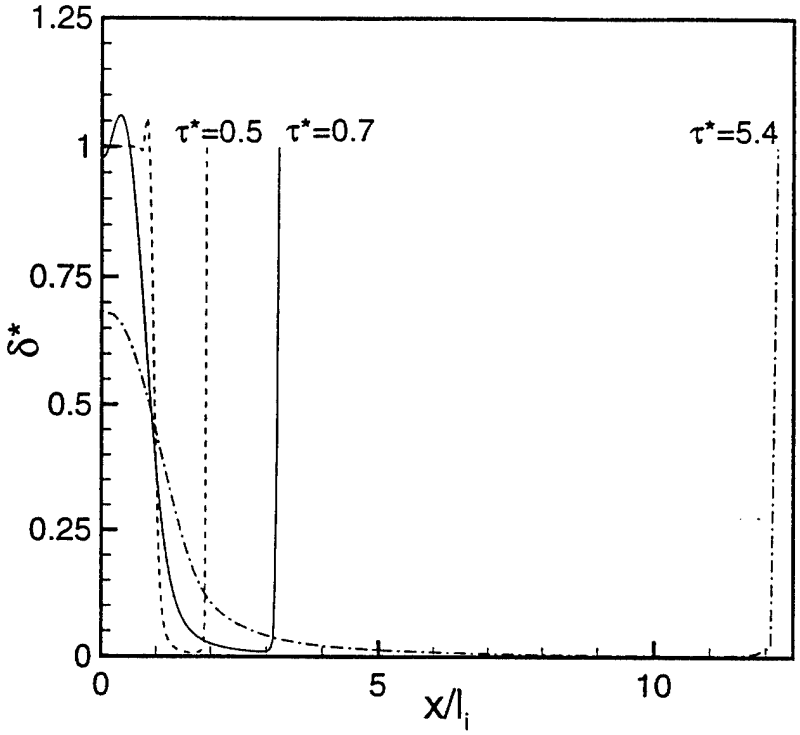

FIG. 22. Mehring, Phys. Fluids

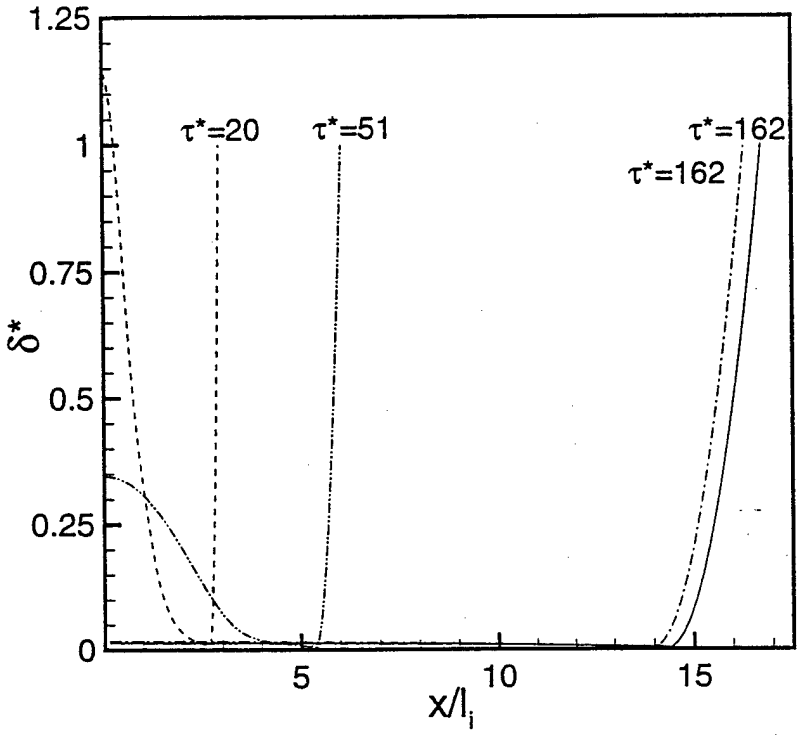

FIG. 23. Mehring, Phys. Fluids

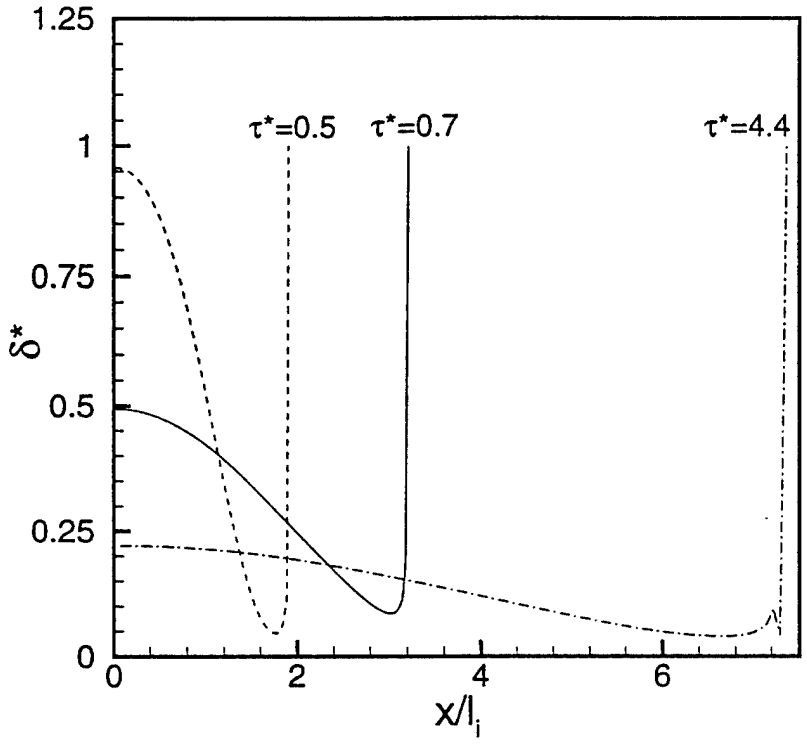

FIG. 24. Mehring, Phys. Fluids

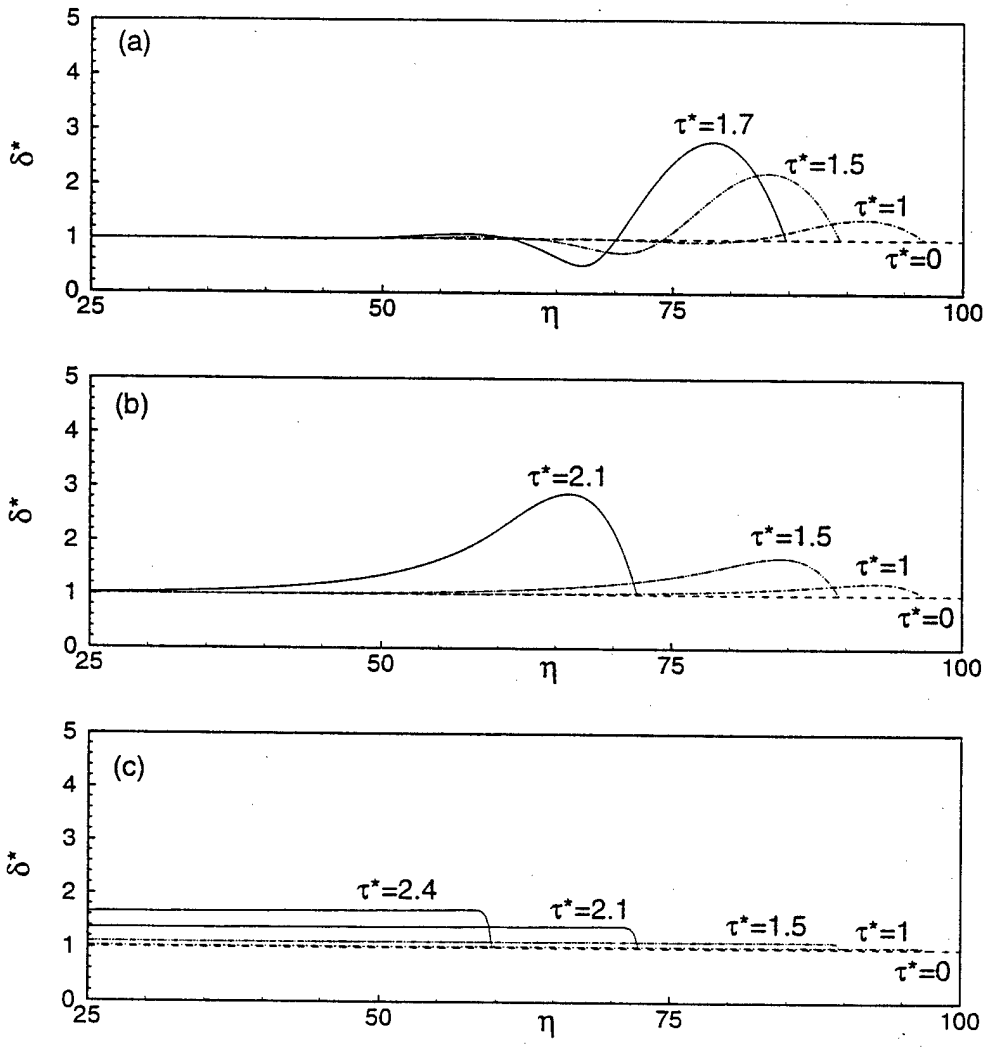

FIG. 25. Mehring, Phys. Fluids

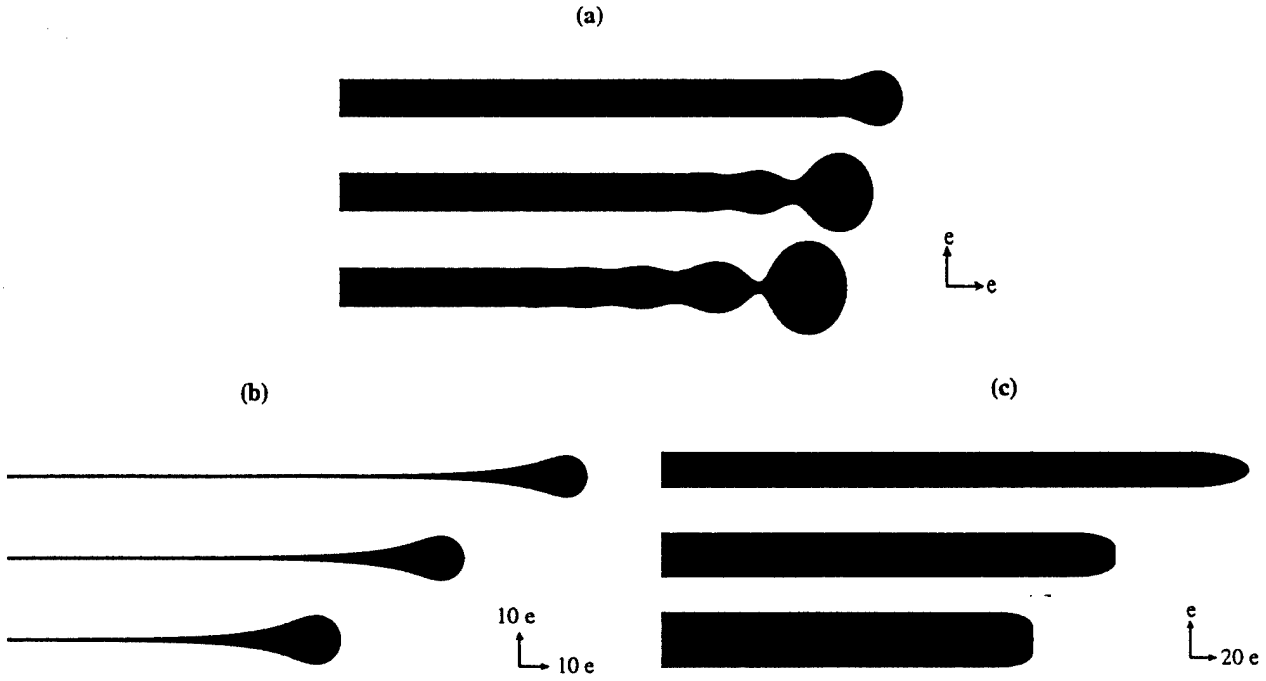

FIG. 26. Mehring, Phys. Fluids

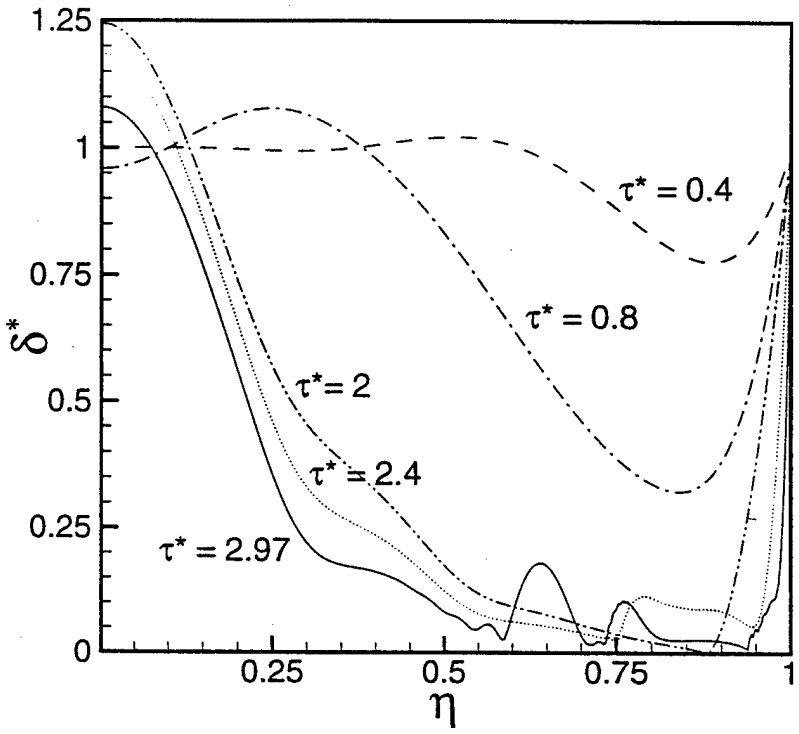

FIG. 27. Mehring, Phys. Fluids